

THERMOPLASTIC SIZINGS: EFFECTS ON PROCESSING, MECHANICAL
PERFORMANCE, AND INTERPHASE FORMATION IN PULTRUDED
CARBON FIBER/VINYL-ESTER COMPOSITES

By

Norman S. Broyles

Dissertation submitted to the faculty of the Virginia Polytechnic Institute and State University in
partial fulfillment of the requirements for the degree of

Doctor of Philosophy

in

Chemical Engineering

Professor R. Davis, Co-chair

Professor J. Lesko, Co-chair

Professor D. Baird

Professor E. Marand

Professor J. Riffle

December 9, 1999
Blacksburg, Virginia

Keywords: Sizings, Composites, Pultrusion, Interdiffusion, Finite Element Method

THERMOPLASTIC SIZINGS: EFFECTS ON PROCESSING, MECHANICAL PERFORMANCE, AND INTERPHASE FORMATION IN PULTRUDED CARBON FIBER/VINYL-ESTER COMPOSITES

Norman S. Broyles

(ABSTRACT)

Carbon fiber composites have typically been used in high-end aerospace applications. In order for these composites to find acceptance in civilian markets, like infrastructure and high-speed civil transportation, the cost of the processing steps and raw materials must be reduced while maintaining or improving their performance.

Sizings, a thin polymer coating applied to the surface of the carbon fiber before impregnation with the matrix, have been shown to affect the mechanical performance of the composite. These sizings affect the processability and wettability of the carbon fiber that translates into a composite with less fiber breakage and improved fiber/sizing/matrix adhesion. In addition, the interdiffusion of the sizing and the bulk matrix results in the formation of an interphase. This interphase can alter damage initiation and propagation that can ultimately affect composite performance. This suggests that optimizing the sizing constituent for the composite's matrix material could drastically improve composite properties without significantly affecting their cost. The overall objective of the work detailed in this thesis is to ascertain the effects that sizing agents have on composite performance (composite surface finish, cost of processing, and mechanical properties of the composite) and determine the phenomenological events associated with the effects. Specifically, the three major objectives for the work presented in this thesis were as follows:

1. To elucidate the *relative* importance of the sizing's processability, fiber/sizing/matrix adhesion, interphase, and matrix plasticization effects on the mechanical performance of the final composite.
2. To obtain constitutive data on the sizing/matrix interdiffusion process.
3. To fundamentally predict the interphase profile from mass transfer concepts.

Hexcel AS-4 carbon fibers were sized at Virginia Tech with two thermoplastic materials and Dow Derakane™ vinyl-ester composites were pultruded from these. In addition, the standard G' sized Hexcel carbon fibers were pultruded for a benchmark comparison. The thermoplastic sizing agents were poly(hydroxyether)/Phenoxy™ and K-90

poly(vinylpyrrolidone) PVP. The various carbon fibers were processed into composites utilizing a pilot scale pultruder and a pultrudable Dow Derakane™ vinyl-ester resin. All of the thermoplastic sizings had improved processability (i.e. less fiber breakage and improved fiber alignment) over the traditional G' sizing. In addition, the Phenoxy™ sizing reduced the pull-force required to produce the composite part by a factor of two. These improvements in processability translated into a composite with less fiber damage and improved surface quality. In addition, all of the thermoplastic sizings outperformed the industrial benchmark sizing G' by at least 25% in static tensile strength, 11% in longitudinal flexure strength, and 30% in short beam shear strength. All moduli were found to be unaffected by the addition of a sizing.

These processability and mechanical performance enhancements were achieved by altering a 1-3 wt% feature on the surface of the carbon fiber reinforcement. This corresponds to a material that occupied less than 2 wt% in the final composite. Because these thermoplastic sizing materials were commercially available materials and because such a low amount of them was needed to greatly improve mechanical properties, these sizing materials would make excellent replacements for the standard G' or oligomeric epoxies that are presently being utilized in pultrusion of carbon fiber/vinyl-ester composites.

In a second pultrusion trial, the interphase effect on longitudinal flexure strength was investigated. K-90 and K-30 PVP sized carbon fiber/vinyl-ester composites were produced. Due to identical repeat units but drastically different molecular weights, the K-90 and K-30 PVP interphase concentration profiles were drastically different. However, the difference in interphase concentration profiles between the K-90 and K-30 PVP systems did not alter the longitudinal flexure strength or modulus of the final composite.

The interphase formed in K-90 PVP sized carbon fiber composites was fundamentally predicted from the constitutive properties of K-90 PVP/Derakane™ interdiffusion and fundamental mass transport equations. In order to evaluate the interdiffusion phenomena being modeled, dielectric properties of K-90 PVP/Derakane™ bilayer films undergoing interdiffusion were examined. The relative time scales of swelling, relaxation, and dissolution were determined. The K-90 PVP sizing material interdiffusing with the Derakane™ matrix was found to be dissolution controlled. The swelling and relaxation stages were found to be negligible compared to the dissolution stage. The K-90 PVP/Derakane™ dissolution coefficient was

determined from the Stokes-Einstein equation. The dissolution diffusion coefficient was highly non-fickian and had an exponential concentration dependence.

Fundamental mass transport models and the finite element method (FEM) were utilized to predict the interphase profile as a function of the non-fickian dissolution diffusion coefficient, processing parameters, and physical properties of the K-90 PVP/Derakane™. The non-fickian FEM model was applied to the constitutive properties determined for the K-90 PVP/Derakane™ system. The predicted K-90 PVP interphase concentration profile displayed steep gradients at the fiber/matrix interface but essentially no gradients at points distant from the fiber surface. This was indicative of the exponential concentration dependence in the dissolution diffusion coefficient. The predicted mechanical property profile was essentially flat for the modulus but did show a steep gradient in the strain-to-failure and shrinkage properties. However, the K-90 PVP interphase compared to the unsized/pure Derakane™ interphase showed improvements in strength and strain-to-failure and a reduction in cure shrinkage without significantly affecting the interphase tensile or shear moduli. Because the interphase shear modulus is unaffected by the addition of the K-90 PVP, the K-90 PVP and unsized composite interphases will have identical interfacial shear strengths assuming no-slip at the fiber/matrix interface. However, the higher K-90 PVP interphase strength and strain-to-failure for a given modulus will allow a much greater interfacial shear stress to exist before transverse cracking and composite catastrophic failure resulted. As a result, the applied load at which transverse cracking initiated will be shifted to higher values for the K-90 PVP interphase compared to the unsized interphase. The presence of K-90 PVP in the Derakane™ matrix resulted in a reduction in cure shrinkage. As a result, the residual stresses present at the fiber/matrix interface after cure will be significantly less for the K-90 PVP interphase as compared to the unsized system.

The predicted interphase mechanical property profile can be used to partially explain the improvements in composite performance observed in the K-90 PVP sizing system. In view of the best theories for interfacial effects on unidirectional composite tensile strength, the improvements discussed previously cannot be attributed to changes in fiber/sizing/matrix adhesion or interphase formation alone. The large increases in composite tensile strength were most likely due to fiber/sizing/matrix adhesion and interphase effects as well as alterations in the fiber properties as a result of better fiber protection.

The model developed in conjunction with this work can be utilized as a screening tool for selecting potential sizing materials. With the acquisition of limited experimental data such as rheological and tensile properties of sizing/matrix blends, the model can be utilized to determine the interphase mechanical property profile existing in the final composite. This information can be utilized to determine whether a proposed sizing material will have a positive impact on composite performance.

ACKNOWLEDGMENTS

The author would like to thank Dr. R. M. Davis and Dr. J. J. Lesko, co-committee chairmen, for their support and patience over the past several years. Appreciation is also expressed to committee members, Dr. J. S. Riffle, Dr. D. Baird, and Dr. E. Marand.

This work was financially supported by a number of organizations. The National Science Foundation Science and Technology Center at Virginia Tech provided a three-year fellowship that was utilized from 1996 through 1999. The Adhesive and Sealant Council Educational Foundation provided a fellowship for both 1998 and 1999. Finally, the Virginia Space Grant Consortium also provided a fellowship for both 1998 and 1999.

The author would like to thank the Designed Interphase Group (DIG) at Virginia Tech for their assistance in the completion of this work. The material presented in this thesis is just a small sampling of the sizing related knowledge that exists within the DIG. In particular, Dr. J. S. Riffle, Dr. Nikhil Verghese, Ms. Maggie Bump, Ms. Ellen Burts, Mr. Mark Flynn, and Mrs. Angie Flynn are gratefully acknowledged.

The author would also like to thank Dr. David Kranbuehl and his students at the College of William and Mary. Their assistance in completing the dielectric work discussed in Chapter 5 was of paramount importance to the overall understanding of sizing/matrix interdiffusion.

The author would like to thank Mr. Herbert Engelen of the Dow Chemical Company for his help and assistance in conducted a set of pultrusion trials discussed in Chapter 3. In addition, Mr. Engelen is gratefully acknowledged for his help in establishing a pultrusion system at Virginia Tech.

The author would also like to thank Strongwell, Inc. for their assistance in conducting two sets of pultrusion trials. Their knowledge in the area of pultrusion greatly assisted the DIG in further designing sizings for the composites community.

A special thanks is extended to Mrs. Diane Cannaday, Mrs. Chris Moore, and Mrs. Diane Patty for their patience in dealing with the multitude of issues the author presented them with over the years. Their smiles and helpfulness made my stay much more pleasant.

The author would like to thank the many friends he meet during his stay at Virginia Tech. Appreciation is expressed to all the professors whose knowledge and wisdom were invaluable. The author wishes to thank all the graduate students who have made his stay enjoyable.

The author would like to thank his parents for their emotional support over the past few years. A special thanks goes to his mom, Sandra L. Spangler, for her help in making it through the tough times. She was the one who encouraged him when times were rough.

In addition, the author would like to thank his beautiful, loving, and sweet wife, Jill. Her patience and support have made his final two years in graduate school much more enjoyable.

Finally, the author would like to thank God for His patience with him. The author prays that all of his future endeavors will be in service of Him and the greater good of humankind.

CONTENTS

ACKNOWLEDGEMENTS	vi
TABLE OF CONTENTS	viii
LIST OF FIGURES	xii
LIST OF TABLES	xx
1 MOTIVATION	1
1.1 BACKGROUND	2
1.2 SIZED FIBER LIFE CYCLE	3
1.2.1 Stage I: The Sizing Process	3
1.2.2 Stage II: Pultrusion — Pre-Processing	7
1.2.3 Stage III: Pultrusion — Resin Dip Bath	7
1.2.4 Stage IV: Pultrusion — Preforming	10
1.2.5 Stage V: Pultrusion — The Die/Cure	11
1.3 MECHANISMS FOR SIZINGS EFFECTS	12
1.4 RESEARCH OBJECTIVES	13
1.5 THESIS OUTLINE	13
1.6 REFERENCES	14
2 INTRODUCTION	16
2.1 SIZINGS: EFFECTS ON COMPOSITE PERFORMANCE	16
2.1.1 <i>Sizings: Effect on Fiber Processability</i>	17
2.1.1.1 Processability: Sizing’s Effect on Fiber Protection.....	18
2.1.1.2 Sizings: Effect on Wettability.....	19
2.1.2 <i>Sizings: Effect on Fiber/Matrix Adhesion</i>	23
2.1.2.1 Fundamental: ISS - Relation to Fiber and Matrix Properties	23
2.1.2.2 Fundamental: On-Axis Properties - Correlation with ISS.....	24
2.1.2.3 Experimental: Sizings and or Surface Treatments - Effects on ISS and Bulk Composite Mechanical Performance	27
2.1.3 <i>Sizings: Effect on the Formation of an Interphase</i>	38
2.2 FUNDAMENTALS OF INTERPHASE FORMATION	43
2.2.1 <i>Interdiffusion of a Polymer and a Solvent</i>	44
2.2.2 <i>Preferential adsorption of a matrix and/or sizing constituent</i>	49
2.3 THEORY OF DIELECTRIC SPECTROSCOPY	49
2.4 FINITE ELEMENT METHOD APPLIED TO PARABOLIC DEQ’S	51
2.5 REFERENCES	51
3 INTRODUCTION	57
3.1 MECHANICAL PERFORMANCE OF PULTRUDED HEXCEL AS-4 CARBON FIBER/VINYL ESTER COMPOSITES PROCESSED WITH G’, PHENOXY, AND K-90 PVP SIZING AGENTS	64
3.1.1 <i>Abstract</i>	64
3.1.2 <i>Introduction</i>	65
3.1.3 <i>Experimental</i>	68
3.1.3.1 Materials	68
3.1.3.2 Processing.....	70
3.1.3.2.1 <i>Sizing Solution/Suspension Preparation</i>	70
3.1.3.2.2 <i>Sized Fiber Preparation</i>	71
3.1.3.2.3 <i>Pultrusion</i>	72
3.1.3.3 Characterization Methods	72

3.1.3.3.1	<i>Sized Fiber Characterization</i>	72
3.1.3.3.2	<i>Composite Characterization</i>	74
3.1.3.4	Mechanical Testing	76
3.1.3.4.1	<i>Tension Testing</i>	76
3.1.3.4.2	<i>Flexure and Short Beam Shear Testing</i>	76
3.1.3.4.3	<i>Compression Testing</i>	77
3.1.3.4.4	<i>Normalization of Mechanical Properties for Fiber Volume Fraction Variations</i>	78
3.1.4	Results and Discussion	79
3.1.4.1	Processing	79
3.1.4.1.1	<i>Sized Fiber Preparation</i>	79
3.1.4.1.2	<i>Pultrusion</i>	83
3.1.4.2	Composite Characterization	84
3.1.4.2.1	<i>Fiber Volume Fraction</i>	84
3.1.4.2.2	<i>Visual Inspection of Cut Composite</i>	85
3.1.4.2.3	<i>Optical Micrographs of Composite Cross-sections</i>	86
3.1.4.2.4	<i>Ultrasonic C-Scan</i>	89
3.1.4.3	Mechanical Properties	89
3.1.4.3.1	<i>Static Tensile Properties</i>	89
3.1.4.3.2	<i>Longitudinal Flexure Properties</i>	92
3.1.4.3.3	<i>Short Beam Shear Properties</i>	96
3.1.4.3.4	<i>Compressive Properties</i>	98
3.1.5	Conclusions	100
3.1.6	Acknowledgments	101
3.2	MECHANICAL PERFORMANCE OF PULTRUDED HEXCEL AS-4 CARBON FIBER/VINYL ESTER COMPOSITES PROCESSED WITH G', PHENOXY, K-90, AND K-30 PVP SIZING AGENTS	102
3.2.1	Abstract	102
3.2.2	Introduction	103
3.2.3	Experimental	104
3.2.3.1	Materials	104
3.2.3.2	Processing	106
3.2.3.2.1	<i>Sizing Solution/Suspension Preparation</i>	106
3.2.3.2.2	<i>Sized Fiber Preparation</i>	107
3.2.3.2.3	<i>Pultrusion</i>	107
3.2.3.3	Characterization Methods	108
3.2.3.3.1	<i>Sized Fiber Characterization</i>	108
3.2.3.3.2	<i>Composite Characterization</i>	109
3.2.3.4	Mechanical Testing	112
3.2.3.4.1	<i>Flexure and Short Beam Shear Testing</i>	112
3.2.3.4.2	<i>Normalization of Mechanical Properties for Fiber Volume Fraction Variations</i>	112
3.2.4	Results and Discussion	113
3.2.4.1	Processing	113
3.2.4.1.1	<i>Sized Fiber Preparation</i>	113
3.2.4.1.2	<i>Pultrusion (Completed by and observed by H. Engelen of Dow Chemical)</i>	114
3.2.4.2	Composite Characterization	120
3.2.4.2.1	<i>Fiber Volume Fraction</i>	120
3.2.4.3	Mechanical Testing	123
3.2.4.3.1	<i>Longitudinal Flexure Properties</i>	123
3.2.4.3.2	<i>Short Beam Shear Properties</i>	125
3.2.5	Conclusions	127
3.2.6	Acknowledgments	128
3.3	STATIC COMPRESSIVE PERFORMANCE OF PULTRUDED CARBON FIBER/VINYL ESTER COMPOSITES PROCESSED WITH PHYSICALLY DISSIMILAR SIZING AGENTS	129
3.3.1	Abstract	129
3.3.2	Introduction	129
3.3.3	Experimental	130
3.3.3.1	Materials	130
3.3.3.2	<i>Sized Fiber Preparation (discussed earlier in section 3.1.3.2.2)</i>	131
3.3.3.3	Pultrusion	132
3.3.3.4	Material Testing	132
3.3.4	Results and Discussion	133

3.3.4.1	Pultrusion.....	133
3.3.4.2	Static Compressive Properties	133
3.3.5	Conclusions.....	135
3.3.6	Acknowledgments.....	136
3.4	OVERALL SUMMARY.....	137
3.5	REFERENCES	139
4	INTRODUCTION.....	141
4.1	GEOMETRY OF INTERDIFFUSION DOMAIN	145
4.2	MASS TRANSFER THEORY	147
4.2.1	Governing Equations for Interphase Formation.....	147
4.2.1.1	Initial Condition.....	148
4.2.1.2	Boundary Conditions	148
4.3	ANALYTICAL MODELS FOR INTERPHASE FORMATION.....	149
4.4	FINITE ELEMENT SIMULATION OF INTERPHASE FORMATION.....	153
4.4.1	Derivation of Finite Element Equations	154
4.4.1.1	Imposition of Boundary Condition at Sizing/Matrix Interface.....	159
4.4.2	Mesh Generation for Idealized Composite Interphase	160
4.4.3	Shape Function Used in FEM Approximation	164
4.4.4	Integrations over the Master Element.....	165
4.4.5	Storage of Matrices in Banded Form.....	169
4.4.6	Verification of the FEM Code Against an Analytical Solution	171
4.4.7	The Effect of Iterative Looping on the Solution	175
4.4.8	The Effect of the Time Step Size	179
4.4.9	The Effect of the Number of Elements in the Mesh	184
4.5	RESULTS OF FICKIAN FEM APPLIED TO THE THEORETICAL COMPOSITE.....	185
4.5.1	Review of the Results for the Fickian FEM Code Applied to the Theoretical Composite.....	185
4.6	NON-FICKIAN FEM MODEL APPLIED TO THE THEORETICAL COMPOSITE.....	188
4.6.1	Theoretical Prediction of the K-90 PVP Composite Interphase	189
4.6.2	Theoretical Prediction of the K-30 PVP Composite Interphase	196
4.7	SUMMARY	199
4.8	DIFFUSION IN PULTRUDER DIE	200
4.9	REFERENCES	202
5	INTRODUCTION.....	203
5.1	THEORY OF DIELECTRIC SPECTROSCOPY	204
5.2	EXPERIMENTAL	210
5.2.1	Materials.....	210
5.2.2	Equipment	212
5.2.2.1	Dielectric Equipment	212
5.2.2.1.1	Sensors	212
5.2.2.1.2	Impedence Analyzer	212
5.2.2.2	Profileometer	212
5.2.3	Separation of Phenoxy TM particles from suspension	212
5.2.4	Preparation of sizing/solvent dip coating solutions.....	213
5.2.5	Profilometry to determine sensor flatness.....	214
5.2.6	Preparing the sensors to be coated.....	214
5.2.7	Dip coating of the micro-dielectric sensors.....	217
5.2.8	Profilometry to determine coating thickness.....	217
5.2.9	Preparing blends for dielectric and mechanical property determination.....	218
5.2.10	Static dielectric experiments on blends.....	219
5.2.11	Static dielectric properties of K-90 PVP films.....	219
5.2.12	Transient dielectric experiments of interdiffusion	220

5.2.13	Density determination of the un-cured blends	220
5.2.14	Curing of the blends.....	221
5.2.15	Density determination of the cured blends.....	222
5.2.16	Shrinkage of Blends upon Cure	222
5.2.17	Glass transition temperature determination of the cured blends.....	222
5.2.18	Rheological Experiments on K-90 and K-30 Blends.....	223
5.2.19	Static tensile property determination of cured blends	223
5.3	RESULTS AND DISCUSSION (NOTE: BASIS FOR ALL ERROR BARS WAS 1- σ).....	223
5.3.1	Microdielectric Results and Discussion	223
5.3.1.1	Profilometry to determine sensor flatness	224
5.3.1.2	Dip coating of the micro-dielectric sensors.....	224
5.3.1.3	Penetration depth for micro-dielectric sensors.....	225
5.3.1.4	Static dielectric experiments on K-90 PVP film	228
5.3.1.5	Static dielectric experiments on K-90 PVP/Derakane Blends.....	229
5.3.1.6	Transient dielectric experiments of interdiffusion	232
5.3.1.6.1	Transient K-90 PVP Diffusing into Derakane	232
5.3.1.6.2	Transient K-90 PVP Diffusing into Styrene.....	236
5.3.2	Mechanical Properties Results and Discussion	238
5.3.2.1	Density determination of the un-cured blends	238
5.3.2.2	Density determination of the cured blends.....	238
5.3.2.3	Shrinkage of Blends upon Cure	238
5.3.2.4	Glass transition temperature determination of the cured blends (Completed by Dr. Chris Robertson).....	241
5.3.2.5	Rheological Experiments on K-90 and K-30 PVP Blends	241
5.3.2.5.1	K-90 PVP in Derakane TM Blends.....	241
5.3.2.5.2	K-30 PVP in Derakane TM Blends.....	246
5.3.2.6	Static tensile property determination of cured blends	248
5.4	ESTIMATION OF CONSTITUTIVE PROPERTIES NEEDED IN FEM MODEL.....	255
5.4.1	<i>Estimation of Dissolution Diffusion Coefficient</i>	255
5.4.1.1	K-90 PVP.....	257
5.4.1.2	K-30 PVP.....	257
5.4.2	<i>Estimation of Fiber/Matrix Interface Boundary Condition</i>	258
5.5	CONCLUSIONS	261
5.6	REFERENCES	262
	Guide to Appendices	263
	APPENDIX I	270
	APPENDIX II	275
	APPENDIX III	304
	VITA	308

FIGURES

Figure 1-1 Schematic of the pultrusion process.....	4
Figure 1-2 Schematic of the sizing process.....	4
Figure 1-3 Sizing life cycle: Sizing line depiction. a). Sketch of aqueous sizing solution or suspension dip bath. b). Sketch of drying portion of the process.....	6
Figure 1-4 Sized Fiber Life Cycle: Resin dip bath. a). Sized fiber wetting with the matrix resin. b). Resin infiltrating the fiber micro-capillaries where the driving force is controlled partially by the contact angle between the fiber and the resin.	8
Figure 1-5 Sized fiber life cycle: Sizing/Matrix interdiffusion. a). Initial configuration of the sizing in contact with the matrix. b). Sizing being swelled by a matrix constituent.....	9
Figure 1-6 Sized fiber life cycle: Sizing/Matrix interdiffusion. a). Polymer chains close to initial sizing/matrix interface are now relaxing. b). Relaxed polymer chains at the relaxed sizing/matrix begin to reptate and diffuse into the bulk matrix.	10
Figure 1-7 Schematic of the Interphase in the final composite. Region near the surface of the fiber represents pure sizing. Region remote from the fiber surface represents pure matrix. Region in between represents the interphase where both sizing and matrix reside.	11
Figure 2.1-1 Theoretical prediction of Reifsnider [2.16]. Variation of composite tensile strength as a function of the fibre/matrix interfacial shear strength, predicted by model.....	25
Figure 2.1-2 Normalized longitudinal flexure data of Madhukar et al [2.23].....	30
Figure 2.1-3 Normalized transverse flexure data of Madhukar et al [2.23].....	31
Figure 2.1-4 Normalized shear data of Madhukar et al [2.22].....	32
Figure 2.2-1 Six possible layers in polymer/solvent interdiffusion: (1) pure polymer (2) infiltrating area (3) swollen polymer (4) relaxed polymer (5) dissolution boundary layer and (6) pure solvent. First noted by K. Uberreiter and F. Asmussen [2.53,2.54].....	46
Figure 3.1-1 a). Chemical structure of poly(hydroxyether)/Phenoxy™ sizing material. b). Chemical structure of poly(vinylpyrrolidone) (PVP) sizing material. c). Chemical structure of vinyl-ester. d). Chemical structure of styrene monomer.....	69
Figure 3.1-2 Phenoxy particulate sized Hexcel AS-4 12K. Note: Surface temperature did not exceed 97°C or Phenoxy’s glass transition.	80
Figure 3.1-3 Phenoxy film sized Hexcel AS-4 12K. Note: Surface temperature exceeded 97°C or Phenoxy’s glass transition. $T_{\text{surface}}^{\text{max}} \approx 220^{\circ}\text{C}$	80
Figure 3.1-4 K-90 PVP sized Hexcel AS-4 12K (≈ 1.97 wt%). Note: Surface temperature exceeded 200°C. 230 X Magnification.	81
Figure 3.1-5 K-90 PVP sized Hexcel AS-4 12K (≈ 1.97 wt%). Note: Surface temperature exceeded 200°C. 1540 X Magnification.	81
Figure 3.1-6 Optical micrographs of cross-sectioned and polished pultruded Hexcel AS-4 G’ sized carbon fiber/vinyl-ester composite. 10 X magnification.	87
Figure 3.1-7 Optical micrographs of cross-sectioned and polished pultruded Hexcel AS-4 low spread Phenoxy sized or LSP carbon fiber/vinyl-ester composite. 10 X magnification.....	87

Figure 3.1-8 Optical micrographs of cross-sectioned and polished pultruded Hexcel AS-4 high-spread Phenoxo sized or HSP carbon fiber/vinyl-ester composite. 10 X magnification. 88

Figure 3.1-9 Optical micrographs of cross-sectioned and polished pultruded Hexcel AS-4 K-90 PVP sized carbon fiber vinyl-ester composite. 10 X magnification. 88

Figure 3.1-10 Static tensile strength of pultruded Hexcel carbon fiber/vinyl-ester composites with various sizing agents. Mechanical property results normalized from the theoretical fiber volume fraction to 65.6% or the theoretical fiber volume fraction of the G' sized composite. 90

Figure 3.1-11 Static tensile modulus of pultruded Hexcel carbon fiber/vinyl-ester composites with various sizing agents. Mechanical property results normalized from the theoretical fiber volume fraction to 65.6% or the theoretical fiber volume fraction of the G' sized composite. 90

Figure 3.1-12 Static tensile strain-to-failure of pultruded Hexcel carbon fiber/vinyl-ester composites with various sizing agents. Mechanical property results normalized from the theoretical fiber volume fraction to 65.6% or the theoretical fiber volume fraction of the G' sized composite. 91

Figure 3.1-13 Optical micrographs of tensile fracture surface for pultruded Hexcel AS-4 G' sized carbon fiber/vinyl-ester composite. 500 X magnification..... 93

Figure 3.1-14 Optical micrographs of tensile fracture surface for pultruded Hexcel AS-4 G' sized carbon fiber/vinyl-ester composite. 2,500 X magnification..... 93

Figure 3.1-15 Optical micrographs of tensile fracture surface for pultruded Hexcel AS-4 low-spread Phenoxo™ (LSP) sized carbon fiber/vinyl-ester composite. 500 X magnification. . 94

Figure 3.1-16 Optical micrographs of tensile fracture surface for pultruded Hexcel AS-4 low-spread Phenoxo™ (LSP) sized carbon fiber/vinyl-ester composite. 2,500 X magnification. 94

Figure 3.1-17 Optical micrographs of tensile fracture surface for pultruded Hexcel AS-4 K-90 PVP sized carbon fiber/vinyl-ester composite. 500 X magnification. 95

Figure 3.1-18 Optical micrographs of tensile fracture surface for pultruded Hexcel AS-4 K-90 PVP sized carbon fiber/vinyl-ester composite. 2,500 X magnification. 95

Figure 3.1-19 Static longitudinal flexure strength of pultruded Hexcel carbon fiber/vinyl-ester composites with various sizing agents. Mechanical property results normalized from the theoretical fiber volume fraction to 65.6% or the theoretical fiber volume fraction of the G' sized composite. 97

Figure 3.1-20 Static longitudinal flexure modulus of pultruded Hexcel carbon fiber/vinyl-ester composites with various sizing agents. Mechanical property results normalized from the theoretical fiber volume fraction to 65.6% or the theoretical fiber volume fraction of the G' sized composite. Normalization for differences in the inherent fiber properties included also. 97

Figure 3.1-21 Short beam shear (SBS) strength of pultruded Hexcel carbon fiber/vinyl-ester composites with various sizing agents. Mechanical property results normalized from the theoretical fiber volume fraction to 65.6% or the theoretical fiber volume fraction of the G' sized composite. 98

Figure 3.1-22 Compression strength of pultruded Hexcel carbon fiber/vinyl-ester composites with various sizing agents. Mechanical property results normalized from the theoretical fiber volume fraction to 65.6% or the theoretical fiber volume fraction of the G' sized composite. 99

Figure 3.1-23 Compression modulus of pultruded Hexcel carbon fiber/vinyl-ester composites with various sizing agents. Mechanical property results normalized from the theoretical fiber volume fraction to 65.6% or the theoretical fiber volume fraction of the nature, the G' composite had numerous kink-bands. These kink-bands lead to a lower static compressive strength for the G' materials. G' sized composite. Normalization for differences in the inherent fiber properties included also.	99
Figure 3.2-1 SEM of G' sized Hexcel carbon fiber. Magnification was 600X. Sizing level was 0.79wt%.....	115
Figure 3.2-2 SEM of G' sized Hexcel carbon fiber. Magnification was 1,800X. Sizing level was 0.79wt%.....	115
Figure 3.2-3 K-30 PVP sized Hexcel AS-4 12k carbon fiber. Magnification was 600X. Sizing level was 0.92 ± 0.06 wt%.	116
Figure 3.2-4 K-30 PVP sized Hexcel AS-4 12k carbon fiber. Magnification was 1,800X. Sizing level was 0.92 ± 0.06 wt%.	116
Figure 3.2-5 K-90 PVP sized Hexcel AS-4 12k carbon fiber. Magnification was 600X. Sizing level was 0.99 ± 0.19 wt%.	117
Figure 3.2-6 K-90 PVP sized Hexcel AS-4 12k carbon fiber. Magnification was 1,800X. Sizing level was 0.99 ± 0.19 wt%.	117
Figure 3.2-7 Phenoxy™ sized Hexcel AS-4 12k carbon fiber. Magnification was 600X. Sizing level was 0.89 ± 0.08 wt%.	118
Figure 3.2-8 Phenoxy™ sized Hexcel AS-4 12k carbon fiber. Magnification was 1,800X. Sizing level was 0.89 ± 0.08 wt%.	118
Figure 3.2-9 Pull-force required to produce composite of 15mm X 3mm cross-section for various sizing materials. K-90 PVP 52 represents a composite produced from 52 ends of fiber sized with K-90 PVP. Phenoxy 52 represents a composite produced from 52 ends of fiber sized with Phenoxy™.....	120
Figure 3.2-10 Theoretical and experimental fiber volume fraction for the various sizings. No error bars were determined for the experimental fiber volume fractions due to a lack of data points.	121
Figure 3.2-11 Filler weight fraction in the matrix (note: carbon fiber constituent has been removed to determine extent of filler inclusion in the composite as compared to the virgin matrix. The filler weight fraction in the virgin matrix was 0.089. No standard deviations were determined for the experimental fiber volume fractions due to a lack of data points.....	122
Figure 3.2-12 Longitudinal flexure strength of the pultruded Hexcel carbon fiber/vinyl-ester composites with various sizing agents. The strengths were normalized for variations in fiber volume fraction utilizing the value for the theoretical fiber volume fraction. Values shown are for a theoretical composite having a 59.2% fiber volume fraction.....	124
Figure 3.2-13 Longitudinal flexure modulus of the pultruded Hexcel carbon fiber/vinyl-ester composites with various sizing agents. The moduli were normalized for variations in fiber volume fraction utilizing the value for the theoretical fiber volume fraction. Values shown are for a theoretical composite having a 59.2% fiber volume fraction.	126
Figure 3.2-14 Short beam shear (SBS) strength of pultruded Hexcel carbon fiber/vinyl-ester composites with various sizing agents. The moduli were normalized for variations in fiber volume fraction utilizing the value for the theoretical fiber volume fraction. Values shown are for a theoretical composite having a 59.2% fiber volume fraction.	126

Figure 3.3-1 Static compressive strength of pultruded vinyl-ester composite with the following carbon fiber reinforcements. G' sized Hexcel AS-4, poly(urethane) sized Zoltek Panex, and K-30 PVP sized Zoltek Panex. Note: Data not normalized for fiber volume fraction variations.	134
Figure 3.3-2 Static compressive modulus of pultruded vinyl-ester composite with the following carbon fiber reinforcements. G' sized Hexcel AS-4, poly(urethane) sized Zoltek Panex, and K-30 PVP sized Zoltek Panex. Note: Data not normalized for fiber volume fraction variations.	135
Figure 4.1-1 Optical Micrograph of a 65 volme % unidirectional pultruded Hexcel AS-4 G' carbon fiber/vinyl-ester composite cross-section.....	145
Figure 4.1-2 a.) Theoretical packing array: hexagonal packing array with lines drawn for the axis of symmetry b.) 60-30° triangular packing representing the fundamental unit of the theoretical composite.....	146
Figure 4.3-1 Planar source geometry utilized for simplification of the idealized composite.	150
Figure 4.3-2 Planar source model interphase profile as a function of the dissolution diffusion coefficient, D_d . Note: Processing time equal to 15 minutes. Units on D_d are cm^2/s	152
Figure 4.4-1 Schematic of angular subdivision of solution domain.	161
Figure 4.4-2 Finite Element mesh with angular subdivision, radial subdivision, element numbering, and node numbering shown.	162
Figure 4.4-3 Schematic of four noded Master Element.	163
Figure 4.4-4 a). Schematic of a symmetric banded matrix of dimension 12X12. b.) Schematic of the same matrix stored in banded form with dimension now 12X6.....	170
Figure 4.4-5 Comparison of Analytical Solution to Simplified Domain versus FEM Solution to Simplified Domain. ($D_d = 1.0 \mu\text{m}^2/\text{s}$, $w_s^{\text{eq}} = 0.3$, $M_s = 0.02$, $\theta = 0.5$, $dt = 0.0001$). Time = 0.000001 seconds.	173
Figure 4.4-6 Comparison of Analytical Solution to Simplified Domain versus FEM Solution to Simplified Domain. ($D_d = 1.0 \mu\text{m}^2/\text{s}$, $w_s^{\text{eq}} = 0.3$, $M_s = 0.02$, $\theta = 0.5$, $dt = 0.0001$). a). Time = 0.008 seconds.	173
Figure 4.4-7 Comparison of Analytical Solution to Simplified Domain versus FEM Solution to Simplified Domain. ($D_d = 1.0 \mu\text{m}^2/\text{s}$, $w_s^{\text{eq}} = 0.3$, $M_s = 0.02$, $\theta = 0.5$, $dt = 0.0001$). a). Time = 0.02 seconds.....	174
Figure 4.4-8 Comparison of Analytical Solution to Simplified Domain versus FEM Solution to Simplified Domain. ($D_d = 1.0 \mu\text{m}^2/\text{s}$, $w_s^{\text{eq}} = 0.3$, $M_s = 0.02$, $\theta = 0.5$, $dt = 0.0001$). Time = 0.125 seconds.	174
Figure 4.4-9 Comparison of Analytical Solution to Simplified Domain versus FEM Solution to Simplified Domain. ($f_s = 1.0\text{E-}7 \text{ g}/\text{cm}^2/\text{s}$, $D_d = 1.0 \mu\text{m}^2/\text{s}$, $w_s^{\text{eq}} = 0.3$, $M_s = 0.02$, $\theta = 0.5$, $dt = 0.0001$). Time = 0.02 seconds (note: $t_d = 63.1$ seconds).....	176
Figure 4.4-10 Comparison of Analytical Solution to Simplified Domain versus FEM Solution to Simplified Domain. ($f_s = 1.0\text{E-}5 \text{ g}/\text{cm}^2/\text{s}$, $D_d = 1.0 \mu\text{m}^2/\text{s}$, $w_s^{\text{eq}} = 0.3$, $M_s = 0.02$, $\theta = 0.5$, $dt = 0.0001$). Note: time = 0.404 seconds < $t_d = 0.631$ seconds).	176
Figure 4.4-11 Comparison of Analytical Solution to Simplified Domain versus FEM Solution to Simplified Domain. ($f_s = 1.0\text{E-}5 \text{ g}/\text{cm}^2/\text{s}$, $D_d = 1.0 \mu\text{m}^2/\text{s}$, $w_s^{\text{eq}} = 0.3$, $M_s = 0.02$, $\theta = 0.5$, $dt = 0.0001$). Time = 0.636 seconds > $t_d = 0.631$ seconds.....	177
Figure 4.4-12 Non-fickian FEM Solution for 1, 10, and 100 iteration loops. Time equal to 0.5 seconds (Note: $dt = 0.001$ seconds).....	178

Figure 4.4-13 Non-fickian FEM Solution for 1, 10, and 100 iteration loops. Time equal to 1.0 seconds (Note: dt = 0.001 seconds).....	178
Figure 4.4-14 Non-fickian FEM Solution for time equal to 0.001 seconds or dt (note: overshoot above thermodynamic equilibrium of 0.10).....	180
Figure 4.4-15 Non-fickian FEM Solution for Time equal to 1.0 seconds or 1000 dt (note: no overshoot).....	180
Figure 4.4-16 Non-fickian FEM solution for flux controlled dissolution (note: same conditions as Figure 4.4.6 but flux = 1.0E-7 g/cm ² /s). Time = 0.001 seconds.	181
Figure 4.4-17 Non-fickian FEM solution to theoretical composite solution domain for various values of the time step. Time is equal to 0.1 seconds. (Note: D _d <μm ² /s> = 0.01exp(-128.41ω _s), ω _s ^{eq} = 0.10, and υ _f = 0.60).....	182
Figure 4.4-18 Non-fickian FEM solution to theoretical composite solution domain for various values of the time step. Time is equal to 5.0 seconds. (Note: D _d <μm ² /s> = 0.01exp(-128.41ω _s), ω _s ^{eq} = 0.10, and υ _f = 0.60).....	182
Figure 4.4-19 Non-fickian FEM solution to theoretical composite solution domain for various values of the time step. Time is equal to 10.0 seconds. (Note: D _d <μm ² /s> = 0.01exp(-128.41ω _s), ω _s ^{eq} = 0.10, and υ _f = 0.60).....	183
Figure 4.4-20 Non-fickian FEM solution to theoretical composite solution domain for two different meshes. Time is 5.0 seconds. (Note: D _d <μm ² /s> = 0.01exp(-128.41ω _s), ω _s ^{eq} = 0.10, and υ _f = 0.60).	184
Figure 4.5-1 Sizing weight fraction profiles for D _d = 10 ⁻⁸ cm ² /sec and a time equal to 0.001 seconds or a D _d = 10 ⁻¹¹ cm ² /sec and a time equal to 1.0 seconds.....	187
Figure 4.5-2 Sizing weight fraction profiles for D _d = 10 ⁻⁸ cm ² /sec and a time equal to 0.05 seconds or a D _d = 10 ⁻¹¹ cm ² /sec and a time equal to 50 seconds.....	187
Figure 4.6-1 Non-fickian FEM solution to theoretical composite solution domain for K-90 PVP at various times. (Note: D _d <cm ² /s> = 0.0071exp(-128.41ω _s), ω _s ^{eq} = 0.10, and υ _f = 0.60). Angle is 0°.....	190
Figure 4.6-2 Non-fickian FEM solution to theoretical composite solution domain for K-90 PVP at various times. (Note: D _d <cm ² /s> = 0.0071exp(-128.41ω _s), ω _s ^{eq} = 0.10, and υ _f = 0.60). Angle is 30°.....	190
Figure 4.6-3 Non-fickian FEM predicted weight uptake of K-90 PVP as a function of time. (Note: D _d <cm ² /s> = 0.0071exp(-128.41ω _s), ω _s ^{eq} = 0.10, and υ _f = 0.60).	191
Figure 4.6-4 Theoretical interphase mechanical property profile for K-90 PVP sized composite. Static Tensile Strength (Note: Pure Derakane value is 55.3 MPa).	193
Figure 4.6-5 Theoretical interphase mechanical property profile for K-90 PVP sized composite. Strain-to-Failure (Note: Pure Derakane value is 1.9%).	193
Figure 4.6-6 Theoretical interphase mechanical property profile for K-90 PVP sized composite. Static Tensile Modulus (Note: Pure Derakane value is 3.44 GPa).	194
Figure 4.6-7 Theoretical interphase mechanical property profile for K-90 PVP sized composite. Static Shear Modulus (Note: Pure Derakane value is 1.31 GPa).....	194
Figure 4.6-8 Theoretical interphase mechanical property profile for K-90 PVP sized composite. Cure shrinkage shown (Note: Pure Derakane value is 8.34%).	195
Figure 4.6-9 Theoretical interphase mechanical property profile for K-90 PVP sized composite. K-90 PVP interphase shown in solid lines. Unsized shown in dashed lines. Mechanical property values normalized to the maximum in that property existing in the K-90 PVP interphase profile.....	196

Figure 4.6-10 Non-fickian FEM solution to theoretical composite solution domain for K-30 PVP at various times. (Note: $D_d <\mu\text{m}^2/\text{s}> = 0.118\text{exp}(-37.27\omega_s)$, $\omega_s^{\text{eq}} = 0.25$, and $\nu_f = 0.60$). Angle is 0°	197
Figure 4.6-11 Non-fickian FEM solution to theoretical composite solution domain for K-30 PVP at various times. (Note: $D_d <\mu\text{m}^2/\text{s}> = 0.118\text{exp}(-37.27\omega_s)$, $\omega_s^{\text{eq}} = 0.25$, and $\nu_f = 0.60$). Angle is 30°	197
Figure 4.6-12 Non-fickian FEM solution to theoretical composite solution domain for K-30 PVP at a time of 900 seconds. (Note: $D_d <\mu\text{m}^2/\text{s}> = 0.118\text{exp}(-37.27\omega_s)$, $\omega_s^{\text{eq}} = 0.25$, and $\nu_f = 0.60$). Angle is 0°	198
Figure 4.6-13 Non-fickian FEM solution to theoretical composite solution domain for K-30 PVP at a time of 900 seconds. (Note: $D_d <\mu\text{m}^2/\text{s}> = 0.118\text{exp}(-37.27\omega_s)$, $\omega_s^{\text{eq}} = 0.25$, and $\nu_f = 0.60$). Angle is 30°	198
Figure 5.1-1 Schematic of micro-dielectric sensor utilized for interdiffusion studies. a). Top view of sensor showing interdigitized gold grid. b). Side view of sensor showing sensing region or the penetration depth. Note: Any material outside of the sensing region does not contribute to the measurement.	204
Figure 5.1-2 Typical ϵ' vs. $\log(\omega)$ plot for a polymeric sample. At low frequencies, the value of ϵ' levels of to the relaxed permittivity or ϵ_r . At high frequencies, the value of ϵ' levels of to the un-relaxed permittivity or ϵ_∞	205
Figure 5.1-3 In-phase permittivity (ϵ') at a certain frequency versus bulk material thickness. End of sensing region noted where ϵ' remains constant. ϵ'_{max} , and $d\epsilon'(x)/dx$ can be easily determined from graph. Weight function $w(x)$ can be determined from equation (5-7). ..	207
Figure 5.1-4 In-phase permittivity (ϵ') at a certain frequency versus a). concentration of bulk material in the penetrant. b). time as the penetrate diffuses into the bulk material which has an intial thickness greater than the thickness of the sensing region. Note: Data fabricated for illustration purposes.	209
Figure 5.2-1 a). Schematic of profileometer utilizing stylus to scan the surface of the sensor. Note: Sensor detects changes in the angle θ per change in the horizontal scanning position b). Output of profileometer scan showing surface topography.....	215
Figure 5.2-2 Schematic of profileometer leveling process. a). A perfectly flat sensor that is level with the stylus scanning direction. b). A perfectly flat sensor that is not level with the stylus scanning direction.	215
Figure 5.2-3 Schematic of micro-dielectric sensor coated with parafilm (Top view shown). Note: Bottom and sides covered also. a). Parafilm coating sensor leads, sides, and bottom. Note: This is the typical configuration for sensors to be tested in a dielectric experiment. b). Parafilm coating sensor leads, end, sides, and bottom. Note: This is the configuration utilized for coating thickness calibrations.....	216
Figure 5.3-1 Coating thickness versus sensor position for 25wt% K-90 PVP in methanol dipping solution and a sensor withdrawl speed of a). 0.25 mm/min. b). 0.75 mm/min.....	226
Figure 5.3-2 Coating thickness versus sensor position for 25wt% K-90 PVP in methanol dipping solution and a sensor withdrawl speed of 0.75 mm/min. a). Sensor F1 b). Sensor F3. ..	226
Figure 5.3-3 Coating thickness versus sensor position for 25wt% K-90 PVP in methanol dipping solution and a sensor withdrawl speed of a). 1.50 mm/min b). 3.00 mm/min.....	227

Figure 5.3-4 K-90 PVP coating thickness for 1.5 mm/min withdrawal rate versus K-90 PVP in methanol dipping solution concentration.	227
Figure 5.3-5 In-phase permittivity versus K-90 PVP coating thickness. Note: Sensing distance is between 7 and 22 μ m.	228
Figure 5.3-6 Dielectric response of 22 μ m thick K-90 PVP film versus log(ω) where ω is in kHz. a). In-phase permittivity b). Out-of-phase permittivity c). Loss tangent.....	229
Figure 5.3-7 Dielectric properties versus log (ω) for K-90 PVP/Derakane blends. a). ϵ' b). ϵ'' and c). $\tan \delta$	230
Figure 5.3-8 In-phase permittivity (ϵ') at 1000kHz versus K-90 PVP in Derakane concentration.	231
Figure 5.3-9 Derakane™ 441-400 vinyl-ester resin diffusing into 42 μ m thick K-90 PVP film. ϵ' versus log (ω) at various times.....	233
Figure 5.3-10 Derakane™ 441-400 vinyl-ester resin diffusing into 42 μ m thick K-90 PVP film. ϵ'' versus log (ω) at various times.	233
Figure 5.3-11 Derakane™ 441-400 vinyl-ester resin diffusing into 42 μ m thick K-90 PVP film. $\tan \delta$ versus log (ω) at various times.	234
Figure 5.3-12 Derakane™ 441-400 vinyl-ester resin diffusing into 42 μ m thick K-90 PVP film. In-phase permittivity, ϵ' , versus log (ω) at various times. Note: fewer times shown for clarity.....	234
Figure 5.3-13 Theoretical prediction of swelling diffusion coefficient, D_s , versus parameter ξ calculated from equation III.5. Note: value of x was 25 μ m and value of t was 70 minutes.	235
Figure 5.3-14 Monomeric styrene diffusing into 42 μ m thick K-90 PVP film. ϵ' versus log (ω).	237
Figure 5.3-15 Monomeric styrene diffusing into 42 μ m thick K-90 PVP film. ϵ'' versus log (ω).	237
Figure 5.3-16 Density at 25°C for K-90 PVP in Derakane™ blends. a). un-cured b). cured...	239
Figure 5.3-17 Percentage blend shrinkage as a function of K-90 PVP in Derakane™.	240
Figure 5.3-18 Glass transition temperature of cured K-90 PVP in Derakane™ 441-400 blends as measured by DSC (10°C/min). 1st heat.	242
Figure 5.3-19 Glass transition temperature of cured K-90 PVP in Derakane™ 441-400 blends as measured by DSC (10°C/min). 2 nd heat (isothermal hold at 250°C for 10 minutes).	242
Figure 5.3-20 Shear viscosity as a function of shear rate for the pure Derakane™ vinyl-ester matrix material. Temperature = 25°C.	243
Figure 5.3-21 Shear viscosity as a function of shear rate for the 0.25wt% K-90 PVP in Derakane™ vinyl-ester matrix material. Temperature = 25°C.....	243
Figure 5.3-22 Shear viscosity as a function of shear rate for the 1.00wt% K-90 PVP in Derakane™ vinyl-ester matrix material. Temperature = 25°C.....	245
Figure 5.3-23 Shear viscosity as a function of shear rate for the 3.00wt% K-90 PVP in Derakane™ vinyl-ester matrix material. Temperature = 25°C.....	245
Figure 5.3-24 Shear viscosity as a function of shear rate for the 5.00wt% K-90 PVP in Derakane™ vinyl-ester matrix material. Temperature = 25°C.....	246
Figure 5.3-25 Zero shear viscosity as a function of K-90 PVP in Derakane™ concentration. $\eta_0=1.33\exp(128.4\omega_{K-90})$ shown in blue. Actual data shown in red.....	247

Figure 5.3-26 Shear viscosity as a function of shear rate for the pure Derakane™ vinyl-ester matrix material. Temperature = 25°C.	247
Figure 5.3-27 Shear viscosity as a function of shear rate for the 1.10wt% K-30 PVP in Derakane™ vinyl-ester matrix material. Temperature = 25°C.	249
Figure 5.3-28 Shear viscosity as a function of shear rate for the 4.30wt% K-30 PVP in Derakane™ vinyl-ester matrix material. Temperature = 25°C.	249
Figure 5.3-29 Shear viscosity as a function of shear rate for the 8.60wt% K-30 PVP in Derakane™ vinyl-ester matrix material. Temperature = 25°C.	250
Figure 5.3-30 Shear viscosity as a function of shear rate for the 17.5wt% K-30 PVP in Derakane™ vinyl-ester matrix material. Temperature = 25°C.	250
Figure 5.3-31 Zero shear viscosity as a function of K-90 PVP in Derakane™ concentration. $\eta_0=0.404\exp(37.27\omega_{K-30})$ shown in blue. Actual data shown in red.	251
Figure 5.3-32 Static tensile strength of K-90 PVP in Derakane™ blends.	251
Figure 5.3-33 Static tensile modulus of K-90 PVP in Derakane™ blends.	252
Figure 5.3-34 Static tensile shear modulus of K-90 PVP in Derakane™ blends.	252
Figure 5.3-35 Static tensile strain-to-failure of K-90 PVP in Derakane™ blends.	253
Figure 5.4-1 Dissolution diffusion coefficient, D_d , for the K-90 PVP/Derakane™ system predicted by equation (5-26).	258
Figure 5.4-2 Dissolution diffusion coefficient, D_d , for the K-30 PVP/Derakane™ system predicted by equation (5-26).	259

TABLES

Table 3-1 Hexcel AS-4 G' lot # D1383-5K and Hexcel AS-4 unsized lot # D1317-4C carbon fiber mechanical properties.	69
Table 3-2 Processing parameters used to produce the sized fibers utilized in this study. In addition, sizing characterization information also displayed.	82
Table 3-3 ESCA results for Hexcel AS-4 carbon fibers sized with various agents. ESCA results for pure sizing materials shown also.	83
Table 3-4 Summary of Results.	86
Table 3-5 Processing parameters used to produce the sized fibers utilized in this study. In addition, sizing characterization information also displayed.	113
Table 3-6 Material testing results for various fiber/sizing systems.	134
Table 4-1 Physical constants utilized for idealized composite FEM simulation. a.) Parameters utilized by the meshing program to generate the mesh. b.) Physical constants used by the FEM program. c.) Numerical parameters needed to approximate the temporal evolution.	186
Table 5-1 Flatness of sensors utilized for dielectric experiments. Nine positions on the sensor surface (see schematic below for position on sensor) were tested. Numeric value shown indicates the deviation from flatness. Note: * indicates sensors that had an acceptable flatness level and were used in the experiments. The other sensors were discarded.	224

Chapter 1

Introduction

1 Motivation [1.1]

The use of metal and concrete in infrastructure applications has been the norm for decades. However, these construction materials have several problems. First, these materials are subject to environmental degradation that limits their service lifetime [1.2,1.3]. Second, the relatively high density of these materials makes their transportation and installation extremely difficult and expensive. In addition, a large portion of the supporting structure itself is present just to support the weight of the supporting structure and not the functional structure. As the United States civilian infrastructure grows older and more prone to failure, a search for technologically advanced materials to replace the traditionally utilized metal and concrete is being conducted. One material system that is being considered as a potential replacement is continuously reinforced fiber/polymer matrix composites. In particular, a pultruded glass/carbon fiber hybrid composite with a Dow™ vinyl-ester matrix has been proposed as a potential replacement [1.4]. These materials offer several advantages over the traditionally utilized materials. First, the chemical nature of the vinyl-ester matrix makes this composite extremely resistant to environmental degradation. In addition, the polymeric nature of the vinyl-ester matrix makes the composite substantially tougher with a greater ability to absorb energy. Second, the high strength to weight ratio of the composite makes it much easier to install and also allows the use of reduced weight support structures [1.2]. In addition, the low weight allows for prefabrication to become more economically feasible.

The principal disadvantage associated with the use of any carbon fiber reinforced polymer matrix composite is its cost per performance measurement. This is due to the high price of the carbon fiber constituent (usually-\$10 - \$30 per pound) and the high cost of the processing steps. Carbon fiber reinforced polymer matrix composites have typically been used in high-end aerospace applications where cost isn't as important as in civil infrastructure applications. In order for these composites to find acceptance in civilian markets like infrastructure and high-speed civil transportation, the cost of the processing steps and raw materials must be reduced while maintaining or improving their performance. The fundamental objective of the work in the

Designed Interphase Group (DIG) is to improve the performance of continuously reinforced carbon fiber/polymer matrix composites. While efforts are underway elsewhere to reduce the cost of the carbon fiber constituent, our efforts are focused upon improving the performance of these composites *without* increasing their cost.

1.1 Background

Fiber reinforced polymer composites consist of a reinforcing fiber embedded in a polymeric matrix material. The resulting composite material has a high strength/weight ratio when compared to traditional metallic materials [1.5]. The matrix protects the brittle reinforcing fiber and transfers the load to the fiber. Carbon fibers possessing high modulus and strength are often used. A third constituent, a *sizing*, is applied to the surface of the carbon fiber before impregnation with the matrix material and is applied in amounts ranging from 1 to 3 wt%. Typically, sizings have been used by industry to protect the brittle carbon fiber from damage during processing steps and to enhance the handling characteristics of the fiber [1.6]. Sizings have now been shown to affect the mechanical performance of the composite [1.7]. For example, a 50% increase in fatigue limit has been demonstrated for a thermoplastic PHENOXY™ sized composite compared to an unsized composite in work by this author and others at Virginia Tech [1.8]. What is still not understood is why the addition of a sizing produces these effects on mechanical properties.

The primary objective of the proposed work is to develop a fundamental understanding of why *thermoplastic* sizings have such a profound affect on the mechanical performance of carbon fiber composites. If a fundamental understanding such as this can be obtained, then scientists and engineers will be in a better position to tailor the sizing chemistry and optimize the sizing process such that mechanical performance is maximized. For this work, the material system investigated is a carbon fiber/Dow 441 vinyl-ester composite produced from pultrusion. As will be discussed below, this material system is ideally suited for civilian applications.

The Dow™ 441 vinyl-ester matrix is composed of a vinyl-ester component and a monomeric styrene component that is cured by a free-radical polymerization. The Dow™ 441 vinyl-ester matrix offers cost savings over the traditional epoxy matrices that are used for high cost aerospace applications. The civilian market demands composite materials at a very low cost thus making the Dow™ 441 vinyl-ester a viable option for these applications. The hydrophobic nature of the poly(styrene) present in the cured Dow 441™ resin allows this system to be less

sensitive to water and hence more environmentally stable. Unfortunately, the presence of the poly(styrene) causes the cured resin to experience large amounts of shrinkage (5-11%) [1.9] and hence relatively large static stress concentrations at the fiber/matrix interface in the composite. The chemical structure of the Dow 441™ vinyl-ester matrix and the additives necessary for the pultrusion process are discussed later in Chapter 3.

Pultrusion represents the most cost-effective means of rapidly producing continuous fiber reinforced composites with a thermoset matrix such as the Dow™ 441 vinyl-ester. Because civilian markets often require uncomplicated parts of constant cross-section, pultrusion also represents the most economical means of producing composites for these applications. Some general details of the pultrusion process (Figure 1-1) will now be discussed. There are four steps involved in the pultrusion process. Step 1 is the *preprocessing step* where multiple carbon fiber tow ends are directed into the process. Step 2 is the *resin dip bath step* where the sized carbon fibers are completely wetted with the matrix material. Step 3 is the *preforming step* where the individual tows are brought together before entering the pultrusion die. Step 4 is the *die/curing step* where the final compaction of the tows into the final part cross-section occurs. In addition, the matrix is cured through application of heat. The composite part is then ready for its intended use.

1.2 Sized fiber life cycle

In order to understand the role that sizings play in affecting composite mechanical performance, the life cycle of the sized carbon fiber must be identified throughout the composite fabrication process. What happens to the sizing during the course of the coating process? What form does the sizing material take on the fiber surface? What phenomenological events are associated with the sizing process? What happens to the sizing during the course of: (i) the wet-out portion of the pultrusion process? (ii) the preforming portion of the pultrusion process? (iii) the curing portion of the pultrusion process? In order to answer these questions, a sized fiber life cycle is proposed that tracks the sizing from its introduction to the carbon fiber surface to its final place in the composite.

1.2.1 Stage I: The Sizing Process

Stage I of the sized fiber life cycle involves the coating of the carbon fibers with the polymeric sizing agents. The details of this work are presented elsewhere [1.6]. The carbon fibers are sized on a custom made small scale sizing line [1.6,1.10] (Figure 1-2). The unsized

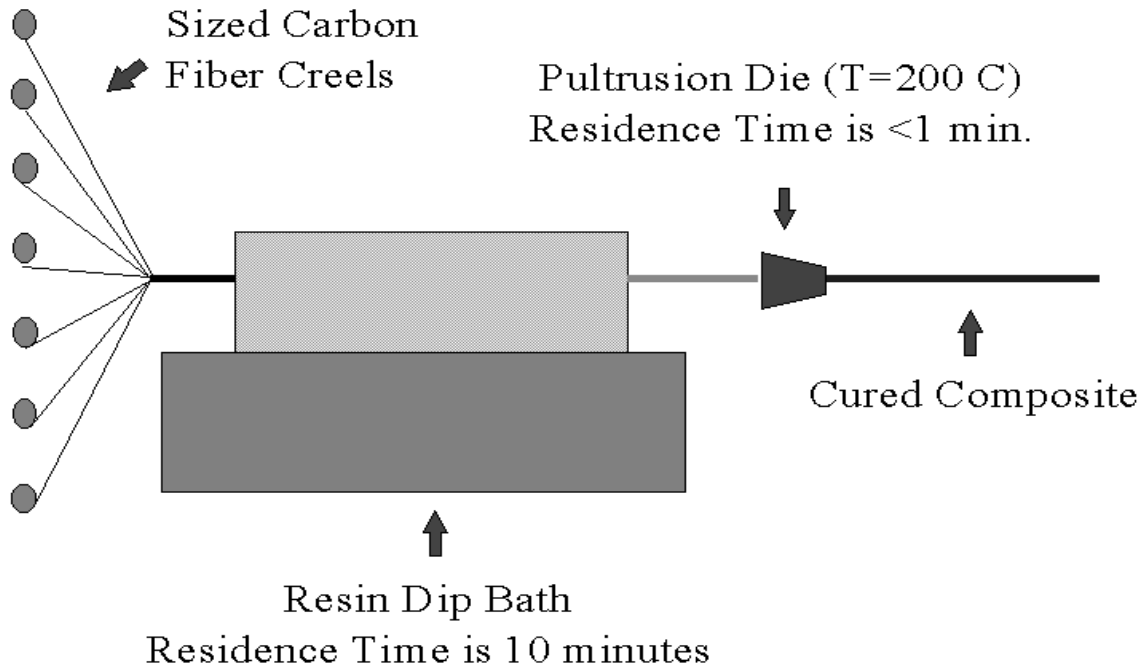


Figure 1-1 Schematic of the pultrusion process.

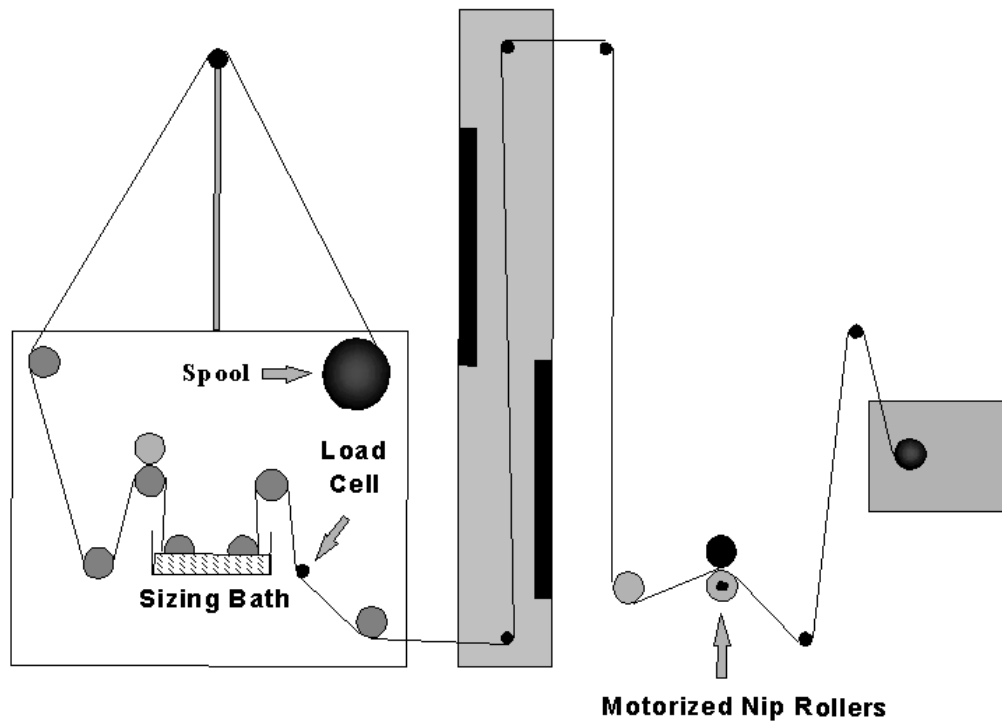


Figure 1-2 Schematic of the sizing process.

carbon fiber tow is pulled off a standard spool at a set speed. The fibers are put under tension by a nip roller, which is connected to a particle brake. The fibers then pass through a sizing dip bath that contains the aqueous sizing solution/suspension. In the dip bath, capillary forces provide the driving force for rapid tow wetting. The time required to completely wet the tow can be estimated from the following equation [1.6]:

$$t_f = \frac{l^2 \mu_s V_{void}}{2S_b \left(\frac{2}{R}\right) \gamma_{sizing} \cos \theta} \quad (1-1)$$

where t_f is the time required to wet the tow, l is the characteristic length or thickness of the tow, μ_s is the sizing dip bath viscosity, V_{void} is the void volume of the tensioned unsized carbon fiber, S_b is the unsized tow permeability, R is the characteristic radius for the carbon fiber packing array, γ_{sizing} is the surface tension of the sizing dip bath solution, and θ is the contact angle established between the unsized carbon fiber and the dip bath solution. This equation neglects inertial effects and assumes the sizing dip bath solution/suspension behaves as a Newtonian fluid. Utilizing typical values for these parameters in systems involving dilute aqueous polymeric solutions and unsized Hexcel AS-4 carbon fibers, the predicted time for complete tow wet-out is on the *order* of microseconds [1.6]. Because the dip bath residence time is on the *order* of seconds, it can be safely concluded that the internal voids of the unsized carbon fiber exits the dip bath completely saturated with the sizing solution/suspension. Once the sizing solution/suspension comes into intimate contact with the surface of the fiber, the surface energies may be such that the sizing material is preferentially adsorbed to the surface of the carbon fiber. This wet-out and adsorption process are depicted in Figure 1-3.a.

After the unsized carbon fiber has exited the dip bath and is now saturated with the sizing solution/suspension, the fibers are then dried in an IR forced convection dryer. The amount of sizing material deposited onto the fiber surface can be quantitatively related to the wet fiber moisture content by the following expression [1.6]:

$$\omega_s = \frac{C_{sizing}}{\left(\frac{1}{X_{moisture}} - 1\right)} \quad (1-2)$$

where ω_s is the weight fraction sizing deposited onto the unsized carbon fiber, C_{sizing} is the dip bath sizing concentration (wt/wt), and $X_{moisture}$ is the fiber moisture content (mass of

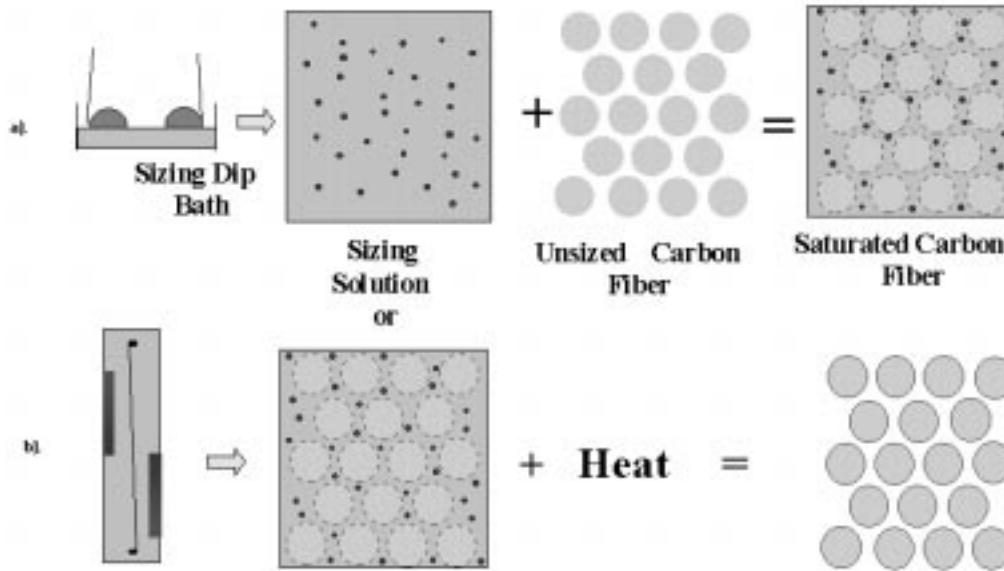


Figure 1-3 Sizing life cycle: Sizing line depiction. a). Sketch of aqueous sizing solution or suspension dip bath. b). Sketch of drying portion of the process.

moisture/mass of wet unsized tow). This equation assumes that C_{sizing} is small and that negligible sizing mass is preferentially *absorbed* from the **bulk** solution into the internal confines of the carbon fiber tow (note: this does **not** imply zero *adsorption* of the sizing to the carbon fiber surface). The moisture is stripped from the inside of the tow by evaporation. The sizing material is left deposited on the surface of the fiber. As will be discussed in Chapter 3, the constitutive nature of the sizing material and the processing temperature experienced in the dryer tower determines the morphology of the deposited sizing. In most cases, the processing is adjusted until the sizing material is deposited in the form of a homogeneous thin film around the individual carbon filaments with negligible or minimal filament-filament adhesion. This portion of the sized fiber life cycle is depicted in Figure 1-3.b. Assuming a homogeneous coating around the carbon fiber surface, the thickness of the sizing layer can be computed from the following equation:

$$t_s = R_f \left(\sqrt{1 + \frac{\rho_f}{\rho_s} \left(\frac{1}{\omega_s} - 1 \right)} - 1 \right) \quad (1-3)$$

where t_s is the sizing thickness, R_f is the fiber radius, ρ_f is the fiber density, ρ_s is the sizing density, and ω_s is the weight fraction sizing present on the fiber surface. This completes the specification for Stage I of the sized fiber life cycle. After the fibers are sized, they are processed into composites via pultrusion.

1.2.2 Stage II: Pultrusion – Pre-Processing

The pre-processing portion of the pultrusion process involves the transportation of the sized carbon fiber tow from the spools to the entrance of the resin dip bath (Figure 1-1). The individual tows are pulled from their respective spools and directed into the dip bath by a series of metal guide pins. During this stage of the process, the fibers are placed into intimate contact with the metal surfaces, which can lead to damage. This damage cannot be predicted quantitatively. However, the qualitative effect that the sizing plays on this damage can be hypothesized based upon the physical nature of the sizing present. For instance, a tough polymeric sizing material should better protect the fiber than a non-polymeric material.

1.2.3 Stage III: Pultrusion – Resin Dip Bath

After the fibers have been pre-processed and directed to the entrance of the resin dip bath, they are compressed between static roller bars that convert the tow into a flat band. Additional fiber damage occurs at this portion of the process that is also affected by the sizing material (Figure 1-1).

Inside the resin dip bath, capillary forces drive the infiltration of the tow with the matrix material (Figure 1-4.a & b). In order to maximize mechanical performance of the final composite, the matrix must be in complete intimate contact with the carbon fiber surface without the presence of voids in the matrix. Therefore, the purpose of the dip bath section is to allow complete infiltration of the matrix material into the carbon fiber tow while evacuating all the air. The importance of this stage in the pultrusion process cannot be over-emphasized. The equation presented earlier for tow wet-out time applies to the resin dip bath also and can be expressed by the following:

$$t_f = \frac{l^2 \mu_r V_{void}}{2S_b \left(\frac{2}{R} \right) \gamma_r \cos \theta} \quad (1-4)$$

where t_f is the time required to wet the tow, l is the characteristic length or thickness of the tow, μ_r is the matrix viscosity, V_{void} is the void volume of the sized carbon fiber entering the dip bath,

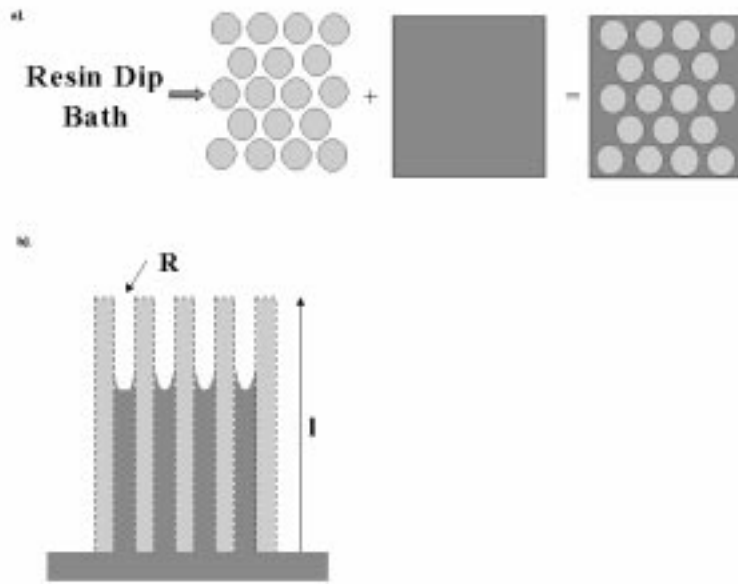


Figure 1-4 Sized Fiber Life Cycle: Resin dip bath. a). Sized fiber wetting with the matrix resin. b). Resin infiltrating the fiber micro-capillaries where the driving force is controlled partially by the contact angle between the fiber and the resin.

S_b is the tow permeability, R is the characteristic radius for the carbon fiber packing array, γ_r is the surface tension of the matrix, and θ is the contact angle established between the sized carbon fiber and the matrix. Due to the approximations in the derivation of equation (1-4), it should only be used for order of magnitude estimates of wet-out time. The sizing material and how it was processed in the sizing line greatly affects some parameters used in this equation: the characteristic length, void volume, permeability, and characteristic radius. For instance, the width and thickness of the sized carbon fiber tow has been shown to be a function of the sizing and the sizing lines processing parameters such as line tension, line speed, etc.

In addition, the sizing affects the contact angle established between the sized carbon fiber and the matrix (Figure 1-4.b). If the sizing and the matrix are extremely compatible, then a small contact angle would be expected and the time required for tow wet-out would be reduced. Therefore, the time required for wet-out is greatly affected by the nature of the sizing agent present.

After the matrix comes into intimate contact with the sizing material, the sizing and matrix will begin to interdiffuse (Figure 1-5.a). As will be discussed in the next chapter, the sizing/matrix interdiffusion is characterized by four stages (note: for a high T_g thermoplastic sizing material). First, the matrix or one of its constituents (Figure 1-5.b) swells the high T_g

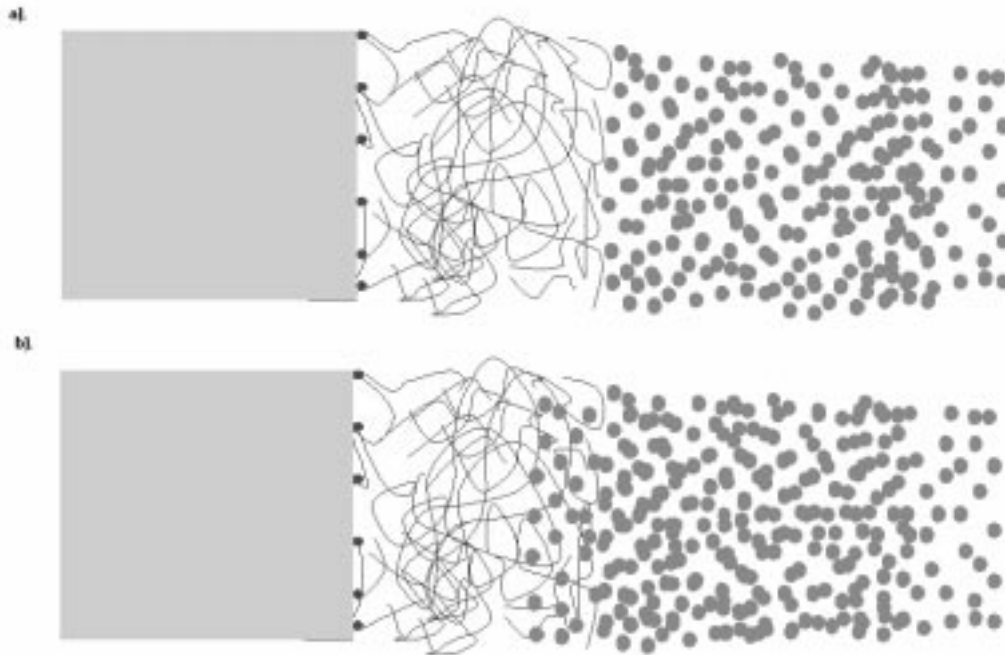


Figure 1-5 Sized fiber life cycle: Sizing/Matrix interdiffusion. a). Initial configuration of the sizing in contact with the matrix. b). Sizing being swelled by a matrix constituent.

thermoplastic sizing material. Second, the swelled sizing material begins to relax at a finite rate (Figure 1-6.a). After this relaxation has occurred and the T_g of this relaxed material is equal to the temperature of the processing environment, the third stage begins. The third stage involves the disentanglement of the entangled sizing. After the sizing is disentangled, the final stage, the dissolution stage, can proceed. The final stage involves the reptation and diffusion of the relaxed sizing into the bulk matrix material (Figure 1-6.b). It is important to note that these four stages occur in the order listed but one stage does not necessarily terminate when the other initiates. For instance, all four stages can be occurring simultaneously for a period of time. For the remainder of this thesis, these four stages are given the following identifications.

1. **Swelling Stage**
2. **Relaxation Stage**
3. **Disentanglement Stage**
4. **Dissolution Stage**

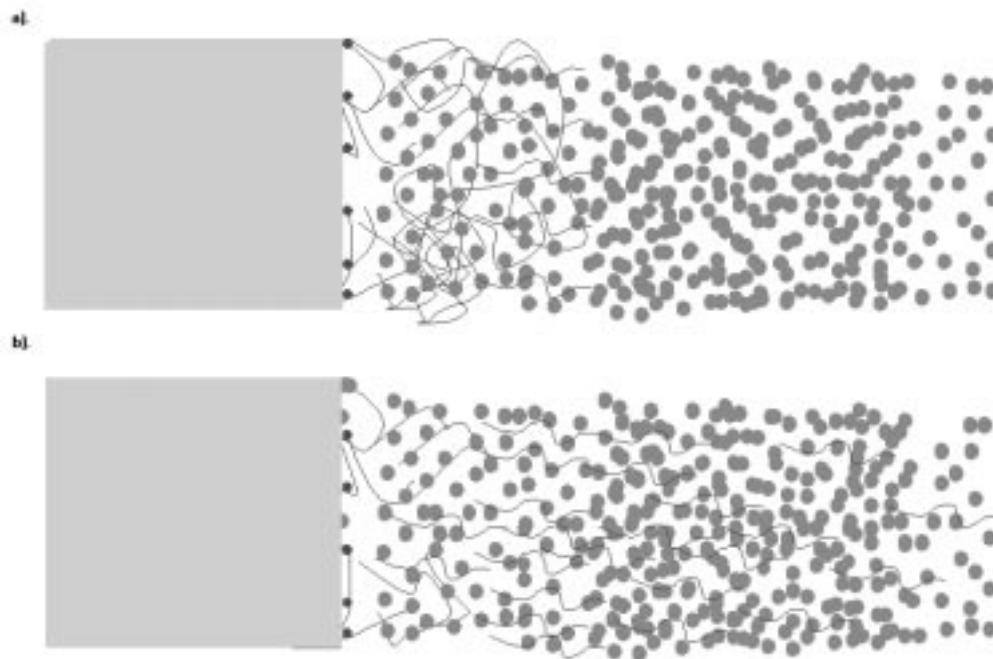


Figure 1-6 Sized fiber life cycle: Sizing/Matrix interdiffusion. a). Polymer chains close to initial sizing/matrix interface are now relaxing. b). Relaxed polymer chains at the relaxed sizing/matrix begin to reptate and diffuse into the bulk matrix.

All four of these stages continue to take place while the fiber passes through the resin dip bath. In addition, the swelling, relaxation, disentanglement, and dissolution stages continue to take place in the preforming section of the pultrusion process. As was discussed in the previous section, there could be a small amount of adsorbed sizing material that will not be available for the interdiffusion process. This material may be locked in place and may permanently reside at the fiber/matrix interface.

1.2.4 Stage IV: Pultrusion – Preforming

Once the carbon fiber exits the dip bath saturated with resin, it is sent through a series of compaction units where the individual tow bundles are slowly brought together. After the last compaction unit, the cross section of the wet-tow bundles or the agglomerate is only slightly larger than the die cross section. The final compaction takes place in the die entrance. During these compaction steps, the fibers are again subject to damage. The sizing material and its state on the fiber surface determine the degree to which the fibers are damaged. It is important to realize that the handling characteristics of the carbon fiber at this point could be distinctly different than the characteristics it had at the dip bath entrance. For instance, if the sizing existed

as a glassy/tough material at the dip bath entrance, then it could now exist as a rubbery/tough material because of the swelling/relaxation phenomena that takes place inside the dip bath and preforming sections. As an alternative, the glassy/tough sizing material may have completely dissolved off the fiber surface leaving no material for protection. Again, the physical and chemical nature of the sizing agent greatly affects the Damage State of the carbon fiber.

1.2.5 Stage V: Pultrusion – The Die/Cure

The preformed carbon fiber agglomerate that is saturated with the resin is then cured in a heated die. Within this section, carbon fiber damage can occur due to the friction experienced at the part surface. The sizing material can act as a lubricant that assists the part in sliding through the die.

In addition, the interdiffusion of the sizing and the matrix continues in the heated portion of the die (Figure 1-1). The interdiffusion continues until such time as the matrix material gels. After that point, the sizing/matrix composition profile from the surface of the fiber to the bulk matrix is locked in place. The region that forms as a result of the sizing/matrix interdiffusion is called the *interphase* (Figure 1-7).

This completes the specification of the sized fiber life cycle. With the phenomenological events associated with the sized fiber life cycle identified, the mechanisms responsible for a sizing's dramatic effects on composite performance can be postulated.

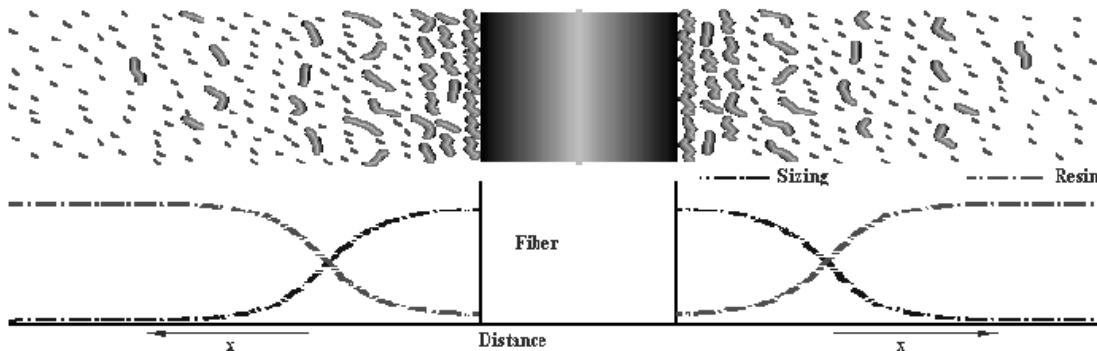


Figure 1-7 Schematic of the Interphase in the final composite. Region near the surface of the fiber represents pure sizing. Region remote from the fiber surface represents pure matrix. Region in between represents the interphase where both sizing and matrix reside.

1.3 Mechanisms for Sizings Effects

From the sized fiber life cycle just hypothesized, the ways in which sizings can influence the mechanical performance of the final composite can be enumerated. Sizings can influence the mechanical performance of a composite in four distinct ways.

1. **Processability-** Sizings can protect the brittle carbon fiber from damage. In addition, the sizing can affect the inherent stiffness of the sized fiber. Sized fiber stiffness plays an important role in determining fiber alignment in the final composite, which is important in on-axis performance. The sizings can also affect the surface free energy of the carbon fiber, which controls the contact angle established between the fiber and the infiltrating matrix. The sizings can also influence the geometric packing of the fiber that provides a resistance to tow wet-out. All of these variables affect the time required to completely wet-out the fiber with resin and establish intimate fiber/matrix contact that is essential for good fiber/matrix adhesion.
2. **Fiber/Matrix Adhesion-** A sizing can alter the fiber/matrix interfacial strength. This results from a sizing that is chemically or physically bonded to the carbon fiber surface and is also interacting strongly with the matrix. It is believed that fiber/matrix adhesion should be qualitatively related to the processability/wettability of the sized carbon fiber with the matrix. A sizing that lowers the contact angle of the fiber/matrix should also promote better fiber/matrix adhesion in the cured composite.
3. **The Interphase-** The *interphase* is a region of finite mass located at the fiber/matrix interface that results from the interdiffusion of the sizing and the matrix. The interphase controls the way in which stresses are transferred from a failed fiber to the surrounding fibers. Micro-mechanical models have predicted vast improvements in mechanical properties when such a sizing concentration gradient exists near the fiber/matrix interface [1.5]. This gradient may be tailored by controlling the sizing and matrix chemistry and the processing history.
4. **Matrix Plasticization-** If the diffusion of the sizing into the matrix is so rapid that no gradient is established in the composite, then a homogeneous modification of the matrix results. The sizing could plasticize the matrix, thus changing the manner in which a load is transferred from one fiber to another.

It would be beyond the scope of a single thesis to try and address the quantitative importance of all four of these effects on mechanical performance. Therefore, it is not feasible in this work to quantitatively predict the effects a certain sizing will have on mechanical performance. However, it is feasible to probe the relative importance of these four effects from a carefully chosen set of experiments. In addition, some of the phenomenological events that cause a sizing to affect mechanical performance can be fundamentally modeled by making use of judicious simplification. With this in mind, the major objectives for this work can now be enumerated.

1.4 Research Objectives

The objectives for this thesis are as follows.

1. To elucidate the *relative* importance of the four effects (processability, fiber/matrix adhesion, interphase formation, and matrix plasticization) that sizings have on the mechanical performance of the final composite.
2. To fundamentally predict the interphase profile from mass transfer concepts.
3. To obtain constitutive data on the sizing/matrix interdiffusion process.

Over the past three years, these objectives have been accomplished to varying degrees. A summary of the work is the subject of this thesis. In the next section, an outline for this thesis is presented.

1.5 Thesis Outline

This thesis is organized into the following chapters.

- **Chapter 2: Literature Review**

In Chapter 2, a detailed literature review on all the pertinent work completed in this field will be presented. In addition, the theoretical concepts needed in later chapters will also be presented in this chapter.

- **Chapter 3: Experimental: Pultrusion of Carbon Fiber/Vinyl Ester Composites with Tailored Sizing Agents**

In Chapter 3, pultrusion results are presented that detail the effects of varying sizing agents on the performance of carbon fiber/vinyl-ester composites. The material presented in chapter 3 directly addresses objective #1. The purpose of these experiments was three fold. First, to prove that thermoplastic sizing materials affect the performance of pultruded composite materials. Second, to develop an

understanding of how thermoplastic sized fiber processes differently than the conventionally utilized oligomeric epoxy sizings. Finally, to determine how the interphase affects on-axis composite performance.

- **Chapter 4: Interphase Formation: Mass Transfer Model**

In Chapter 4, the results of interphase formation modeling are presented. The material presented in chapter 4 directly addresses objective #2. Both analytical and numerical models for interphase formation were developed. A finite element code was written that accurately predicts the interphase composition profile as a function of numerous processing variables and sizing/matrix constitutive properties.

- **Chapter 5: Measurements of the Constitutive Properties Relevant to Sizing/Matrix Interdiffusion**

In Chapter 5, experimental dielectric results are presented that reveal some of the constitutive properties of sizing/matrix interdiffusion. The material presented in chapter 5 directly addresses objective #3. Microdielectric sensors were used to monitor the swelling, relaxation, and dissolution of the sizing material into the vinyl-ester matrix. In addition, sizing/matrix blends were characterized for their tensile properties, cured shrinkage, glass transition temperature, and zero-shear viscosity. The information gained from these experiments was to serve as input into the mass transport model developed in Chapter 4 to obtain accurate predictions of interphase formation.

1.6 References

- 1.1 M. D., Hayes, “Characterization and Modeling of a Fiber-Reinforced Polymeric Composite Structural Beam and Bridge Structure for Use in the Tom's Creek Bridge Rehabilitation Project”, M.S. Thesis, Engineering Science and Mechanics Department, Virginia Polytechnic Institute and State University, Blacksburg, VA.
- 1.2 Sotiropoulos, GangaRao, and Barbero, “Static Response of Bridge Superstructures Made of Fiber Reinforced Plastic, “ *Use of Composite Materials in Transportation Systems American Society of Mechanical Engineers, Applied Mechanics Division, AMD, ASME, New York, NY, v129, 57-65.*

- 1.3 R. Lopez-Anido and H. V. S. GangaRao, "Design and Construction of Composite Material Bridges," US-Canada-Europe Workshop on Bridge Engineering, Zurich, Switzerland, July 14-15, 1997, 1-8.
- 1.4 J. J. Lesko, R. Weyers, J. Duke, M. Hayes, R. Formica, Adele Schirmer, J. Gomez, J. Volgyi, E. Villalba, M. Kerley, J. Stewart, D. Witcher, C. Smith, and G. Barefoot, *The Tom's Creek Bridge Project*.
- 1.5 G. Gray and G. Savage, *Metals and Materials* 1989, **5**, 513.
- 1.6 N. S. Broyles, 'Sizing and Characterization of Carbon Fibers with Aqueous-Water Dispersible Polymeric Interphases', MS Thesis, Department of Chemical Engineering, VPI&SU, February 1996.
- 1.7 L. T. Drzal, M. J. Rich, M. F. Koenig, and P. F. Lloyd, 'Adhesion of graphite fibers to epoxy matrices: II. The effect of fiber finish', *Journal of Adhesion*, Vol. 16, 1983, pp. 133-152.
- 1.8 N. S. Broyles, K.N. E. Verghese, S. V. Davis, H. Li, R. M. Davis, J.J. Lesko, and J. S. Riffle, 'Fatigue performance of carbon fibre/vinyl ester composites: the effect of two dissimilar polymeric sizing agents', *Polymer*, **Vol.39**, Number 15, 1998, pp. 3417-3424.
- 1.9 H. Li, 'Synthesis, Characterization, and Properties of Vinyl-Ester Matrix Resins', PhD. Thesis, VPI&SU, Dept. of Chemistry, 1998.
- 1.10 N. S. Broyles, R. C. Chan, and R. M. Davis, 'Sizing of carbon fibers with aqueous solutions of poly(vinyl pyrrolidone)', *Polymer*, Volume 39, Number 12, 1998, pp. 2607-2613.

Chapter 2

Literature Review

2 Introduction

In Chapter 1, the outline for this thesis was detailed. In this chapter, a literature review on the pertinent work completed in this field will be presented. In addition, the theoretical concepts needed to develop the models and analyze the data in the remaining chapters will also be presented.

This chapter is organized into the following sections.

- 2.1 – Sizings: Effects on Composite Performance
- 2.2 – Fundamentals of Interphase Formation
- 2.3 – Theory of Dielectric Spectroscopy
- 2.4 – Finite Element Method Applied to Parabolic DEQ's

In section 2.1, the literature is reviewed in the area of how a sizing affects composite performance. In section 2.2, the literature on polymer/solvent interdiffusion and interface thermodynamics is reviewed. This review will provide the framework for the constitutive theory needed to apply the interphase formation model developed in chapter 4. In section 2.3, an experimental study on the use of dielectric spectroscopy to characterize polymer/solvent interdiffusion will be reviewed. Finally, in section 2.4, a reference for the detailed theory behind the Finite Element Method and how it is applied to parabolic differential equations is presented. This theory will be utilized to develop the interphase formation model discussed in chapter 4.

2.1 Sizings: Effects on Composite Performance

As was discussed in the introductory chapter, sizings can affect composite performance in four ways.

1. Processability
2. Fiber/Matrix Adhesion
3. Interphase Formation

4. Matrix Plasticization

Each of these areas will be reviewed within section 2.1 as it relates to composite performance. In particular, section 2.1.1 and 2.1.2 will review the effects of processability and fiber/matrix adhesion, respectively. As will be discussed in section 2.1.2, interphase formation and matrix plasticization effects are considered sub-classes of the fiber/matrix adhesion effect for the purpose of this review. As such, interphase formation and matrix plasticization are discussed in a subsection of section 2.1.2.

The review will not be restricted to carbon fiber reinforcements or thermosetting matrices because information gained from other material systems will certainly be applicable to this research. In addition, processing methods other than pultrusion will be presented when the focus of the research is on fiber surface treatments or sizings.

The composites industry has focused primarily upon the processability issues related to carbon fibers and in particular, the role sizings play in protecting the brittle carbon fiber from damage. On the other hand, the academic community has spent the majority of their efforts focused upon the role of sizings in fiber/matrix adhesion and interphase formation. Because literature reviews inherently focus upon information available to the public, the industrial perspective due to its proprietary nature sometimes gets overlooked in a review of this type. As such, a deficiency in information on a sizing's effect on processability will clearly become apparent. However, the literature contains vast information on the role sizings have in affecting fiber/matrix adhesion and to a less extent, in the formation of an interphase.

2.1.1 Sizings: Effect on Fiber Processability

As was discussed in chapter 1, the processability of fiber reinforcements can be separated into two phenomenological events.

1. Fiber Protection
2. Fiber Wettability

Each of these areas will be reviewed in section 2.1.1. Fiber protection will be reviewed in section 2.1.1.1 and fiber wettability will be reviewed in section 2.1.1.2.

Fiber protection relates to the ability of the fiber to retain its original mechanical performance after the course of the composite processing steps. For processing methods such as

pultrusion, the fibers are placed in numerous situations where damage can occur (see Chapter 1). Therefore, the ability of the fiber to withstand this damage will inherently affect composite performance.

Fiber wettability is defined as the ability of a fiber to fully infiltrate with the matrix resin and establish intimate contact between the fiber and the resin. The driving force for wetting is controlled by thermodynamics (fiber/matrix contact angle) while the resistance is controlled by kinetic parameters such as permeability and viscosity. It is important to realize that good fiber wettability is precedent to good fiber/matrix adhesion. A system cannot have optimal fiber/matrix adhesion without good fiber wettability. However, a system that has good fiber wettability can still have poor fiber/matrix adhesion as will be discussed in the fiber/matrix adhesion section.

2.1.1.1 Processability: Sizing's Effect on Fiber Protection

There is very little data in the literature that addresses a sizing material's effect on fiber protection and hence composite mechanical performance [1.7]. However, it is well known in the composites community that sizings were first introduced in order to protect the brittle carbon fiber from damage and to enhance the handling characteristics of the fiber. In fact, carbon fiber processability is still the most important property for the commercial composite producer [2.1].

Drzal and co-workers [2.1,2.2] investigated the effect that an oligomeric epoxy sizing had on fiber protection, fiber wettability, and fiber/matrix adhesion in single fiber composites. Two fiber systems were investigated: a Hercules A-1 and a Hercules A-4. Each of these fiber systems was supplied with three different surface treatments: untreated and unsized, treated and unsized, and treated and sized. The sizing provided with these fibers was identified as a diglycidyl ether of bisphenol-A. The matrix utilized for the single fiber composites was a stoichiometric mixture of EPON 828 (a diglycidyl ether of bisphenol-A) and 14.5 phr meta-phenylene diamine. The researchers concluded that fiber protection was not important because the single filament tensile strength of all the fibers **as supplied by the manufacturer** were identical. The researchers argued that if fiber protection had been important then the unsized fibers would have had more damage and hence lower single filament tensile strengths. Unfortunately, this conclusion cannot be viewed as universal because the state of fiber damage is proportional to the process utilized to make the composite and not the process utilized to produce

the fiber. In addition, the tensile strength of a single filament may not be degraded by physical damage to the tow. Only the tow tensile strength may be affected by damage due to processing. Therefore, the conclusion that fiber protection can be ignored is certainly not valid for material systems and processing schemes not equivalent to the ones utilized in this narrow study.

2.1.1.2 Sizings: Effect on Wettability

Sellitti [2.3] and co-workers found a qualitative relationship between the contact angle and the fiber/matrix adhesion in the final composite. In this work, un-saturated polyester resins with different amounts of a monomeric styrene diluent were contacted with e-glass fibers. The e-glass fibers were sized with two different silanes that had different chemical affinity for the styrene portion of the resin. One silane was soluble in styrene due to favorable interactions with the organic functionality on the silane. The other silane was insoluble with the styrene due to unfavorable interactions with styrene. The researchers found that the styrene soluble sized fiber (henceforth known as the S fiber) had an appreciably lower contact angle when compared to the contact angle observed with the styrene insoluble sized fiber (henceforth known as the I fiber). In addition, the researchers showed that the static tensile and flexure strengths of the final composite were considerably higher for the S fiber as compared to the I fiber. Qualitative inspection of the composite failure surface revealed that the S fiber reinforced composite had improved fiber/matrix adhesion compared to the I fiber-reinforced composite. The researchers concluded that the improved fiber/matrix adhesion was the result of the lower contact angle and hence better wettability of the S fiber compared to the I fiber.

Larson and coworkers [2.4] investigated the effect of sizing chemistry on glass fiber wettability, fiber/matrix adhesion, and bulk composite mechanical performance. In this work, the researchers utilized commercially sized e-glass fibers and a Dow 411-C50 vinyl-ester resin to produce composites. The sized e-glass fibers were analyzed for surface free energies utilizing a Wilhelmy technique. They were able to calculate a theoretical work of adhesion and contact angle between the sized fibers and the un-reacted matrix. The researchers qualitatively defined a more wettable sizing/fiber system as one that resulted in a higher work of adhesion and hence a lower contact angle with the un-reacted matrix. The final composite was characterized for fiber/matrix adhesion, flexural strength, and short beam shear (SBS) strength. The fiber/matrix adhesion in the actual composite was assessed with a micro-indentation technique. The results

showed that sized fibers with the highest work of adhesion or lowest contact angle with the unreacted matrix displayed the highest values of fiber/matrix adhesion in the cured composite. The researchers tested a variety of sizing materials that were either soluble or insoluble in the Dow 411-C50 matrix. In addition, the researchers tried to separate the affects of wettability and sizing/matrix interdiffusion on fiber/matrix adhesion by coating a vinyl-ester soluble sized e-glass fiber with a mold release compound. The purpose of this was to make the surface energy of the system unfavorable for wetting while still allowing the sizing/matrix interdiffusion to occur. The results for this system showed that the mold release coated fibers had a low work of adhesion while the fiber/matrix adhesion was still high. The researchers concluded that this was an indication that the mold release had been washed away by the infiltrating resin. The researchers were unsuccessful at proving whether the work of adhesion/wettability or sizing/matrix interdiffusion had the greatest affect on fiber/matrix adhesion. The researchers indirectly concluded that the increase in fiber/matrix adhesion was the result of interphase formation or sizing/matrix interdiffusion and not improvements in wettability as a result of a higher work of adhesion. The longitudinal flexure strength of the composites was directly proportional to the measured fiber/matrix adhesion (a higher fiber/matrix adhesion corresponded to a higher longitudinal flexure strength). The composites also displayed drastic difference in their failure modes which was dependent upon the fiber/matrix adhesion. For sizing systems with a high fiber/matrix adhesion the failure mode was found to be (Mode I or tensile failure). For the sizings systems with a low fiber/matrix adhesion the failure modes was found to be (Mode II or shear failure). The SBS strengths for the composites were also found to be directly proportional to the fiber/matrix adhesion. In this case, the failure mode was always Mode II but the degree of hackles or “triangular regions of matrix resulting from the shear failure path” were always greater for the systems with higher fiber/matrix adhesion and higher SBS strengths. In summary, these researchers were able to show that sizings drastically affect fiber wettability, fiber/matrix adhesion, and composite mechanical performance. Unfortunately, they were unable to determine if improved wettability as a result of surface energy modification or interphase formation from sizing/matrix interdiffusion was more strongly contributing to the improvement.

E. Mäder [2.5] investigated the effect of sizing chemistry on carbon and glass fiber wettability, fiber/matrix adhesion, and bulk composite mechanical performance. Two DGEBA epoxy resins were utilized for this work: Rütapox L20 and LB64. The L20 resin contained

hexandioldiglycidether as a diluent to lower the viscosity. The e-glass fibers were coated with several different polymeric sizing agents. Two different carbon fibers were utilized in this work. The first was a Tenax unsized and un-surface treated and the second was a Tenax sized and surface treated. The chemical identity of the sizing material was not specified. The contact angle of the matrix with the fiber was determined by a Wilhelmy technique. Fiber/matrix adhesion was assessed through a fiber pullout technique and calculation of an interfacial shear strength (ISS). Composite properties determined included transverse tension, short beam shear (SBS), and compressive strength. The results indicated that the contact angle was directly affected by the presence of a sizing. Sizings that produced smaller contact angles and hence more wettable fibers in general displayed higher ISS and correspondingly higher transverse tensile strengths and SBS strengths. In a similar study, E. Mader and co-workers found similar results with a series Akzo carbon fibers (unsurface treated/unsized, surface treated/unsized, and surface treated/sized), an Epilox epoxy resin, and an Epilox H curing agent [2.6].

E. Mäder also investigated the effect [2.7] that different silane coupling agents had on the wettability, single fiber interfacial shear strength, composite tensile, flexural, short beam shear, interlaminar shear and impact performance in e-glass reinforced polypropylene. The specific materials utilized in this study will not be discussed here but the general results of this study can be summarized. The results of the study indicated that the wettability of the e-glass reinforcement with the molten polypropylene matrix was a strong function of the sizing agent utilized. Sizing agents that had specific acid/base interactions with the matrix resulted in a lower contact angle, higher ISS, and better bulk composite mechanical performance.

Patel and co-workers [2.8] investigated the effect that wet-out time had on e-glass fiber/fabric wettability, fiber/matrix adhesion, and composite mechanical performance. In addition, the researchers investigated the effect that various silane sizings had on e-glass fiber/fabric wettability, fiber/matrix adhesion, and thermoset composite mechanical performance. Two matrix materials were utilized in this study. The first was a polyurethane (PU) based on a diphenylmethane diisocyanate mixed stoichiometrically with a polyester triol. The second matrix material was a 50:50 mixture of the polyurethane resin discussed above and a UPE resin that consisted of 32.5wt% propylene glycol, 32.5wt% maleic anhydride, and 35wt% monomeric styrene. Three different e-glass fibers were utilized for the PU matrix (unsized, 0.5 wt% gamma methacryloxypropyltrimethoxy silane, and 0.5 wt% gamma aminopropyltriethoxy silane) and a

single sizing was used for the PU-UPE resin (0.5 wt% of a 1:17 ratio gamma methacryloxypropyltrimethoxy and unsaturated polyester). The effect of wet-out time was addressed by varying the injection pressure and temperature for the RTM process. The wettability of the fibers was assessed qualitatively by flow visualization experiments on a transparent mold that approximated the RTM process utilized to produce the composites for mechanical testing. Fiber/matrix adhesion was assessed by single fiber fragmentation tests that utilized the Weibull distribution method. The composites were analyzed for tensile properties and voids. The highest composite tensile strength within a sizing system was observed when the injection pressure was the lowest and the injection temperature was the highest. These processing conditions should correlate to a minimum in the theoretical wet-out time expressed by equation (1.2). Therefore, within a sizing system, the completeness of fiber wet-out drastically affected composite tensile strength. The researchers also found that the composite void volume was higher in the systems with less fiber wet-out. Unfortunately, the researchers did not test the effect of sizing chemistry on fiber/fabric wet-out. In addition, the researchers did not attempt to separate the effects of wet-out and interphase formation on improving fiber/matrix adhesion and hence composite tensile strength. The researchers tested the effect of sizing chemistry on fiber/matrix adhesion in a single filament composite. The interfacial shear strength was found to be significantly affected (40% variation) by a change in sizing chemistry. The gamma aminopropyltriethoxy silane sizing (ISS = 45.77 MPa) outperformed both the gamma methacryloxypropyltrimethoxy silane sizing (ISS = 35.46 MPa) and the untreated fiber (ISS = 31.06 MPa).

Numerous other researchers have found correlations between better fiber wettability and hence improved composite mechanical performance as a function of sizing and or surface treatments [2.9,2.10,2.11]. However, due to space limitations, only the articles most pertinent to this work were reviewed in detail.

This concludes section 2.1.2. The studies reviewed in the literature clearly show that a sizing significantly affects the processability of the composite reinforcement. In addition, mechanical properties are significantly affected by improvements in processability. In the next section, the literature is reviewed in the area of the effect of sizings on fiber/matrix adhesion.

2.1.2 Sizings: Effect on Fiber/Matrix Adhesion

The effects of fiber/matrix adhesion, interphase formation, and matrix plasticization are difficult to distinguish phenomenologically. Depending upon one's definition of fiber/matrix adhesion, the interphase and matrix plasticization effects may or may not be separate and distinct. For instance, if one views fiber/matrix adhesion as the phenomena responsible for improvements in interfacial shear strength (ISS), then the interphase is a sub-class of fiber/matrix adhesion because the interphase partially controls the interfacial shear strength (discussed later in section 2.1.2.1). However, if one views fiber/matrix adhesion as the *interfacial* phenomena responsible for improvements in interfacial shear strength, then the interphase is truly separate because it is a three dimensional entity (the same applies for matrix plasticization). For the purpose of this review, the effect of fiber/matrix adhesion is considered to be the summation of the fiber, matrix, fiber/matrix interface, and interphase effects.

This section is divided into three subsections. The first subsection details the theoretical work of Cox that fundamentally predicts the ISS as a function of fiber and matrix properties for single fiber composites. The second subsection details the work of Reifsnider and a host of others that predicts the static tensile and compressive response of uni-directional polymer matrix composites as a function of the ISS. In the final section, experimental work that establishes a link between sizing/surface modification, ISS, and bulk mechanical properties is reviewed.

2.1.2.1 Fundamental: ISS - Relation to Fiber and Matrix Properties

Several micro-mechanical models predicting the interfacial shear strength as a function of matrix properties have been developed [2.12,2.13]. Cox used a shear lag analysis on a single fiber composite to predict the interfacial shear stress as a function of fiber and matrix properties. The quantitative formulation for the ISS is as follows:

$$\tau = E_f \varepsilon_m \left[\frac{G_m}{2E_f \ln\left(\frac{R}{r}\right)} \right]^{.5} \frac{\sinh\{\beta(0.5L-x)\}}{\cosh\left(\frac{\beta L}{2}\right)} \quad (2-1)$$

where τ is the interfacial shear stress, E_f is the fiber tensile modulus, ε_m is the matrix strain, G_m is the matrix shear modulus, R is the fiber radius, r is the radial position, β is a scaling factor, L is the embedded fiber length, and x is the position along the fiber. The derivation for equation

(2-1) assumed perfect fiber/matrix bonding, and, hence, there was a no slip condition at the interface. In addition, the matrix properties were assumed to be isotropic and constant as a function of the radial coordinate. Therefore, if fiber properties are constant and there is no slip at the fiber/matrix interface, then a plot of ISS versus $\epsilon_m^f G_m^{1/2}$ should yield a linear relationship (ϵ_m^f is the strain-to-failure of the matrix). However, other researchers have shown [2.14 and 2.15 discussed later] that experimental data more closely follows this theory if ϵ_m^f is replaced by ϵ_m^s or the strain in the matrix at the critical fiber fragmentation length. Therefore, the ISS is increased when the shear modulus of the matrix is also increased. However, matrix strength and strain-to-failure do not affect ISS if the assumptions used in this derivation are valid. This concludes the discussion of how fiber and matrix properties influence ISS. Equation (2.1) did not incorporate the interphase into the analysis because matrix properties were considered constant. However, the same qualitative trend would be observed if an interphase were present. A graded interphase that had a higher shear modulus than the pure matrix would result in a higher ISS.

2.1.2.2 Fundamental: On-Axis Properties - Correlation with ISS

The sizing material greatly affects the properties of the interphase and hence the ISS. The Cox theory established a link between interphase modifications and alterations in ISS. In order to fully establish the theoretical effect a sizing has on bulk mechanical performance, a link between ISS and mechanical performance must be established. The material presented in this section establishes that link.

Reifsnider [2.16] modeled the effect of matrix or interphase compliance on the static tensile and compressive strength of uni-directional polymer matrix composites. In this work, the researchers predicted that a stiff matrix or interphase and hence, a high ISS would lead to a composite with higher stress concentrations near failed fibers. This resulted in a higher tendency of failure in adjacent fibers and catastrophic failure transverse to the fiber direction. On the other hand, a more compliant matrix or interphase and hence, a lower ISS led to lower stress concentrations but a higher ineffective length. This higher ineffective length led to an increase in “the region of influence” which could then interact with other “regions of influence” to induce catastrophic failure. Thus, the conclusion was reached that in order to optimize static tensile properties of uni-directional polymer matrix composites, there exists an optimal value for the

ISS. The same result was found for compressive strength predictions where an optimal ISS was again predicted. However, instead of using ineffective length arguments, the researcher used critical micro-buckling length arguments that were again affected by the ISS. The normalized composite strength versus ISS predicted by the model is shown (Figure 2.1-1). As the figure shows, the effect of ISS on strength is most significant at ISS values below the optimal ISS. Above the optimal ISS, the strength levels off to a value only 3% lower than the maximum. In addition, for an ISS 1/3 that of the optimal ISS, the strength only drops 10%. Therefore, the unidirectional tensile strength is not a strong function of the ISS (note: above approximately 1/3 of the optimal ISS). The researchers suggested that fatigue properties were more sensitive to alterations in ISS than the static properties previously discussed. This is in agreement with research published by this author and co-workers [1.8].

Zeng and co-workers [2.17] presented a similar analysis where the static tensile properties were again predicted to achieve a maximum value for a given ISS. The quantitative predictions of Zeng were close to those of Reifsnider though not exact. Zeng predicted a drop in strength of approximately 15% for an ISS equivalent to 1/3 of the optimal value. Again, the strength values tended to level off at ISS values well above the optimal ISS. However, the tensile strength at which this leveling off occurred was considerably lower than that predicted by

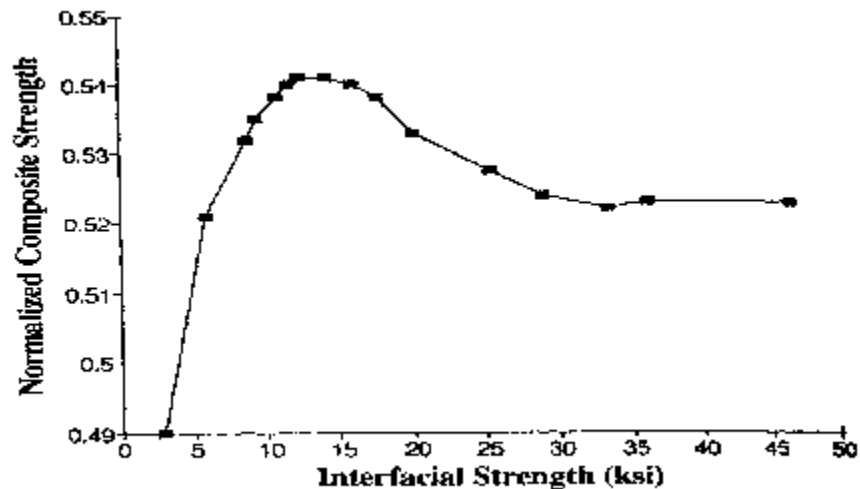


Figure 2.1-1 Theoretical prediction of Reifsnider [2.16]. Variation of composite tensile strength as a function of the fibre/matrix interfacial shear strength, predicted by model.

Reifsnider (Zeng: -10% deviation from maximum. Reifsnider: -3% deviation from maximum).

Neither one of these theories predicted an effect of matrix/interphase strength or strain-to-failure on static on-axis composite mechanical response. However, Ivens and researchers [2.18] discuss the qualitative implications of a higher matrix/interphase strength and strain-to-failure on tensile failure in an actual composite. In this work, the researchers concluded that for high interface bond strengths (note: not ISS) the matrix/interphase strain-to-failure limits the interface stress to values below the interface bond strength. In this type of situation, the strain-to-failure controls the load at which transverse cracking and subsequent catastrophic failure of the composite occurs. For two composites with identical fiber/matrix bond strengths (no slip boundary condition assumed in Cox's theory) and identical matrix/interphase shear moduli, Ivens' fundamental research suggests that the on-axis strength based properties will be higher for the matrix/interphase with a higher strain-to-failure. A higher interphase strength and strain-to-failure for a given modulus will allow much greater interfacial shear stresses to exist before transverse cracking and composite catastrophic failure results. As a result, the applied load at which interfacial debonding or transverse cracking initiated would be shifted to higher values. A similar analysis utilizing finite element analysis was completed by Nishiyabu and co-workers [2.19] and A. Di Anselmo and co-workers [2.20].

In this section, the link between changes in interphase/interface properties and bulk mechanical properties has been established. The role the interphase plays in fiber dominated properties like tensile and compressive strength can be considered important but certainly not dominant. The inherent strength of the continuous reinforcement still has the greatest affect on these properties. However, off-axis properties like transverse flexure and tension are much more sensitive to changes in interphase properties. In addition, fatigue properties are also very sensitive to changes in the interphase [1.8,2.16].

With a theoretical link between interphase properties and macroscopic composite mechanical performance established, experimental results that prove or disprove these theoretical predictions are presented in the next section.

2.1.2.3 Experimental: Sizings and or Surface Treatments - Effects on ISS and Bulk Composite Mechanical Performance

Cox's theory for ISS as a function of fiber and matrix properties equation (2-1) was verified experimentally by Drzal and Rao [2.14,2.15]. These researchers investigated the effect that matrix modulus had on the interfacial shear strength. In this work, the researchers varied the modulus of an epoxy matrix while keeping the interface chemistry constant. This was achieved by varying the molecular weight between cross-links while maintaining the chemical nature of the matrix and hence preserving the nature of the fiber/matrix interface bonds. The reinforcement utilized in this study was unsized but surface treated Hercules AS-4 carbon fibers. Two different epoxy matrices were utilized in this study. The first was a DGEBA based epoxy and the second was a tetrafunctional MY720. The curing agents utilized in this work were all difunctional amines. The authors claimed that the reactants were chosen such that the interface chemistry remained constant while the matrix properties were varied from stiff and brittle to compliant and ductile. The interfacial shear strength was determined from single fiber fragmentation tests. The matrix properties determined in the study were tensile properties and the glass transition temperature. The interfacial shear strength was found to decrease non-linearly with decreasing matrix shear modulus as predicted by Cox's theory [section 2.1.2.1 equation (2-1)]. In fact, the interfacial shear strength was found to quantitatively follow Cox's theory as long as the matrix failure strain was replaced by the matrix strain at the critical fiber length, ϵ_f . With this correction, the ISS was found to be directly proportional to the product of ϵ_f and the matrix shear modulus as predicted by the Cox theory.

An experimental study that validates some of the predictions by Reifsnider and Zeng [2.16,2.17] is a study by P. van den Heuvel and co-workers [2.21]. These researchers studied the influence of fiber/matrix adhesion and fiber spacing on the fracture process in uni-directional carbon fibre/epoxy matrix composites failed in tension. Model composites were produced from five Courtaulds carbon fiber filaments equally spaced in a DGEBA epoxy resin. The spacing was varied from 15 to 100 μ m to ascertain the effect of fiber spacing on the failure process. In addition, three levels of surface treatment were compared at the same fiber spacing to investigate the treatment's effect on the failure process. The results showed that fiber spacing affected the stress concentrations on adjacent fibers after a single fiber break. Systems with lower fiber spacing showed coordination of fiber fracture while systems with higher fiber spacing showed a

random distribution of fiber breaks. In addition, the systems with higher levels of surface treatment showed a strong coordination of the fiber breaks in agreement with the theory just presented: higher levels of fiber/matrix adhesion (higher bond strength and ISS) tended to promote transverse cracking and adjacent fiber failure. As was discussed earlier, this can be counteracted by having a tougher interphase region. The later portion of this statement was not verified in van den Heuvel's work. In the systems with no or little surface treatment, the fibers were seen to fracture in a random manner. Therefore, systems with low fiber/matrix adhesion (low bond strength and ISS) tend to fail by classic bundle failure. Both of these experimentally observed trends are in agreement with the theory developed in the previous section.

Madhukar and co-workers [2.22,2.23] developed an extensive database of composite properties as a function of ISS. The carbon fibers utilized were Hercules AU-4, AS-4 unsized, and AS-4C. The AU-4 fibers were unsized and unsurface treated. The AS-4 material was unsized but surface treated. The AS-4C was surface treated and sized with a 100-200 nm coating of the oligomeric epoxy. The matrix utilized was a DGEBA based epoxy and 14.5 parts per hundred by weight of mPDA. ISS values were determined by a single fiber fragmentation technique. The fibers were impregnated with the epoxy resin utilizing a prepregger and then autoclaved into the composite with a specific lay-up sequence. The mechanical properties determined included longitudinal tension and flexure [2.23], transverse tension and flexure [2.23], and inplane and interlaminar shear [2.22]. The ISS was found to correspond directly with the level of surface treatment. The AU-4, AS-4, and AS-4C fibers had ISS values of 37.2, 68.3, and 81.4 MPa, respectively. The 83% increase in ISS from the AU-4 to the AS-4 was attributed to the removal of a weak surface layer present on the AU-4 [2.2,2.24]. Because of the presence of this weak surface layer, the AU-4 fiber results are not particularly germane to this discussion because the fiber properties were distinctly different. However, the locus of failure in the AU-4 fiber composites was the interface due to the degraded fiber surface. Therefore, the mechanical property results for the AU-4 fiber represent the case of extremely poor fiber/matrix adhesion. The longitudinal tension results showed the following trend: 1403 ± 107 MPa (AU-4), 1890 ± 143 MPa (AS-4), and 2044 ± 256 MPa (AS-4C). These results correlate with the ISS in the following manner. An 83% increase in ISS lead to a 35% improvement in strength; an additional 19% increase in ISS lead to an 8% increase in strength. A plot of normalized tensile strength versus normalized ISS suggests an optimum in strength had been reached at the highest ISS

(Figure 2.1-2 -> note: when ISS is zero, the theoretical strength should be approximately zero). Therefore, some of the predictions of Reifsnider and Cheng have been confirmed by this set of experiments. The longitudinal strain-to-failure was also found to correlate with the ISS. The longitudinal tensile modulus and Poisson's ratio were found to be relatively insensitive to variations in the treatment level. The AU-4 composite failure surfaces appeared clean and void of matrix an indication of poor fiber/matrix adhesion. The AS-4 composite failure surface showed a mixed failure mode. The failed fibers had both clean and matrix encapsulated areas indicating improved fiber/matrix adhesion. The composite failure surface had a "brush-like" structure where fiber/matrix splitting was predominate. The AS-4C composites failed fiber surface looked similar to the AS-4. However, the composite failure mechanisms were different. The composite failed by a transverse cracking mechanism due to the higher amount of fiber/matrix adhesion. This type of transition in failure was discussed earlier. The composite surface displayed a "brittle" type of failure.

The longitudinal flexure strength did not follow the same trend as the tensile strength. The AS-4C was again found to have the highest strength but the AU-4 had the intermediate value which was inconsistent with the ISS: 1662 ± 92.2 MPa (AU-4), 1557 ± 102 (AS-4), and 1827 ± 51.5 (AS-4C) MPa. The longitudinal flexure modulus and strain-to-failure were found to be constant and not a function of the surface treatment. A summary of the normalized longitudinal data versus normalized ISS is shown (Figure 2.1-2).

The transverse flexure strength and strain-to-failure were found to correlate with the ISS: 18.0 ± 3.86 MPa and $0.20 \pm 0.05\%$ (AU-4), 34.2 ± 6.16 MPa and $0.36 \pm 0.07\%$ (AS-4), and 41.2 ± 4.74 MPa and $0.40 \pm 0.04\%$ (AS-4C). The transverse tensile and flexural moduli were found to be insensitive to surface treatment. The transverse strength and strain-to-failure were much more sensitive to variations in fiber/matrix adhesion as was hypothesized earlier. For an 83% increase in ISS, the transverse strength and strain-to-failure increased by 72 and 79%, respectively. For an additional 19% increase in ISS, the strength and strain-to-failure increased by 20 and 13%, respectively. The transverse flexure strength and strain-to-failure data correlated well with the ISS: 21.4 ± 5.76 MPa and $0.22 \pm 0.05\%$ (AU-4), 50.2 ± 3.37 MPa and $0.53 \pm 0.04\%$ (AS-4), and 75.6 ± 14.0 MPa and $0.71 \pm 0.14\%$ (AS-4C). Therefore, the transverse flexure strength and strain-to-failure appeared to be the most sensitive test method for variations in fiber/matrix adhesion. The transverse flexure modulus was not found to correlate with ISS.

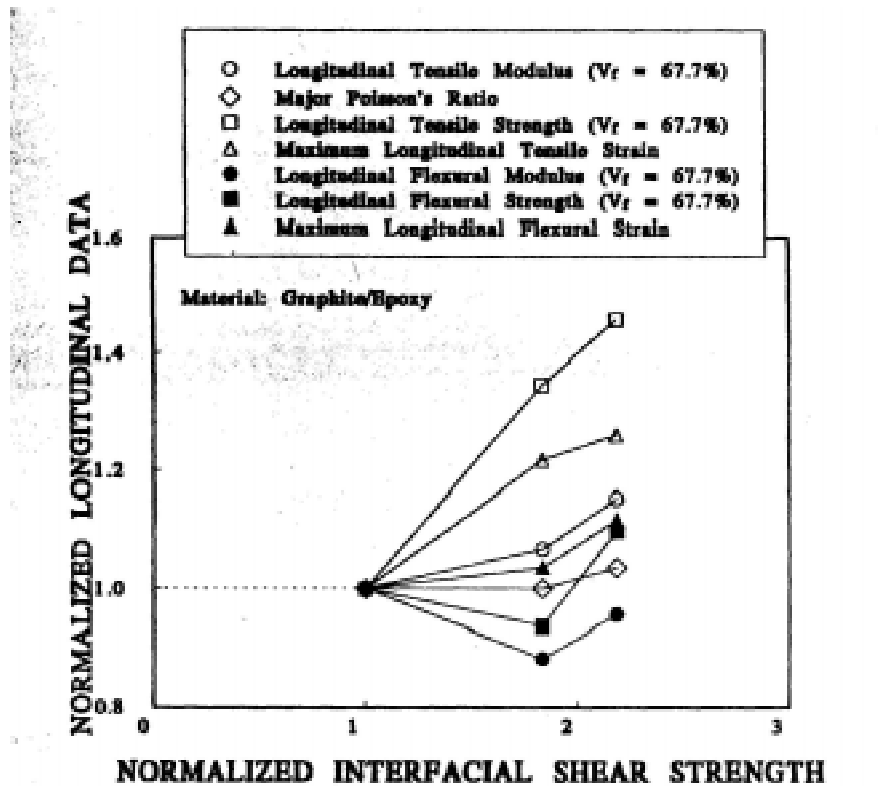


Figure 7. Effect of the ISS on longitudinal tensile and flexural properties of graphite/epoxy composites. Tensile modulus and Poisson's ratio are unaffected. Tensile strength and maximum tensile strain increase and then level off when the ISS is increased from the low to the high values. Flexural properties are relatively insensitive to the ISS.

Figure 2.1-2 Normalized longitudinal flexure data of Madhukar et al [2.23]

The transverse properties are summarized in normalized form (Figure 2.1-3).

The inplane and interlaminar shear mechanical responses were also determined for these same materials [2.22]. The test methods utilized to ascertain inplane and interlaminar shear properties were $[\pm 45]_{3s}$ tension, Iosipescu shear, and short beam shear(SBS). The $[\pm 45]_{3s}$ tensile strength and SBS were found to be significantly affected by the ISS: 37.2 ± 1.81 and 47.5 ± 5.43 MPa (AU-4), 72.2 ± 12.4 and 84.0 ± 6.95 MPa (AS-4), and 97.54 ± 7.38 and 93.2 ± 3.79 MPa (AS-4C). The in-plane modulus was found to be insensitive to changes in ISS (Figure 2.1-4).

In summary, the longitudinal tensile strength of uni-directional polymer matrix composites is affected by the ISS. However, the effect of ISS is small as long as a minimal level of fiber/matrix adhesion is present. Therefore, the longitudinal tensile strength is a fiber dominated property that is relatively insensitive to changes in fiber/matrix adhesion.

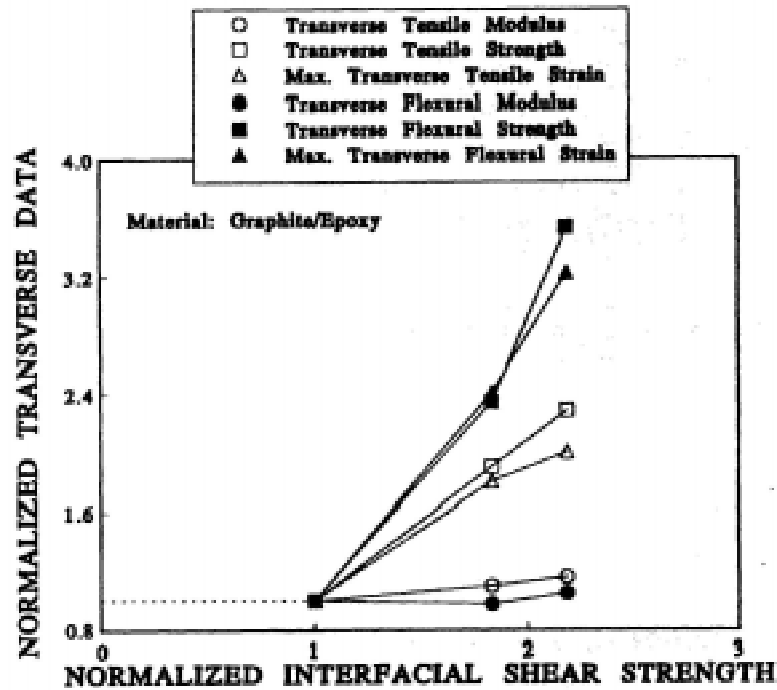


Figure 13. Effect of the ISS on transverse tensile and flexural properties of graphite/epoxy composites. There is little effect on modulus, however, both strength and maximum strain significantly increase with the ISS.

Figure 2.1-3 Normalized transverse flexure data of Madhukar et al [2.23].

The remainder of the studies reviewed in this section will provide experimental verification that sizings and/or surface treatments significantly affect the mechanical performance of the composite. Some of the remaining studies reviewed will discuss both single fiber and composite data thus providing a link between the micro and macro scales.

Hoecker and co-workers [2.25] investigated the effect that two different sizing agents had on the interfacial shear strength, contact angle, transverse tensile strength, transverse flexure strength, interlaminar shear strength (both short beam and iosipescu) and impact testing (both Charpy and drop weight impact) of carbon fiber/epoxy matrix composites. The two sized carbon fibers utilized were PAN based Tenax HTA. One sizing consisted of 1.25wt% oligomeric epoxy that was optimized for interaction with the matrix (designated compatible sizing in the discussion that follows). The second sizing consisted of 0.15wt% of an anti-static agent that was known to be incompatible with the matrix (designated in-compatible sizing in the discussion that follows). The matrix utilized in these studies was an Araldit LY 556 bisphenol-A based epoxy resin cured with HY 917 anhydride hardener and DY 070 heterocyclic amine catalyst. Two types of single

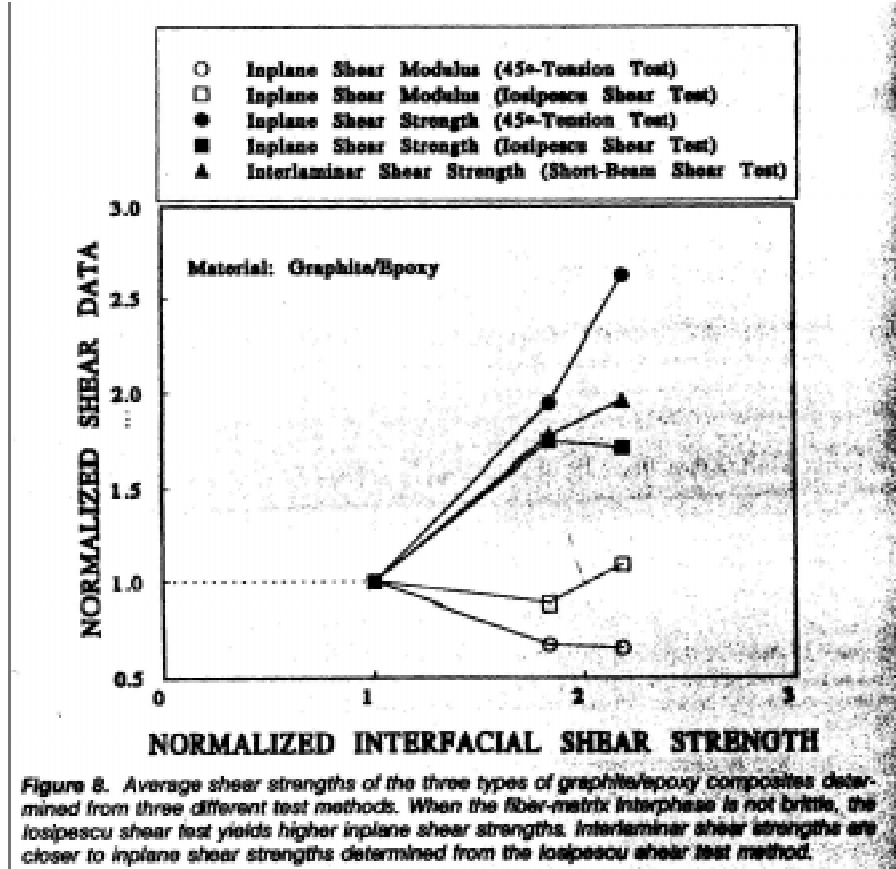


Figure 2.1-4 Normalized shear data of Madhukar et al [2.22].

fiber fragmentation tests were performed. The first was a simple single fiber fragmentation test and the second was a micro-droplet pull-off test. The failure mechanisms for the fiber fragmentation tests were analyzed with transmitted light and crossed polarizers. The interfacial shear strength of the compatible sized carbon fibers were 40% greater than that of the incompatible sizing as determined by the single fiber fragmentation test. Good bonding between the compatible sized fiber and the matrix was apparent with the transmitted light. For the case of the incompatible anti-static sizing, the transmitted light pattern showed non-optimal fiber/matrix adhesion. The micro-droplet pull-off test confirmed the qualitative trend observed with the single fiber fragmentation technique. The compatible sized fiber was found to have a considerably higher interfacial shear strength (94 MPa and 64 MPa). The wetted micro-droplet specimens were examined with SEM before and after pull-off. The micrographs showed no difference in the contact angle established between the matrix and the sized fibers. This was

surprising considering the fact that the interface chemistries were so distinctly different. However, this result must be viewed with caution because the researchers did not comment on how they measured the contact angle. The matrix bead was so large compared to the filament diameter that it would be nearly impossible to determine the true fiber/matrix contact angle. In addition, the contact angle was determined on the cured matrix bead and it was not readily apparent if thermodynamics or kinetics controlled the contact angle measured.

The pulled-off fiber samples displayed different surface morphologies dependent upon the sizing agent present. The compatible sized fiber showed a rough surface with large amounts of matrix still attached while the incompatible sized fiber showed a smooth surface. The transverse tensile and flexure strengths were determined on uni-directional filament wound composites. The transverse tensile strength of the compatible sized fiber was found to be 42% higher than the strength of the incompatible sizing. This result matches the single fiber fragmentation data where the interfacial shear strength was 42% higher for the compatible sizing compared to the incompatible sizing. However, the researchers correctly identified that this result must be viewed with caution because the stress state in the interface will not be identical between the actual composite and the idealized single fiber composite. There were no apparent differences in the transverse flexure strength of the two fiber sizings. This result is surprising considering the similarity of this test with the transverse tension test. However, the researchers argue that the probability of interface failure was greater in the case of transverse tension due to critical stresses being concentrated onto a larger volume and hence creating a higher probability of interface failure. In their case, the transverse flexure test was unable to discern differences in the sizing system due to the lack of sensitivity of the test. However, in systems where differences in the fiber/matrix adhesion are more pronounced, the transverse flexure strength should be a function of the sizing constituent. The interlaminar shear properties of the composites showed that the SBS was not a function of the sizing constituent but the iosipescu shear results were dependent upon the sizing. The iosipescu shear strength of the compatible sizing was approximately twice that of the incompatible sizing. The researchers could not provide an explanation as to why no differences in SBS were observed in their systems despite distinct differences in fiber/matrix adhesion. The impact resistance of the uni-directional composites was found to be 20% higher for the compatible sizing as compared to the incompatible. From fractograms, the researchers concluded that for the case of the compatible

sizing with the higher fiber/matrix adhesion a larger percentage of the energy was absorbed by delamination as compared to the compatible system where transverse matrix cracking dominated the energy contribution. The impact resistance of the 0/90 cross-ply composites was not statistically affected by the nature of the sizing agent.

Blackletter and co-workers [2.26] investigated the effects of carbon fiber surface treatment and sizing on the mechanical performance of EPON 828 epoxy matrix composites. The three fiber systems investigated were AU4 (un-surface treated and unsized), AS4 (surface treated and unsized), and AS4-C (surface treated and sized with the standard oligomeric epoxy G'). The mechanical properties investigated included short beam shear (SBS) and transverse flexure (TF). The SBS strength and TF strength were greatest for the AS4-C fiber with the G' sizing (SBS: 39.6 MPa for AU4, 71.2 MPa for AS4, and 73.1 MPa for AS4-C TF: 29.6 MPa for AU4, 39.7 MPa for AS4, and 78.2 MPa for AS4-C). The SBS strength was not significantly affected by the G' sizing agent while the TF strength was affected. In addition, the G' sizing level of 0.7 wt% outperformed the same fiber with a 1.2 wt% sizing level. The researchers concluded that for the case of brittle matrix composites like the epoxy, the SBS and TF strengths are limited by the tensile strength of the matrix (tensile strength = 85 MPa and shear strength = 52 MPa). A maximum in these properties is achieved when the interfacial shear strength or fiber/matrix adhesion is sufficient to support these matrix loads. However, for a ductile matrix, the researchers concluded that the SBS strength is limited by the matrix shear strength and the TF strength is limited by the matrix tensile strength. Unfortunately, the researchers failed to include in their analysis the effect of sizing material on the bulk matrix properties. The matrix properties tested were for the pure EPON 828 matrix with the appropriate hardener. In order to fully prove their conclusions, the researchers needed to prepare blends of EPON 828 and G' sizing at the concentration appropriate for complete sizing/matrix interdiffusion and compare these to the measured SBS and TF strengths. The researchers utilized scanning electron microscopy (SEM) to investigate the fracture surface of the failed composites. In cases where the EPON 828 composite properties were lower than matrices tensile strength, SEM showed that failure occurred at the fiber/matrix interface which was an indication of poor fiber/matrix adhesion. In cases where the EPON 828 composite properties were aproxi to the matrices tensile strength, SEM showed that failure occurred within the matrix which was an indication of good fiber/matrix adhesion.

T. Cheng and co-workers [2.27] investigated the effect that carbon fiber surface treatment and sizing had on the interfacial shear strength of single fiber/epoxy matrix composites. Type A Tenax carbon fibers supplied with three different surface treatments (un-oxidized and unsized, oxidized and unsized, and oxidized and sized with an oligomeric epoxy of unknown composition). Single fiber fragmentation tests were conducted in order to determine the interfacial shear strength. The data indicated that the oxidized/unsized fiber had a considerably higher interfacial shear strength than that of the oxidized/sized fiber. This result was surprising and is in conflict with most data available in the literature on this system. The researchers concluded that the epoxy functionality of the sizing was interacting strongly with the fiber surface preventing its dissolution into the bulk matrix and hence preventing the formation of an interphase. This conclusion is not logical considering the fact that only a monolayer should be involved in the physical or chemical bonding of sizing to the fiber. The largest percentage of the sizing should be unbound and available for interdiffusion. The literature presented in this section clearly shows that the presence of an oligomeric epoxy only positively affects fiber/matrix adhesion with an epoxy matrix composite. In all likelihood, these researchers damaged the sized fibers in the process of trying to separate a filament from the tow. In addition, the filaments that are most assessable for extraction from the tow bundle inherently have the least amount of sizing on them. The researchers also tested the effect of sizing molecular weight on the interfacial shear strength and found that the highest interfacial shear strength was obtained with the sizing that had the lowest molecular weight. The researchers concluded that sizing dissolution (i.e. sizing/matrix compatibility) is paramount to good fiber/matrix adhesion.

S. Yumitori and co-workers [2.28] studied the adhesion of carbon fibers to epoxy and PES thermoplastic matrices. Four different chemical surface treatments were used for the Tenax carbon fibers (1. unoxidized/unsized 2. oxidized/unsized 3. oxidized/sized with an oligomeric epoxy 4. oxidized/sized with amine terminated-PES). The fibers were sized on a small scale sizing apparatus. The epoxy was coated from an aqueous emulsion while the PES was sized from a solution of chloroform. Before the sized fibers were used, they were extracted with solvent to remove the unbound sizing. XPS results indicated that in both the epoxy and PES sizing cases, remnants (approximately 2-4nm thick) of the sizing remained. This was an indication that chemical bonding and/or very strong physical interactions with the fiber surface were present. In addition, the researchers discovered that the PES material strongly interacted

with the epoxy sizing. The interfacial shear strength was determined by a single fiber fragmentation technique. For the case of the PES matrix, the interfacial shear strength was found to be highest for the sized single fiber composites. The epoxy sized fiber had a considerably higher ISS compared to the PES sized composite. This was explained by noting that the epoxy and the PES were very compatible as determined during the XPS experiments. However, the opposite trend was observed for the epoxy matrix composites. The highest interfacial shear strengths were obtained from the oxidized/unsized fibers. The researchers tried to explain these trends by making arguments about interphase formation through preferential adsorption of the amine hardener into the epoxy sizing. Unfortunately, the researchers failed to realize that the thickness of their sizing (<4 nm) prevented the formation of any appreciable interphase. However, the preferential adsorption of a matrix constituent onto the carbon fiber surface would be possible and could explain the results observed (discussed later).

Paipetis and co-workers [2.29] determined the effect the sizing material had on the ISS through the use of laser Raman spectroscopy. The fibers utilized in this study were sized and unsized Soficar M40B-40B and M40B-MUS high modulus carbon. The resin used was a two part MY-750/HY-951 epoxy system provided by Ciba-Geigy. Single fiber composites were prepared and the experiments were conducted at different levels of strain. The researchers found that the sized fiber had a considerably higher ISS compared to the unsized. For the sized fiber, the ISS was comparable to the yield strength of the matrix indicating that matrix strain-to-failure and not fiber/matrix bond strength was limiting the ISS. For the unsized fiber, the low ISS as a result of a low fiber/matrix bond strength lead to extensive fiber debonding.

Most researchers have shown that the effect of fiber/matrix chemical bonding on the fiber/matrix bond strength is negligible in the case of carbon and aramid fiber reinforcements [2.24,2.30,2.31] and is only partially responsible in the case of e-glass reinforcement [2.32]. The mechanisms responsible for the fiber/matrix bond were purely physical/polar interactions with the fiber surface and/or the interphase.

In a classic paper written by Drzal and co-workers [2.2,2.24], the role that carbon fiber surface treatment (note: not sizing) played in fiber/matrix adhesion was addressed. The researchers showed that an epoxy matrix did exhibit a small degree of chemical bonding with the fiber but was not significant enough to affect fiber/matrix adhesion. The percentage of the carbon fiber surface that was chemically bonded to a matrix constituent was found to be less than

4%. Therefore, improvements in fiber/matrix adhesion could not be attributed to improvements in the fiber/matrix bond strength as a result of chemical bonding. The researchers concluded that the fiber surface treatment step removed a weak outer layer of the carbon fiber that enabled better fiber/matrix adhesion.

J. Mahy and co-workers [2.33] investigated the chemical bonding present between Twaron® aramid fibers and chemically dissimilar epoxy sizings. The data collected from a series of SIMMS experiments showed that chemical bonding between this fiber/sizing system was negligible and that physical interactions were prevalent due to polar interactions. These polar interactions were strong enough to greatly improve the interfacial adhesion between this sized fiber system and an epoxy matrix.

Atkinson and co-workers [2.34] studied the chemistry at the interface of an epoxy matrix and an unsized carbon fiber. The matrix utilized was a 1,2-epoxy-3-phenoxypropane and the carbon fibers were Courtaulds XA. The researchers discovered by SIMMS that chemical bonds existed between the matrix and the carbon fiber that resulted in lower contact angles and higher interfacial shear strengths. These researcher's data are in contradiction to the bulk of the literature that has found chemical bonding to be only a minor factor in determining ISS. However, the researchers did not quantify the amount of chemical bonding prevalent in their systems.

M. Shaker and I. Kamel [2.35] studied the effect of Kevlar fiber surface treatment on the interfacial adhesion with an epoxy matrix. In this study, RF-plasma was first used to modify the surface of the Kevlar fiber and then was used to polymerize an allylamine monomer onto the fiber surface. The researchers showed through single fiber fragmentation tests that the interfacial shear strength was increased by a factor of two for the RF-plasma/allylamine sized fibers over the untreated fibers. They concluded that this was the result of improved fiber/matrix adhesion achieved through chemical bonding of the Kevlar fiber with the allylamine sizing which was known to be highly compatible with the epoxy matrix. Unfortunately, the researchers did not establish their chemical bonding hypothesis through experimentation. Therefore, this chemical bonding theory must be viewed with skepticism.

2.1.3 Sizings: Effect on the Formation of an Interphase

The theoretical work of Cox reviewed in section 2.1.2.1 provided a link between fiber and matrix properties to the ISS. However, the rigorous inclusion of an interphase was left out in this derivation. Cox considered the matrix properties constant and the interphase effect could only be incorporated through changes in the bulk matrix properties. While this does not invalidate the qualitative trends predicted by Cox (i.e. ISS increasing with increasing matrix and/or interphase modulus), the quantitative features cannot be represented by this theory. In this section, fundamental work completed by Ho [2.36] is reviewed that incorporates a graded interphase into predictions of stress distribution around a fiber for the micro-indentation test. The rest of this section is devoted to reviewing some literature studies on the effect sizing materials have on bulk matrix properties. The sizing/matrix blend concentrations were selected to approximately match those expected in the interphase region. Thus, the mechanical properties determined were hypothesized to approximate the interphase mechanical properties.

Ho and co-workers [2.36] utilized the finite element method to predict the stress distribution around a single fiber undergoing an idealized micro-indentation test. The researchers incorporated an interphase region of variable thickness and modulus into the analysis. The results of this modeling showed that for interphase to matrix moduli ratios (E_I/E_M) of 30 or greater, the interfacial hoop and compressive stresses were three to six times greater than the interfacial shear stress. For E_I/E_M of 7, the interfacial hoop and compressive stresses were found to be equal to the interfacial shear stress, indicating that for interphases with extremely high moduli, the failure mechanisms and modes would change from shear to compressive. Therefore, the ISS measured by indentation techniques would be compromised for specimens with high moduli interphases. The effect of interphase thickness on the stress distribution was found to be negligible. How these results translate into the actual composite is unclear. A similar analysis was completed by A. Di Anselmo and co-workers [2.20].

E. Drown and co-workers at Michigan State [2.32] extensively studied the effect that a silane sizing had on the adhesion of an e-glass fiber to an epoxy matrix. The effect of the interphase on the fiber/matrix adhesion was assessed by preparing blends of the silane sizing and the epoxy. These blends were characterized by DMA and by static tensile testing. In this work, a DER 383 epoxy resin and a 1,2-Diaminocyclohexane hardener were used as the matrix constituents. A PPG 1.6K e-glass tow with two different surface treatments was used as the

reinforcements. The first treatment was deionized water while the second treatment consisted of an epoxy compatible sizing that contained film formers, antistatic agents, lubricants, and a silane coupling agent. The interfacial shear stress was determined with an interfacial testing system (ITS) that utilized single fiber composites. In addition, short beam shear (SBS) tests were conducted on the uni-directional composites. The results showed that the glass transition temperature of the epoxy was significantly affected by the presence of the sizing. In addition, the tensile modulus was shown to increase with increasing epoxy concentration. If the blends are assumed to be isotropic, then this would correspond to a substantial increase in the interphase shear modulus. According to the Cox theory presented earlier, if these two systems had perfect interface bonding, then the fiber/matrix adhesion or interfacial shear strength should be higher for the systems with the interphase. The ITS results reflected this improvement. The interfacial shear strength was found to be 44.6 MPa for the unsized composites and 60.1 MPa for the epoxy sized composite. Polarized transmitted light photomicrographs showed that the failure in the unsized composite was strictly fiber/matrix debonding while it was radial matrix splitting in the case of the sized. This change in failure modes could either be attributed to changes in fiber/matrix adhesion and/or interphase properties. The macroscopic mechanical properties also reflected an improvement. The SBS strength of the sized composite was approximately 12.4% greater than that of the unsized. The transverse and longitudinal flexure strengths were 35% and 25% greater for the sized compared to the unsized, respectively.

Al-Moussawi and co-workers [2.37] investigated blend properties of silane sizing agents and epoxy matrices. The researchers showed that the amount of silane sizing agent present in the epoxy matrix significantly affected matrix tensile properties and glass transition temperature. The blend concentrations tested were 10 and 25wt% silane sizing in a stoichiometric mixture of the epoxy and amine. In general, silane sizing agents typically utilized in e-glass/epoxy matrix composites produced blend properties with higher stiffness but lower toughness. The researchers speculated that the interphase properties would follow the same trend. Therefore, silane sizing agents not only affect the fiber/matrix bond strength due to specific covalent bond formation but also affect the matrix properties through interphase formation.

As mentioned briefly in one of the preceding paragraphs, interphases can also form from the preferential movement of a multi-component matrix constituent toward the fiber surface as a result of favorable interactions with the fiber or the sizing [2.34,2.38,2.39,2.40]. In addition,

systems with polydisperse matrix and/or sizing constituents can form interphases from the preferential exclusion of lower molecular weight species from the bulk and toward the interface. The lower molecular weight species tend to migrate toward interfaces with specific attractions due to entropic driving forces.

Dirand and co-workers [2.38] studied the effect of curing Dow 411-45 vinyl-ester resin in contact with different surfaces. The Dow 411-45 vinyl-ester resin (52 wt% vinyl-ester 45 wt% styrene monomer 3 wt% initiator and catalyst) was cured in contact with the following surfaces: PTFE, aluminum, glass (with various sizings), steel, and water. The polar and dispersive components of the solid free energy were determined for the cured matrix that had been contacted with the surface. The results indicated that the matrix components are preferential attracted or excluded from the interface region due to interactions with the solid surface. FTIR experiments on the cross-section revealed interphase regions that spanned several hundred microns. The results for the Dow 411-45 cured in contact with water and/or air showed that styrene was preferentially excluded from the interface region resulting in poor network formation. In addition, the researchers analyzed the interphase region in a single fiber composite through the use of ^{13}C NMR on thin cross-sections. These results showed that a 250 μm interphase region existed. This interphase was formed from either preferential movement of a matrix constituent toward the fiber surface as a result of favorable surface interactions and/or the interdiffusion of the matrix and the silane sizing/coupling agent.

Palmese and co-workers [2.40] investigated the effect of varying amine curing agent concentration on the mechanical spectra of cured epoxy blends. The results indicated that small changes in the ratio of amine curing agent to un-reacted epoxy had drastic effects on the cured epoxies glass transition and flexure modulus without significantly affecting the coefficient of thermal expansion. The significance of this work was that preferential movement of the amine towards the carbon fiber surface as a result of interactions with the fiber and/or interactions with the oligomeric epoxy size could produce an interphase with drastically different glass transitions and flexure properties.

Attwood and co-workers [2.41] examined the surface chemistry of carbon fibers through the use of inverse gas chromatography. The researchers concluded that a typical AS-4 and HTA type carbon fibers were/are basic in nature and that epoxy matrices would preferentially adsorb onto the carbon fiber surface.

The matrix and/or sizing can interact strongly with the surface of the fiber thus restricting the molecular movement and hence promoting an interphase with a higher glass transition [2.42,2.43,2.44,2.46]. Thomason [2.42] showed that epoxy sizings on e-glass fibers displayed significantly higher glass transitions than the pure sizing. Therefore, not only can an interphase form due to preferential adsorption of a matrix and/or sizing constituent but also can form due to a restriction in free volume.

Many methods have been proposed to measure the mechanical properties of the interphase region [2.29,2.42,2.43,2.44,2.46,2.47,2.48,2.49] in either the actual composite [2.42,2.43,2.44,2.46] or in a single fiber composite [2.29,2.47,2.48,2.49]. The latter method is much easier to implement experimentally than the former but the applicability of this idealized case limits its relevance to the actual composite. The difficulty in applying single fiber composite interphase studies to the actual composite lies in the mass/energy transport phenomena responsible for interphase formation. For example, the sizing to matrix mass ratio is much larger in the single fiber case. In addition, the cure time is greatly increased in the single fiber case due to the inability to transport thermal energy as effectively to the sample. These and many other factors make the interpretation of single fiber composite data as it applies to the actual composite qualitative at best.

The use of dynamic mechanical analysis on composite specimens has been proposed as a method for interphase characterization [2.42,2.43,2.44]. The presence of a second peak in the loss modulus well above the matrix glass transition temperature has been experimentally observed in numerous e-glass reinforced polymer matrix composites. The second peak is well above the glass transition of the sizing and cannot be explained by phase separation of the sizing from the matrix. Most researchers have concluded that this second peak is experimental verification of a high glass transition temperature interphase. The high T_g results from restricted movement of the sizing in the region around the interphase. However, other researchers believe the second peak in the storage modulus is due to experimental artifacts and not an interphase [2.45].

Another method for assessing the interphase mechanical property profile is through the use of atomic force microscopy (AFM). Robertson and co-workers [2.46] have developed methods for determining interphase mechanical properties in single fiber model composites. In addition, these researchers are presently trying to extend this method to the actual c-fiber

composite. The difficulty in making this transition lies in the fact that c-fiber composites cannot be easily micro-tomed to the level needed for AFM investigation.

Williams and co-workers developed a method for determining interphase deflection and hence interphase mechanical properties in a single fiber composite [2.47]. This method consisted of tagging a micro-tomed single fiber composite surface and utilizing a stereoinaging technique to determine the matrix displacements as a function of fiber tensile load and the radial position. The method was found to be sensitive to ± 1 nm matrix displacements. The method was applied to an epoxy resin cured with m-phenyldenediamine and an unsized carbon fiber system. The results showed the presence of a “soft” interphase that spanned a distance of 0.5 μ m into the bulk matrix. The interphase formed from the preferential adsorption of one of the matrix constituents. A similar method was developed by Meurs and co-workers [2.48]. Another method for characterizing interphases in single fiber composites by measuring the displacements as a function of load and computing interphase properties is Raman spectroscopy [2.29,2.49].

While these methods have found some success, they still lack the accuracy needed to apply them to any fundamental micro-mechanics model. In addition, because these methods determine the interphase properties, they do not allow one to determine the mechanisms responsible for its formation. There have been limited experimental efforts aimed at trying to directly measure the concentration profile existing in a composite interphase. Most of the effort has been focused upon measuring the extent of interdiffusion in sizing/matrix bilayer films.

As will be discussed later in section 2.3, Larson and co-workers [2.50] utilized dielectric sensors to measure the diffusion characteristics of a series of sizing materials with a Derakane™ vinyl-ester matrix. This study was limited to determining the diffusion characteristics and no attempt was made at actually predicting the composite interphase concentration profile.

Oyama and co-workers at Virginia Tech have recently measured the extent of interdiffusion between thermosetting composite matrices and PVP utilizing an electron microprobe technique [2.51 and 2.52]. In one particular study [2.52], a DGEBA epoxy and a DDS curing agent were utilized with a series of PVP sizing agents. The PVP sizing material was cast into a film of unspecified thickness. The epoxy/DDS mixture was then placed on top of the PVP film. The bilayer was then cured in a forced convection oven. Several different cure cycles were implemented to determine the effect of this processing parameter. In all cases, the cure cycle time was on the order of several hours due to the limited heat transfer available with the

forced convection system. The electron probe detected the presence of individual species by tracking certain atoms present in the species: Sulfur was used to track DDS, and nitrogen was used to track PVP and DDS. The researchers utilized a series of normalizations to approximate the concentration profile existing after cure. From the normalized concentration profiles, these researchers concluded that the DDS was preferentially absorbed into the PVP film. As a result, the interphasial region in the composite would be deficient in epoxy and the cross-link density would be affected which is in agreement with the findings of other researchers. The final normalized concentration profile was found to be symmetrical. This implies that the interphase was composed of a single phase, which also implies infinite solubility of PVP sizing in the matrix. The interphase thickness was approximated to be 10 to 25 μm thick depending upon the processing parameters. The fiber-fiber separation in a 60% fiber volume fraction composite is 1.6 μm . However, this data does not provide any indication as to the existence of an interphase in a DGEBA epoxy/DDS/PVP sizing system due to the unrealistic processing times utilized in this set of trials. In typical pultrusion operations, the matrix is cured in minutes not hours. Therefore, the time available for non-isothermal diffusion is at least one, possibly two, orders of magnitude higher for this experimental setup as compared to the pultrusion operation. These researchers also determined that there was negligible interdiffusion after the matrix had reached its gel point. In addition, the researchers discovered that the sizing molecular weight greatly influenced the interphase thickness. The epoxy/K-90 PVP ($M_w = 1,200,000 \text{ g/mol}$) had an interphasial thickness of 22 μm compared to 53 μm for the epoxy/K-17 PVP ($M_w = 9,000 \text{ g/mol}$). Therefore, the longer chains of the K-90 PVP reduced the mobility of the material compared to that of the shorter chained K-17 PVP. The results of this study provide only a qualitative look into composite interphase concentration profiles. In order to obtain a more quantitative prediction of the interphase concentration profile existing in an actual composite, the mechanisms responsible for its formation must be determined.

2.2 Fundamentals of Interphase Formation

As was discussed in the previous section, interphases can be formed from two distinct mechanisms.

1. Limited interdiffusion of the sizing and the matrix constituents.

2. Preferential adsorption of a matrix and/or sizing constituent at the fiber/matrix interface.

Items (1) and (2) will be reviewed in section 2.2.1 and 2.2.2 respectively. The fundamental modeling work discussed in chapter 4 and the future work proposed for chapter 5 will be based upon the theory reviewed in section 2.2.1. Because this theory is utilized as a “black box”, a detailed review is not presented. Only the theoretically based information needed to apply the fundamental interphase formation model will be presented. In section 2.2.2, the theoretical considerations of preferential adsorption will be superficially reviewed because this theory was not utilized during the course of this research.

2.2.1 Interdiffusion of a Polymer and a Solvent

The matrix material utilized for this work is a Dow Derakane™ vinyl-ester resin. This material is composed of a 690 g/mol vinyl-ester oligomer and monomeric styrene (in certain ratios). For the purpose of the work presented in this thesis, the vinyl-ester is considered a solvent and **not** a polymer. Therefore, the interdiffusion partially responsible for interphase formation can be considered diffusion between a polymer and a two-component solvent. The literature discussing the fundamental aspects of polymer-solvent interdiffusion is presented in this section. The majority of the literature available is for the interdiffusion of a polymer with a single solvent. Most of the fundamental work in the area of interdiffusion of a polymer with a binary solvent is still in its infancy and is far too complex to be applied to the task of predicting interphase formation. Therefore, the bulk of the research presented will involve the interdiffusion of a polymer with a single solvent. As will be discussed in chapter 4, the fundamental model developed for interphase formation assumes the interphase follows pseudo-binary behavior. In other words, the matrix moves as one material body and does not preferentially separate into its components. This assumption will be discussed in more detail in chapter 4.

The dissolution of macromolecules differs from that of micromolecules in that the resistance to achieving thermodynamic equilibrium may not be transport limited. When two micromolecules are placed in intimate contact, they instantaneously achieve thermodynamic equilibrium. Therefore, equilibrium is controlled by the ability of the species to achieve a state of intimate contact. However, when a macromolecule is placed in intimate contact with a

compatible solvent, the macromolecule may not achieve instantaneous equilibrium. The macromolecule undergoes a phenomena called relaxation. Therefore, equilibrium is controlled by transport and relaxation phenomena. In addition, a macromolecule below its glass transition temperature cannot easily diffuse into a compatible solvent due to the restrictions in motion accompanying the glassy state. The process of polymer segments migrating into the solvent is called dissolution. Before dissolution can occur in a glassy polymer, the polymer must be relieved of the glassy state restrictions. Even with these restrictions on polymer mobility, the solvent is small enough to penetrate into the free-volume of the glassy polymer. This process is called swelling. If the solvent and macromolecule are compatible, then the swelling process can invoke relaxation in the polymer thus making the chains conveyable after the chains disentangle (if entanglements are present).

An infinite plane of polymer placed in contact with an infinite plane of solvent can develop six layers depending upon material and processing parameters: (1) pure polymer (2) infiltrating area (3) swollen polymer (4) relaxed polymer (5) dissolution boundary layer and (6) pure solvent (Figure 2.2-1). These layers were first noted in a classic paper published by K. Uberreiter and F. Asmussen [2.53,2.54]. The quantitative description of the phenomena associated with polymer dissolution didn't appear until some time later.

The transport of micromolecular materials is well described by Fick's 1st Law Diffusion:

$$\underline{j}_s = -\rho D_{sp} \underline{\nabla} \omega_s \quad (2-2)$$

where \underline{j}_s is the mass flux of component s relative to the mass average velocity, ρ is the mass density, D_{sp} is the binary mutual diffusion coefficient, and ω_s is the weight fraction of component s . The applicability of equation (2-2) to polymer/solvent diffusion is dependent upon the state of the polymeric constituent, which will be discussed later in this section. In polymer/solvent systems, it is customary to assume that the system density remains constant. Completing a component s mass balance and applying equation (2-2) with the assumption of constant density gives the following:

$$\frac{\partial \omega_s}{\partial t} + (\underline{v} \cdot \underline{\nabla} \omega_s) - \underline{\nabla} \cdot (D_{sp} \underline{\nabla} \omega_s) = \frac{r_s}{\rho} \quad (2-3)$$

where \underline{v} is the mass average velocity and r_s is the mass of species s reacting per unit volume. An equation similar to equation (2-3) can be generated for species p . In most instances, the reaction

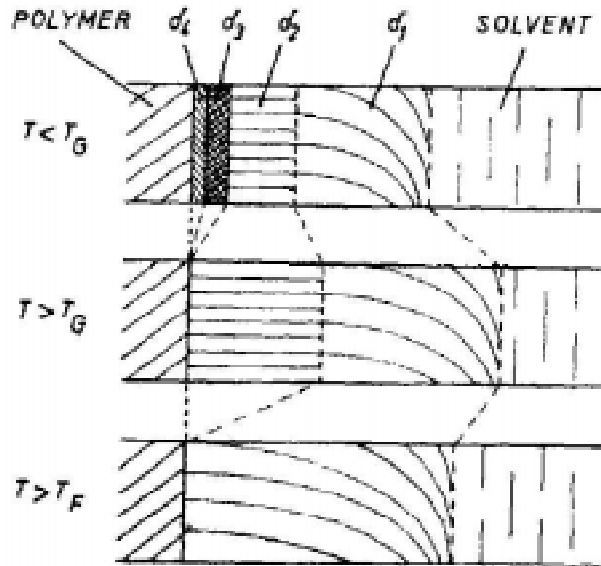


Fig. 3. Schematic picture of the layers composing δ at three temperatures.

Figure 2.2-1 Six possible layers in polymer/solvent interdiffusion: (1) pure polymer (2) infiltrating area (3) swollen polymer (4) relaxed polymer (5) dissolution boundary layer and (6) pure solvent. First noted by K. Uberreiter and F. Asmussen [2.53,2.54].

term is zero. In certain situations, the bulk flow term can be neglected. For this case, equation (2-3) reduces to the following (note: p species equation becomes trivial):

$$\frac{\partial \omega_s}{\partial t} = \nabla \cdot (D_{sp} \nabla \omega_s) \quad (2-4)$$

For the case of a constant diffusion coefficient, equation (2-4) reduces to Fick's 2nd Law of Diffusion:

$$\frac{\partial \omega_s}{\partial t} = D_{sp} \nabla^2 \omega_s \quad (2-5)$$

For the case presented earlier of two planes in contact (one polymer and one solvent), the amount of polymer dissolved as a function of time will be linear versus the square root of time if equation (2-4) is applicable. Systems that follow the square root time dependence are said to follow case I transport or Fickian transport [2.55]. In situations such as these, the diffusion phenomena controls the dissolution process. However, some systems do not follow this square root dependence. In some systems, the amount of polymer dissolved as a function of time will

be linear with respect to time. Systems that follow this linear dependence are said to follow case II transport. In systems such as these, the relaxation phenomena controls the dissolution process. Systems that have other functional time dependencies (t^n where $\frac{1}{2} \leq n \leq 1$) are said to exhibit anomalous behavior. In systems such as these, the diffusion and relaxation phenomena time scales are similar.

In dissolution of glassy polymers, the six layers discussed previously can be collapsed into two distinct layers as discussed by Narasimhan and Peppas [2.56]. The first layer consists of both glassy and rubbery materials that are undergoing interdiffusion and relaxation. Diffusion in glassy polymers is known to be highly non-Fickian due to a non-constant diffusion coefficient. As such, free volume based models have been developed for the concentration dependent diffusion coefficient as a function of the self-diffusion coefficients and the gradient in chemical potential. One such model was proposed by Duda and co-workers [2.57]. Narasimhan [2.56] applied the model to a swollen polymer network characterized by Flory-Huggins theory. The solvent flux was found to be a combination of diffusion and osmotic pressure terms. The osmotic pressure term resulted from the internal stresses present in the swollen polymer. The final transport equation for the glassy/rubbery phase contained a concentration dependent diffusion and an osmotic pressure term. The diffusion coefficient for the glassy/rubbery phase was assumed to be equal to the solvent's self diffusion coefficient for solvent concentrations in the dilute region and equal to the reptation diffusion coefficient in the concentrated region.

The second layer consisted of the relaxed polymer segments diffusing into the bulk solvent. Diffusion in this phase was assumed to be controlled by Brownian motion that could be described by the Stokes-Einstein relationship. The characteristic radius of the polymer was assumed to be equal to the radius of gyration:

$$D_d = \frac{kT}{6\pi\eta_s \cdot r_g} \quad (2-6)$$

where k is Boltzman's constant, η_s is the solvent viscosity, T is the absolute temperature, and r_g is the polymer radius of gyration. Narasimhan treated the η_s and r_g as constants, which resulted in a constant D_d . This is not rigorously accurate because both η_s and r_g are functions of the solvent concentration. Thus, D_d will be a strong function of concentration if the model were applied more correctly.

In addition, Narasimhan hypothesized that the rate at which relaxed material becomes available for dissolution is related to the reptation time of the relaxed polymer. Because the polymer segment travels approximately one radius of gyration during one reptation time, the researchers concluded that the rate at which relaxed material enters the bulk phase was approximately equal to the following [2.56]:

$$k_d = \frac{r_g}{t_{rep}} \quad (2-7)$$

where k_d is the relaxation rate, r_g is the polymer radius of gyration, and t_{rep} is the reptation time.

The thermodynamic equilibrium established between the rubbery/bulk interface was calculated utilizing Flory-Rehner and Flory-Huggins theory for chemical potentials. The rubbery region was assumed to have entanglements and the chemical potential of the solvent in that region was the following [2.56]:

$$\mu_1^+ = \mu_1^o + RT \left[\ln v_1 + \left(1 - \frac{1}{r}\right)(1 - v_1) + \chi(1 - v_1)^2 + \bar{V}_1 \rho_2 \left(\frac{2}{M_c} - \frac{1}{M} \right) \left(\frac{2}{1 - v_1} \right) - (1 - v_1) \right] \quad (2-8)$$

where μ_1^- is the chemical potential of the solvent in the rubbery phase, μ_1^o is the standard state chemical potential, R is the molar gas constant, T is the absolute temperature, v_1 is the solvent volume fraction in the rubbery phase, r is the molar volume of the polymer divided by the molar volume of the solvent, χ is the interaction parameter, V_1 is the solvent molar volume, ρ_2 is the polymer density, M_c is the critical entanglement molecular weight, and M is the number average molecular weight. The chemical potential of the solvent in the bulk phase was determined by Flory-Huggins theory to give the following [2.56]:

$$\mu_1^+ = \mu_1^o + RT \left[\ln v_1^+ + \left(1 - \frac{1}{r}\right)(1 - v_1^+) + \chi(1 - v_1^+)^2 \right] \quad (2-9)$$

where μ_1^+ is the chemical potential of the solvent in the bulk phase and v_1^+ is the solvent volume fraction in the bulk phase. Equations (2-8) and (2-9) establish the link between the two phases that are needed for the solution of equation (2-3) applied to both phases.

For an MEK-polystyrene system, Narasimhan and Peppas [2.56] applied the model after the thermodynamic parameters had been determined experimentally. The system was predicted to follow case II transport where relaxation controls the dissolution. As expected in case II

transport, the amount of polymer dissolved was found to be linear with time. In addition, the model was able to account for case I transport when the dissolution switched from relaxation controlled to diffusion controlled.

The applicability of the Narasimhan and Peppas' theory to the modeling work completed in chapter 4 will be discussed in chapter 5. Other researchers have tried to fundamentally predict polymer/solvent dissolution behavior [2.57,2.58] but this work will not be reviewed at this time.

2.2.2 Preferential adsorption of a matrix and/or sizing constituent

The preferential adsorption of a matrix or sizing constituent is controlled by interface thermodynamics. The experimental verification of preferential adsorption was provided in section 2.1. The theoretical considerations for preferential adsorption are beyond the scope of this review. However, an extensive treatment of the subject is given by Palmese and McCullough [2.59]. Presently, the theory can only predict the adsorption behavior of a two-component mixture in contact with a solid surface. Therefore, this theory can only be applied to interphase formation in systems without sizings. The theory cannot handle a third component such as a sizing. However, the theory is applicable to interphase formation in unsized carbon fiber composites in contact with a matrix resin. Because the research discussed in this thesis is focused upon a sizing's effect on composite mechanical performance, the theories developed for preferential adsorption are not applicable and hence will not be reviewed any further. In addition, the preferential absorption will affect the concentration profile within the thin sizing film. As will be discussed in chapter 4, the focus of this thesis is on interphases that have profile lengths similar to the diameter of the fiber (micron-scale interphases). The interphase that exists inside the thin sizing film (nanometer-scale interphases) is considered by this author to be an interfacial phenomena that is well-characterized by the interfacial shear strength and is not a subject under investigation.

2.3 Theory of Dielectric Spectroscopy

As will be discussed in chapter 5, dielectric spectroscopy was utilized in this work to determine the interdiffusion behavior of the sizing materials with the Derakane™ matrix. The theory of dielectric spectroscopy needed to analyze the data will be discussed in chapter 5. The review presented in this section will be restricted to a single paper written by Larson and co-

workers at Michigan State [2.50]. This paper describes a dielectric method for determining the swelling and dissolution diffusion coefficients for polymeric sizing materials in a Derakane™ matrix.

In this work [2.50], dielectric sensors (described in chapter 5) were coated with the polymeric sizing agent. After the coating had been applied, the sensors were coated with the Derakane™ matrix material. The dielectric response, conductivity in this case, was measured as a function of time. The sizing agents investigated included a soluble polyester, a semi-soluble poly(vinylacetate), and an insoluble polyurethane. The Derakane™ matrix was the 411-C50 series containing 50 wt% vinyl-ester oligomer and 50 wt% styrene monomer.

The dielectric response was measured as a function time. In order to generate concentration versus time data, the dielectric response of sizing/matrix blends were determined. In all cases, the dielectric response of the blends versus sizing concentration was found to be linear. The concentration versus time data were determined for each sizing material interdiffusing with the Derakane™. The concentration versus time data was fit to a Fickian model, which assumed a constant diffusion coefficient and assumed the sizing and matrix were one continuous phase. From the experimental data, the researchers were able to compute a swelling and dissolution diffusion coefficient at room temperature. The researchers determined that the swelling diffusion coefficients were on the order of 10^{-7} cm²/s for all materials tested. The dissolution diffusion coefficients were 10^{-11} cm²/s, 10^{-10} cm²/s, and 0 cm²/s for the soluble polyester, semi-soluble PVA, and insoluble polyurethane, respectively. The swelling diffusion coefficient was consistently three to four orders of magnitude higher than the dissolution diffusion coefficient. In the actual composite, the dissolution process will control the interdiffusion and hence interphase formation in these sizing materials. Case I Fickian transport was observed in all these materials. This is a strong indication that the glass transition temperature of the sizing materials tested were most likely below room temperature. This method would be significantly more difficult to apply to the dissolution of glassy materials, which was attempted in chapter 5.

2.4 Finite Element Method Applied to Parabolic DEQ's

As will be discussed in chapter 4, the Finite Element Method (FEM) is a powerful technique for solving differential equations over non-rectangular regions. It has several advantages over finite differencing schemes (FDS).

1. The FEM method can be easily extended to any solution domain whereas the FDS can only be applied to a solution domain for which the program was designed. Once a program utilizing the FEM has been written, it is easily applied to any geometry by simply modifying the mesh.
2. The FEM method automatically insures continuity of fluxes across material boundaries that must be independently programmed in FDS.
3. The FEM method can more easily handle flux boundary conditions than the FDS.

The finite element method has been utilized extensively to solve transport related problems. Because the method is now common to the scientific community, the specific theory utilized to apply the method is not reviewed. A good introductory book on the subject has been written by J. N. Reddy [2.60].

2.5 References

- 2.1 Personal communication with Strongwell, Inc.
- 2.2 L. T. Drzal, 'Composite Interphase Characterization', *SAMPE Journal*, 1983, pp. 7-13.
- 2.3 C. Sellitti, S. Vargiu, E. Martuscelli, and D. Fabbro, 'Wettability of glass fibers with different sizings and their adhesion to unsaturated polyester matrices', *Journal of Materials Science*, 22, 1987, pp. 3477-3484.
- 2.4 B. K. Larson and L. T. Drzal, 'Glass fibre sizing/matrix interphase formation in liquid composite moulding: effects on fibre/matrix adhesion and mechanical properties', *Composites*, Volume 25, Number 7, 1994, pp. 711-721.
- 2.5 E. Mäder, 'Study of fibre surface treatments for control of interphase properties in composites', *Composites Science and Technology*, **57**, 1997, pp. 1077-1088.
- 2.6 E. Mäder, K. Grundke, H. Jacobasch, and G. Wachinger, 'Surface, interphase and composite property relations in fibre-reinforced polymers', *Composites*, **Volume 25**, Number 7, 1994, pp. 739-744.

- 2.7 E. Mäder, H. –J. Jacobasch, K. Grundke, and T. Gietzelt, ‘Influence of an optimized interphase on the properties of polypropylene/glass fibre composites’, *Composites-Part A- (Applied Science and Manufacturing)*, **Vol. 27A**, No. 9, 1996, pp. 907-912.
- 2.8 N. Patel, V. Rohatgi, and L. J. Lee, ‘Influence of processing and material variables on resin-fiber interface in liquid composite molding’, *Polymer Composites*, **Vol. 14**, Number 2, pp. 161-172.
- 2.9 J. Mayer, S. Giorgetta, B. Koch, E. Wintermantel, J. Patsheider, and G. Spescha, ‘Characterization of thermally oxidized carbon fibre surfaces by ESCA, wetting techniques and scanning probe microscopy, and the interaction with polyethylmethacrylate. Development of a biocompatible composite material’, *Composites*, **Volume 25**, Number 7, 1994, pp. 763-769.
- 2.10 J. Mayer, E. Wintermantel, P. Zemp, E. Freitag, and M. Flemming, ‘Solid body wetting, a new method for studying the wetting behaviour of thermoplastics on carbon fibres’” *Proc Interfacial Phenomena in Composite Materials 91*, Butterworth-Heinemann, Oxford, UK, 1991, pp. 97-100.
- 2.11 C. G. Pantano, G. Chen, and D. Qi, ‘Interface Reactions and Wetting in Carbon-fiber-reinforced Glass Matrix Composites’, *Materials Science and Engineering*, A126, 1990, pp. 191-201.
- 2.12 H. L. Cox, *British Journal of Applied Physics*, **3**, 1952.
- 2.13 B. W. Rosen, *Fibre Composite Materials*, American Society for Metals, Metals Park, OH, 1965.
- 2.14 V. Rao and L. T. Drzal, ‘The Dependence of Interfacial Shear Strength on Matrix and Interphase Properties’, *Polymer Composites*, **Vol. 12**, No. 1, February, 1991, pp.48-56.
- 2.15 L. T. Drzal, ‘The Effect of Polymeric Matrix Mechanical Properties on the Fiber-Matrix Interfacial Shear Strength’, *Materials Science and Engineering*, A126, 1990, pp. 289-293.
- 2.16 K. L Reifsnider, ‘Modelling of the interphase in polymer-matrix composite material systems’, *Composites*, **Volume 25**, Number 7, 1994, pp. 461-469.
- 2.17 Q. D. Zeng, L. Ling, and Z. L. Wang, ‘Statistical Strength of Unidirectional Composites and the Effect of the Interfacial Shear Strength’, *Composites-Part A- (Applied Science and Manufacturing)*, **Vol. 56**, No. 10, 1996, pp. 1191-1200.

- 2.18 J. Ivens, M. Wevers, and I. Verpoest, 'Influence of carbon fibre surface treatment on composite UD strength', *Composites*, **Volume 25**, Number 7, 1994, pp. 722-728.
- 2.19 K. Nishiyabu, A. Yokoyama, and H. Hamada, 'Assessment of the Influence of Interfacial Properties on Stress Transfer in Composites by a Numerical Approach', *Composites Science and Technology*, **57**, 1997, pp. 1103-1111.
- 2.20 Di Anelmo, M. L. Accorsi, and A. T. DiBenedetto, 'The effect of an interphase on the stress and energy distribution in the embedded single fibre test', *Composites Science and Technology*, 0266-3538/92, pp. 215-225.
- 2.21 P. W. J. van den Heuvel, Y. J. W. van der Bruggen, and T. Peijs, 'Failure phenomena in multi-fibre model composites: Part 1. An experimental investigation into the influence of fibre spacing and fibre-matrix adhesion', *Composites-Part A- (Applied Science and Manufacturing)*, **Vol. 27A**, No. 9, 1996, pp. 855-859.
- 2.22 M. S. Madhukar and L. T. Drzal, 'Fiber-Matrix Adhesion and Its Effect on Composite Mechanical Properties: I. Inplane and Interlaminar Shear Behavior of Graphite/Epoxy Composites', *Journal of Composite Materials*, **Vol. 25**, 1991, pp. 932-957.
- 2.23 M. S. Madhukar and L. T. Drzal, 'Fiber-Matrix Adhesion and Its Effect on Composite Mechanical Properties: II. Longitudinal (0°) and Transverse (90°) Tensile and Flexure Behavior of Graphite/Epoxy Composites', *Journal of Composite Materials*, **Vol. 25**, 1991, pp. 958-991.
- 2.24 L. Drzal, M. Rich, and P. Lloyd, 'Adhesion of Graphite Fibers to Epoxy Matrices: I. The Role of Fiber Surface Treatment', *J. Adhesion*, **Vol. 16**, 1982, pp. 1-30.
- 2.25 F. Hoecker and J. Karger-Kocsis, 'Effects of the interface on the mechanical response of CF/EP microcomposites and macrocomposites', *Composites*, **Volume 25**, Number 7, 1994, pp. 729-738.
- 2.26 D. Blackketter, D. Upadhyaya, T. King, and J. King, 'Evaluation of fiber surface treatment and sizing on the shear and transverse tensile strengths of carbon fiber-reinforced thermoset and thermoplastic matrix composites', *Polymer Composites*, **Vol. 14**, Number 5, pp. 430-436.
- 2.27 T. H. Cheng, J. Zhang, S. Yumitori, F. R. Jones, and C. W. Anderson, 'Sizing resin structure and interphase formation in carbon fibre composites', *Composites*, **Volume 25**, Number 7, 1994, pp. 661-670.

- 2.28 S. Yumitori, D. Wang, and F. Jones, 'The role of sizing resins in carbon fibre-reinforced polyethersulfone (PES)', *Composites*, **Volume 25**, Number 7, 1994, pp. 698-705.
- 2.29 Paipetis and C. Galiotis, 'Effect of fibre sizing on the stress transfer efficiency in carbon/epoxy model composites', *Composites-Part A- (Applied Science and Manufacturing)*, **Vol. 27A**, No. 9, 1996, pp. 755-767.
- 2.30 Garton and J. Daly, 'The crosslinking of epoxy resins at interfaces. II. At an aromatic polyamide surface', *Journal of Polymer Science: Polymer Chemistry Edition*, **Vol. 23**, 1985, pp. 1041-1059.
- 2.31 L. Penn, T. Byerley, T. Liao, 'The study of reactive functional groups in adhesive bonding at the aramid-epoxy interface', *J. Adhesion*, **Vol. 23**, 1987, pp. 163-185.
- 2.32 E. Drown, H. Moussawi, and L. Drzal, 'Glass fiber 'sizings' and their role in fiber-matrix adhesion', *Journal of Adhesion Science and Technology*, **Vol. 5**, No. 10, 1991, pp. 865-881.
- 2.33 J. Mahy, L. Jenneskens, and O. Grabandt, 'The fibre/matrix interphase and the adhesion mechanism of surface-treated Twaron® aramid fibre', *Composites*, **Volume 25**, Number 7, 1994, pp. 653-660.
- 2.34 K. E. Atkinson, G. J. Farrow, and C. Jones, 'Study of the interaction of carbon fibre surfaces with a monofunctional epoxy resin', *Composites-Part A- (Applied Science and Manufacturing)*, **Vol. 27A**, No. 9, 1996, pp. 799-804.
- 2.35 M. Shaker, I. Kamel, F. Ko, and J. Song, 'Improvement of the Interfacial Adhesion Between Kevlar Fiber and Resin by Using R-F Plasma', *Journal of Composites Technology & Research*, JCTRER, **Vol. 18**, No. 4, October 1996, pp. 249-255.
- 2.36 H. Ho and L. T. Drzal, 'Evaluation of interfacial mechanical properties of fiber reinforced composites using the microindentation method', *Composites-Part A- (Applied Science and Manufacturing)*, **Vol. 27A**, No. 10, 1996, pp. 961-971.
- 2.37 H. Al-Moussawi, E. K. Drown, and L. T. Drzal, 'The Silane/Sizing Composite Interphase', *Polymer Composites*, **Vol. 14**, No. 3, 1993, pp. 195-200.
- 2.38 X. Dirand, B. Hilaire, E. Lafontaine, B. Mortaigne, and M. Nardin, 'Crosslinking of vinyl ester matrix in contact with different surfaces', *Composites*, **Volume 25**, Number 7, 1994, pp. 645-652.
- 2.39 P. I. Marshall, D. Attwood, and M. J. Healey, 'Interface chemistry in carbon fibre/epoxy matrix composites', *Composites*, **Volume 25**, Number 7, 1994, pp. 752-756.

- 2.40 G. R. Palmese and R. L. McCullough, 'Effect of Epoxy-Amine Stoichiometry on Cured Resin Material Properties', *Journal of Applied Polymer Science*, **Vol. 46**, 1992, pp. 1863-1873.
- 2.41 D. Attwood and P. I. Marshall, 'Atomistic modelling of the adsorption of epoxy and amine molecules on the surface of carbon fibers', *Composites-Part A- (Applied Science and Manufacturing)*, **Vol. 27A**, No. 9, 1996, pp. 775-779.
- 2.42 J. L. Thomason, 'A note on the investigation of the composite interphase by means of thermal analysis', *Composites Science and Technology*, **44**, 1992, pp. 87-90.
- 2.43 J. Mijovic and K. F. Lin, *Polymer Blends and Composites in Multiphase Systems*, chapter 19, Advanced Chemical Series, No. 206, American Chemical Society, Washington, D.C., 1984.
- 2.44 K. E. Reed, *Polymer Composites*, **1**, 44, 1980.
- 2.45 J. L. Thomason, 'Investigation of Composite Interphase Using Dynamic Mechanical Analysis: Artifacts and Reality', *Polymer Composites*, **Vol. 11**, No. 2, 1990, pp. 105-113.
- 2.46 M. Robertson, J. Riffle, and M. Bump. The Designed Interphase Group at VPI. Personal communication.
- 2.47 J. G. Williams, M. R. James, and W. L. Morris, 'Formation of the interphase in organic-matrix composites', *Composites*, **Volume 25**, Number 7, 1994, pp. 757-762.
- 2.48 P. F. M. Meurs, P. J. G. Schreurs, T. Peijs, and H. E. H. Meijer, 'Characterization of interphase conditions in composite materials', *Composites-Part A- (Applied Science and Manufacturing)*, **Vol. 27A**, No. 9, 1996, pp. 781-786.
- 2.49 C. Galiotis, C., 'A study of mechanisms of stress transfer in continuous- and discontinuous-fibre model composites by laser Raman spectroscopy', *Composites Science and Technology*, **48**, 15, 1993.
- 2.50 B. K. Larson, L. T. Drzal, and J. Van Antwerp, 'Swelling and Dissolution Rates of Glass Fiber Sizings in Matrix Resin via Micro-Dielectrometry', *Polymer Composites*, **Vol. 16**, No. 5, 1995.
- 2.51 H. T. Oyama, J. P. Wightman, J. J. Lesko, *Journal of Polymer Science, Polymer Physics Edition*, **35**, 331

- 2.52 H. T. Oyama, T. N. Solberg, J. P. Wightman, 'Electron Microprobe Analysis As a Novel Technique to Study the Interface Between Thermoset and Thermoplastic Polymers', submitted to *Polymer*.
- 2.53 K. Ueberreiter and F. Asmussen, 'Velocity of Dissolution of Polymers. Part I', *Journal of Polymer Science*, **Vol. 57**, 1962, pp. 187-198.
- 2.54 K. Ueberreiter and F. Asmussen, 'Velocity of Dissolution of Polymers. Part II', *Journal of Polymer Science*, **Vol. 57**, 1962, pp. 199-208.
- 2.55 T. Alfrey, E. F. Gurnee, and W. G. Lloyd, 'Diffusion in Glassy Polymers', *Journal of Polymer Science*, Part C, **12**, 1966, pp. 249-261.
- 2.56 B. Narasimhan and N. Peppas, 'On the Importance of Chain Reptation in Models of Dissolution of Glassy Polymers', *Macromolecules*, **Vol. 29**, Number 9, 1996.
- 2.57 Vrentas, J. S. and J. L. Duda, 'Diffusion of Small Molecules in Amorphous Polymers,' *Macromolecules*, **9**, 785, 1976.
- 2.58 J. S. Papanu, D. S. Soane, A. T. Bell, and D. W. Hess, 'Transport Models for Swelling and Dissolution of Thin Polymer Films', *Journal of Applied Polymer Science*, **Vol. 38**, pp. 859-885, 1989.
- 2.59 G. R. Palmese and R. L. McCullough, 'Analytical models for the equilibrium behavior of binary mixtures in the presence of a solid surface', *Composites: Part A*, **30**, pp. 3-10, 1999.
- 2.60 J. N. Reddy, *An Introduction to the Finite Element Method*, (Second Edition), McGraw-Hill 1993.

Chapter 3

Experimental: Pultrusion of Carbon Fiber/Vinyl Ester Composites with Tailored Sizing Agents

3 Introduction

In this chapter, a summary of the experimental results for pultrusion of thermoplastic sized carbon fiber/vinyl ester matrix composites will be presented. The material presented in this chapter addresses objective #1 listed in the introductory chapter. The objective of these experiments was to validate that thermoplastic sizings affect the performance of continuously reinforced polymer matrix composites. It was also hoped that the source of these effects could be elucidated from a carefully constructed set of experimental trials. As was discussed in Chapter 1, it is believed that sizings can affect composite performance in four ways.

1. Alterations in composite processability through modification of the carbon fiber handling characteristics and through modification of carbon fiber tow wettability.
2. Alterations in damage evolution and propagation as a result of modifications in fiber/sizing and sizing/matrix adhesion. In chapters 1 and 2, the fiber/sizing and sizing/matrix adhesion were not differentiated and were lumped into a general fiber/matrix adhesion. In this chapter, the term fiber/matrix adhesion is again used to express both a fiber/sizing and sizing/matrix adhesion.
3. Alterations in damage evolution and propagation as a result of an interphase formed by the interdiffusion of the sizing and matrix materials.
4. Alterations in damage evolution and propagation as a result of matrix plasticization.

The difficulty in determining which of these effects has the most influence upon final composite performance lies in the fact that it is almost impossible to separate these effects in an experimental situation. For instance, because an interphase effect should be dependent on the time available for interdiffusion, then this effect can be probed by varying the processing time in the dip bath. However, varying the time available for interdiffusion might affect the processability of the fiber by varying the degree to which sizing relaxation can occur and the

time available for tow wet-out. Unfortunately, there is no way that processing parameters (line speed, dip bath length, sizing level, etc.) can be varied in order to probe the relative importance of the interphase effect, matrix plasticization effect, and the fiber/matrix adhesion effect **without** altering the processability of the fiber. If the processability effect could be eliminated, then it would be feasible to determine the relative importance of the other effects on mechanical performance through a carefully designed set of experimental trials.

How can one assess the effect that **processability** of the carbon fiber alone has on the mechanical performance of the final composite? This question cannot be quantitatively answered because the phenomenological events associated with it are far too complex and interconnected. As was discussed in the introduction chapter, sizings can affect processability in two ways.

1. The sizing can alter the handling characteristics of the fiber (i.e. fiber protection and alignment). Because the carbon fiber is very brittle, the processing equipment can easily damage it. A sizing helps to protect the fiber from this damage by coating it with a tough material and/or by lubricating the surface. Hexcel's oligomeric epoxy sizing, G', is used for this purpose. The G' sizing is very oily and helps to lubricate the carbon fiber and prevent damage to the fiber. A thermoplastic material such as those utilized in this work may or may not help to lubricate the carbon fiber surface but they should provide a tough coating that prevents damage. The qualitative implications of this effect can be addressed by carefully observing the pultrusion process and visually noting the degree to which the fibers are damaged. For instance, the amount of fiber build-up at the dip bath entrance can be easily observed and differences between sizing systems can be noted. In addition, differences in the final composite surface finish can be visually noted. The pull force required to maintain steady pull speeds in the pultruder is indicative of the contact friction experienced at the surface of the die. Assuming a static gel-zone, if more pull force is required for a particular sizing system (note: holding other processing parameters constant), then more composite surface damage will result. A sizing system that better lubricates the fiber system will present a considerably lower pull force than sizing systems with less lubrication. Hence, the sizing plays a key role in fiber protection through surface toughening and lubrication. In addition, a sizing influences the inherent stiffness of the carbon fiber. In particular, thermoplastic sized carbon fibers are

considerably more stiff than the oligomeric epoxy sized fibers. The fiber alignment is a key parameter for optimizing on-axis properties such as tension, longitudinal flexure, and compression. A sizing that produces a stiffer fiber will improve the alignment and hence on-axis performance.

2. The sizing affects the wettability of the carbon fiber tow with the matrix material. The sizing material and how it was processed in the sizing line affects the geometric packing of the tow (a kinetic parameter) and also affects the contact angle (a thermodynamic parameter) established between the fiber and the matrix. The quantitative significance of this effect was expressed in the introductory chapter by the following equation:

$$t_f = \frac{l^2 \mu_r V_{void}}{2S_b \left(\frac{2}{R}\right) \gamma_r \cos \theta} \quad (1-4)$$

where t_f is the time required to wet the tow, l is the characteristic length or thickness of the tow, μ_r is the matrix viscosity, V_{void} is the void volume of the sized carbon fiber entering the dip bath, S_b is the tow permeability, R is the characteristic radius for the carbon fiber packing array, γ_r is the surface tension of the matrix, and θ is the contact angle established between the sized carbon fiber and the matrix. The contact angle θ can be determined for the sizing/matrix interface from idealized bi-layer films and optical methods, which were not completed for this thesis. The other physical parameters needed to evaluate equation (1-4) are not experimentally accessible. However, the qualitative effect that sizings have on the wettability of the carbon fiber with the matrix can again be assessed from visually observing the pultrusion process. At the dip bath exit, visual inspection of the wetted tows allows one to examine the internal tow to determine if the matrix has fully penetrated the tow bundle. At the compaction portion of the pultrusion process, the amount of excess matrix squeezed from the tow can be used to assess the degree to which the internal tow is wet. After the composite has been produced, the voids can be assessed through the use of optical methods and ultra-sonic c-scan. However, the absence of macroscopically measurable voids does not necessarily guarantee intimate fiber/matrix/sizing contact.

The overall objective of the work presented in this chapter was to demonstrate the performance enhancing capabilities of carbon fibers sized with thermoplastic materials optimized

for the vinyl-ester matrix and the pultrusion process. In addition, a second objective was to determine the difference in processability of the thermoplastic sizing materials compared to the G' or oligomeric epoxy as discussed in the previous few paragraphs. A final objective was to determine the role of the interphase on on-axis composite performance. This chapter is organized into the following sections.

- 3.1 – Mechanical Performance of Pultruded Hexcel AS-4 Carbon Fiber/Vinyl Ester Composites Processed with G', Phenoxy, and K-90 PVP Sizing Agents
- 3.2 – Mechanical Performance of Pultruded Hexcel AS-4 Carbon Fiber/Vinyl Ester Composites Processed with G', Phenoxy, K-90, and K-30 PVP Sizing Agents
- 3.3 – Mechanical Performance of Pultruded Carbon Fiber/Vinyl Ester Composites Processed with Physically Dissimilar Sizing Agents
- 3.4 – Summary

In section 3.1, a paper compiling the detailed experimental results of a joint plant trial between the Designed Interphase Group (DIG) and Strongwell Inc. is presented. The overall objective of this work was to determine whether thermoplastic sized carbon fibers were processable via pultrusion. A second objective was to determine how thermoplastic sizings altered the mechanical properties of the final composite. It was also hoped that the relative importance of the effects listed in the introduction could be elucidated. In this work, Hexcel carbon fibers were sized at Virginia Tech with two thermoplastic materials and vinyl-ester composites were pultruded from these. In addition, the standard G' sized Hexcel carbon fibers were pultruded for a benchmark comparison. The paper details comparisons between these systems in terms of their processability and their final composite part mechanical performance. As with any experimental trial of this magnitude, there were several individuals responsible for the experimental work presented in Section 3.1. The author initiated and planned the experimental work presented in this section. The author and Dr. Nikhil Verghese completed the bulk of the experimental work presented. The author completed the following experimental work presented: sizing of the carbon fibers, characterization of the sized fibers for sizing level, scanning electron microscopy, pultrusion at Strongwell, specimen preparation for all mechanical tests, longitudinal flexure testing, and short beam shear testing. Dr. Nikhil Verghese completed the following experimental work presented in Section 3.1: optical microscopy, static tensile testing, and compression testing. In addition, Dr. Verghese assisted the author in setting up the

Instron equipment utilized for the longitudinal flexure and short beam shear testing. Mr. Steve McCartney performed the ESCA experiments presented in Section 3.1. Finally, Mr. Mack McCord completed the ultrasonic c-scan results discussed. The detailed discussion that is presented in Section 3.1 was written entirely by this author. The pultrusion results presented in this section must be viewed with caution. The G' sized composites were produced from the equivalent of 32 ends of the 12k material (including the difference in linear density between AS-4 lots) compared to only 30 ends used for the thermoplastic fibers. While this difference in number of ends was corrected for in the mechanical property results presented, the effect these two additional ends had on composite damage has not been assessed. The damage exhibited on the G' surface was attributed to the fraying that was observed in the preprocessing and dip bath portions of the pultrusion process. This fraying was not seen as extensively in the thermoplastic sized fibers. It was therefore natural to conclude that the sizing and not the two additional ends was the cause for the surface damage on the G' composite. Therefore, the conclusions reached in section 3.1.4 will be verified with more pultrusion trials that utilize the same number of ends (including differences in linear density) to more concretely establish that the sizing was the cause for the improved surface finish (3.1.4.1.2).

In section 3.2, a paper compiling the detailed experimental results of a joint plant trial between DIG and Dow is presented. This study differs from the one discussed in Section 3.1 in the following ways:

1. The sizing levels for the thermoplastic materials was considerably less for the present trial.
2. The composite cross-section was approximately double the cross-section utilized in Section 3.1.
3. The pultruder was outfitted with a load cell that could monitor pull-force as a function of the sizing constituent.
4. The matrix utilized in the present study had $\frac{1}{2}$ the styrene level that the Section 3.1 matrix had.
5. The fiber volume fraction was more consistent from sizing to sizing, which was not the case for the trial discussed in Section 3.1.

6. Finally, the K-30 PVP sizing material was tested in addition to the K-90 PVP and Phenoxy™ tested in Section 3.1. The K-30 PVP and K-90 PVP differ only in their inherent molecular weight (K-30: $M_w = 49,000$ g/mol K-90: $M_w = 1,200,000$ g/mol).

The overall objective of the trial discussed in Section 3.2 was to reconfirm the drastic effects the thermoplastic sizing materials had on pultrusion processability and composite mechanical performance. The pultrusion setup utilized in the present trial allowed more process variables to be monitored, such as pull-force and the peak cure exotherm. This allowed the process to be more closely monitored and allowed conclusions about differences in sized fiber processability more accessible. Another objective of the current trial was to determine the effect of sizing molecular weight on composite mechanical performance. A variation in sizing molecular weight should not change the fiber processability and/or fiber/matrix interfacial characteristics. However, the interdiffusion should be drastically different (discussed more in chapters 4 and 5) and hence the interphase should be different. Therefore, the effect of altering the interphase was probed with the K-30 and K-90 PVP sizing systems. In particular, Hexcel AS-4 12K carbon fibers were sized with three different thermoplastic sizing agents. The sizing agents tested were K-90 poly(vinylpyrrolidone), K-30 poly(vinylpyrrolidone) and Phenoxy™. In addition, Hexcel AS-4 12K carbon fibers sized commercially with the standard G' were tested. The paper details comparisons between these systems in terms of their processability and their final composite part mechanical performance. As with the other pultrusion trial, several individuals were responsible for the experimental work presented in section 3.2. The author initiated and planned the experimental work presented in this section. Mainly the author and Mr. Herbert Engelen of the Dow Chemical Company completed the experimental work presented. The author completed the following experimental work presented: sizing of the carbon fibers, characterization of the sized fibers for sizing level, scanning electron microscopy, specimen preparation for longitudinal flexure testing and short beam shear testing, fiber volume fraction determination, and filler content determination. Dr. Nikhil Verghese assisted in the measurement of the longitudinal flexure and short beam shear testing. The material presented in section 3.2 was written entirely by this author.

In section 3.3, a modified form of a preprint submitted and published in the SPE ANTEC '98 Proceedings is presented. Again, this set of experiments was a joint plant trial between DIG

and Strongwell Inc. The overall objective of this experimental trial was to determine whether the traditionally utilized Hexcel carbon fibers sized with G' could be replaced with the cheaper Zoltek Panex materials sized with our thermoplastic sizings without compromising performance. Strongwell presently utilizes Hexcel AS-4 G' sized carbon fibers in a pultruded vinyl-ester composite drive shaft. The Zoltek Panex fibers offer considerable cost savings over the Hexcel fibers. However, composites produced from the Zoltek Panex fibers sized with Zoltek's proprietary oligomeric epoxy sizing, Z', typically have inferior mechanical properties when compared to the Hexcel AS-4 G' composite. It was hoped that utilizing our thermoplastic sizings could considerably improve the performance of the Zoltek Panex fibers up to the level achieved with the Hexcel AS-4. This would allow the use of the cheaper Zoltek fibers without compromising performance. In this work, Zoltek Panex 48K carbon fibers were sized at Virginia Tech with three thermoplastic materials and vinyl-ester composites were pultruded from these. In addition, the standard Z' sized Panex 48K and G' sized Hexcel AS-4 12K carbon fibers were pultruded for a benchmark comparison. The paper details differences in the static compressive performance between the composite systems. Because sections 3.1 and 3.3 both detail experimental pultrusion trials conducted under similar experimental conditions, there is repetition of material between the two experimental sections. As was discussed in the previous paragraph, this trial also involved the contributions of several individuals. The author completed the following experimental work presented in section 3.3: sizing of the Zoltek carbon fibers, characterization of the sized fibers for sizing level, and scanning electron microscopy. Dr. Nikhil Verghese completed the compression testing presented. Various other members of the DIG assisted Strongwell in the pultrusion of the Zoltek fiber. Strongwell completed the fiber volume fraction analysis presented. Again, the discussion presented in Section 3.3 was written entirely by this author.

In section 3.4, a summary of the work presented in chapter 3 is presented. This concludes the introductory portion of this chapter. In the next section, portions of a paper to be submitted to Composites Journal are presented.

3.1 Mechanical Performance of Pultruded Hexcel AS-4 Carbon Fiber/Vinyl Ester Composites Processed with G', Phenoxy, and K-90 PVP Sizing Agents

3.1.1 Abstract

Hexcel AS-4 12K carbon fibers were sized with two different thermoplastic sizing agents. The sizing agents tested were K-90 poly(vinylpyrrolidone)(BASF) and Phenoxy™ (PKHW-35 from Phenoxy™ Associates). In addition, Hexcel AS-4 36K carbon fibers sized commercially with the standard G' were tested. The sized carbon fibers were processed into composites utilizing a pilot scale pultruder and a pultrudable Derakane™ 411-35Li vinyl-ester resin.

All of the thermoplastic sizing materials, especially the Phenoxy™ sizing had improved processability over the traditionally utilized G' sizing material. These improvements in processability translated into improvements in final composite surface finish and quality. The thermoplastic sizings optimized for interaction with the vinyl-ester matrix caused rapid tow wetting. In addition, the thermoplastic sized fibers entered the dip bath stiff, thus minimizing fraying and damage but exited the dip bath saturated with resin and pliable, thus minimizing kinking in the die.

The static mechanical performance of the composites produced from these thermoplastic sizings were greatly enhanced compared to the standard G' sizing. All of the thermoplastic sized composites outperformed the standard sizing G' by at least 25% in static tensile strength, by at least 11% in longitudinal flexure strength, by at least 30% in short beam shear strength, and 31% in static compressive strength. The tensile, longitudinal flexure, and compressive modulus appeared to be unaffected by variations in the sizing.

Therefore, the mechanical performance of pultruded carbon fiber/vinyl-ester composites is greatly affected by the nature of the sizing agent present. These improvements in mechanical properties are believed to be the result of improved fiber processability and altered interphase properties. The effect of improved fiber/matrix adhesion is also believed to be a contributing factor but is secondary to the effects of processability and altered interphase properties.

3.1.2 Introduction

Carbon fiber composites have traditionally been used in high-end aerospace applications. This is changing, however, with composites finding increasing uses in offshore oil exploration and civil infrastructure applications. In order for composites to find acceptance in civilian markets like infrastructure, the cost of the processing steps and raw materials must be reduced while maintaining or improving their performance. The overall goal of this research is to improve the performance of continuously reinforced carbon fiber/vinyl-ester composites without increasing their cost.

Pultrusion represents one of the most cost-effective means of rapidly producing continuous fiber reinforced composites with a thermoset matrix. Because civilian markets often require uncomplicated parts of constant cross-section, pultrusion represents one of the most economical means of producing composites for these applications.

Sizings, a thin coating applied to the surface of the carbon fiber before impregnation with the matrix, have been shown to affect the mechanical performance of the composite [3.1,3.2,3.3,3.4]. Even a matrix dominated property like compressive strength can be affected by the sizing constituent [3.5]. A sizing can affect composite performance by altering the processability of the carbon fiber and/or by altering the manner in which load gets transferred from one failed fiber to another. The processability of a carbon fiber depends on three distinct characteristics: (1) fiber protection (2) fiber alignment and (3) fiber wettability. Unsized carbon fiber is extremely brittle and susceptible to damage. Traditionally, a sizing is placed on the surface of the fiber to protect it from damage. In addition, a sizing can alter the handling characteristics of the tow such as pliability. The pliability of the tow directly influences the fiber alignment/waviness in the final composite. Fiber alignment is a key parameter in determining composite mechanical performance especially in compression [3.6,3.7,3.8]. A sizing also alters the surface free energy of the carbon fiber thus altering the thermodynamic driving force for wetting [3.9]. The manner in which load gets transferred from a failed fiber to surrounding fibers is controlled by two characteristics: (1) fiber/matrix adhesion and (2) graded matrix properties/interphase formation. In the composite community, the term fiber/matrix adhesion is typically quantified by an interfacial shear strength (ISS). However, the physical parameters affecting ISS are not exclusively interfacial. For instance, Cox [3.10] derived a theoretical expression relating ISS to fiber and matrix properties assuming a no-slip fiber/matrix/sizing

boundary condition as shown in equation (2-1). In this classic treatment, the ISS was found to be proportional to the square root of the product of the fiber tensile modulus and matrix shear modulus. Rao and Drzal [3.11,3.12] experimentally confirmed the matrix shear modulus dependence. Therefore, a sizing can alter ISS through modification of fiber properties through enhanced fiber protection, modification of interfacial properties through improvements in fiber/sizing/matrix interactions, and modification of matrix properties through matrix plasticization or interphase formation. An interphase can form from the interdiffusion of the sizing and the matrix that results in a concentration gradient extending radially from the fiber. The interphase ultimately affects the way damage is propagated in the composite system.

Traditionally, on-axis unidirectional composite properties such as 0° tension and longitudinal flexure are thought to be fiber dominated. In other words, the role of the matrix and the interphasial zone are believed to be secondary to the fiber properties. Reifsnider et al [3.5] derived a theoretical expression for uni-directional tensile and compressive strength as a function of ISS that predicted a maximum in strength at intermediate values of ISS (Figure 2.1-1). The trends predicted by this model have been verified by Madhukar [3.2,3.3]. However, the model only predicts a 5% variation in strength as a function of ISS above a critical value of ISS (5 ksi for the conditions tested). Below the critical ISS value, the strength becomes a strong function of ISS. In order to achieve ISS values below the critical ISS, the fiber/matrix adhesion would have to be poor. Due to the compatibility of the matrix and sizing materials tested in this study, it is believed that all the systems will have fiber/matrix adhesion above the critical ISS. Therefore, any effect on on-axis composite performance will probably not be attributable to variations in fiber/matrix/sizing adhesion. This can be verified experimentally by investigating composite fracture surfaces via spectroscopy.

As was discussed above, static compressive strength is also relatively insensitive to changes in ISS above the critical ISS. The static compressive strength of uni-directional composite materials is strongly affected by the fiber properties and the degree of fiber alignment [3.6,3.7,3.8]. Fiber waviness has been shown to have a detrimental effect on compressive strength. As will be explained later in the processing section, the thermoplastic nature of the Phenoxy™ and K-90 PVP sizing materials utilized in this study significantly alter the fiber waviness due to their inherent stiffness.

In previous work completed by this author [3.4], Hexcel AS-4 carbon fibers sized with Phenoxy™ (PKHW-35) and K-17 PVP (BASF) were made into composites utilizing a Derakane 441-400 vinyl-ester matrix and a Resin Film Infusion (RFI) processing method. The RFI method can best be described as a “batch” molding process where processing related differences between sizing systems are minimized. The results of this study showed that static strength based mechanical properties, both on-axis and off, were not significantly affected by variations in the sizing constituent. However, tensile/compressive fatigue limits were significantly altered by a change in sizing. For instance, a 20-fold increase in lifetime was observed in the Phenoxy™ system compared to the unsized case.

In the present study, Hexcel carbon fibers were sized with Phenoxy™ and K-90 PVP sizing materials and composites were produced from a pultrudable Dow Derakane™ 411-35Li vinyl-ester resin and a small scale pultruder. Comparisons were made with Hexcel carbon fibers sized with the Hexcel sizing G'. The fibers were compared in terms of their pultrusion processability, composite surface finish quality, on-axis mechanical performance, short beam shear, fatigue lifetime, and environmental durability. In addition, a series of fundamental modeling studies were performed to better characterize the phenomenological events associated with a sizing's effect. These included micro-mechanical and interphase formation modeling. The paper presented herein details the processing, composite quality, on-axis mechanical performance, and short beam shear experiments. The remaining sets of experiments and the modeling work will be presented in papers to be published in the near future and are not presented in this thesis.

Typically, the industrial composite manufacturer is only concerned with the handling and wetting characteristics of the fiber and isn't concerned with the complex mechanisms of fiber/matrix adhesion. However, the academic community has focused its efforts primarily upon how a sizing effects fiber/matrix interfacial bond strength and interphase formation. The overall objective of this first paper is to determine whether thermoplastic sizing materials optimized for interaction and adhesion with carbon fibers and the corresponding Derakane™ vinyl-ester resin are processable via pultrusion. Because processability of a sized fiber is of paramount importance to the composite manufacturer, the establishment of processability precludes all other criteria for prospective sizing materials developed in academic settings.

3.1.3 Experimental

3.1.3.1 Materials

Hexcel AS-4 12K unsized carbon fiber (lot # D1317-4C) was sized at Virginia Tech with two different thermoplastic materials: a polyhydroxyether-Phenoxy™ and a K-90 PVP™.

The Phenoxy™ sizing material (PKHW-35 lot # 217013) (Figure 3.1-1.a) was obtained from Phenoxy Associates, Rock Hill, SC. This material was obtained as a 30wt% dispersion of approximately 1-micron diameter particles in 57wt% water [3.13]. The balance of the suspension contained 10 wt% of a cosolvent, butoxyethanol, and 3wt% of a neutralant, dimethylethanolamine. In order to make the hydrophobic Phenoxy™ shown in Figure 3.1-1.a water dispersible, the commercially available Phenoxy™ suspension contained a modified version of the Phenoxy™ backbone shown in Figure 3.1-1.a. For approximately every ten repeat units, a carboxylic acid functional group had been grafted onto the chain [3.13]. The M_n of the Phenoxy™ was 19,000 g/mol (GPC) and it had a T_g of 97°C (DSC) [1.8].

The K-90 PVP sizing material (LUVISKOL lot # 20421501) (Figure 3.1-1.b) was obtained from BASF. The M_w of this material was 1,250,000 g/mol and it had a T_g of 180°C [3.14].

Hexcel AS-4D G' sized 36K carbon fiber (lot # D1383-5K) was used as the control fiber for these trials. The G' sizing present on this fiber is Hexcel's commercial sizing for the vinyl-ester matrix. The precise chemical structure of the G' is not known but it is known to be an epoxy oligomer.

The AS-4D family of carbon fibers utilized for the G' sizing differs only slightly from the AS-4 family utilized for the thermoplastics sizings (Table 3-1). The AS-4D family is processed at a higher draw ratio thus decreasing the filament diameter and hence linear density (weight/length). The linear density of the AS-4D is approximately 11% lower than the AS-4. Therefore, less tow ends per 12K bundle of the unsized material were needed to achieve the same fiber volume fraction composite as compared to the G' sized fiber. Due to the higher draw ratio and improved orientation of the carbon crystals, the AS-4D fiber has a 4% higher modulus (Table 3-1). The tensile strength is unaffected by the increase in draw ratio. Due to the similarity of the fibers utilized in this study, direct comparisons between the G' and

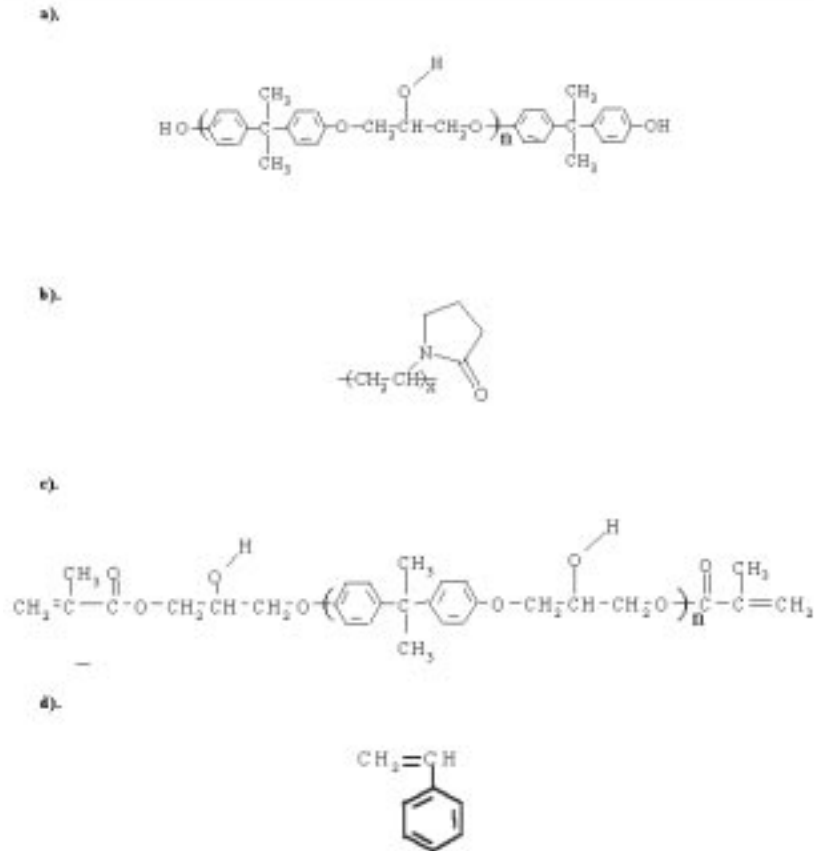


Figure 3.1-1 a). Chemical structure of poly(hydroxyether)/Phenoxy™ sizing material. b). Chemical structure of poly(vinylpyrrolidone) (PVP) sizing material. c). Chemical structure of vinyl-ester. d). Chemical structure of styrene monomer.

Table 3-1 Hexcel AS-4 G' lot # D1383-5K and Hexcel AS-4 unsized lot # D1317-4C carbon fiber mechanical properties.

Hexcel Fiber Type	G'	Unsize
Lot #	D1383-5K	D1317-4C
Tow Tensile Strength/12K (ksi)	593.8	591.2
Tow Tensile Modulus/12K (msi)	38.1	36.5
Tow SecMod/12K (msi)	35.4	33.8
Tow Strain to Failure/12K (%)	1.56	1.63
Sizing Level (wt%)	0.79	0.00
Linear Density/12K (lb/in)	42.87 X 10 ⁻⁶	48.16 X 10 ⁻⁶

thermoplastic sized composites could be made after properties were normalized for fiber volume fraction variations. The effect of increased G' modulus due to the inherent 4% stiffer AS-4D fiber was accounted for in the normalization.

The matrix/resin utilized for pultrusion was a modified Derakane™ 411-35 LI vinyl-ester resin (Figure 3.1-1.c&d), supplied by the Dow Chemical Company. The pultrudable resin was comprised of *approximately* 42 wt% vinyl-ester, 42 wt% styrene monomer, 15 wt% clay, 0.5 wt% release agents, and 0.5 wt% of a proprietary initiator package. The same resin batch was utilized for all the experimental work presented in this paper.

Deionized water was used to make the sizing solutions/suspensions for the sizing line's dip bath. The deionized water came from a NanoPure II™ unit equipped with a 0.2 μm filter and had a resistivity typically of 15 M Ωcm or higher.

Composite specimens were examined with optical microscopy. Before the specimens could be examined utilizing this technique, they had to be mounted in epoxy. The materials utilized to accomplish this potting were Buehler Epoxide resin No.20-8130-032 and Buehler Epoxide Hardener No. 20-8132-032.

3.1.3.2 Processing

3.1.3.2.1 Sizing Solution/Suspension Preparation

Before sizing of the carbon fibers could be conducted, aqueous solutions/suspensions of the sizing materials had to be prepared. In previous work by Broyles et.al [3.4], it was discovered that a sizing level of approximately 1.7 wt% produced good results in a carbon fiber/vinyl ester composite produced via resin infusion molding. For this work, it was decided that this sizing level of 1.7 wt% would be utilized. In order to achieve this final sizing level, the sizing dip bath concentration needed to be approximately 2.0wt%. Therefore, aqueous dip bath solutions/suspensions of 2.0wt% sizing material in deionized water were prepared.

The K-90 PVP sizing material was dried in a convection oven at 110°C for approximately 18 hours before solutions were prepared. Approximately 320g of this dried K-90 PVP was added directly to 15,700g of deionized water. This mixture yielded a 2.0 wt% K-90 PVP in water solution. This solution was then allowed to stir for seven days at room temperature

due to the high molecular weight of the K-90 PVP. This solution was then added to the sizing dip bath without further agitation.

The Phenoxy™ material was insoluble in water and was supplied as a 35wt% aqueous suspension. Approximately 143g of the suspension was added to 2360g of deionized water to yield a 2.0 wt% Phenoxy™ in water suspension. This suspension was allowed to stir rapidly overnight. This suspension was then added to the sizing dip bath and vigorous stirring was applied.

3.1.3.2.2 Sized Fiber Preparation

The carbon fibers were sized on a custom made small scale sizing line described in reference [3.9]. The unsized carbon fiber tow was pulled off a spool at a set speed ranging from 0.3 to 6.0 cm/sec. The fiber tension was controlled by a nip roller, which was connected to a particle brake. A load cell located at the exit of the sizing dip bath measured the tension. The fibers were then passed through a sizing dip bath that contained the aqueous sizing solution/suspension discussed earlier. In the dip bath, capillary forces provided the driving force for rapid tow wetting. The high fiber tension and extensive use of rollers after the sizing bath spread the tow bundle and also prevented the wet tow from clumping. The spread carbon fiber tow containing the sizing solution was dried online in an infrared (IR) forced convection dryer.

The emitter surface temperature of the two IR heating panels embedded in the dryer was controllable from ambient temperature up to 500°C. The inlet air temperature was controlled at ambient conditions. The emitter surface temperature directly controlled the surface temperature of the carbon fiber. The surface temperature of the fiber was measured by a hand held thermocouple. A time/temperature profile was generated by placing the thermocouple on the fiber surface at various positions in the IR dryer. Placement of the thermocouple was such that no background IR interfered with the surface temperature measurement. The surface temperature history of the sized carbon fiber affected the handling characteristics of the final sized tow. It also affected the morphology of the sizing deposited onto the fiber surface. For each sizing material, an optimal time temperature dryer profile was determined.

The fiber that exited the dryer was pulled through a motorized nip roller where line speed was controlled and line tension was developed. The fiber was then wound onto a standard

carbon fiber spool utilizing a constant tension Izumi rewinder. The fibers were then sealed in a plastic bag to prevent moisture from being re-absorbed by the sizing material or the carbon fiber.

3.1.3.2.3 Pultrusion

Pultrusion was performed at Strongwell, Inc., utilizing their pilot scale pultruder. Thirty spools of the Hexcel AS-4 12K material sized at Virginia Tech were placed in the creel rack for its processing. Twelve spools of the AS-4 G' 36K material were placed in the creel rack for its processing. The line speed utilized for all trials was approximately 2 feet/minute. The individual tows were directed into the process via a board of perforated Teflon. The fibers were then dipped in the resin bath where the fibers were fully wetted with the resin. After the fibers were pre-formed, they were cured in a die of rectangular cross section.

The die was approximately 30" long and had three zones where temperatures could be monitored and controlled. The three zones were located at the beginning, middle, and end of the die. The first zone required heat input in order to control the surface temperature at approximately 220 °F. The second zone required less heat input to control the surface temperature at 280 °F due to the exotherm associated with the matrix curing. In addition, the third zone required no heat input to control the surface temperature at 260 °F.

After the cure was complete, the composite was air cooled in the roll-out portion of the pultrusion process. The part was then cut utilizing a saw and the final dimension of the composite part was 12.7mm wide by 2.0mm thick by 15.24m long.

3.1.3.3 Characterization Methods

3.1.3.3.1 Sized Fiber Characterization

3.1.3.3.1.1 Sizing Level Determination

The amount of sizing deposited on the carbon fiber was determined via pyrolysis in a nitrogen atmosphere. Approximately 8 grams of sized carbon fiber were used for the analysis. The fibers were first dried in a convection oven for a period of eight hours. The temperature of the convection oven was set above the T_g of the particular sizing material being tested. After being dried, the fibers were placed in a high temperature Blue-M furnace with a nitrogen purge

at a flow rate of approximately 40 cm³/sec. This led to a purge gas residence time of 30 seconds. Typically 20 minutes were required for heating the chamber from room temperature to the pyrolysis temperature of 600°C. Thus, the pyrolysis chamber typically was purged with gas for about 40 residence times prior to reaching the pyrolysis temperature. This ensured that there was no unwanted oxidation of the carbon fibers. Pyrolysis then proceeded for 30 minutes at 600°C. The amount of sizing material was computed from the differences in mass of the dry sized fiber and the pyrolyzed fiber:

$$S = 100 \cdot \frac{(M_1 - M_2)}{M_1} \quad (3-1)$$

where S was the weight percent of sizing on the fiber, M_1 was the dry sized fiber mass, and M_2 was the pyrolyzed fiber mass.

3.1.3.3.1.2 SEM

The quality of the sized fiber was determined by inspection of the fibers under Scanning Electron Microscopy (SEM). The fibers were secured on a standard ESCA mount. The fibers were sputter coated with gold for approximately 2 minutes. Analysis was conducted in an International Scientific Instruments Model SX-40 SEM.

3.1.3.3.1.3 ESCA

Uniformity of the coating was also assessed via ESCA, which was conducted by Mr. Steve McCartney. The sized carbon fiber samples were mounted in a specially designed holder that secured the fibers. The area of examination was about 1mm by 3mm. A survey scan was conducted first to determine the identity of the elements present and then a series of narrow scans were conducted for the primary photoelectron peak of the detected elements. All experiments were conducted utilizing a 400 watt Mg anode.

3.1.3.3.2 Composite Characterization

3.1.3.3.2.1 Fiber Volume Fraction

The fiber volume fraction of the composite panels produced in these experiments was determined by two methods. The first method utilized data collected before the composite part was produced and was termed the theoretical fiber volume fraction. The second method utilized data collected after the composite part was produced and was termed the experimental fiber volume fraction.

For the first method, the number of tow ends and their respective linear density allowed the determination of the volume of fiber per unit length entering the pultrusion die. The fiber volume fraction could then be computed from the following equation.

$$v_f = \frac{(n \cdot l_f)}{A_c \cdot \rho_f} \quad (3-2)$$

Where v_f is the fiber volume fraction, n is the number of tow ends, l_f is the weight per unit length per bundle, A_c is the cross-sectional area of the composite, and ρ_f is the filament density. The cross-sectional area of the composite, A_c , was determined from the die cross-sectional area (neglecting matrix shrinkage) or from the final composite cross-sectional area (including matrix shrinkage). This method neglects the mass of fiber lost in the pre-processing portions of the pultrusion process, which is negligible in most cases.

For the second method, the density of the composite was determined and a rule of mixtures was used to determine the fiber volume fraction. A 4g sample of the composite was dried and weighed. The sample was then immersed in isopropyl alcohol and weighed again. The density of the composite was calculated using Archimedes' principle using the following equation

$$\rho_{composite} = \frac{W_{air}}{(W_{air} - W_{IPA})} \cdot \rho_{IPA} \quad (3-3)$$

where $\rho_{composite}$ = density of composite, ρ_{IPA} = density of Isopropyl alcohol, W_{air} = weight of sample in air and W_{IPA} = weight of sample in isopropyl alcohol. The fiber volume fraction was then calculated using the rule of mixtures.

$$v_f = \frac{(\rho_{composite} - \rho_{resin})}{(\rho_f - \rho_{resin})} \quad (3-4)$$

where v was the fiber volume fraction, $\rho_{composite}$ was density of the composite calculated from equation (3-2), ρ_f was density of the carbon fiber, ρ_{resin} was the cured resin density. Equation (3-3) assumes that the composite has zero void volume. The difficulty in applying equation (3-3) is that the resin density, ρ_{resin} , is not known exactly. However, if it is treated as a constant between the different fiber systems, then fiber volume fraction comparisons can be made.

3.1.3.3.2.2 *Visual Inspection of the Cut Composite*

Composite specimens for mechanical testing were cut using a Felker saw. The cut specimens were examined visually for defects.

3.1.3.3.2.3 *Optical Microscopy*

Voids and fiber packing in the pultruded composites were analyzed using a Nomarski Optics Optical Microscope. This work was completed by Dr. Nikhil Verghese. Sections of the composite panel were cut and placed in a Buehler potting cup. Epoxide resin and epoxide hardener were mixed in a ratio of 5:1 by weight and poured into the potting cup. The mixture was cured at room temperature for approximately 6 hours. The cured samples were polished using a Buehler ECOMET 3 (variable speed) polisher-grinder. The samples were placed in a carousel and attached to the spindle of the AUTOMET 2 (power head). The power head ensured controlled loading of the specimens during polishing and resulted in specimens with a high gloss surface.

3.1.3.3.2.4 *Ultrasonic C-Scan*

As a quality control step, linear ultrasonic C-scans were performed on all the composite materials. These tests were performed on a Sonix HS1000 HiSPEED instrument by Mr. Mac McCord. A 15MHz, 32mm. focal length sensor was used. Data was analyzed using the FlexSCAN-C software provided with the instrument. The scans were gated both to the midplane as well as the bottom surface of the specimens.

3.1.3.4 Mechanical Testing

3.1.3.4.1 Tension Testing

Quasistatic tension tests were performed on all the composites to assess the tensile strength, modulus and strain to failure. The test specimens were prepared by N. Broyles but the actual tests were completed by Dr. Nikhil Verghese. These tests were performed on a servo-hydraulic MTS test frame in load control mode. A loading rate of 200 pounds per second was applied. This loading cycle was programmed into the Microprofiler™, which controlled the machine once a test was begun. A pair of MTS, Model 647 hydraulic wedge grips, a 448.82 test controller, a 418.91 Microprofiler™, a 413.81 master controller and a 464.80 data display unit were utilized. The specimens were loaded into the grips at a grip pressure of 7 MPa and specimen alignment was ensured by the use of a spirit level. The total specimen length was 15.24 cm and a gage length of 5.08 cm was used. In order to protect the specimens from crushing inside the grips, high pressure laminated glass-epoxy tabs were adhesively bonded to the specimens. A special fixture was used to align the tabs and specimens prior to bonding. Both, the tabs as well as the specimen surfaces to be bonded were grit blasted in order to prepare the surface for bonding and a two-part epoxy (3M's DP40) was used as the adhesive. The adhesive was cured in an oven for 1 hour at 50°C under load so as to prevent any movement. An MTS Model 632 extensometer with a gage length of 2.54 cm and a maximum strain limit of 4% was used to monitor strain. The signal from the extensometer was amplified using a 2310 Vishay Measurements Group amplifier box. The knife-edges on the extensometer were made to rest in the aluminum tabs on the specimen and fastened via rubber bands. These aluminum tabs were bonded on the specimen using a silicone (GE 2310 RTV) adhesive. LabView® software was used to monitor the load, stroke and strain signals during the tests.

3.1.3.4.2 Flexure and Short Beam Shear Testing

Flexure tests were performed in accordance with ASTM D790-90 [3.15]. Specimens were cut using a Felker cutting saw using water as a coolant. The specimens were 30 mm long by 2 mm thick. The specimens were mounted in a three-point bend fixture and loaded at a rate of 0.8 mm/min by an Instron 4104 test frame.

Short beam shear tests were performed in accordance with ASTM D 2344-84 [3.16]. The specimens were 11 mm long by 2 mm thick. The specimens were mounted in a three-point bend fixture and loaded at a rate of 1.3 mm/min by an Instron 4104 test frame.

For both tests, a 5KN load was used to monitor load and LabView[®], a National Instruments Corporation data acquisition software, was used to monitor load versus displacement.

3.1.3.4.3 Compression Testing

In-plane compressive properties were evaluated by performing compression tests in accordance with ASTM 3410 [3.17]. These tests were performed by Dr. Nikhil Verghese. This test introduces the compressive load into the specimen through shear at the wedge grip interface. An Illinois Institute of Technology Research Institute, IITRI compression test fixture was used. Meticulous care was taken to ensure that the surfaces of the specimens were parallel to each other, which is a requirement by the standard. In order to achieve this, specimens 15.24 cm long were placed in a fixture and two 7 cm long tabs were surface treated and bonded on one side. The specimens were then ground in the machine shop in order to maintain a reference surface. The second sets of tabs were then bonded on and final grinding was done both on the surfaces and the edges. A gage section of 1.27 cm was used which was considered to be short enough to prevent Euler buckling at the same time, long enough to allow for the decay of stresses to uniaxial compression and minimize Poisson restraint effects due to the grips. Next, strain gages (type: CEA 06 125 UN-350) from Micromeritics[™] were glued on the front and back surfaces of the gage section. This is required by the standard in order to compare front and back surface strains during the test to check for bending. A 100 KN, Instron load-frame along with a 100 KN load cell was used for the tests. A cross-head displacement rate of 1.5 mm/minute was used in accordance with the standard. Each specimen was carefully inserted into the rectangular wedges with the help of an alignment cradle that was held between the faces of a bench top vice. A torque of 150 inch-pound was used to tighten the faces of the wedges onto the specimen tabs. The strain gage lead wires were then hooked up to the amplifier box and the strains zeroed. The specimen and the wedges were then gently lifted off the cradle and lowered into the bottom wedge housing assembly of the IITRI fixture, which rests on the lower platen of the test frame and contains a mating wedge cavity. Next, the top wedge housing assembly was lowered

carefully to make contact with the second set of wedges. The downward motion continued until failure of the specimen. Perfect alignment was ensured apriori, and was checked for each test by closely monitoring the strains. Once again, LabView[®], a National Instruments Corporation data acquisition software, was used to monitor load, front surface strain and back surface strain and displacement against each other.

3.1.3.4.4 Normalization of Mechanical Properties for Fiber Volume Fraction Variations

Before comparisons could be made between composite systems, the mechanical properties had to be normalized with respect to fiber volume fraction. The type of normalization used in this section was a rule of mixtures expression that neglected the mechanical response of the matrix. Even though this type of normalization does not rigorously apply to strength based properties where statistical events control the failure, it will still be reasonably accurate for the fiber volume fraction variation observed in these composites. The equation utilized for the normalization was as follows,

$$\sigma_c^n = \sigma_c^o \cdot \left[\frac{v_f^n}{v_f^o} \right] \cdot \phi_f \quad (3-5)$$

where σ_c^n is the normalized property (strength or stiffness) at a fiber volume fraction equal to v_f^n (in all cases, v_f^n was set equal to 0.656 or the theoretical fiber volume fraction of the G' sized composite), v_f^o is the original fiber volume fraction of the composite to be normalized, σ_c^o is the original property (strength or stiffness) at a fiber volume fraction equal to v_f^o , and ϕ_f is the ratio of the inherent strength or stiffness of AS-4D G' sized fiber to the inherent strength or stiffness of the AS-4 unsized fiber. The value of ϕ_f is approximately equal to 1.00 (593.8 MPa/591.2 MPa) when the property being normalized is a strength based property. The value of ϕ_f is approximately equal to 1.04 (38.1 Gpa/36.5 Gpa) when the property being normalized is a modulus based property. Strain-to-failure values were not normalized due to a lack of knowledge of how to properly complete the normalization.

3.1.4 Results and Discussion

3.1.4.1 Processing

3.1.4.1.1 Sized Fiber Preparation

In order to completely dry the sized fiber in the sizing line's forced convection dryer, a surface temperature above the sizing materials T_g was needed. In addition, processing the material above its T_g allowed the sizing to soften and fully encapsulate the carbon fiber. For instance, a Phenoxy™ sizing processed below its T_g ($< 97^\circ\text{C}$) resulted in a fiber coated with particulates (Figure 3.1-2). These particulates were merely the 1 micron particles that were originally dispersed in the sizing dip bath suspension. However, if the surface temperature greatly exceeded the Phenoxy's T_g , then a smooth fiber surface was developed (Figure 3.1-3). For the Phenoxy™ sizing, the optimal fiber surface temperature was found to be above 200°C (Figure 3.1-3). As will be discussed later, this temperature was sufficient to completely dry the fiber. Two different processing techniques were utilized for the Phenoxy™ material, which resulted in two different forms of the Phenoxy™ sized fiber. One form was a high-spread Phenoxy™ (HSP) and the other was a low-spread Phenoxy™ (LSP). The HSP sized fiber had a width twice that of the LSP. It was felt that the higher spreading would lower the resistance to tow wetting and hence enhance its processability. The higher degree of spreading was achieved by placing a high temperature blower at the sizing dip bath exit. This allowed for quicker drying which allowed less time for the wet fiber to contract under the forces of surface tension. For the case of fiber sized with K-90 PVP ($T_g \approx 180^\circ\text{C}$), the optimal fiber surface temperature was found to be above 200°C . As will be discussed later, this fiber surface temperature resulted in a fiber that had negligible moisture content. This surface temperature was also sufficient to allow the K-90 PVP to fully encapsulate and uniformly coat the carbon fiber (Figure 3.1-4 and Figure 3.1-5). The K-90 PVP sized fiber had a width approximately equivalent to the HSP. The processing parameters used to produce the sized fibers utilized in this study are noted (Table 3-2). Pyrolysis of these sized fibers showed that the LSP material had a final moisture content of 0.05 ± 0.02 wt% and a sizing level of 1.56 ± 0.07 wt% (Table 3-2). The HSP material had a final moisture content of 0.13 ± 0.16 wt% and a sizing level of 2.90 ± 0.26 wt%. The K-90 PVP material had a final moisture content of 0.24 ± 0.06 wt% and a sizing level of 1.97 ± 0.07 wt%. The low levels of moisture (< 0.30 wt%) indicated that the drying conditions were sufficient to

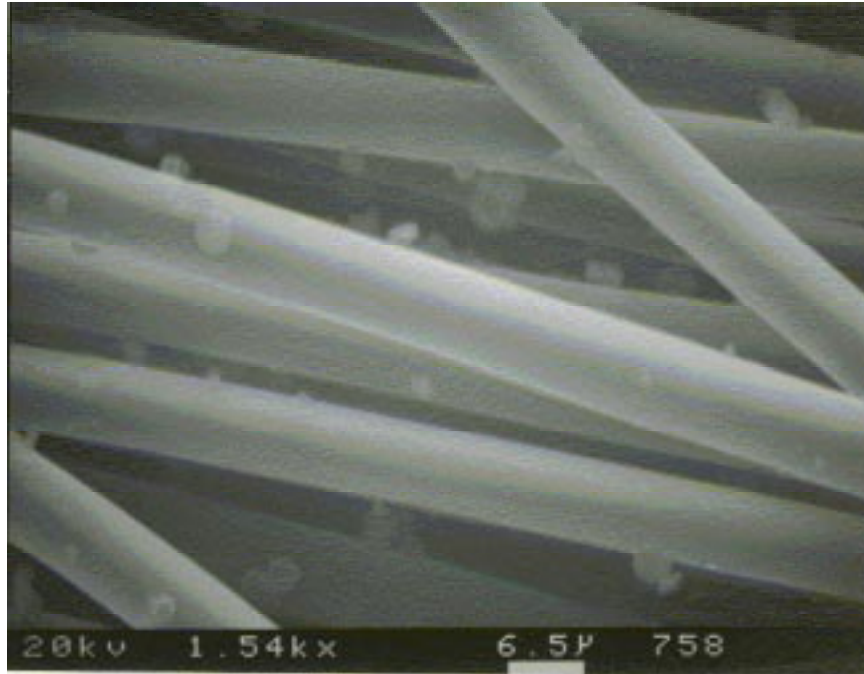


Figure 3.1-2 Phenoxy particulate sized Hexcel AS-4 12K. Note: Surface temperature did not exceed 97°C or Phenoxy's glass transition.

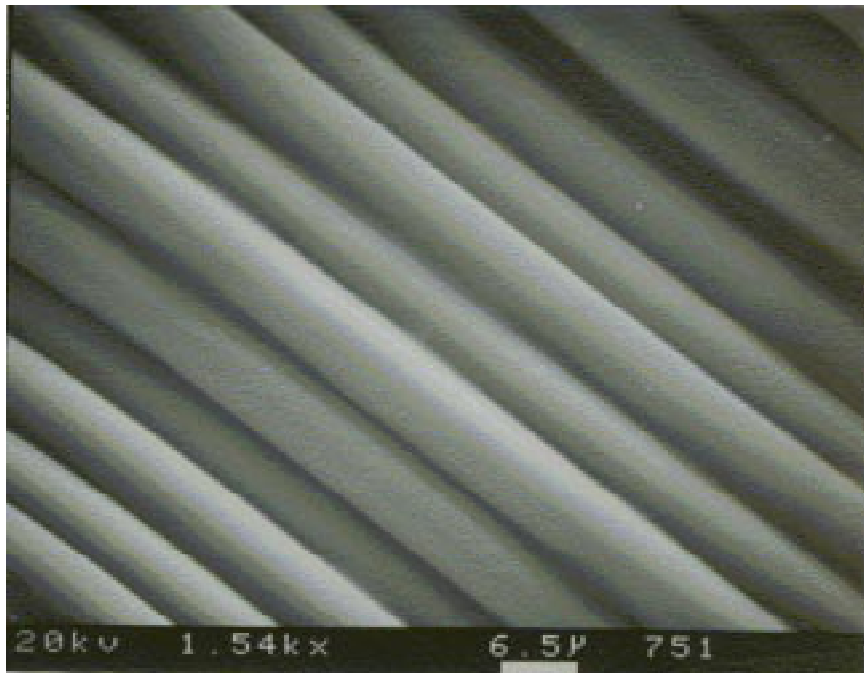


Figure 3.1-3 Phenoxy film sized Hexcel AS-4 12K. Note: Surface temperature exceeded 97°C or Phenoxy's glass transition. $T_{\text{surface}}^{\text{max}} \approx 220^{\circ}\text{C}$.

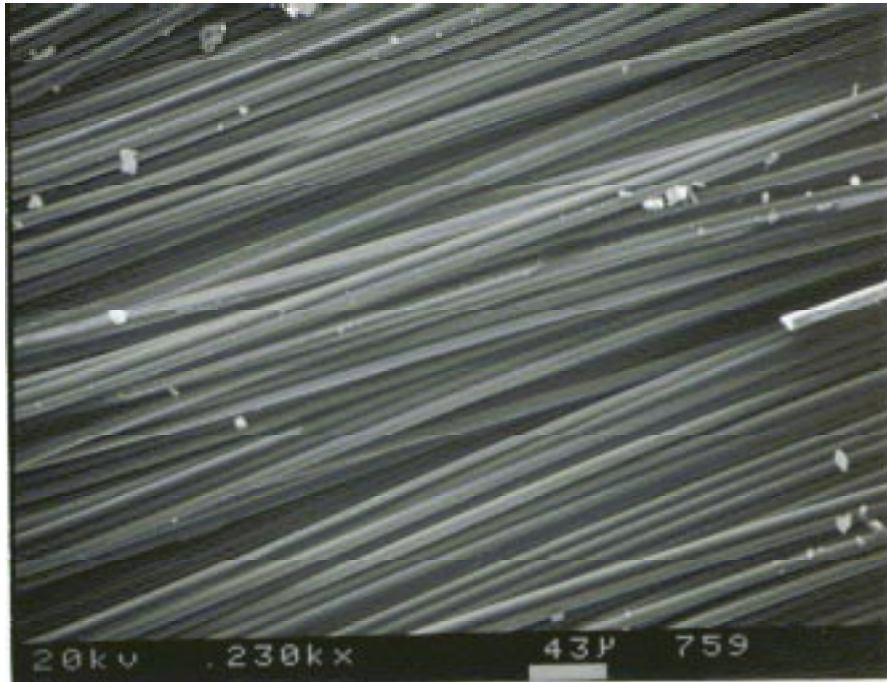


Figure 3.1-4 K-90 PVP sized Hexcel AS-4 12K (≈ 1.97 wt%). Note: Surface temperature exceeded 200°C. 230 X Magnification.

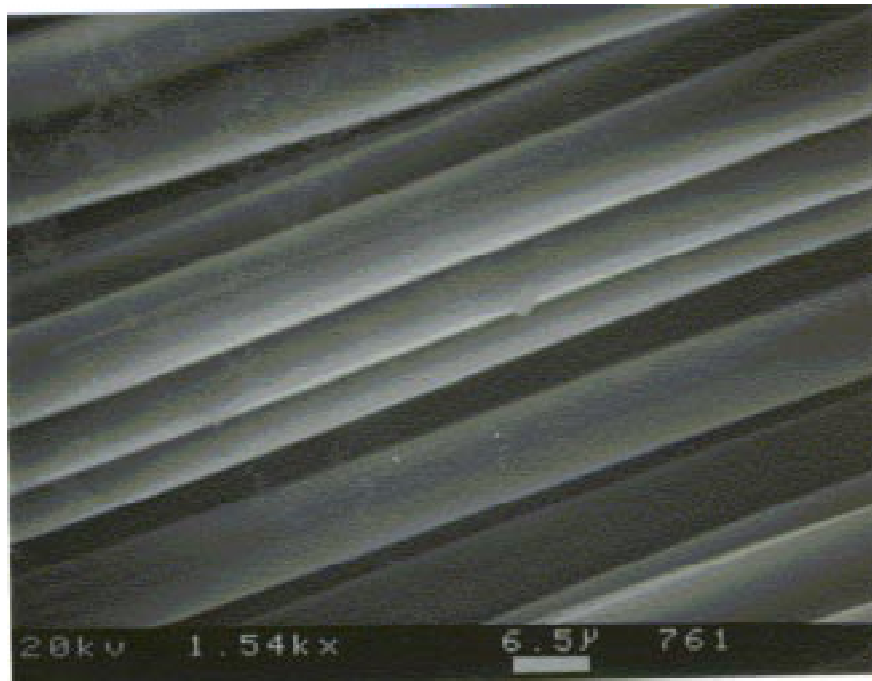


Figure 3.1-5 K-90 PVP sized Hexcel AS-4 12K (≈ 1.97 wt%). Note: Surface temperature exceeded 200°C. 1540 X Magnification.

Table 3-2 Processing parameters used to produce the sized fibers utilized in this study. In addition, sizing characterization information also displayed.

Sizing System	Low Spread Phenoxy	High Spread Phenoxy	K-90 PVP
Dip Bath Concentration (wt%)	2.0	2.0	2.0
Auxillary Heat Blower On (Yes/No)	No	Yes	Yes
First IR Heating Panel (°C)	400.0	400.0	415.0
Second IR Heating Panel (°C)	400.0	400.0	415.0
Main Heat Blower On (Yes/No)	No	No	No
Maximum Fiber Surface Temperature (°C)	215.0	225.0	245.0
Line Tension at Dip Bath Exit (lbs)	2.30	2.30	2.30
Tension Setting onto Spool	2.0	2.0	2.0
Approximate Width of Sized Fiber (in.)	1/8	¼	¼
Fiber Moisture Content (wt%)	0.05 ± 0.02	0.13 ± 0.16	0.24 ± 0.06
Dry Fiber Sizing Level (wt%)	1.56 ± 0.07	2.90 ± 0.26	1.97 ± 0.07

completely dry the fiber. In addition, the low standard deviations on the sizing level indicated the consistency of the sizing process.

ESCA was completed on all the sized fibers utilized for the pultrusion trials (Table 3-3). In all cases, the theoretical sizing thickness was significantly greater than the penetration depth of the ESCA. In addition, ESCA was completed on some of the as-received sizing materials (Table 3-3). The unsized Hexcel AS-4 carbon fiber surface had an atomic element composition of 88.36% carbon, 8.03% oxygen, and 3.60% nitrogen. The Hexcel G' sized AS-4 carbon fiber surface had an atomic element composition of 84.59% carbon and 15.41% oxygen. This is an indication that the surface of the G' sized material was completely covered with the oligomeric epoxy sizing because nitrogen was no longer detected. The Phenoxy™ material does not contain nitrogen. The ESCA trace on the pure Phenoxy™ sizing material verified this hypothesis. Therefore, if the surface of the carbon fiber were completely covered with the Phenoxy™ material, then no nitrogen should be present on the surface. The ESCA traces of both the LSP

Table 3-3 ESCA results for Hexcel AS-4 carbon fibers sized with various agents. ESCA results for pure sizing materials shown also.

Element (%)	C1s	O1s	N1s	Na1s	Si2p
Unsize Hexcel AS-4	88.36	8.03	3.60	0.00	0.00
G' Sized Hexcel AS-4	84.59	15.41	0.00	0.00	0.00
Pure Phenoxy	81.17	18.29	0.00	0.00	0.54
LSP Sized Fiber	87.10	10.83	2.06	0.00	0.00
HSP Sized Fiber	85.92	11.58	2.49	0.00	0.00
Pure K-90 PVP	76.32	12.52	11.16	0.00	0.00
K-90 PVP Sized Fiber	78.62	11.32	10.07	0.00	0.00

and HSP sized fibers showed some presence of nitrogen (LSP: 2.06% N HSP: 2.49% N) indicating incomplete surface coverage. There were no apparent differences in the surface atomic element composition between the LSP and HSP sized fibers. In both the cases, the Phenoxy™ sizing did not completely cover the Hexcel carbon fiber surface. The pure K-90 PVP sizing material's ESCA trace showed an atomic composition of 76.32% carbon, 12.52% oxygen, and 11.16% nitrogen. The K-90 PVP sized Hexcel fiber showed a similar atomic surface composition of 78.62% carbon, 11.32% oxygen, and 10.07% nitrogen. Therefore, it can be safely concluded that the K-90 sizing material completely covered the Hexcel fiber.

3.1.4.1.2 Pultrusion

As was noted in the experimental section, pultrusion of the Hexcel AS-4 G' material was conducted on Day 1 of the trial. During the processing of the G' sized material, it was noted that the carbon fibers were not protected sufficiently by the G' sizing. The guide and spreader bars damaged the fiber extensively. At the entrance to the resin dip bath, the fibers were compacted between stationary metal bars. The purpose of these bars was to force the cylindrical G' tow into a tape configuration that would minimize tow wet-out time. This resulted in tremendous fiber damage and build-up on the dip bath entrance. The extensive fiber fraying and damage that resulted upstream was further exaggerated by the compaction experienced at the die entrance. The resulting composite had a surface finish that was rough, resulting in a relatively dull, non-

reflective surface. Also, fiber breaks and fiber kink-bands could be readily observed in the composite.

Pultrusion of the LSP was conducted on Day 2 of the trials. During the loading of the spools onto the creel rack, it was noted that the Phenoxy™ sized fiber was very stiff and difficult to keep on its respective spool due to memory effects of the high T_g sized fibers. However, after tension was applied to the spools, the Phenoxy™ sized fiber processed efficiently. Because of its stiff and spread configuration, the Phenoxy™ sized fiber displayed no fraying as was observed and is customarily observed with the standard G' sizing. Significant fiber loss and damage always occurs with the G' system because of its cylindrical and soft nature. In addition, because of the inherent compatibility of the Phenoxy™ sizing with the vinyl-ester matrix, rapid wetting of the fibers was observed. The Phenoxy™ sized fiber, protected by the tough thermoplastic sizing, entered the resin dip bath in a spread/tape configuration, minimizing the resistance to wet-out and minimizing the damage caused by the static spreader bars. The Phenoxy™ sized fiber exited the resin dip bath saturated with resin and with no fiber damage as a result of fraying. Also, the fibers were now more pliable as a result of the vinyl-ester matrix possibly softening the thermoplastic Phenoxy™ sizing. The compatibility of the Phenoxy™ sizing with the vinyl-ester matrix may have allowed the Phenoxy™ sizing to swell and relax thus making it more rubbery. The composite that exited the pultruder die had a very different surface finish compared to the Hexcel G' sized fiber composite. The LSP sized composite had a very smooth surface finish. In addition, the surface appeared very reflective and had no traces of fiber breakage. The internal fibers appeared parallel to the processing direction and no-kink bands were apparent.

Pultrusion of the HSP and the K-90 PVP was conducted on Day 3 of the trials. These materials processed very similarly to the LSP processed on Day 2. The thermoplastic nature of these sizing materials provided a stiff fiber before the resin dip bath and a pliable/rubbery fiber after the dip bath. The resulting composites also had a smooth and glassy surface.

3.1.4.2 Composite Characterization

3.1.4.2.1 Fiber Volume Fraction

The theoretical composite fiber volume fraction was computed for all four fiber systems. Utilizing equation (3-2) and the corresponding G' sized AS-4 linear density (Table 3-1) and fiber

density ($\rho_f = 1.78 \text{ g/cm}^3$), the G' sized AS-4 composite had a theoretical fiber volume fraction of approximately 65.6%. Utilizing equation (3-2) and the corresponding unsized AS-4 linear density (Table 3-1) and fiber density ($\rho_f = 1.78 \text{ g/cm}^3$), the thermoplastic sized AS-4 composites had a theoretical fiber volume fraction of approximately 61.1%.

The experimental composite fiber volume fraction was computed for all four fiber systems. Utilizing a cured resin density of 1.16 g/cm^3 , this method determined the pultruded composites to have fiber volume fractions that ranged from 61% to 68% (Table 3-4). The G', LSP, HSP, and K-90 PVP sized composites had fiber volume fractions of $68.0 \pm 0.3\%$, $65.0 \pm 0.6\%$, $61.1 \pm 0.6\%$, and $63.9 \pm 0.2\%$ respectively. Within a system, the pultrusion process produced composites with a very consistent fiber volume fraction as indicated by the low standard deviations. Because the equivalent of thirty-six 12K tows were utilized for the G' pultrusion and thirty 12K tows were utilized for the other systems (ignoring the differences in linear density between the lots), it was not surprising that the G' system had a considerably higher fiber volume fraction. It was surprising that the HSP experimental fiber volume fraction of 61.1% was so much lower than that of the LSP and the K-90 PVP (65.0% and 63.9%). Because the HSP contained such a high sizing level (2.9 wt%), it is believed that excess Phenoxy™ prevented the vinyl-ester resin from fully penetrating the tow. This left a larger degree of void space that compromised the integrity of the rule of mixtures calculation expressed by equation (3-4). If the cured resin density could accurately be determined, then the void volume could be calculated from the theoretical composite fiber volume fraction and a modified rule of mixtures that included an air phase in the contribution. Before mechanical property results could be compared between the various systems, normalization with respect to the theoretical fiber volume fraction was completed.

3.1.4.2.2 Visual Inspection of Cut Composite

Visual inspection of cut sections of the pultruded composites revealed a dramatic difference in composite cross-section quality. Upon cutting the composites for mechanical testing, differences were again noted. The G' sized composite system produced a large quantity of dust when the composites were cut. The cut G' cross-section displayed numerous dry carbon fibers and was quite rough. The Phenoxy™ (both LSP and HSP) and K-90 PVP sized composite systems cut like a brittle glass and produced no carbon fiber dust during the cutting stage. The

Table 3-4 Summary of Results.

Property	G'	LS Phenoxy	HS Phenoxy	K-90 PVP
Sizing Level (wt%)	0.79⁴	1.95 ± 0.07	2.90 ± 0.26	1.97 ± 0.07
Fiber Volume Fraction ¹ (%)	65.6	61.1	61.1	61.1
Fiber Volume Fraction ² (%)	68.0 ± 0.3	65.0 ± 0.6	61.1 ± 0.6	63.9 ± 0.2
Tensile Strength (MPa)	1673 ± 39	2035 ± 35	1940 ± 72	1964 ± 71
Normalized ³ Strength (MPa)	1673 ± 39	2185 ± 38	2083 ± 77	2109 ± 76
Tensile Modulus (GPa)	120.3	n.a.	105.0	113.3
Normalized ³ Modulus (GPa)	120.3	n.a.	112.7	121.7
Strain-to-Failure (%)	1.47 ± 0.08	1.41 ± 0.09	1.08 ± 0.46	1.33 ± 0.11
Normalized ³ STF (%)	1.47 ± 0.08	1.51 ± 0.49	1.16 ± 0.49	1.42 ± 0.11
Flexure Strength (MPa)	983 ± 67	1186 ± 28	1091 ± 41	1113 ± 20
Normalized ³ Strength (MPa)	983 ± 67	1274 ± 30	1171 ± 44	1195 ± 22
Flexure Modulus (GPa)	102.3 ± 3.4	95.7 ± 1.0	95.1 ± 1.6	94.2 ± 1.2
Normalized ³ Modulus (GPa)	102.3 ± 3.4	102.7 ± 1.0	102.1 ± 1.8	101.1 ± 1.3
SBS Strength (MPa)	43.0 ± 1.4	61.6 ± 0.6	55.5 ± 2.1	55.6 ± 0.3
Normalized ³ Strength (MPa)	43.0 ± 1.4	66.1 ± 0.7	59.6 ± 2.3	59.7 ± 0.3

¹Theoretical fiber volume fraction determined from fiber denier and density.

²Calculated from density determination after composite fabrication.

³Normalized to 65.6% fiber volume fraction from the theoretical fiber volume fraction.

⁴Data supplied by Hexcel.

cut Phenoxy™ (both LSP and HSP) cross-section was clean and very smooth. The visual observations made both before and after the cutting step reinforced the observations made during the pultrusion trials. The Phenoxy™ (both LSP and HSP) and K-90 PVP sizings produced a composite with improved fiber wet-out and less fiber breakage.

3.1.4.2.3 Optical Micrographs of Composite Cross-sections

Optically micrographs of cross-sections of the pultruded composites showed some interesting differences amongst the various sizings (Figure 3.1-6, Figure 3.1-7, Figure 3.1-8, and Figure 3.1-9). The G' sized composite cross-section showed an extremely uniform fiber distribution (Figure 3.1-6) which was an indication of good inter-tow consolidation. No resin



Figure 3.1-6 Optical micrographs of cross-sectioned and polished pultruded Hexcel AS-4 G' sized carbon fiber/vinyl-ester composite. 10 X magnification.

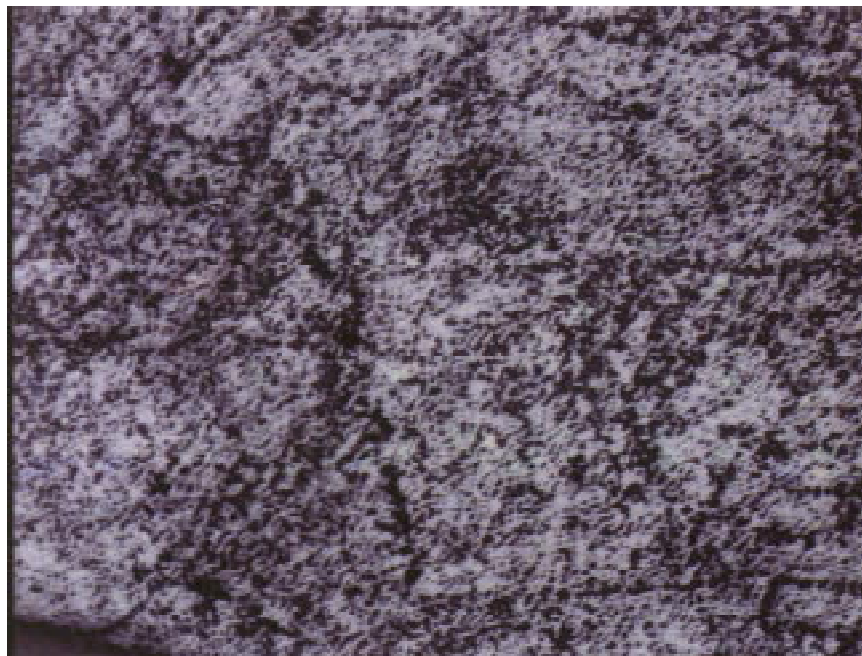


Figure 3.1-7 Optical micrographs of cross-sectioned and polished pultruded Hexcel AS-4 low spread Phenoxy sized or LSP carbon fiber/vinyl-ester composite. 10 X magnification.



Figure 3.1-8 Optical micrographs of cross-sectioned and polished pultruded Hexcel AS-4 high-spread Phenoxy sized or HSP carbon fiber/vinyl-ester composite. 10 X magnification.



Figure 3.1-9 Optical micrographs of cross-sectioned and polished pultruded Hexcel AS-4 K-90 PVP sized carbon fiber vinyl-ester composite. 10 X magnification.

rich or poor regions were readily visible. This was also the case for the LSP sized composite (Figure 3.1-7). Again, this was an indication of extremely good inter-tow consolidation. However, the HSP sized composite had extensive resin rich and poor regions. The various resin rich areas appeared to form lines that existed parallel to one another. The fiber rich areas had a geometrical shape and size very similar to that of the sized fiber tow that entered the pultruder die. This was an indication of poor inter-tow consolidation. The thick (2.9 wt%) Phenoxy™ sizing on each of the tow strands apparently prevented the individual tows from inter-consolidating. Although not apparent in the optical micrographs, some air voids could be present on the inside of the tow because of the thick Phenoxy™ coating resident on the outside. This was hypothesized earlier when the fiber volume fraction of the HSP calculated from equation (3-4), appeared to be too low. The mechanical property results for the HSP composites presented later in this paper must be viewed with caution considering the poor inter-tow consolidation and possible presence of voids. The K-90 PVP sized composite also had some resin rich and poor regions (Figure 3.1-9) but overall had good inter-tow consolidation.

3.1.4.2.4 Ultrasonic C-Scan

Ultrasonic c-scan showed no apparent differences between the composites made from the differently sized carbon fibers.

3.1.4.3 Mechanical Properties

The mechanical property results for the pultruded composites are summarized in Table 3-4. All the mechanical property results were normalized from the theoretical fiber volume fraction to 65.6% or the theoretical fiber volume fraction of the G' sized composite utilizing equation (3-5). In addition, the differences in the inherent properties of the AS-4 and AS-4D fibers was taken into account utilizing the ϕ_f factor in equation (3-5).

3.1.4.3.1 Static Tensile Properties

Static tensile strength, modulus, and strain-to-failure were determined for all sizing combinations (Figure 3.1-10, Figure 3.1-11, and Figure 3.1-12). The LSP composites had the highest tensile strength at a value of 2185 ± 38 MPa while the G' composite had the lowest value of 1673 ± 39 MPa (Note: 30% increase). All the thermoplastic sized fiber composites

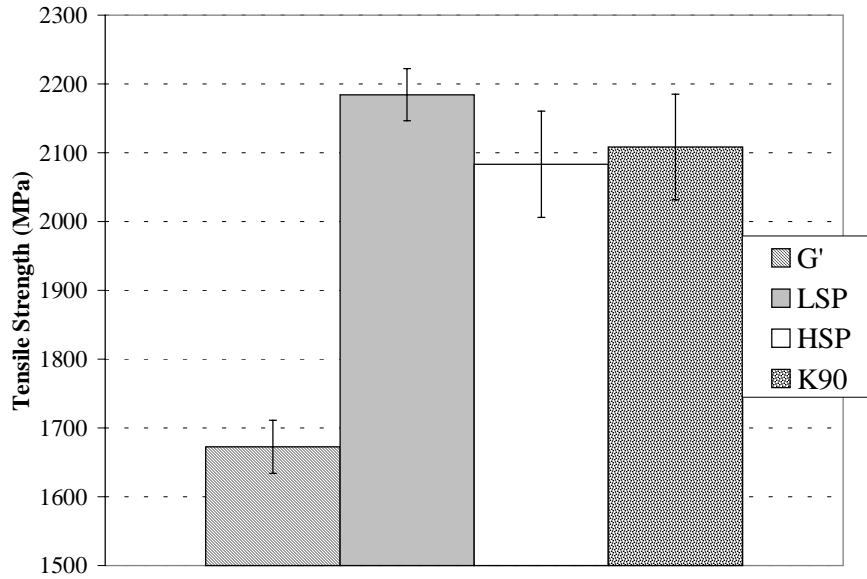


Figure 3.1-10 Static tensile strength of pultruded Hexcel carbon fiber/vinyl-ester composites with various sizing agents. Mechanical property results normalized from the theoretical fiber volume fraction to 65.6% or the theoretical fiber volume fraction of the G' sized composite.

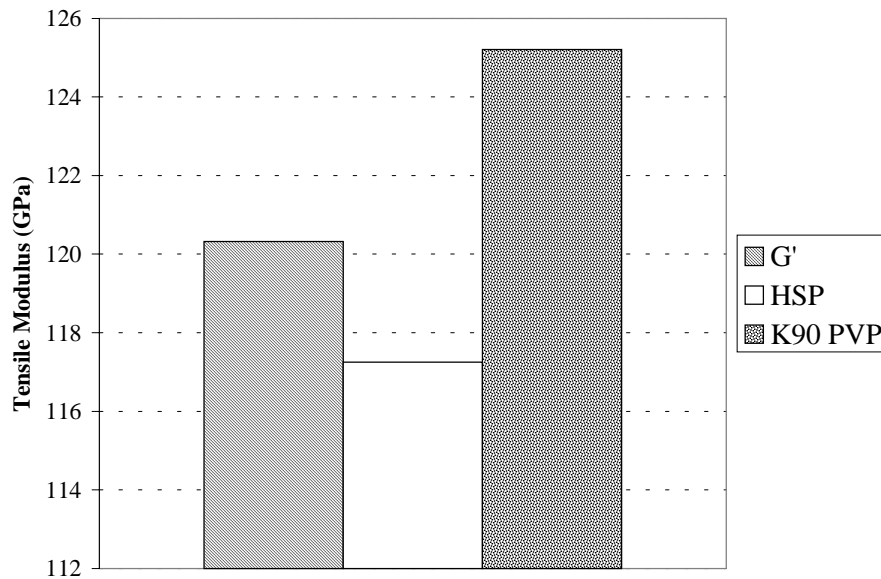


Figure 3.1-11 Static tensile modulus of pultruded Hexcel carbon fiber/vinyl-ester composites with various sizing agents. Mechanical property results normalized from the theoretical fiber volume fraction to 65.6% or the theoretical fiber volume fraction of the G' sized composite.

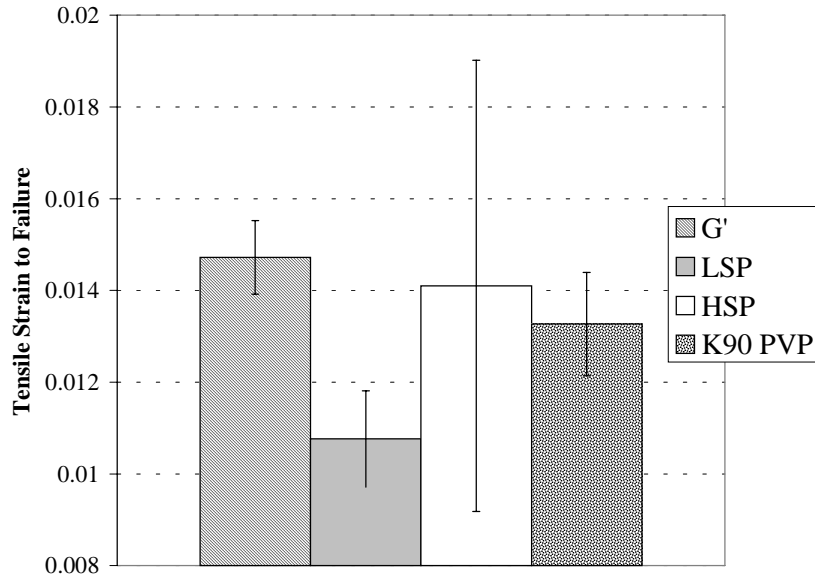


Figure 3.1-12 Static tensile strain-to-failure of pultruded Hexcel carbon fiber/vinyl-ester composites with various sizing agents. Mechanical property results normalized from the theoretical fiber volume fraction to 65.6% or the theoretical fiber volume fraction of the G' sized composite.

outperformed the standard G' by **at least 25%**. The HSP composite had the lowest tensile strength amongst the thermoplastic sizings at a value of 2083 ± 77 MPa which was a manifestation of the poor inter-tow consolidation and possibly voids.

The tensile modulus was determined for the G', HSP, and K-90 PVP composites (Figure 3.1-11). Due to a data acquisition problem encountered during the early portions of the tensile tests, no initial stress-strain data were obtained for the LSP sized composite system and only two sets of replicate initial stress-strain curves were obtained for the G', HSP, and K-90 PVP sizing systems. Because only two data points were available for the tensile modulus calculation, no standard deviation was determined. For the HSP and K-90 PVP sized composites, the modulus was nearly identical to that measured in the standard G' sizing. (G': 121.7 GPa HSP: 117.5 GPa and K-90 PVP: 125.2). However, the significance of this variation cannot be assessed due to the limited modulus data. Theoretically, the tensile modulus should only be a function of fiber properties and not a function of the sizing constituent.

The strain-to-failure was determined for all four composite systems (Figure 3.1-12). The strain-to-failure data were not normalized for variations in fiber volume fraction and/or

differences in the inherent fiber strain-to-failure. Due to the inability to normalize this data, no conclusions about a sizing's affect on this property can be postulated.

Fracture Surface Investigation

SEM was used to investigate the tensile specimen's fracture surfaces (excluding HSP) (Figure 3.1-13 through Figure 3.1-18). The failed surfaces of the tensile specimens showed differences in terms of the qualitative level of fiber/matrix adhesion. However, in all cases, the failed fibers had extensive regions where matrix remained attached which was an indication of good fiber/matrix adhesion. The G' fracture surface showed the least amount of matrix attached to the fiber surface (Figure 3.1-13 and Figure 3.1-14). The LSP displayed the largest extent of matrix covering the fiber surface (Figure 3.1-15 and Figure 3.1-16). The K-90 PVP fracture surface displayed only slightly more matrix intact with the fiber surface as compared to the G' (Figure 3.1-17 and Figure 3.1-18). From this data, it can be concluded that all three sizing systems had good fiber/matrix adhesion but LSP had the highest level of fiber/matrix. As was discussed in the introduction, on-axis static properties are not strong functions of fiber/matrix adhesion unless the fiber/matrix adhesion is poor. The fiber/matrix adhesion could not be classified as poor for any sizing system tested in these experiments. Therefore, the differences in static tensile strength discussed in the previous section cannot be entirely attributed to differences in fiber/matrix adhesion. In addition, if fiber/matrix adhesion were controlling the observed differences in static tensile strength, then the K-90 PVP composite tensile strength should have been very different from that of the LSP composite. However, Figure 3.1-10 shows that the LSP and K-90 PVP systems had similar tensile strengths (2185 MPa and 2109 MPa). This suggests that mechanisms other than alterations in fiber/matrix adhesion expressed quantitatively by an ISS are affecting the tensile properties determined in these experiments. The other mechanisms include alterations in fiber processability (fiber protection, wettability, and alignment) and alterations in the interphase mechanical property profile.

3.1.4.3.2 Longitudinal Flexure Properties

The geometry and load placement of the longitudinal flexure tests were such that the top of the specimen was exposed to compressive forces while the bottom was exposed to tensile

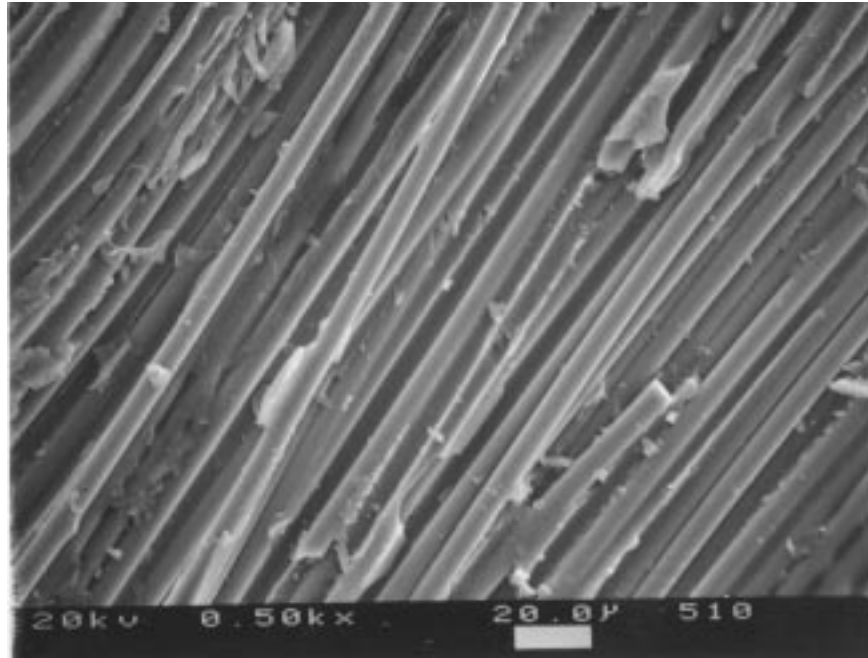


Figure 3.1-13 Optical micrographs of tensile fracture surface for pultruded Hexcel AS-4 G' sized carbon fiber/vinyl-ester composite. 500 X magnification.

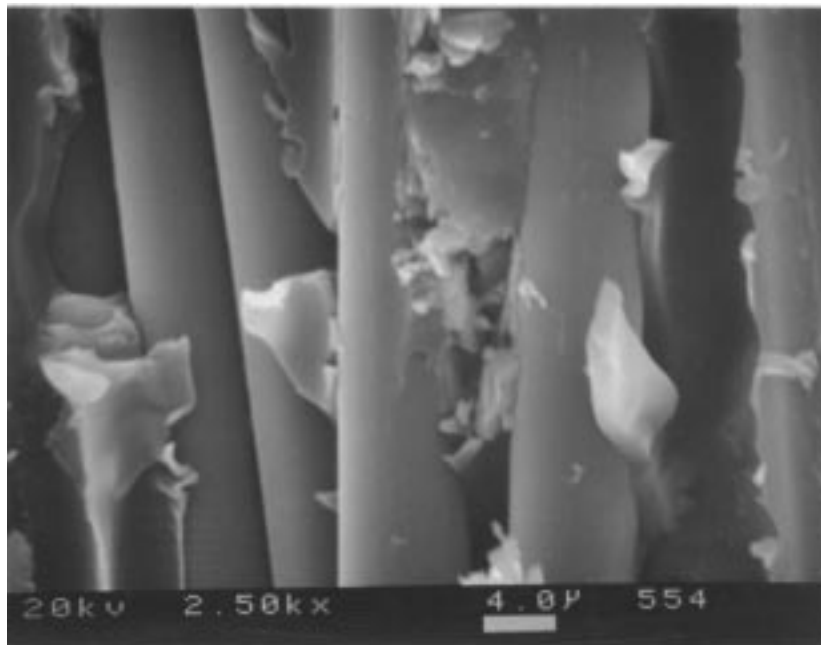


Figure 3.1-14 Optical micrographs of tensile fracture surface for pultruded Hexcel AS-4 G' sized carbon fiber/vinyl-ester composite. 2,500 X magnification.

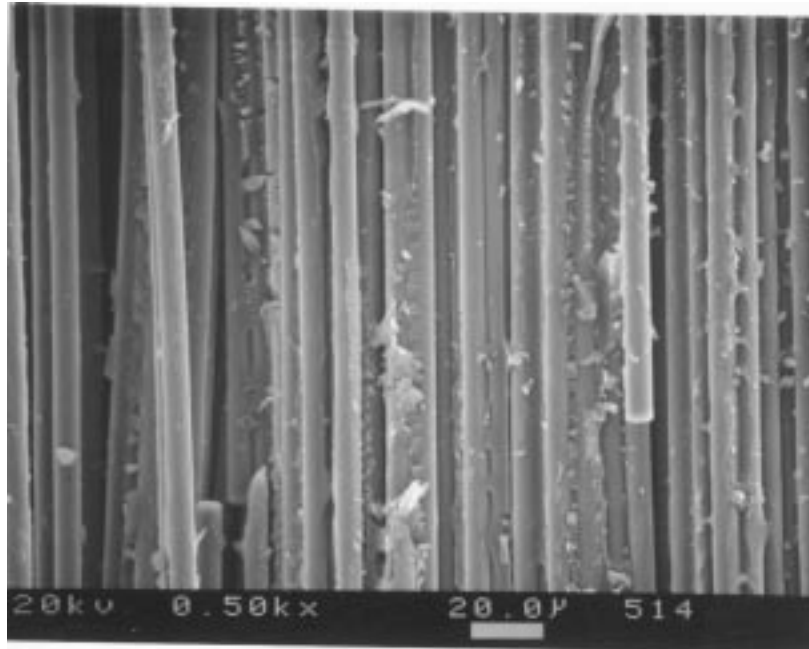


Figure 3.1-15 Optical micrographs of tensile fracture surface for pultruded Hexcel AS-4 low-spread Phenoxy™ (LSP) sized carbon fiber/vinyl-ester composite. 500 X magnification.

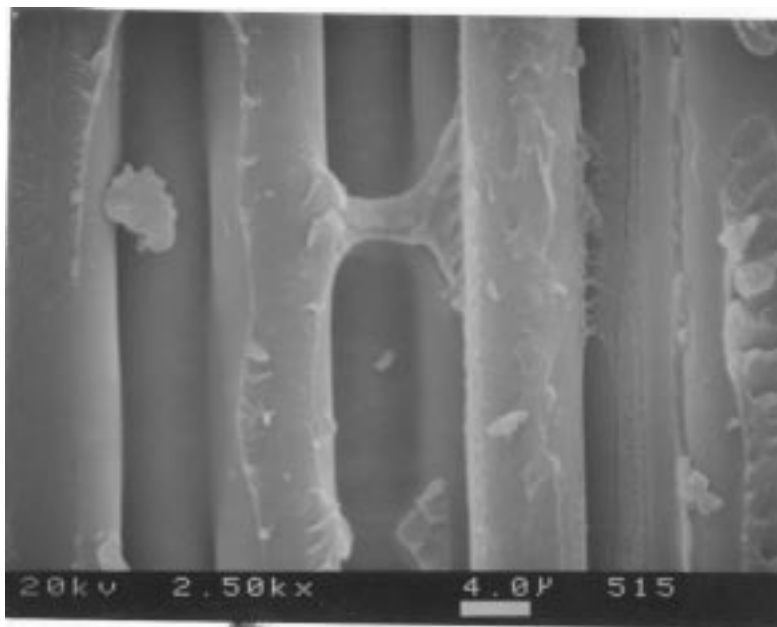


Figure 3.1-16 Optical micrographs of tensile fracture surface for pultruded Hexcel AS-4 low-spread Phenoxy™ (LSP) sized carbon fiber/vinyl-ester composite. 2,500 X magnification.

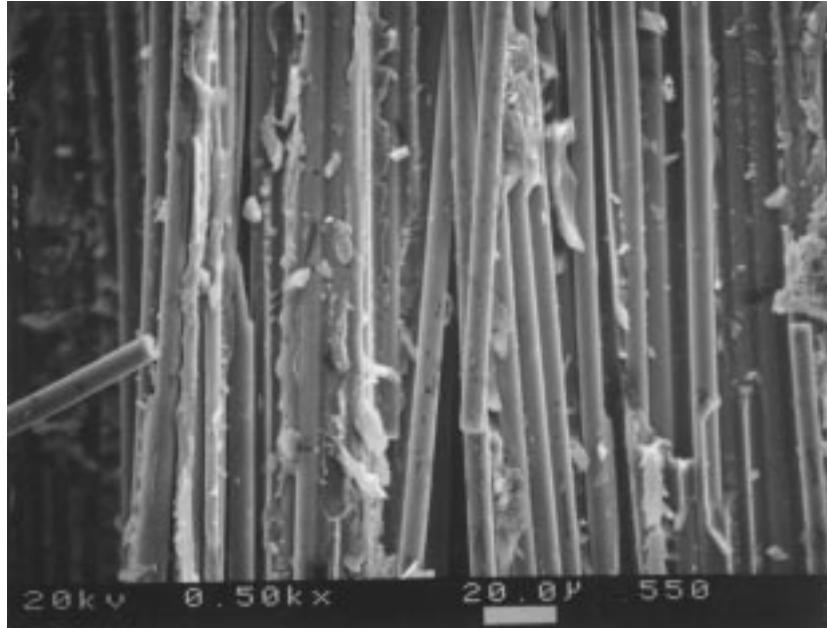


Figure 3.1-17 Optical micrographs of tensile fracture surface for pultruded Hexcel AS-4 K-90 PVP sized carbon fiber/vinyl-ester composite. 500 X magnification.

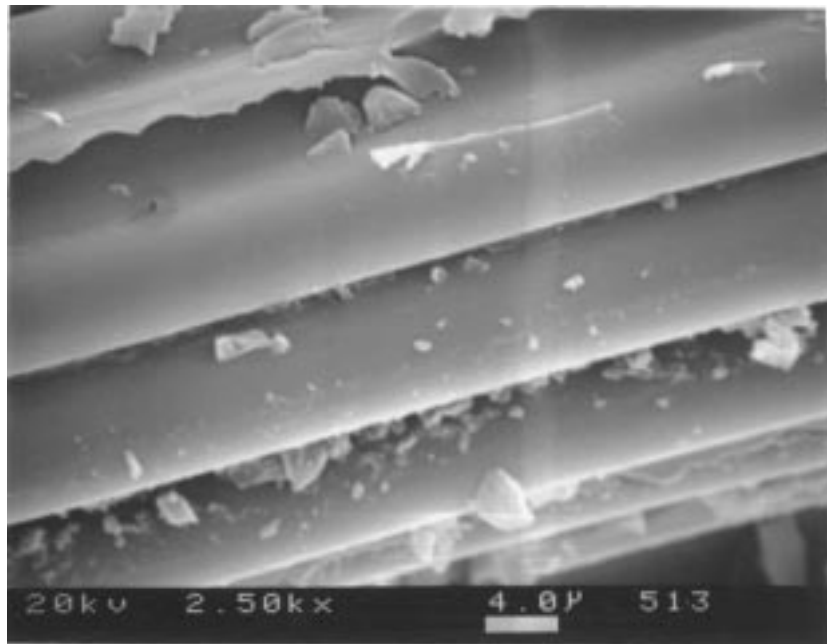


Figure 3.1-18 Optical micrographs of tensile fracture surface for pultruded Hexcel AS-4 K-90 PVP sized carbon fiber/vinyl-ester composite. 2,500 X magnification.

forces while interlaminar shear was minimized. Therefore, this property can be considered on-axis and should not depend heavily on fiber/matrix adhesion as long as a minimum level of adhesion is present. The longitudinal flexure strengths for the thermoplastic sized composites were **at least 11%** higher than that for the standard G' sizing (Figure 3.1-19). The trend was consistent with the static tensile strength findings. The LSP sized composite again showed the highest strength at a value of 1274 ± 30 MPa compared to the 983 ± 67 MPa with the G' (Note: a 30% increase). The HSP and the K-90 PVP sized composite showed statistically equivalent longitudinal flexure strengths at a value of approximately 1180 MPa.

The modulus was found to be statistically equivalent between all four composite systems (Figure 3.1-20) with values ranging from 102.3 ± 3.4 GPa to 106.9 ± 1.1 GPa. This was in agreement with the literature discussed in chapter 2 where sizings were found not to affect on-axis property moduli.

3.1.4.3.3 Short Beam Shear Properties

The geometry and load placement of the short beam shear test was conducted such that interlaminar shear was maximized at the specimen mid-section while minimizing tensile and compressive loads on the bottom and top respectively. Due to the shearing nature of the forces, the short beam shear (SBS) strength will be very sensitive to alterations in ISS and hence fiber/matrix adhesion. SBS testing showed that the thermoplastic sized composites outperformed the G' by **at least 30%** (Figure 3.1-21) which was a slightly larger improvement than the on-axis mechanical properties discussed previously. The HSP and K-90 PVP sized composites had statistically equivalent SBS strengths at values around 60 MPa compared to the 43.0 ± 1.4 MPa observed with the G'. The LSP sized composite again had the best overall properties with a short beam shear strength of 66.1 ± 0.7 MPa. This represented a 10% increase over the K-90 PVP which was an indication of the higher ISS and improved fiber/matrix adhesion observed in the LSP system as compared to the K-90 PVP.

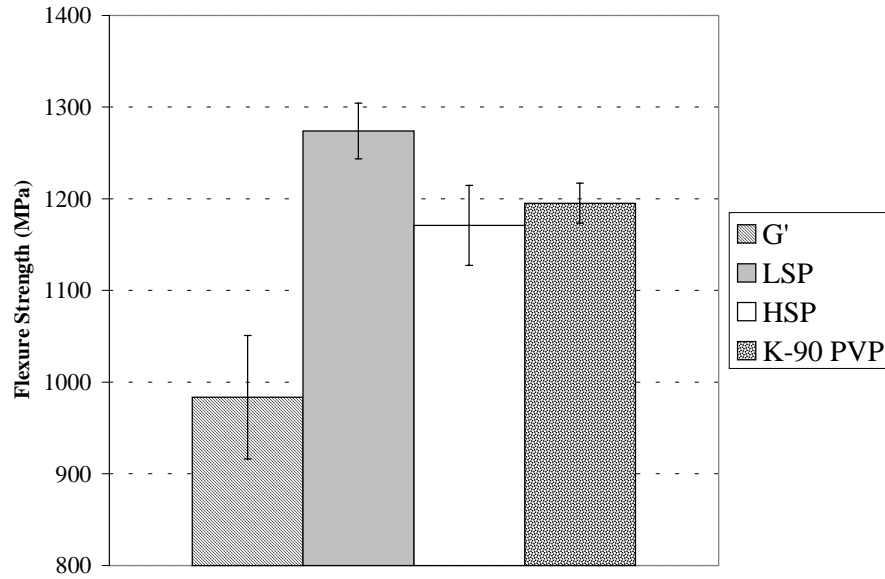


Figure 3.1-19 Static longitudinal flexure strength of pultruded Hexcel carbon fiber/vinyl-ester composites with various sizing agents. Mechanical property results normalized from the theoretical fiber volume fraction to 65.6% or the theoretical fiber volume fraction of the G' sized composite.

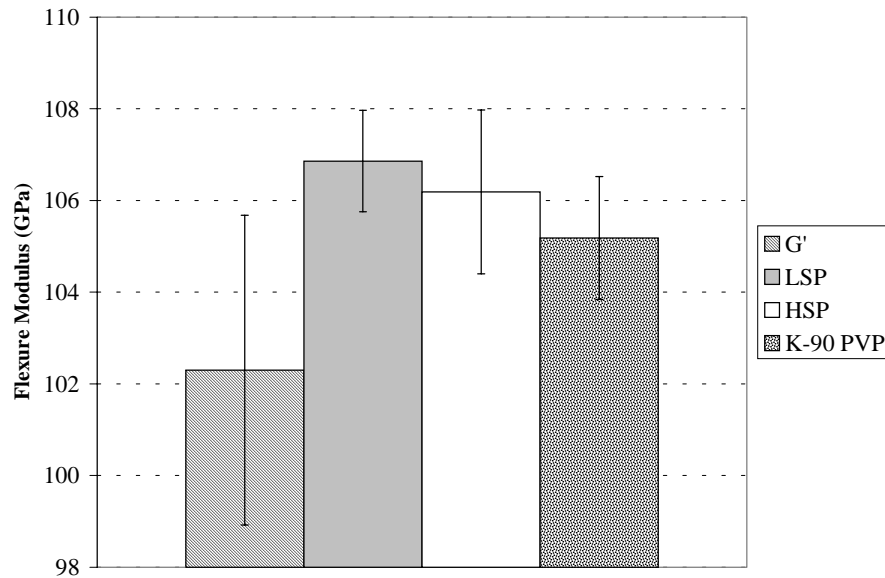


Figure 3.1-20 Static longitudinal flexure modulus of pultruded Hexcel carbon fiber/vinyl-ester composites with various sizing agents. Mechanical property results normalized from the theoretical fiber volume fraction to 65.6% or the theoretical fiber volume fraction of the G' sized composite. Normalization for differences in the inherent fiber properties included also.

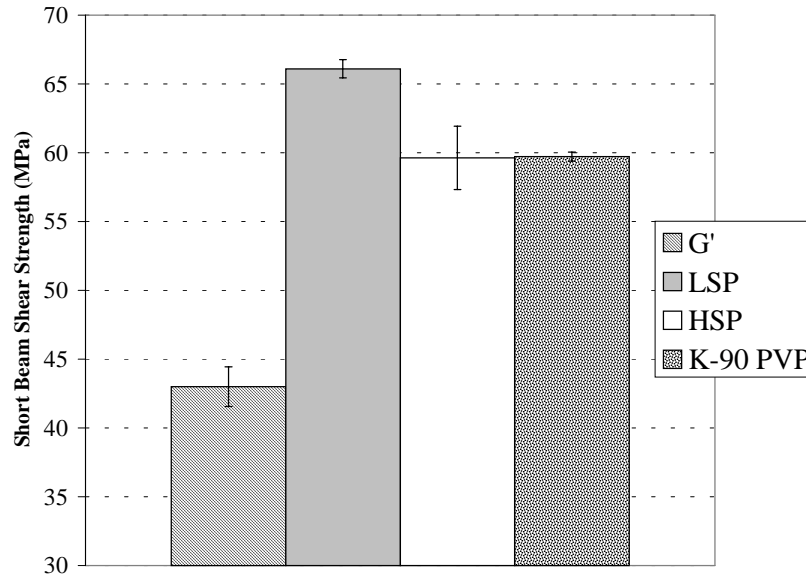


Figure 3.1-21 Short beam shear (SBS) strength of pultruded Hexcel carbon fiber/vinyl-ester composites with various sizing agents. Mechanical property results normalized from the theoretical fiber volume fraction to 65.6% or the theoretical fiber volume fraction of the G' sized composite.

3.1.4.3.4 Compressive Properties

The compressive strength and modulus for the LSP, K-90 PVP and G' composites were determined (Figure 3.1-22 and Figure 3.1-23). The compressive strength of the thermoplastic sized composites was at least **31%** greater than that of the G' (≈ 990 MPa compared to 747 ± 110 MPa) (Figure 3.1-22). There were no statistical differences between the static compressive strengths of the LSP and K-90 PVP composites. These results were consistent with the static tensile strength. As discussed in the introduction, the static compressive strength is only a weak function of fiber/matrix adhesion. Even though the fiber/matrix adhesion was hypothesized to be greater for the LSP sized composite compared to the K-90 PVP, the static compressive strength is relatively insensitive to these variations. The processability enhancements achieved with the thermoplastic sizing materials are the dominant factors in determining the static compressive performance. As discussed in the introduction, a key parameter in optimizing composite compressive performance is the degree of fiber alignment. As the fibers are increasingly aligned with the compressive loading axis, the failure is delayed and the compressive strength elevated to its maximum value. However, if misalignment or kink-bands are present, then failure will occur

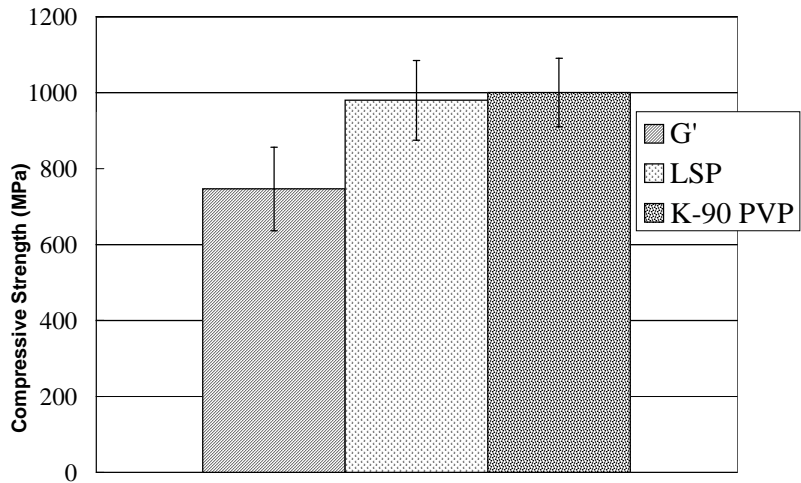


Figure 3.1-22 Compression strength of pultruded Hexcel carbon fiber/vinyl-ester composites with various sizing agents. Mechanical property results normalized from the theoretical fiber volume fraction to 65.6% or the theoretical fiber volume fraction of the G' sized composite.

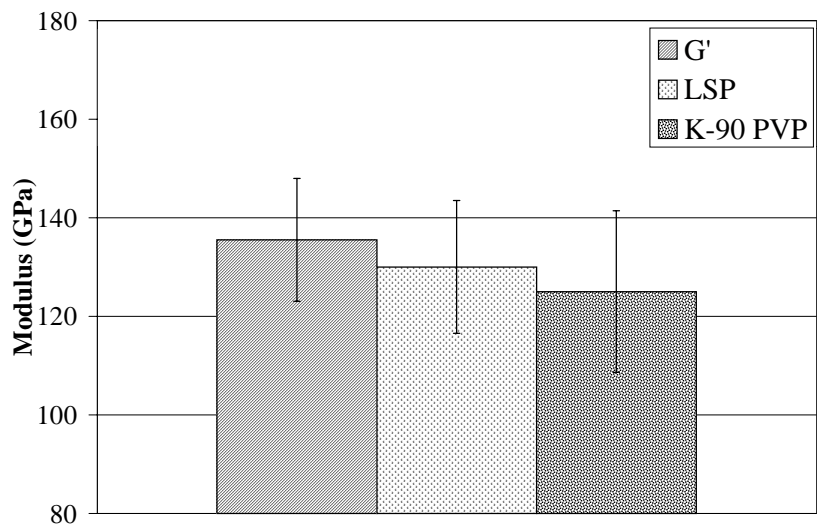


Figure 3.1-23 Compression modulus of pultruded Hexcel carbon fiber/vinyl-ester composites with various sizing agents. Mechanical property results normalized from the theoretical fiber volume fraction to 65.6% or the theoretical fiber volume fraction of the nature, the G' composite had numerous kink-bands. These kink-bands lead to a lower static compressive strength for the G' materials. G' sized composite. Normalization for differences in the inherent fiber properties included also.

at a lower load value. As was discussed earlier in the pultrusion section, the stiff nature of the thermoplastic sizing materials ensured better fiber protection and alignment.

The compressive modulus was determined (Figure 3.1-23). The compressive modulus was found to be statistically equivalent for all the sizing materials tested (≈ 122 GPa), which was to be expected based upon the literature presented in chapter 2.

3.1.5 Conclusions

In summary, the thermoplastic sizing materials offered numerous processing related advantages over the traditionally utilized G' or oligomeric epoxy sizings.

1. The high T_g thermoplastic sizings produced a stiff carbon fiber that was less susceptible to damage during the pre-wet-out portions of the pultrusion process. In addition, the inherent fiber stiffness produced a composite with improve fiber alignment.
2. The spread/tape-like thermoplastic sized fibers minimized damage in the dip bath entrance and also minimized wet-out time due to a reduction in wet-out distance.
3. The high T_g thermoplastic sizing materials swelled and then relaxed with the vinyl-ester matrix thus making them rubbery at the resin dip bath exit. This allowed the fibers to be more easily compacted and compressed in the pultrusion die.

These processability improvements translated into a composite with improved surface finish and better fiber alignment. In addition, the mechanical performance of the final composite was greatly affected by variations in the composite's sizing agent.

1. All of the thermoplastic sized composites outperformed the standard G' sizing by **at least 25%** in static tensile strength.
2. All of the thermoplastic sized composites outperformed the standard G' sizing by **at least 11%** in longitudinal flexure strength.
3. All of the thermoplastic sized composites outperformed the standard G' sizing by **at least 30%** in short beam shear strength.
4. All of the thermoplastic sized composites outperformed the standard G' sizing by **at least 31%** in compressive strength.
5. The tensile, longitudinal flexure, and compressive moduli were found to be unaffected by variations in the sizing.

These mechanical performance enhancements were achieved by altering a 1 to 3 wt% feature on the surface of the carbon fiber reinforcement. This corresponds to a material that occupied less than 3 wt% in the final composite. Because these thermoplastic sizing materials were commercially available materials and because such a low amount of them was needed to greatly improve mechanical properties, these sizing materials would make excellent replacements for the standard G' or oligomeric epoxies that are presently being utilized in pultrusion of carbon/vinyl-ester composites.

3.1.6 Acknowledgments

This work was sponsored in part by the National Science Foundation Science and Technology Center for High Performance Polymeric Adhesives and Composites (NSF grant # DMR-9120004). In addition, financial support was provided by the Adhesives and Sealant Council Educational Foundation (ASCEF) through the Center for Adhesives and Sealant Science (CASS) at Virginia Tech. Financial support was also provided by the Virginia Space Grant Consortium. Pultrusion access was provided by Strongwell, Inc. and their assistance is gratefully acknowledged. Material contributions from Phenoxy Associates and BASF are acknowledged. Mr. Steve McCartney is gratefully acknowledged for his completion of the ESCA analysis. Mr. Mac McCord is acknowledged for his completion of the ultrasonic C-scan analysis.

This concludes section 3.1 of this chapter. In the next section, a related pultrusion trial is discussed that more quantitatively addresses the differences in processability between the various sizing systems. In addition, the interphase effect is probed by utilizing two sizing materials, K-30 and K-90 PVP that differ only in molecular weight.

3.2 Mechanical Performance of Pultruded Hexcel AS-4 Carbon Fiber/Vinyl Ester Composites Processed with G', Phenoxy, K-90, and K-30 PVP Sizing Agents

3.2.1 Abstract

Hexcel AS-4 12K carbon fibers were sized with three different thermoplastic sizing agents. The sizing agents tested were K-30 poly(vinylpyrrolidone), K-90 poly(vinylpyrrolidone) and Phenoxy™. In addition, Hexcel AS-4 36K carbon fibers sized commercially with the standard G' were tested. The sized carbon fibers were processed into composites utilizing a pilot scale pultruder and a pultrudable vinyl-ester resin.

The Phenoxy™ sizing had improved processability over the traditionally utilized G' sizing material. These improvements in processability translated into improvements in final composite surface finish and quality. In addition, the pull-force required to pultrude the Phenoxy™ sized carbon fiber was approximately ½ of that required for all the other sizing materials.

The static mechanical performance of the composites produced from the thermoplastic sizings were distinctly better than that of the composites made with the standard G' sizing. All of the thermoplastic sized composites outperformed the standard sizing G' by at least 8% in longitudinal flexure strength and by at least 15% in short beam shear strength. These improvements in mechanical properties were believed to be the result of improved fiber processability, altered interphase properties, and altered fiber/matrix adhesion.

These improvements in static mechanical performance were considerably less than those observed in the previous pultrusion trial discussed in section 3.1. There are several possible explanations for the reduced level of improvement. First, the fiber volume fractions between the G' and thermoplastic sized composites was more consistent in the present trial. As was discussed in the introductory section to this chapter, for the first pultrusion trial, the G' fiber volume fraction was considerably higher than that utilized for the thermoplastic sized composites. The additional G' fiber volume fraction could have partially contributed to the increased composite surface damage observed in the first trial. In section 3.1, it was hypothesized that composite surface damage (caused by both inferior G' fiber protection and to a lesser extent, the additional G' composite fiber volume fraction) was largely responsible for the

improvements in performance discussed in section 3.1. Because the fiber volume fraction was more consistent in the present trial, the additional fiber damage caused by inherent differences in fiber volume fraction have been eliminated. Second, in order to improve upon non-optimal inter-tow consolidation observed in section 3.1, a lower sizing level (≈ 0.9 wt%) was utilized for the present trial compared to the previous trial (≈ 2.0 wt%). This would have resulted in the thermoplastic sized fibers having less protective material surrounding the fibers and making them more susceptible to damage and incomplete wetting. In addition, the interphase mechanical property profile will be altered thus affecting damage initiation and propagation in the composite. Third, the composite cross-section produced in the present trial was considerably larger than the cross-section produced in the previous trial. This would have reduced the effect of surface damage and fiber protection due to a reduction in the composite surface area to volume ratio. Finally, the matrix utilized in the present trial had approximately $\frac{1}{2}$ the styrene amount contained in the matrix discussed in section 3.1, which lowered the inherent matrix shrinkage and minimized the effect of residual stresses. Because a sizing can affect composite performance through alterations in the matrix shrinkage prevailing in the interphase region, this effect is less predominant in matrix systems with inherently less shrinkage as a result of a lower styrene content.

For the longitudinal flexure and short beam shear properties investigated, the effect of alterations in the interphase mechanical property profile were found to be insignificant for the case of K-90 and K-30 PVP sizing systems. This does not imply that the interphase does not affect these properties but does imply the variation developed in the K-90 and K-30 PVP sizing systems was not large enough to produce an effect. All the thermoplastic sizing materials may produce interphase mechanical property profiles that are similar to each other but significantly different than the G' interphase mechanical property profile.

3.2.2 Introduction

It has been proven in section 3.1 that the mechanical performance of pultruded carbon fiber/vinyl-ester composites are significantly affected by the sizing agent present on the fiber surface. High temperature thermoplastic materials such as Phenoxy™ and K-90 PVP improve the processability of the carbon fiber by making it stiffer and better protected from damage. However, as was noted in section 3.1, the sizing levels tested were hypothesized to be higher

than optimal because non-optimal inter-tow consolidation was observed. Therefore, it was desirable to test the Phenoxy™ and K-90 PVP sizing materials at levels lower than those utilized in section 3.1.

In addition, the effect of the interphase on composite mechanical performance was not probed in the previous trial. The processing effect (i.e. fiber protection and alignment) was believed to be dominant in controlling the mechanical performance of the on-axis properties discussed in section 3.1. If the processing effect can be minimized while varying the interphase properties between sizing systems, then the effect of the interphase can be effectively probed. The interphase effect can be assessed by varying the molecular weight of the sizing material. A variation in molecular weight will change the diffusion characteristics of the sizing but not significantly change the handling characteristics or the wettability issues because the interface chemistry is held constant. For instance, K-90 and K-30 PVP have drastically different molecular weights (K-90 PVP: $MW_w = 1,200,000$ g/mol K-30 PVP: $MW_w = 49,000$ g/mol). Because both materials are above the critical entanglement molecular weight for PVP, they should provide adequate protection for the brittle carbon fiber. In addition to similar handling characteristics, the two materials should have identical wetting characteristics. However, the interphase concentration profile produced by these two materials will be drastically different as will be discussed in chapters 4 and 5. Due to the extreme variation in molecular weight, the K-90 and K-30 PVP materials will diffuse at drastically different rates. In addition, the thermodynamic equilibrium amount of sizing material dissolvable in the Derakane™ matrix will be different for the two PVP materials. This will result in a dramatic change in the interphase concentration profile and hence interphase mechanical property profile. Therefore, the magnitude of the interphase effect on composite mechanical performance might be assessable.

3.2.3 Experimental

3.2.3.1 Materials

Hexcel AS-4 12K G' sized carbon fiber (lot # D1317-4C) was used as the control fiber for the trials presented in this section. The G' sized fiber was donated by the Dow Chemical Company. The properties of this fiber were similar to the G' sized fiber discussed in section 3.1.3.1.

Hexcel AS-4 12K unsized carbon fiber (lot # D1317-4C) was sized at Virginia Tech with three different thermoplastic materials: K-30 PVP, K-90 PVP, and polyhydroxyether-Phenoxy™.

The K-30 poly(vinylpyrrolidone) (PVP) sizing material (Figure 3.1-1.b) was obtained from BASF. The M_w of this material was 49,000 g/mol and it had a T_g of 168°C [3.14].

The K-90 PVP sizing material (LUVISKOL lot # 20421501) (Figure 3.1-1.b) was obtained from BASF. The M_w of this material was 1,250,000 g/mol and it had a T_g of 180°C [3.14].

The Phenoxy™ sizing material (PKHW-35 lot # 217013) (Figure 3.1-1.a) was obtained from Phenoxy Associates, Rock Hill, SC. This material was obtained as a 30wt% dispersion of approximately 1-micron diameter particles in 57wt% water [3.13]. The balance of the suspension contained 10 wt% of a cosolvent, butoxyethanol, and 3 wt% of a neutralant, dimethylethanolamine. In order to make the hydrophobic Phenoxy™ shown in Figure 3.1-1.a water dispersible, the commercially available Phenoxy™ suspension contained a modified version of the Phenoxy™ backbone shown in Figure 3.1-1.a. For approximately every ten repeat units, a carboxylic acid functional group had been grafted onto the chain [3.13]. The M_n of the Phenoxy™ was 19,000 g/mol (GPC) and it had a T_g of 97°C (DSC) [1.8].

The matrix/resin utilized for pultrusion was a Derakane™ 441-400 vinyl-ester resin (Figure 3.1-1.c&d), supplied by the Dow Chemical Company. The pultrudable resin was composed of *approximately* 62.0 wt% vinyl-ester, 26.6 wt% styrene monomer, 8.9 wt% clay, 1.5 wt% release agents, and 1.0 wt% of a proprietary initiator package. The same resin batch was utilized for all the experimental work presented in this paper.

Deionized water was used to make the sizing solutions/suspensions for the sizing line's dip bath. The deionized water came from a NanoPure II™ unit equipped with a 0.2 μm filter and had a resistivity typically of 15 MΩcm or higher.

Composite specimens were examined with optical microscopy. Before the specimens could be examined utilizing this technique, they had to be mounted in epoxy. The materials utilized to accomplish this potting were Buehler Epoxide resin No.20-8130-032 and Buehler Epoxide Hardener No. 20-8132-032.

3.2.3.2 Processing

3.2.3.2.1 Sizing Solution/Suspension Preparation

Before sizing of the carbon fibers could be conducted, aqueous solutions/suspensions of the sizing materials had to be prepared. In section 3.1, Hexcel carbon fibers were sized with the thermoplastics, Phenoxy and K-90 PVP, at a 1.9 – 2.9 wt% level. As was discussed in section 3.1, this sizing level resulted in improved fiber protection and significant improvements in composite mechanical performance. However, it was noted in section 3.1.4.2 that these sizing levels may have prevented the fiber from fully saturating with the resin, which may have resulted in poor inter-tow consolidation. Therefore, for this set of trials, the sizing levels were reduced to approximately 0.9 wt%. In order to achieve this final sizing level, the sizing dip bath concentration needed to be approximately 1.0wt%. Therefore, aqueous dip bath solutions/suspensions of 1.0wt% sizing material in deionized water were prepared.

The K-30 PVP sizing material was dried in a convection oven at 110°C for approximately 18 hours before solutions were prepared. Approximately 160g of this dried K-90 PVP was added directly to 15,700g of deionized water. This mixture yielded a 1.0 wt% K-90 PVP in water solution. This solution was then allowed to stir for seven days at room temperature due to the high molecular weight of the K-90 PVP. This solution was then added to the sizing dip bath without further agitation.

The K-90 PVP sizing material was dried in a convection oven at 110°C for approximately 18 hours before solutions were prepared. Approximately 160g of this dried K-90 PVP was added directly to 15,700g of deionized water. This mixture yielded a 1.0 wt% K-90 PVP in water solution. This solution was then allowed to stir for seven days at room temperature due to the high molecular weight of the K-90 PVP. This solution was then added to the sizing dip bath without further agitation.

The Phenoxy™ material was insoluble in water and was supplied as a 35wt% aqueous suspension. Approximately 72g of the suspension was added to 2360g of deionized water to yield a 1.0 wt% Phenoxy in water suspension. This suspension was allowed to stir rapidly overnight. This suspension was then added to the sizing dip bath and vigorous stirring was applied.

3.2.3.2.2 *Sized Fiber Preparation*

The carbon fibers were sized on a custom made small scale sizing line described in reference [3.9]. The unsized carbon fiber tow was pulled off a spool at a set speed ranging from 0.3 to 6.0 cm/sec. The fiber tension was controlled by a nip roller, which was connected to a particle brake. A load cell located at the exit of the sizing dip bath measured the tension. The fibers were then passed through a sizing dip bath that contained the aqueous sizing solution/suspension discussed earlier. In the dip bath, capillary forces provided the driving force for rapid tow wetting. The high fiber tension and extensive use of rollers after the sizing bath spread the tow bundle and also prevented the wet tow from clumping. The spread carbon fiber tow containing the sizing solution was dried online in an infrared (IR) forced convection dryer.

The emitter surface temperature of the two IR heating panels embedded in the dryer was controllable from ambient temperature up to 500°C. The inlet air temperature was controlled at ambient conditions. The emitter surface temperature directly controlled the surface temperature of the carbon fiber. The surface temperature of the fiber was measured by a hand held thermocouple. A time/temperature profile was generated by placing the thermocouple on the fiber surface at various positions in the IR dryer. Placement of the thermocouple was such that no background IR interfered with the surface temperature measurement. The surface temperature history of the sized carbon fiber affected the handling characteristics of the final sized tow. It also affected the morphology of the sizing deposited onto the fiber surface. For each sizing material, an optimal time temperature dryer profile was determined.

The fiber that exited the dryer was pulled through a motorized nip roller where line speed was controlled and line tension was developed. The fiber was then wound onto a standard carbon fiber spool utilizing a constant tension Izumi rewinder. The fibers were then sealed in a plastic bag to prevent moisture from being re-absorbed by the sizing material or the carbon fiber.

3.2.3.2.3 *Pultrusion*

Pultrusion was performed at Dow in Freeport, TX, utilizing their pilot scale pultruder. For the Hexcel AS-4 G' sized material, 51 ends of the carbon fiber were directed into the pultrusion process. For the K-30 and K-90 sized Hexcel carbon fibers, 52 ends were utilized. For the Phenoxy™ sized Hexcel carbon fiber, 52, 53, and 54 ends were utilized to make a three composite series. For the remainder of this section, the 52, 53, and 54 end Phenoxy™

composites are given the following designations: 52 end: Phenoxy™ 52, 53 end: Phenoxy™ 53 and 54 end: Phenoxy™ 54. The line speed utilized for all trials was approximately 21 inches/minute. The individual tows were directed into the process via a board of perforated polyethylene. The fibers were then pulled through a resin bath where the fibers were fully wetted with the resin. After the fibers were pre-formed, they were cured in a die of rectangular cross section.

The die was approximately 762mm long and had three zones where temperatures could be monitored and controlled. The three zones were located at the beginning, middle, and end of the die. The first zone required heat input in order to control the surface temperature at approximately 225 °F. The second zone required less heat input to control the surface temperature at 280 °F due to the exotherm associated with the matrix curing. In addition, the third zone required no heat input to control the surface temperature at 260 °F.

After the cure was complete, the composite was air cooled in the roll-out portion of the pultrusion process. The part was then cut utilizing a saw and the final dimension of the composite part was 15mm wide by 3mm thick by 15.24m long.

3.2.3.3 Characterization Methods

3.2.3.3.1 Sized Fiber Characterization

3.2.3.3.1.1 Sizing Level Determination

The amount of sizing deposited on the carbon fiber was determined via pyrolysis in a nitrogen atmosphere. Approximately 8 grams of sized carbon fiber were used for the analysis. The fibers were first dried in a convection oven for a period of eight hours. The temperature of the convection oven was set above the T_g of the particular sizing material being tested. After being dried, the fibers were placed in a high temperature Blue-M furnace with a nitrogen purge at a flow rate of approximately 40 cm³/sec. This led to a purge gas residence time of 30 seconds. Typically 20 minutes were required for heating the chamber from room temperature to the pyrolysis temperature of 600°C. Thus, the pyrolysis chamber typically was purged with gas for about 40 residence times prior to reaching the pyrolysis temperature. This ensured that there was no unwanted oxidation of the carbon fibers. Pyrolysis then proceeded for 30 minutes at 600°C.

The amount of sizing material was computed from the differences in mass of the dry sized fiber and the pyrolyzed fiber.

$$S = 100 \cdot \frac{(M_1 - M_2)}{M_1} \quad (3-1)$$

where S was the weight percent of sizing on the fiber, M_1 was the dry sized fiber mass, and M_2 was the pyrolyzed fiber mass.

3.2.3.3.1.2 SEM

The quality of the sized fiber was determined by inspection of the fibers under Scanning Electron Microscopy (SEM). The fibers were secured on a standard ESCA mount. The fibers were sputter coated with gold for approximately 2 minutes. Analysis was conducted in an International Scientific Instruments Model SX-40 SEM.

3.2.3.3.2 Composite Characterization

3.2.3.3.2.1 Fiber Volume Fraction

The fiber volume fraction of the composite panels produced in these experiments was determined by two methods. The first method utilized data collected before the composite part was produced and was termed the theoretical fiber volume fraction. The second method utilized data collected after the composite part was produced and was termed the experimental fiber volume fraction.

For the first method, the number of tow ends and their respective linear density allowed the determination of the volume of fiber per unit length entering the pultrusion die. The fiber volume fraction could then be computed from the following equation.

$$v_f = \frac{(n \cdot l_f)}{A_c \cdot \rho_f} \quad (3-2)$$

where v_f is the fiber volume fraction, n is the number of tow ends, l_f is the weight per unit length per bundle, A_c is the cross-sectional area of the composite, and ρ_f is the filament density. The cross-sectional area of the composite, A_c , was determined from the die cross-sectional area (neglecting matrix shrinkage) or from the final composite cross-sectional area (including matrix

shrinkage). This method neglects the mass of fiber lost in the pre-processing portions of the pultrusion process, which is negligible in most cases.

For the second method, the density of the composite and non-volatile (fiber + filler) composite content was determined and then a rule of mixtures was used to determine the fiber and filler volume fraction. The composite density was determined by Archimedes' principle. A 4g sample of the composite was dried and weighed. The sample was then immersed in isopropyl alcohol and weighed again. The density of the composite was calculated using Archimedes' principle using the following equation

$$\rho_c = \frac{W_{air}}{(W_{air} - W_{IPA})} \cdot \rho_{IPA} \quad (3-3)$$

where ρ_c = density of composite, ρ_{IPA} = density of Isopropyl alcohol, W_{air} = weight of sample in air and W_{IPA} = weight of sample in isopropyl alcohol. In section 3.1, the fiber volume fraction was determined from the composite density and application of the rule of mixtures (equation (3-4)). With this method of determining fiber volume fraction, the matrix density (Derakane™ + filler) had to be known and was set equal to the theoretical matrix density calculated from the starting matrix formulation. After the initial pultrusion trial, it was suspected that the filler was being preferentially included in the composite due to a filtering effect occurring in the squeeze-out portion of the pultrusion process. If this were the case, then the cured matrix density utilized in equation (3-4) cannot be specified from the starting matrix formulation. Therefore, the cured matrix (Derakane™ + filler) density had to be treated as an unknown. The amount of filler existing in the matrix at the end of the pultrusion process was determined by pyrolyzing the composite. The non-volatile content of the composite was determined by pyrolyzing the composite in a 600°C nitrogen furnace. The weight fraction of non-volatiles was assumed to be equal to the weight fraction (filler + fiber) and was calculated from the following equation.

$$\omega_{filler+fiber} = 1 + \frac{1}{\alpha} \left(\frac{W_c^{ab}}{W_c} - 1 \right) \quad (3-6)$$

where $\omega_{filler+fiber}$ was the (filler + fiber) weight fraction, α was the resin volatile fraction (note: weight fraction of resin volatilized during the pyrolysis cycle, assumed to equal 1.0), W_c^{ab} was the composite weight after the pyrolysis cycle, and W_c was the composite weight before the pyrolysis cycle. The resin weight fraction, ω_R , in the final composite was determined from the following equation.

$$\omega_R = 1 - \omega_{\text{filler+fiber}} \quad (3-7)$$

The relative non-volatile ratio, R (wt Filler/wt Fiber), was determined from the following equation where the rule of mixtures was assumed to be valid (voids neglected).

$$R = \frac{\left(\frac{1}{\rho_c} - \frac{\omega_R}{\rho_R} - \frac{(1-\omega_R)}{\rho_f} \right)}{\left(\frac{\omega_R}{\rho_R} + \frac{(1-\omega_R)}{\rho_F} - \frac{1}{\rho_c} \right)} \quad (3-8)$$

where ρ_R was the cured matrix density of the pure Derakane™ 441-400 (1.151 g/cc), ρ_f was the fiber density (1.78 g/cc), and ρ_F was the filler density (2.72 g/cc). The weight fraction filler in the final composite, ω_F , was calculated from the following equation.

$$\omega_F = \left(\frac{R}{R+1} \right) (1 - \omega_R) \quad (3-9)$$

The fiber volume fraction, v_f , was then calculated using the rule of mixtures.

$$v_f = \frac{1}{\left[1 + R \cdot \frac{\rho_f}{\rho_F} + \frac{\rho_f}{\rho_R} \left(\frac{\omega_R}{1 - \omega_R - \omega_F} \right) \right]} \quad (3-10)$$

The filler weight per unit matrix (filler + Derakane™ 441-400) weight, ω_F^{Matrix} , was determined from the following equation.

$$\omega_F^{\text{Matrix}} = \frac{1}{\left(1 + \frac{\omega_R}{\omega_F} \right)} \quad (3-11)$$

The value for ω_F^{Matrix} was compared to the filler content in the starting matrix, which was 0.089 for all the trials conducted in section 3.2.

3.2.3.3.2.2 Visual Inspection of the Cut Composite

Composite specimens for mechanical testing were cut using a Felker saw. The cut specimens were examined visually for defects.

3.2.3.4 Mechanical Testing

3.2.3.4.1 Flexure and Short Beam Shear Testing

Flexure tests were performed in accordance with ASTM D790-90 [3.15]. Specimens were cut using a Felker cutting saw using water as a coolant. The specimens were 180 mm long, 12.7 mm wide, and 2.96 mm thick. The specimens were mounted in a three-point bend fixture and loaded at a rate of 0.8 mm/min by an Instron 4104 test frame.

Short beam shear tests were performed in accordance with ASTM D 2344-84 [3.16]. The specimens were 75 mm long, 6.2 mm in width, and 3 mm thick. The specimens were mounted in a three-point bend fixture and loaded at a rate of 1.3 mm/min by an Instron 4104 test frame.

For both tests, a 5KN load was used to monitor load and LabView[®], a National Instruments Corporation data acquisition software, was used to monitor load versus displacement.

3.2.3.4.2 Normalization of Mechanical Properties for Fiber Volume Fraction Variations

Before comparisons could be made between composite systems, the mechanical properties had to be normalized with respect to fiber volume fraction. The type of normalization used in this section was a rule of mixtures expression that neglected the mechanical response of the matrix. Even though this type of normalization does not rigorously apply to strength based properties where statistical events control the failure, it will still be reasonably accurate for the fiber volume fraction variation observed in these composites. The equation utilized for the normalization was as follows,

$$\sigma_c^n = \sigma_c^o \cdot \left[\frac{v_f^n}{v_f^o} \right] \cdot \phi_f \quad (3-5)$$

where σ_c^n is the normalized property (strength or stiffness) at a fiber volume fraction equal to v_f^n (in all cases, v_f^n was set equal to 0.592 or the theoretical fiber volume fraction of the G' sized composite), v_f^o is the original fiber volume fraction of the composite to be normalized, σ_c^o is the original property (strength or stiffness) at a fiber volume fraction equal to v_f^o , and ϕ_f is the ratio of the inherent strength or stiffness of AS-4D G' sized fiber to the inherent strength or stiffness of the AS-4 unsized fiber. The value of ϕ_f is equal to 1.00 for the results presented in this section.

Strain-to-failure values were not normalized due to a lack of knowledge of how to properly complete the normalization.

3.2.4 Results and Discussion

3.2.4.1 Processing

3.2.4.1.1 Sized Fiber Preparation

As was discussed in section 3.1, the surface temperature of the fiber had to exceed the sizing material's T_g to fully dry the sizing and also to allow the sizing to soften and fully encapsulate the carbon fiber. The processing parameters used to produce the sized fibers utilized in this study are noted (Table 3-5). Pyrolysis of these sized fibers showed that the K-30 PVP material had a final moisture content of 0.05 ± 0.03 wt% and a sizing level of 0.92 ± 0.06 wt% (Table 3-5).

Table 3-5 Processing parameters used to produce the sized fibers utilized in this study. In addition, sizing characterization information also displayed.

Sizing System	K-30 PVP	K-90 PVP	Phenoxy™
Dip Bath Concentration (wt%)	1.0	1.0	1.3
Auxillary Heat Blower On (Yes/No)	Yes	Yes	No
First IR Heating Panel (°C)	375.0	375.0	425.0
Second IR Heating Panel (°C)	375.0	375.0	425.0
Main Heat Blower On (Yes/No)	No	No	No
Maximum Fiber Surface Temperature (°C)	175.0	175.0	225.0
Line Tension at Dip Bath Exit (lbs)	2.30	2.30	2.30
Tension Setting onto Spool	2.0	2.0	2.0
Approximate Width of Sized Fiber (in.)	¼	¼	1/8
Fiber Moisture Content (wt%)	0.05 ± 0.03	0.10 ± 0.04	0.00 ± 0.02
Dry Fiber Sizing Level (wt%)	0.92 ± 0.06	0.99 ± 0.19	0.89 ± 0.08

The K-90 PVP material had a final moisture content of 0.10 ± 0.04 wt% and a sizing level of 0.99 ± 0.19 wt%. The Phenoxy™ material had a final moisture content of 0.00 ± 0.02 wt% and a sizing level of 0.89 ± 0.08 wt%. The low levels of moisture (<0.10 wt%) indicated that the drying conditions were sufficient to completely dry the fiber. In addition, the low standard deviations on the sizing level indicated the consistency of the sizing process.

For the commercially available G' sized Hexcel fiber, the coating was found to be extremely smooth when investigated by SEM (Figure 3.2-1 and Figure 3.2-2). The G' sized fiber had its typical oily handling characteristic. The K-30 PVP sizing was uniformly coated onto the fiber surface and did not bond adjacent fibers together (Figure 3.2-3 and Figure 3.2-4). The K-30 PVP sizing resulted in the fibers being only slightly stiff compared to the thermoplastic sized fibers discussed in section 3.1. The K-90 PVP sizing was uniformly coated onto the fiber surface (Figure 3.2-5 and Figure 3.2-6). However, the K-90 PVP did bond adjacent filaments together in numerous locations. As was the case for the K-30 PVP sizing, the 0.99 wt% K-90 PVP sizing level resulted in the fiber being marginally stiff and considerably less stiff than the 1.97wt% K-90 PVP sized fiber discussed in section 3.1. The Phenoxy™ sized fiber displayed a rough and non-homogeneous surface coverage when investigated by SEM (Figure 3.2-7 and Figure 3.2-8). The micrographs suggested that the surface temperature was not high enough to allow the Phenoxy™ material to soften and fully encapsulate the carbon fiber. The 0.89 wt% Phenoxy™ coating resulted in the fiber being slightly stiff though considerably less than that observed with the 1.56 and 2.90 wt% Phenoxy™ sized fibers discussed in section 3.1.

3.2.4.1.2 Pultrusion (Completed by and observed by H. Engelen of Dow Chemical)

The Hexcel AS-4 G' material was pultruded on Day 1 of the trial. During the processing of the G' sized material, it was noted that the carbon fibers were not protected sufficiently by the G' sizing. As was noted in the previous pultrusion trial discussed in section 3.1, the G' sized fibers were damaged extensively during the processing steps. The average pull-force required to produce the G' sized composite was approximately 300 ± 70 pounds. The surface finish of the final composite was rough and somewhat dull and non-reflective to light. However, the extent of surface damage was less than that observed with the G' sizing system in the previous pultrusion trial discussed in section 3.1.

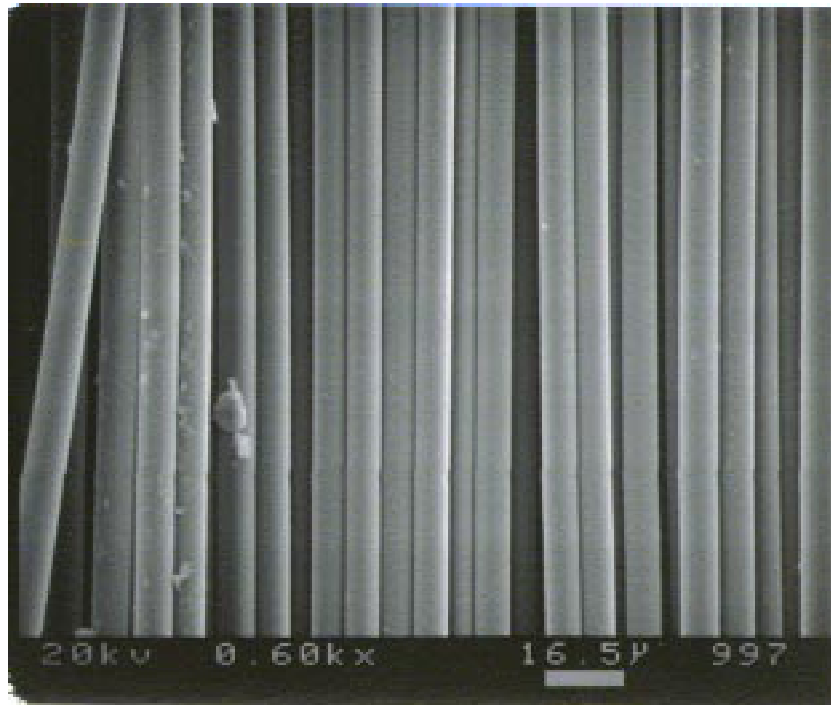


Figure 3.2-1 SEM of G' sized Hexcel carbon fiber. Magnification was 600X. Sizing level was 0.79wt%.

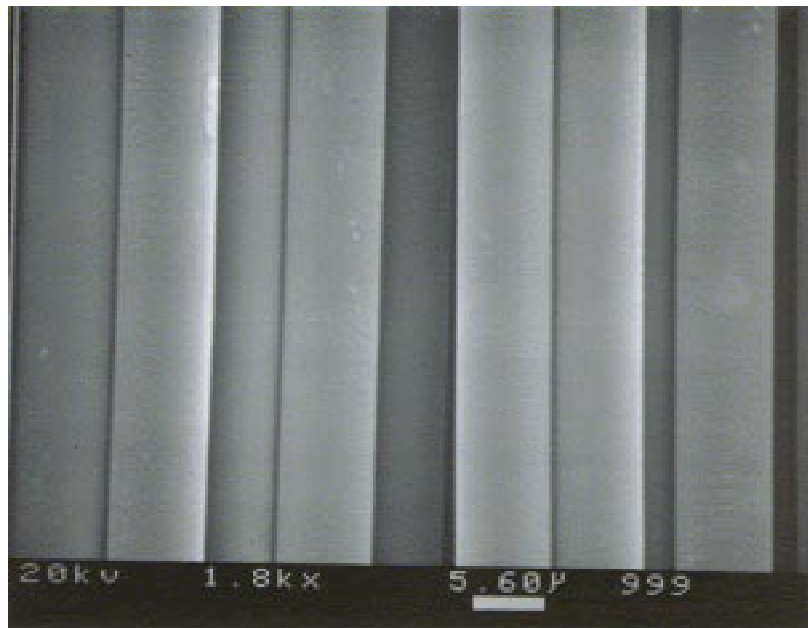


Figure 3.2-2 SEM of G' sized Hexcel carbon fiber. Magnification was 1,800X. Sizing level was 0.79wt%.

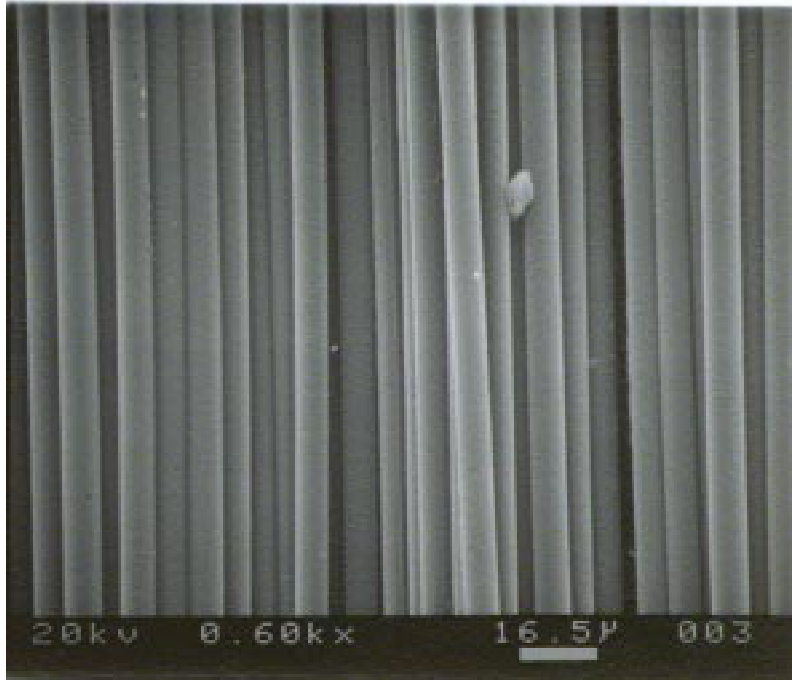


Figure 3.2-3 K-30 PVP sized Hexcel AS-4 12k carbon fiber. Magnification was 600X. Sizing level was 0.92 ± 0.06 wt%.

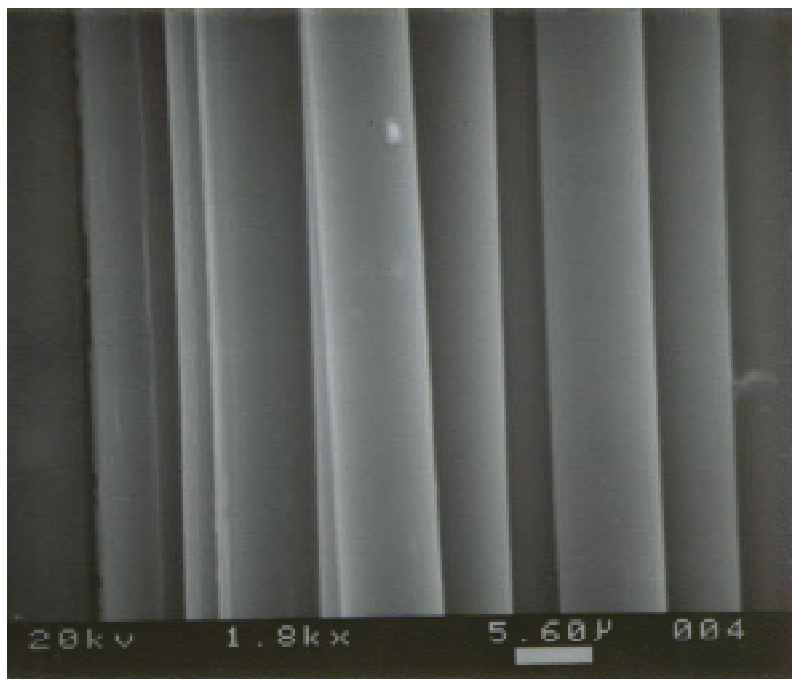


Figure 3.2-4 K-30 PVP sized Hexcel AS-4 12k carbon fiber. Magnification was 1,800X. Sizing level was 0.92 ± 0.06 wt%.

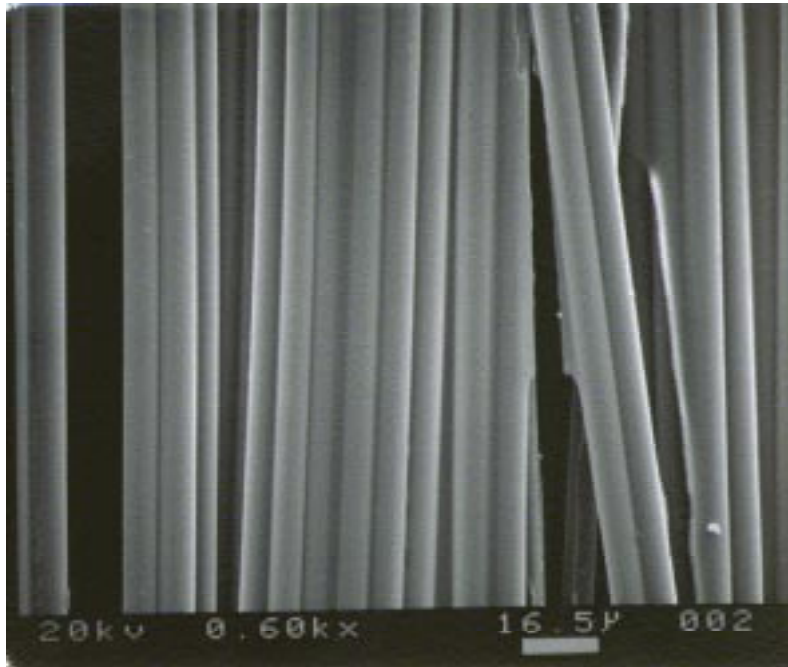


Figure 3.2-5 K-90 PVP sized Hexcel AS-4 12k carbon fiber. Magnification was 600X. Sizing level was 0.99 ± 0.19 wt%.

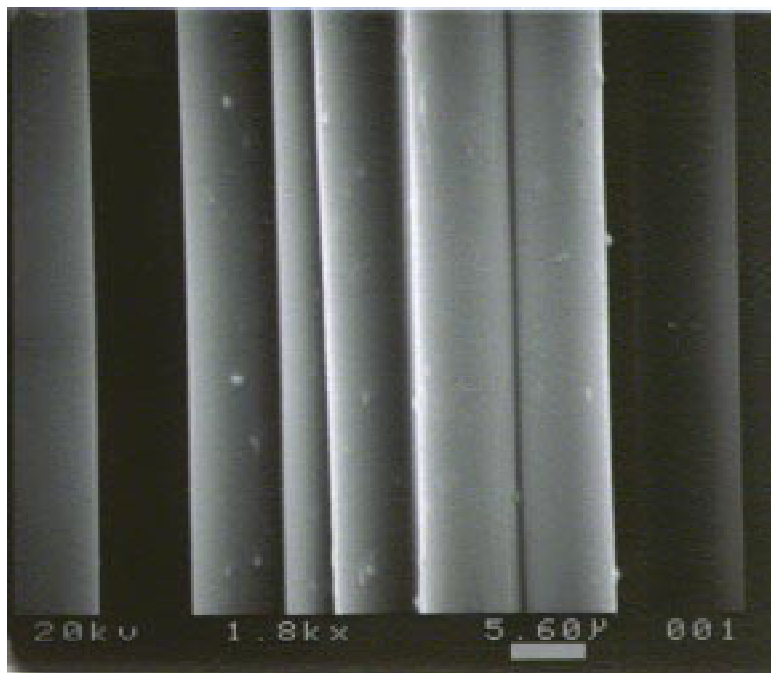


Figure 3.2-6 K-90 PVP sized Hexcel AS-4 12k carbon fiber. Magnification was 1,800X. Sizing level was 0.99 ± 0.19 wt%.

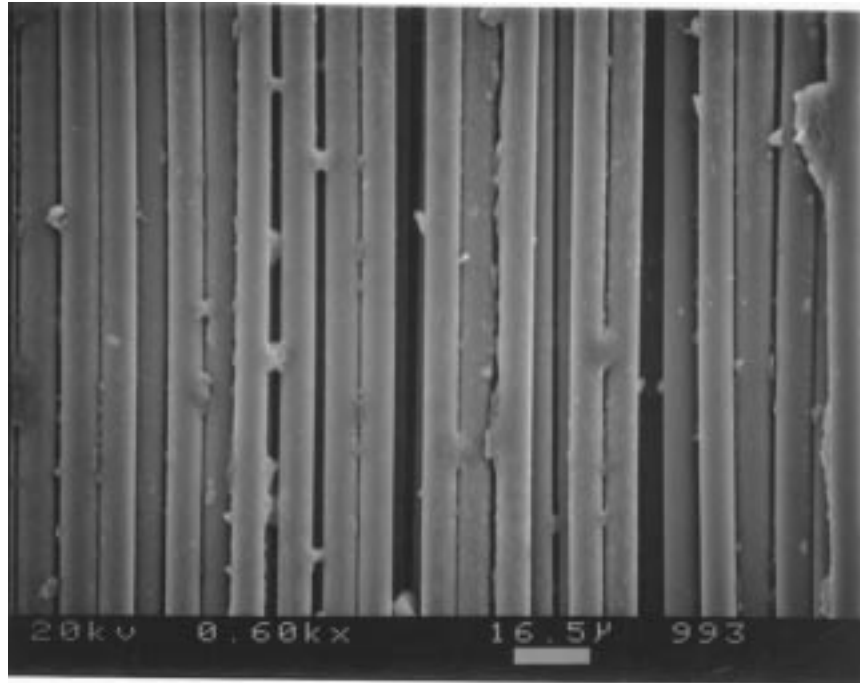


Figure 3.2-7 Phenoxy™ sized Hexcel AS-4 12k carbon fiber. Magnification was 600X. Sizing level was 0.89 ± 0.08 wt%.

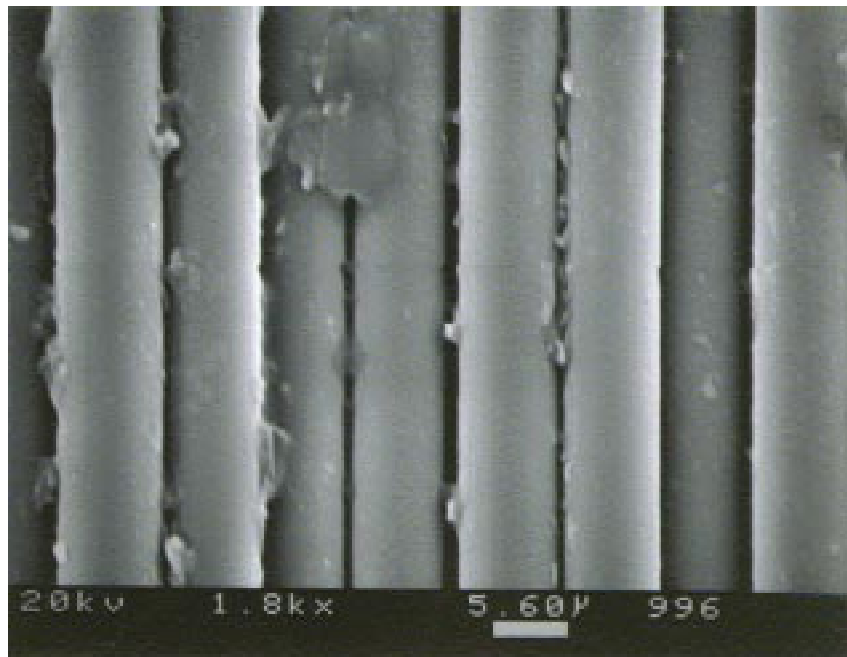


Figure 3.2-8 Phenoxy™ sized Hexcel AS-4 12k carbon fiber. Magnification was 1,800X. Sizing level was 0.89 ± 0.08 wt%.

The pultrusion of the K-30 PVP sized Hexcel carbon fiber was conducted on Day 2 of the trial (note: the days were not consecutive). Unfortunately, the low sizing level of 0.92 wt% K-30 PVP utilized for this trial was not sufficient to adequately protect the carbon fiber and damage did occur during the processing. However, the extent of damage was less than that observed in G' sizing system. The final composite surface finish was similar to that of the G' sized composite. The surface did not display extensive damage but was rough and non-reflective. The pull-force required to produce the K-30 PVP sized composite was not determined.

Also on Day 2, the K-90 PVP sizing system was pultruded. Again, the low K-90 PVP sizing level did not provide adequate protection for the brittle carbon fiber. The fiber was damaged during the processing step and the resulting composite reflected this damage. The final composite surface finish was dull and rough, which closely resembled the surface finish for the G' and K-30 PVP sized composites. The pull-force required to produce the K-90 PVP sized composite was approximately 280 ± 15 pounds, which was not significantly different than that of the G' sized composite.

Pultrusion of the Phenoxy™ sized carbon fiber was conducted on Day 3 of the trials. As discussed in section 3.1, the stiff nature of the Phenoxy™ sized fiber prevented the brittle fiber from being damaged during the processing steps. The carbon fiber fraying and build-up that was observed with the other sizing systems was not appreciably observed for the Phenoxy™ sizing system. The resulting composite surface finish was very glassy and smooth. There were no broken filaments or kink-bands presented on the Phenoxy™ sized composite. The pull-force required to produce the Phenoxy™ sized composite was approximately 80 ± 15 pounds which was considerably less than that required by the other sizing systems. The mechanisms responsible for this reduction in pull-force are unclear. However, the Phenoxy™ sizing was clearly lubricating the surface of the composite thus reducing friction and its associated damage. In addition, the Phenoxy™ sizing could be distributing the filler particles differently within the composite, which will drastically affect pull-force and surface quality. A summary of the required pull-force versus sizing system can be found in Figure 3.2-9.

3.2.4.2 Composite Characterization

3.2.4.2.1 Fiber Volume Fraction

The theoretical composite fiber volume fraction was computed for all six fiber systems (G', K-30, K-90, Phenoxy™ 52 ends, Phenoxy™ 53 ends, and Phenoxy™ 54 ends). Utilizing equation (3-2) and the corresponding G' sized AS-4 linear density (Table 3-1) and fiber density ($\rho_f = 1.78 \text{ g/cm}^3$), the G' sized AS-4 composite had a theoretical fiber volume fraction of approximately 59.2%. Utilizing equation (3-2) and the corresponding unsized AS-4 linear density (Table 3-1) and fiber density ($\rho_f = 1.78 \text{ g/cm}^3$), the thermoplastic sized AS-4 composites had the following theoretical fiber volume fractions. The K-30 PVP, K-90 PVP, and Phenoxy™ 52 ends all had theoretical fiber volume fractions of 60.3%. The Phenoxy™ 53 and Phenoxy™ 54 had theoretical fiber volume fractions of 61.5% and 62.7%, respectively.

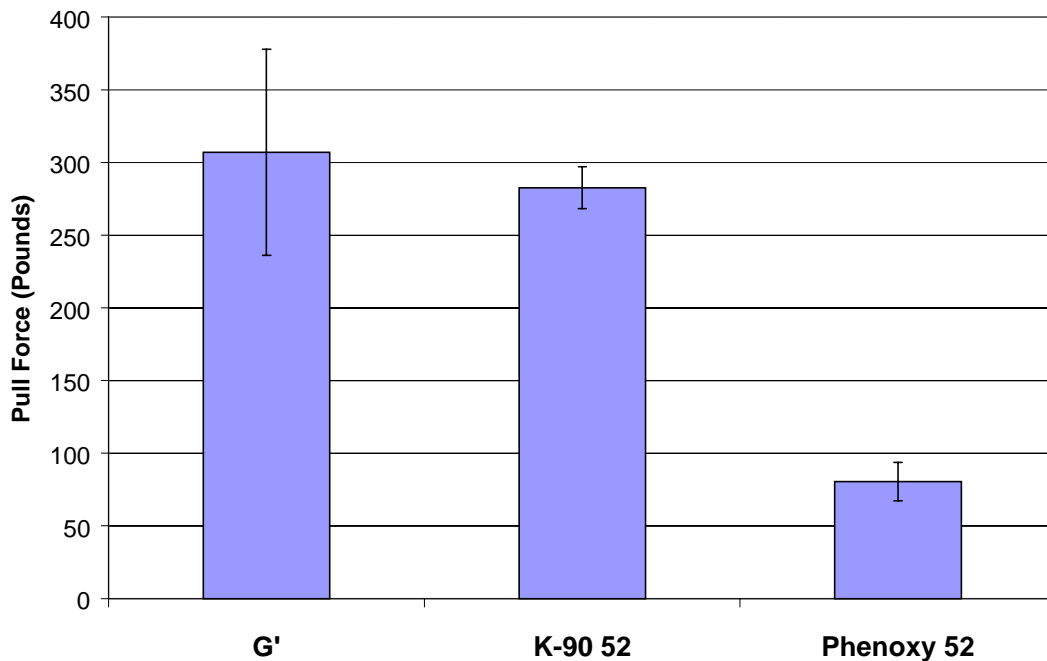


Figure 3.2-9 Pull-force required to produce composite of 15mm X 3mm cross-section for various sizing materials. K-90 PVP 52 represents a composite produced from 52 ends of fiber sized with K-90 PVP. Phenoxy 52 represents a composite produced from 52 ends of fiber sized with Phenoxy™.

The experimental composite fiber volume fraction was computed for all six fiber systems (Figure 3.2-10). In addition, the filler weight fraction in the resin excluding the fiber fraction was determined (Figure 3.2-11). The experimental fiber volume fractions were consistently higher than the theoretical fiber volume fractions. The reason for this discrepancy was the inability to accurately measure the composite cross-sectional area, A_c , utilized in equation (3-2). The die cross-sectional area of 42.88mm^2 was corrected for an **assumed** matrix shrinkage of 7%, a filler weight fraction in the matrix of 0.089, and a fiber volume fraction of 60% to give a final composite cross-sectional area of 41.68mm^2 . Therefore, the assumptions utilized in the calculation of the final composite cross-sectional area compromised the values calculated for the theoretical fiber volume fraction.

The experimentally determined filler content in the resin was considerably greater than the filler content in the original resin (Figure 3.2-11). This suggested that the filler was being preferentially included in the composite, which is believed to be something that has not been

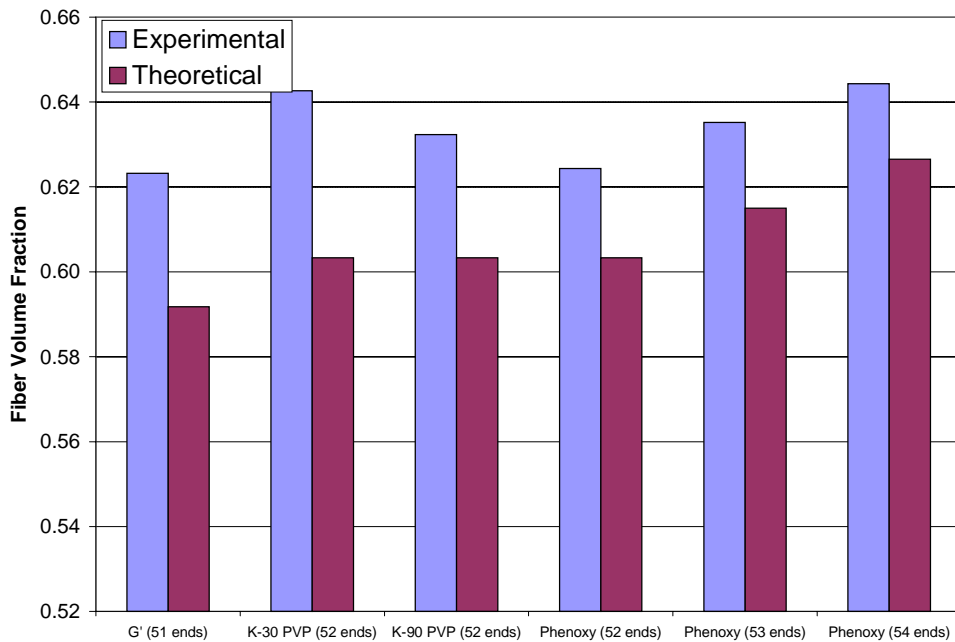


Figure 3.2-10 Theoretical and experimental fiber volume fraction for the various sizings. No error bars were determined for the experimental fiber volume fractions due to a lack of data points.

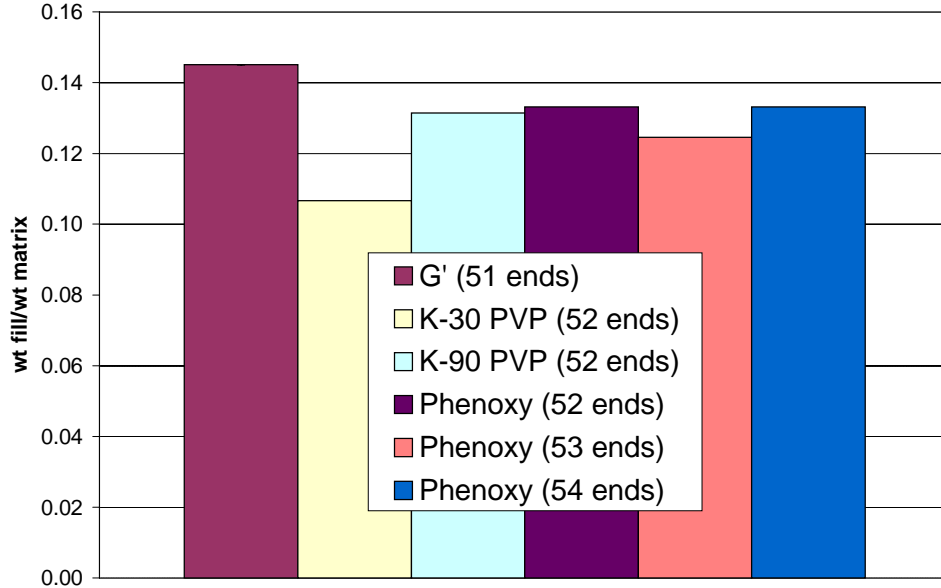


Figure 3.2-11 Filler weight fraction in the matrix (note: carbon fiber constituent has been removed to determine extent of filler inclusion in the composite as compared to the virgin matrix. The filler weight fraction in the virgin matrix was 0.089. No standard deviations were determined for the experimental fiber volume fractions due to a lack of data points.

established before in the pultrusion industry. The mechanism responsible for this preferential inclusion was the filtering of the filler as the excess resin was squeezed from the internal portions of the tow. In the dip bath, the filament/filament and tow/tow separation was large and easily allowed the resin and filler to penetrate. As the filaments and tows were brought closer together in the preforming portion of the pultrusion process, the excess resin was squeezed-out and a portion of the filler was filtered-out by the filaments.

As a function of the sizing constituent, the G' sizing material was most prolific at trapping filler with a filler content of 0.153 compared to the 0.089 existing in the virgin resin. The thermoplastic sized carbon fibers were not as efficient at filtering the filler with the filler content averaging 0.125. The K-30 PVP was least efficient at filtering the filler with a final filler content of 0.107.

The consequences of having a larger filler content are numerous. First, a higher filler content will alter the matrix properties and thus affect composite performance. Second, a higher filler content will in general lower the pull force required to produce a given cross-section as has

been established by this author in a recent pultrusion trial that is not discussed in this thesis. Third, because most dip-bath pultrusion operations continuously recycle the resin that is squeezed-out by the preforming process, the dip-bath can become deficient in filler as time progresses (Note: For this pultrusion trial, a fresh batch of resin was utilized for each sizing system). Fourth, the filler affects the surface quality of the final pultruded composite. Finally, a higher filler content will lower the matrix cure shrinkage. These effects of variable filler content on processability and composite properties cannot be easily established.

3.2.4.3 Mechanical Testing

3.2.4.3.1 Longitudinal Flexure Properties

As was discussed in section 3.1, the geometry and load placement of the longitudinal flexure test was such that the top of the specimen was exposed to compressive forces while the bottom was exposed to tensile forces while interlaminar shear was minimized. Therefore, this property can be considered on-axis and should not depend heavily on fiber/matrix adhesion as long as a minimum level of adhesion is present. The specimen span length was set such that failure occurred in tension on the bottom of the specimen and compression on the top. In the results that follow, the failure mode was a mixture of both compressive and tensile. The longitudinal flexure strengths for the thermoplastic sized composites were **at least 8%** higher than that for the standard G' sizing (Figure 3.2-12). The K-30 PVP and Phenoxy™ sized composite had statistically the same longitudinal flexure strength at a value of 1700 ± 120 MPa, which was considerably better than the 1500 ± 120 MPa observed in the G' sizing system. However, the improvement in longitudinal flexure strength between the thermoplastic sized and G' sized composites was less than that observed in section 3.1. There are several possible explanations for the reduced level of improvement. First, the fiber volume fractions between the G' and thermoplastic sized composites was considerably more consistent in the present trial. As was discussed in the introductory section to this chapter, for the first pultrusion trial, the G' fiber volume fraction was considerably higher than that utilized for the thermoplastic sized composites. The additional G' fiber volume fraction could have partially contributed to the increased composite surface damage observed in the first trial. In section 3.1, it was hypothesized that composite surface damage (caused by both inferior G' fiber protection and to a

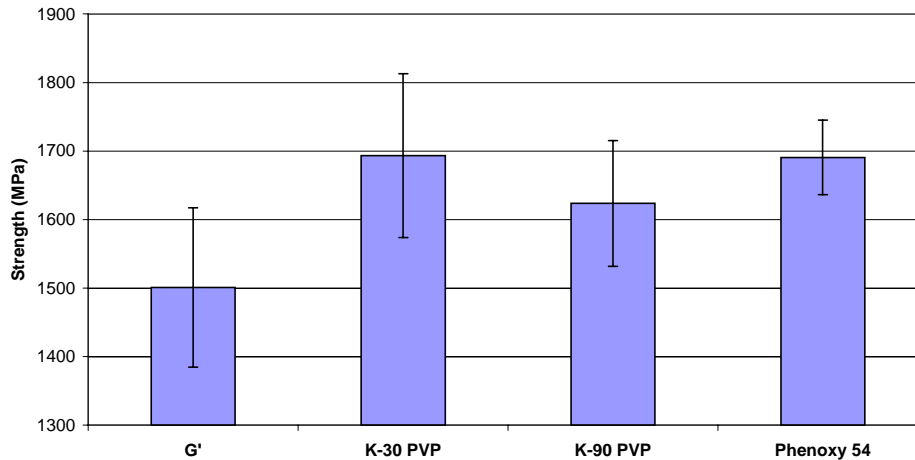


Figure 3.2-12 Longitudinal flexure strength of the pultruded Hexcel carbon fiber/vinyl-ester composites with various sizing agents. The strengths were normalized for variations in fiber volume fraction utilizing the value for the theoretical fiber volume fraction. Values shown are for a theoretical composite having a 59.2% fiber volume fraction.

lessor extent, the additional G' composite fiber volume fraction) was largely responsible for the improvements in performance discussed in section 3.1. Because the fiber volume fraction was more consistent in the present trial, the additional fiber damage caused by inherent differences in fiber volume fraction have been eliminated. Second, a lower sizing level (≈ 0.9 wt%) was utilized for the present trial compared to the previous trial (≈ 2.0 wt%). This resulted in the thermoplastic sized fibers having less protective material surrounding the fibers and making them more susceptible to damage. The lower level of coating could have resulted in incomplete coverage of the fiber surface thus reducing fiber/matrix adhesion. In addition, the interphase mechanical property profile will be altered thus effecting damage initiation and propagation in the composite. Third, the composite cross-section produced in the present trial was considerably larger than the cross-section produced in the previous trial. This reduced the effect of surface damage and fiber protection due to a reduction in the composite surface area to volume ratio. Finally, the matrix utilized in the present trial had approximately $\frac{1}{2}$ the styrene amount contained in the matrix discussed in section 3.1. Therefore, the matrix utilized in the present trial had considerably less inherent shrinkage associated with its cure compared to the section 3.1 matrix. The cure shrinkage influences the residual stress present at the fiber/matrix/sizing interface which ultimately influences damage initiation and propagation in the composite. As will be

discussed more quantitatively in Chapter 5, a sizing forms an interphase region that has a different shrinkage than the pure matrix. Therefore, a sizing/interphase can influence composite performance through a reduction in cure shrinkage. Because the matrix in the present trial had less cure shrinkage associated with the virgin matrix, the magnitude of a sizing's effect on matrix shrinkage and hence composite performance would be reduced from that observed in section 3.1.

The K-30 PVP outperformed the K-90 PVP sizing by approximately 4%, which was not statistically significant. The change in interphase properties between the K-30 and K-90 PVP systems was not enough to produce an effect on this property.

As was the case for the trial discussed in section 3.1, the longitudinal flexure modulus was found to be unaffected by the sizing constituent except for the case of the Phenoxy™ 54 end sizing system (Figure 3.2-13). The longitudinal flexure modulus for the Phenoxy™ 54 end system was 4% less than that observed in the other sizing systems. This 4% reduction was considerably less than the 13% gain in strength discussed previously.

3.2.4.3.2 Short Beam Shear Properties

As was the case in section 3.1, the geometry and load placement of the short beam shear test was conducted such that interlaminar shear was maximized at the specimen mid-section while minimizing tensile and compressive loads on the bottom and top respectively. Due to the shearing nature of the forces, the short beam shear (SBS) strength will be very sensitive to alterations in ISS and hence fiber/matrix adhesion. The cross-sectional area of the test specimens was selected such that failure occurred in shear at the midplane of the specimen. SBS testing showed that the thermoplastic sized composites outperformed the G' by **at least 15%** (Figure 3.2-14). The Phenoxy™ 52 ends had the best overall performance with a strength value of 68.2 MPa. The thermoplastic sizings again did not show the same level of performance enhancement that was observed in section 3.1. The reasons are again believed to be the same as the ones discussed in the longitudinal flexure section. However, the variables affecting fiber/matrix adhesion will be more significant in affecting this on-axis property. These include incomplete sizing coverage on the fiber and a reduction in the effect of matrix shrinkage discussed earlier.

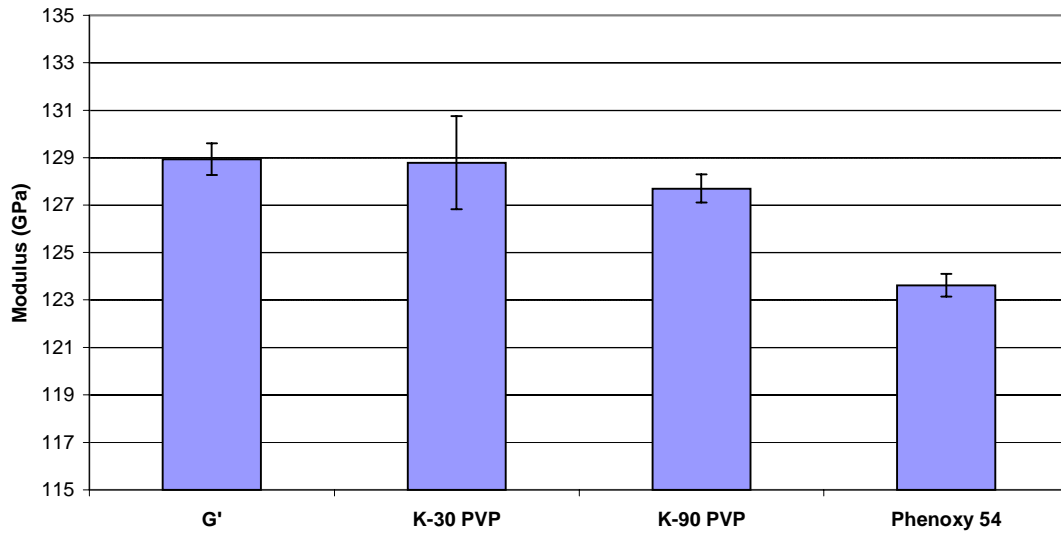


Figure 3.2-13 Longitudinal flexure modulus of the pultruded Hexcel carbon fiber/vinyl-ester composites with various sizing agents. The moduli were normalized for variations in fiber volume fraction utilizing the value for the theoretical fiber volume fraction. Values shown are for a theoretical composite having a 59.2% fiber volume fraction.

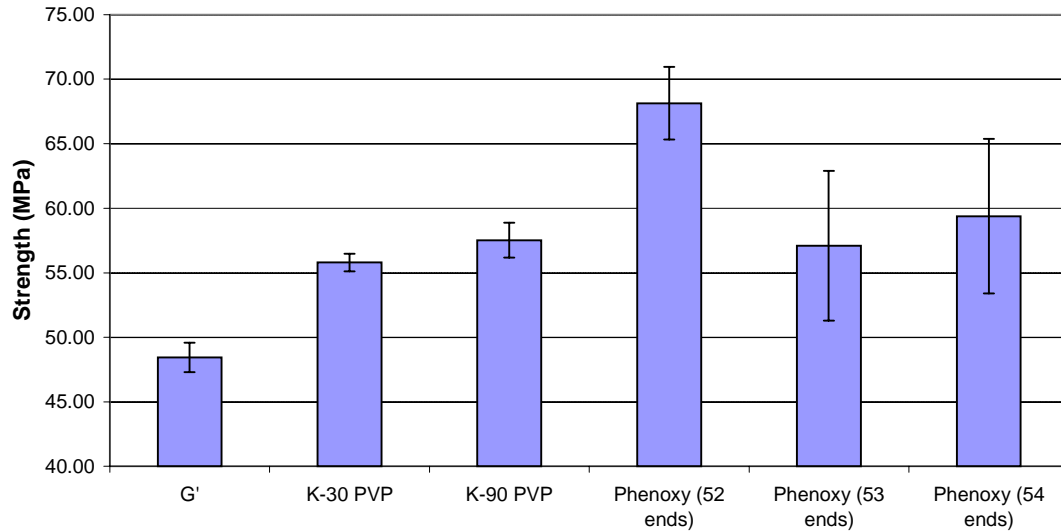


Figure 3.2-14 Short beam shear (SBS) strength of pultruded Hexcel carbon fiber/vinyl-ester composites with various sizing agents. The moduli were normalized for variations in fiber volume fraction utilizing the value for the theoretical fiber volume fraction. Values shown are for a theoretical composite having a 59.2% fiber volume fraction.

The difference in shear strength between the K-30 and K-90 sizing systems was again statistically insignificant. Therefore, the effect of altering the interphase profile did not significantly affect this property.

3.2.5 Conclusions

Despite the reduced level of improvement, the thermoplastic sizings still offered numerous processing and mechanical performance advantages over the traditionally utilized G'. As was the case in section 3.1, the Phenoxy™ sizing had improved processability over the traditionally utilized G' sizing material. These improvements in processability translated into improvements in final composite surface finish and quality. In addition, the pull-force required to pultrude the Phenoxy™ sized carbon fiber was approximately ½ of that required for all the other sizing materials. The K-30 and K-90 PVP sizing materials did not offer the same fiber protection observed with the Phenoxy™ system, which was contrary to the observations made in section 3.1 for the K-90 PVP system. The lower K-90 PVP sizing level utilized in the present trial was believed to be the main reason for the poorer processability of this sized fiber.

The static mechanical properties of the composites produced from the thermoplastic sizings were higher than those of the composites produced from the standard G' sizing. All of the thermoplastic sized composites outperformed the standard sizing G' by at least 8% in longitudinal flexure strength and by at least 15% in short beam shear strength.

These improvements in static mechanical performance are considerably less than those observed in the previous pultrusion trial discussed in section 3.1 where 30% improvements in flexure strength and 50% improvements in SBS strength were observed. There are several possible explanations for the reduced level of improvement. These include a reduced level of fiber protection, a reduction in composite surface damage due to more consistent fiber volume fractions, a reduction in composite surface area to volume ratio, a reduction in inherent matrix shrinkage, and alterations in interphase properties.

For the longitudinal flexure and short beam shear properties investigated in this section, the effect of alterations in interphase mechanical property profile were found to be insignificant for the case of K-90 and K-30 PVP sizing systems. This does not imply that the interphase does not affect the longitudinal flexure and shear strength properties but does imply the variation developed in the K-90 and K-30 PVP sizing systems was not large enough to produce an effect.

3.2.6 Acknowledgments

This work was sponsored in part by the National Science Foundation Science and Technology Center for High Performance Polymeric Adhesives and Composites (NSF grant # DMR-9120004). In addition, financial support was provided by the Adhesives and Sealant Council Educational Foundation (ASCEF) through the Center for Adhesives and Sealant Science (CASS) at Virginia Tech. Financial support was also provided by the Virginia Space Grant Consortium. Pultrusion access was provided by the Dow Chemical Company and their assistance is gratefully acknowledged. In particular, Mr. Herbert Engelen completed the pultrusion of the thermoplastic materials discussed in this section. Mr. Engelen's commentary on the processability of the various fibers formed the foundation for the material discussed in section 3.2.4.1.2. Material contributions from Phenoxy Associates and BASF are acknowledged.

In the next section, a modified version of a paper published in the ANTEC '98 preprint is presented. The overall objective of the material presented in section 3.3 was to determine whether the traditionally utilized Hexcel carbon fibers sized with G' could be replaced with the cheaper Zoltek Panex materials sized with our thermoplastic sizings without compromising composite compressive performance.

3.3 Static Compressive Performance of Pultruded Carbon Fiber/Vinyl Ester Composites Processed with Physically Dissimilar Sizing Agents

3.3.1 Abstract

Zoltek Panex 48K carbon fibers were sized with three dissimilar polymeric materials. The sizing agents tested were K-30 poly(vinylpyrrolidone), Phenoxy™, and a BASF Sancure™ poly(urethane). In addition, Zoltek Panex 48K carbon fibers sized commercially with Z' and Hexcel AS-4 12K carbon fibers sized commercially with G' were tested. The sized carbon fibers were processed into composites utilizing a pilot scale pultruder and a pultrudable vinyl-ester resin.

Composites produced from the Panex 48K carbon fibers sized with poly(urethane) had a compressive strength of 750 ± 50 MPa compared to the 660 ± 50 MPa observed with the composites produced from the Hexcel AS-4 12K G' fiber. This result was surprising considering the inherent lower properties of the 48K carbon fibers compared to the 12K fibers. The compressive modulus was found to correlate with the fiber properties and was not a function of the sizing constituent.

3.3.2 Introduction

Carbon fiber composites have typically been used in high-end aerospace applications. In order for these composites to find acceptance in civilian markets like infrastructure and high-speed civil transportation, the cost of the processing steps and raw materials must be reduced while maintaining or improving their performance.

Pultrusion represents the most cost-effective means of rapidly producing continuous fiber reinforced composites with a thermoset matrix. Since civilian markets often require uncomplicated parts of constant cross-section, pultrusion represents one of the most economical means of producing composites for these applications.

Thick section carbon fiber tow, such as Zoltek Panex 48K, have significant cost savings over the traditionally used fibers such as AS-4 12K. The two factors that are preventing the use of these cheaper fibers in many applications are their lower mechanical properties and their difficulty in processing.

Sizings, a thin polymer coating applied to the surface of the carbon fiber before impregnation with the matrix have been shown to effect the mechanical performance of the composite. Even a matrix dominated property like compressive strength can be affected by the sizing constituent. This suggests that properties could be maximized by optimizing the sizing constituent for the final composite application.

In the present work, the Designed Interphase Group at VPI has combined all of these cost saving/performance-enhancing aspects into a single all-inclusive (pultrusion, cheaper carbon fiber, and optimized sizings) study. The cheaper Zoltek Panex 48K carbon fibers were sized with agents optimized for the vinyl-ester matrix and comparisons were made with the more expensive AS-4 12K material sized with the standard G' sizing. Pultrusion was used to produce the composites to take advantage of the lower processing costs needed for industrial acceptance.

3.3.3 Experimental

3.3.3.1 Materials

The unsized Zoltek Panex 48K carbon fibers were donated by Zoltek Incorporated, St. Louis, MO. Zoltek also donated K-30 poly(vinylpyrrolidone) sized fiber. The Z' sized Zoltek Panex 48K utilized in this study was donated by Strongwell, Inc., Bristol, VA but was manufactured by Zoltek.

The G' sized AS-4 12K carbon fibers were donated by Strongwell but manufactured by Hercules Incorporated, Magna, UT. The material was supplied as a 36K intertwined bundle composed of three 12K tows.

The Phenoxy™ sizing material (PKHW-35 lot # 217013) (Figure 3.1-1.a) was obtained from Phenoxy Associates, Rock Hill, SC. This material was obtained as a 30wt% dispersion of approximately 1-micron diameter particles in 57wt% water [3.13]. The balance of the suspension contained 10 wt% of a cosolvent, butoxyethanol, and 3wt% of a neautralant, dimethylethanolamine. In order to make the hydrophobic Phenoxy™ shown in Figure 3.1-1.a water dispersible, the commercially available Phenoxy™ suspension contained a modified version of the Phenoxy™ backbone shown in Figure 3.1-1.a. For approximately every ten repeat units, a carboxylic acid functional group had been grafted onto the chain [3.13]. The M_n of the Phenoxy™ was 19,000 g/mol (GPC) and it had a T_g of 97°C (DSC) [1.8].

The K-30 poly(vinylpyrrolidone) (PVP) sizing material (Figure 3.1.1.b) was obtained already sized on the Zoltek Panex 48K carbon fiber. The M_w of this material was 49,000 g/mol and it had a T_g of 168°C [3.14].

The poly(urethane) sizing material was obtained from the B. F. Goodrich Co. The precise chemical structure of this material was not known. This material was a polyester based polyurethane elastomer supplied as a 40 weight percent emulsion in water. Its M_n was 36,000 g/mol (GPC) and it had a soft segment T_g of -53°C [1.8].

The matrix/resin utilized for pultrusion was a modified Dow Derakane™ 411-35 vinyl-ester resin (Figure 3.1-1.c&d). The pultrudable resin was composed of *approximately* 42 wt% vinyl-ester, 42 wt% styrene monomer, 15 wt% clay, 0.5 wt% release agents, and 0.5 wt% of a proprietary initiator package. The same resin batch was utilized for all the experimental work presented in this section.

3.3.3.2 Sized Fiber Preparation (discussed earlier in section 3.1.3.2.2)

Fibers were sized on a custom made small scale sizing line [1.6,1.9]. Carbon fiber tow was pulled off a spool at a set speed ranging from 0.3 to 6.0 cm/sec. The fibers were put under tension by a nip roller connected to a particle brake in the range of 0 to 110 N. The fibers were then passed through the sizing solution where capillary forces provided the driving force for rapid tow wetting. The high fiber tension and extensive use of rollers after the sizing bath spread the tow bundle and also prevented the wet tow from clumping. The spread carbon fiber tow containing the sizing solution was dried online in an IR forced convection dryer.

The emitter surface temperature of the two IR heating panels embedded in the dryer was controllable from ambient temperature up to 500°C. The inlet air temperature was controlled at ambient conditions. The emitter surface temperature directly controlled the surface temperature of the carbon fiber. The surface temperature of the fiber was measured by a hand held thermocouple. A time temperature profile was generated by placing the thermocouple on the fiber surface at various positions in the IR dryer.

The fiber that exited the dryer was pulled through a motorized nip roller where line speed was controlled and line tension was developed. The fiber was then wound onto a standard carbon fiber spool utilizing a constant tension Izumi rewinder. The fibers were then sealed in a plastic bag to prevent moisture from being re-absorbed by the sizing material or the carbon fiber.

3.3.3.3 Pultrusion

Pultrusion was performed by Strongwell, Inc. of Bristol, VA utilizing their pilot scale pultruder. Approximately 7 spools of the Zoltek Panex 48K material were placed in the creel rack for its processing. Approximately 12 spools of the AS-4 12K material supplied as a 36K intertwined bundle were placed in the creel rack for its processing. The individual tows were directed into the process via a board of perforated Teflon. The fibers were then dipped in the resin bath where the fibers were fully wetted with the resin. After the fibers were pre-formed, they were cured in a die of rectangular cross section. The dimension of the final composite part was 12.7mm wide by 2.0mm thick by 15.24m long.

3.3.3.4 Material Testing

The amount of sizing deposited on the carbon fiber was determined via pyrolysis in a nitrogen atmosphere. Approximately 8 grams of sized carbon fiber were used for the analysis. The fibers were first dried in a convection oven for a period of eight hours. The temperature of the convection oven was set above the T_g of the particular sizing material being tested. After being dried, the fibers were placed in a high temperature Blue-M furnace with a nitrogen purge at a flow rate of approximately $40 \text{ cm}^3/\text{sec}$. The fibers were pyrolyzed at 600°C for 30 minutes. In all cases, the pyrolysis cycle was found to be sufficient to completely volatilize the sizing while leaving the fiber unaffected. The amount of sizing material was computed from the differences in mass of the dry sized fiber and the pyrolyzed fiber.

$$S = 100 \cdot \frac{(M_1 - M_2)}{M_1} \quad (3-1)$$

where S was the weight percent of sizing on the fiber, M_1 was the dry sized fiber mass, and M_2 was the pyrolyzed fiber mass.

The quality of the sized fiber was determined by inspection of the fibers under Scanning Electron Microscopy. The fibers were secured on a standard ESCA mount. The fibers were sputter coated with gold for approximately 2 minutes. Analysis was conducted in an International Scientific Instruments Model SX-40 SEM.

The fiber volume fractions of the composite panels produced in these experiments were determined by Strongwell. The method utilized for this determination is not known.

Static compression tests were completed on the pultruded materials utilizing the IITRI (Illinois Institute of Technology Research Institute) test fixture in accordance with ASTM D 3410. These tests were completed by Dr. Nikhil Verghese.

3.3.4 Results and Discussion

3.3.4.1 Pultrusion

Pultrusion produced composites with fiber volume fractions that ranged from 59.5 to 73.3% [3.18]. However, all the fiber/sizing systems excluding Zoltek Panex 48K sized with K-30 PVP produced consistent fiber volume fractions that ranged from 59.5 to 62.3%. Therefore, the mechanical property results presented in this paper were comparable between fiber/sizing systems without any normalization because the fiber volume fractions were similar. The results for the Zoltek Panex 48K fiber sized with K-30 PVP must be viewed with caution considering the low sizing level and unusually high fiber volume fractions.

3.3.4.2 Static Compressive Properties

Static compressive performance for the pultruded composites was evaluated for all the fiber/sizing systems except Zoltek Panex 48K fiber sized with Z' (Table 3-6, Figure 3.3-1 & Figure 3.3-2). The results showed that the static compressive strength of the composites produced from the Zoltek Panex 48K fiber sized with poly(urethane) were 10% higher than any of the other fiber/sizing combinations. The static compressive strength of this poly(urethane) sized system was 745 ± 40 MPa. The AS-4 12K material was consistently outperformed in compression by the Zoltek Panex 48K materials sized with the optimized sizings. The tensile strength and modulus of the AS-4 12K *fiber* are higher and more uniform (i.e. lower standard deviation on strength and modulus) than those of the Zoltek Panex 48K *fiber*. Therefore, the higher properties observed within the Zoltek Panex 48K composite systems were most likely caused by alterations in processability, fiber/matrix adhesion, or damage evolution as a result of the formation of an interphase region. The compressive strength seemed to be more highly dependent upon the nature of the sizing agent. The much lower compressive strength observed in the composites produced from Zoltek Panex 48K fiber sized with K-30 PVP was a result of the low amount of sizing available on the fiber (0.3 wt%). The K-30 PVP fiber system could

Table 3-6 Material testing results for various fiber/sizing systems.

Fiber/Sizing System	Compressive Strength (MPa)	Compressive Modulus (GPa)	Sizing Level (wt%)	Fiber Volume Fraction
AS-4/G'	664 ± 43	1.75 ± 0.24	NA	59.8%
Panex/Z'	NA	NA	NA	62.3%
Panex/poly(urethane)	745 ± 40	1.18 ± 0.04	1.5 ± 0.2%	60.0%
Panex/Phenoxy	674 ± 35	1.14 ± 0.03	1.1 ± 0.2%	59.5%
Panex/K-30 PVP	657 ± 23	1.14 ± 0.04	0.3 ± 0.2%	73.3%

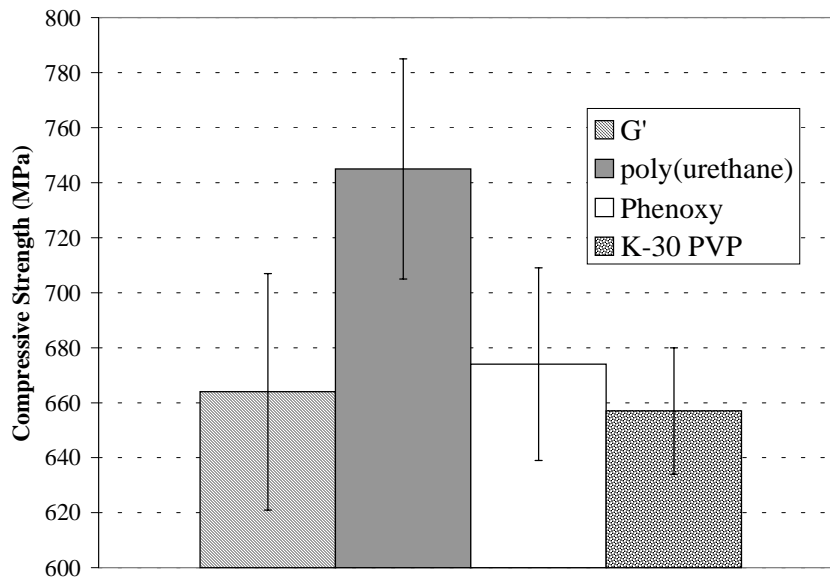


Figure 3.3-1 Static compressive strength of pultruded vinyl-ester composite with the following carbon fiber reinforcements. G' sized Hexcel AS-4, poly(urethane) sized Zoltek Panex, and K-30 PVP sized Zoltek Panex. Note: Data **not** normalized for fiber volume fraction variations.

have been more accurately described as unsized. As a result, the compressive strength was the lowest at a value of 657 ± 23 MPa.

The compressive moduli of the various combinations of fiber and sizing did not depend on the type of sizing agent (Figure 3.3-2). The compressive moduli appeared to be a function of the fiber type only. This was in contrast to the strength where it was observed that the sizing agent played a very important role. The inherently higher tensile modulus of the AS-4 12K *fiber* resulted in a composite of higher compressive modulus.

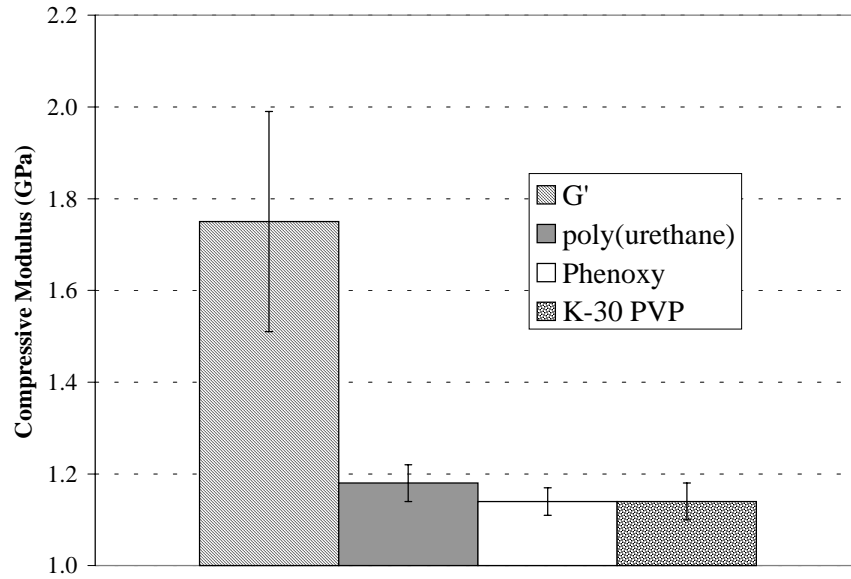


Figure 3.3-2 Static compressive modulus of pultruded vinyl-ester composite with the following carbon fiber reinforcements. G' sized Hexcel AS-4, poly(urethane) sized Zoltek Panex, and K-30 PVP sized Zoltek Panex. Note: Data **not** normalized for fiber volume fraction variations.

3.3.5 Conclusions

Composites produced from the 48K carbon fibers sized with poly(urethane) had a compressive strength of 750 ± 50 MPa compared to the 660 ± 50 MPa observed with the composites produced from the AS-4 12K G' fiber. This result was surprising considering the inherent lower properties of the 48K carbon fibers compared to the 12K fibers. This suggests that significant improvements in fiber processability and/or improvements in fiber/matrix adhesion were obtained with the poly(urethane) sizing material compared to the commercial G'. The compressive strength was found to strongly correlate with the sizing constituent. The compressive moduli was found to correlate with the fiber type and not with the sizing constituent.

The results obtained in the study suggest that the performance of carbon fiber vinyl-ester composites processed by pultrusion are significantly effected by the physical nature of the sizing agent present. They also suggest that cheaper fibers might replace existing ones in applications involving compression if the sizing agent is optimized.

3.3.6 Acknowledgments

This work was sponsored in part by the National Science Foundation Science and Technology Center for High Performance Polymeric Adhesives and Composites (NSF grant # DMR-9120004). Pultrusion access was provided by Strongwell, Inc. and their assistance is gratefully acknowledged. Material contributions from Dow Chemical, Zoltek, Phenoxo Associates, and BF Goodrich are acknowledged.

This concludes section 3.3 of this chapter. In the next section, an overall summary of the work presented in chapter 3 is presented.

3.4 Overall Summary

The work presented in this chapter reemphasizes the fact that the mechanical performance of carbon fiber/vinyl-ester composites is greatly influenced by the nature of the sizing agent present. In addition, the effect that the sizing has on the processability of the carbon fiber cannot be over-emphasized.

1. The thermoplastic sized fibers are **stiff** when they need to be stiff and are **pliable** when they need to be pliable. This makes the carbon fiber less susceptible to damage during the pultrusion process. In addition, better fiber alignment is achieved with the stiffer fibers.
2. The compatibility of the thermoplastic sizing agents with the vinyl-ester matrix allows the matrix material to fully wet-out the internal confines of the carbon fiber tow.
3. The spread and tape-like thermoplastic sized fiber minimizes damage and also minimizes wet-out time due to a reduction in wet-out distance.
4. The Phenoxy™ sizing can reduce the pull-force required to produce the final composite by a factor of two in certain situations.

These processability improvements translated into a composite with improved surface finish and better fiber alignment (see section 3.1.4.1.2). In addition, the mechanical performance of the final composite was greatly affected by variations in the composite's sizing agent.

1. For the sizing level and composite cross-section investigated in section 3.1, all of the thermoplastic sized Hexcel AS-4 composites outperformed the standard G' sized Hexcel AS-4 by **at least 25%** in static tensile strength, by **at least 11%** in longitudinal flexure strength, and by **at least 30%** in short beam shear strength. The tensile and longitudinal flexure moduli were unaffected by the sizing.
2. For the sizing level and composite cross-section investigated in section 3.2, all of the thermoplastic sized Hexcel AS-4 composites outperformed the standard G' sized Hexcel AS-4 by **at least 8%** in longitudinal flexure strength and by **at least 15%** in short beam shear strength. The longitudinal flexure moduli were unaffected by the sizing. Alterations in the interphase concentration profile were found to not affect the longitudinal flexure properties for the K-30 and K-90 PVP sizing systems.

3. Composites produced from poly(urethane) sized Zoltek Panex 48K carbon fibers outperformed the standard G' sized Hexcel AS-4 12K carbon fibers by **14%** in static compressive strength which is surprising considering the inherent lower properties of the 48K carbon fibers compared to the 12K fibers. The compressive moduli was not affected by the sizing constituent and was only a function of the fiber type.

The results obtained between the three pultrusion trials are self consistent. The strength based properties are a strong function of the sizing constituent while the stiffness based properties, which are dominated by the fiber properties, are unaffected. Therefore, sizings cannot significantly alter the stiffness based properties of the composite, which is in agreement with the literature reviewed in Chapter 2.

The mechanical performance enhancements presented in this chapter were achieved by altering a 1-3 wt% feature on the surface of the carbon fiber reinforcement. This corresponds to a material that occupied less than 2 weight % in the final composite. Because these thermoplastic sizing materials are commercially available materials and because such a low amount of them is needed to greatly improve strength based mechanical properties and composite surface finish quality, these sizing materials would make excellent replacements for the standard oligomeric epoxies that are presently being utilized in pultrusion of carbon/vinyl-ester composites. The results also suggest that cheaper fibers such as the Zoltek Panex might replace the more expensive Hexcel AS-4 presently utilized in certain applications **if** the *thermoplastic sizings* are used instead of the *oligomeric epoxy sizings*.

The improvements in properties discussed in this chapter have been largely attributed to differences in the processability made through visually observing the pultrusion process. However, the degree to which processing effects are more significant than the other effects listed in the introduction still remains a mystery. From the data presented in this chapter and the theory presented in chapter 2, it is apparent that fiber/matrix adhesion is of utmost importance when off-axis properties such as short beam shear strength are being measured. As the composite cross-section becomes large, the role of fiber protection on composite performance (mainly on-axis performance) may become less important. However, fiber protection will always play a large role in determining pultrusion processing cost. A fiber with better protection and less breakage,

fuzzing, and fraying will require less operator involvement in the pultrusion process thus reducing cost.

3.5 References

- 3.1 D. Blacketter, D. Upadhyaya, T. King, and J. King, 'Evaluation of fiber surface treatment and sizing on the shear and transverse tensile strengths of carbon fiber-reinforced thermoset and thermoplastic matrix composites', *Polymer Composites*, **Vol. 14**, Number 5, pp. 430-436.
- 3.2 M. S. Madhukar and L. T. Drzal, 'Fiber-Matrix Adhesion and Its Effect on Composite Mechanical Properties: I. Inplane and Interlaminar Shear Behavior of Graphite/Epoxy Composites', *Journal of Composite Materials*, **Vol. 25**, 1991, pp. 932-957.
- 3.3 M. S. Madhukar and L. T. Drzal, 'Fiber-Matrix Adhesion and Its Effect on Composite Mechanical Properties: II. Longitudinal (0°) and Transverse (90°) Tensile and Flexure Behavior of Graphite/Epoxy Composites', *Journal of Composite Materials*, **Vol. 25**, 1991, pp. 958-991.
- 3.4 N. S. Broyles, K.N. E. Verghese, S. V. Davis, H. Li, R. M. Davis, J.J. Lesko, and J. S. Riffle, 'Fatigue performance of carbon fibre/vinyl ester composites: the effect of two dissimilar polymeric sizing agents', *Polymer*, **Vol.39**, Number 15, 1998, pp. 3417-3424.
- 3.5 K. L. Reifsnider, 'Modeling of the interphase in polymer-matrix composite material systems', *Composites*, **Volume 25**, Number 7, 1994, pp. 461-469.
- 3.6 A. S. Argon, "Fracture of Composites", *Treatise of Materials Science and Technology*, Vol. 1, 1972, Academic Press, New York.
- 3.7 N. A. Fleck and B. Budiansky, "Compressive failure in fiber composites due to microbuckling," IUTAM Symposium, Troy, New York, May 29-June1, 1990, 253-273.
- 3.8 P. M. Moran and C. F. Shih, "Kink band propagation and broadening in ductile matrix fiber composites: experiments and analysis," *International Journal of Solids and Structures*, Vol. 35, No.15, 1998, 1709-1722.
- 3.9 N. S. Broyles, R. C. Chan, and R. M. Davis, 'Sizing of carbon fibers with aqueous solutions of poly(vinyl pyrrolidone)', *Polymer*, Volume 39, Number 12, 1998, pp. 2607-2613.

- 3.10 H. L. Cox, *British Journal of Applied Physics*, **3**, 1952.
- 3.11 V. Rao and L. T. Drzal, 'The Dependence of Interfacial Shear Strength on Matrix and Interphase Properties', *Polymer Composites*, **Vol. 12**, No. 1, February, 1991, pp.48-56.
- 3.12 L. T. Drzal, 'The Effect of Polymeric Matrix Mechanical Properties on the Fiber-Matrix Interfacial Shear Strength', *Materials Science and Engineering*, A126, 1990, pp. 289-293.
- 3.13 Phenoxy Associates product literature.
- 3.14 Buhler, Volker, 'Kollidon: Polyvinylpyrrolidone for the Pharmaceutical Industry', BASF publication.
- 3.15 ASTM D790-95a "Standard test methods for flexural properties of unreinforced and reinforced plastics and electrical insulating materials".
- 3.16 ASTM D 2344-84
- 3.17 ASTM 3410/D 3410M-95 "Standard Test Method for Compressive Properties of Polymer Matrix Composite Materials with Unsupported Gage Section by Shear Loading".
- 3.18 Data supplied by Strongwell, Inc., Bristol, VA.

Chapter 4

Interphase Formation: Mass Transfer Model

4 Introduction

In this chapter, fundamental models will be used to predict the interphase composition as a function of a dissolution diffusion coefficient, sizing/matrix thermodynamic equilibrium, and/or a sizing relaxation/disentanglement rate. Before this task can be undertaken, the various phenomenological events involved in interphase formation must be enumerated along with reasonable assumptions used to simplify the analysis.

As was discussed in the introduction and literature review chapters, the sizing is physically or chemically bonded to the fiber surface [2.2]. After the matrix material penetrates the tow bundle in the dip bath, intimate contact is established between the sizing phase and the bulk matrix phase. At this point, the entangled sizing (below T_g in the dip bath) begins to swell with one of the matrix constituents and correspondingly relaxes if the thermodynamics are favorable [2.53]. As time progresses, a portion of the relaxed/swelled sizing will have a T_g equal to that of the processing environment. At that point, the relaxed polymer segments will disentangle and diffuse out into the bulk matrix. Therefore, the interdiffusion process can be broken down into four distinct stages [2.53]. First, a swelling stage, where the entangled sizing swells with the matrix material. Second, a relaxation stage, where the swelled sizing relaxes in the presence of the matrix material. Third, a disentanglement stage (if entanglements are present), where the sizing disentangles and is free for dissolution. Fourth, a dissolution stage, where the relaxed/ disentangled (if entanglements are present) sizing diffuses out into the bulk matrix phase.

During the proposal stage of this work, a fickian FEM model was developed that assumed that the first three stages occurred very rapidly compared to the dissolution stage. This allowed a thermodynamic equilibrium to be established between the relaxed sizing and the matrix. A dissolution diffusion coefficient that was assumed to be constant and not a function of concentration controlled the dissolution. As will be discussed in this chapter, a non-fickian FEM model has been developed to take into account flux controlled interdiffusion processes where the

rate of relaxation/disentanglement is similar to the rate of dissolution. In addition, the non-fickian FEM model allows the incorporation of a non-constant/concentration dependent dissolution diffusion coefficient, which replaces the constant dissolution diffusion coefficient requirement that existed with the earlier fickian FEM. The inclusion of a non-constant dissolution diffusion coefficient introduces non-linearities into the mass balance equation. The significance of these will be discussed later in this chapter.

Because the thickness of the sizing is small compared to the fiber-fiber separation (40nm compared to 1.6 μ m), the presence of this phase can be *neglected* for the interdiffusion process being investigated. The term *neglected* must be carefully defined as it pertains to this interdiffusion process. In reality, a concentration profile will exist within the thin sizing film. Therefore, a second continuity equation would need to be written for this phase and linked to the bulk matrix phase with a flux and essential boundary condition at the sizing/matrix interface. However, the accuracy of continuum based predictions of concentration profiles within thin films ($\sim 10 - 60$ nm) that are very close to attractive surfaces is not good. The best approach for predicting concentration profiles close to attractive surfaces like carbon fibers is based upon interaction energies. These methods have been utilized by other researchers to obtain the interphase concentration profiles that exist on the nanometer scale adjacent to the fiber surface. The interphase that exists within the 10 – 60 nm scale of the fiber/matrix interface is considered by this author to be characterizeable as interfacial and not interphasial. The effects of alterations in interfacial properties can be lumped into the interfacial shear strength (ISS) term discussed in Chapter 2. As was discussed in Chapter 2, the effect of interfacial modification and hence ISS on composite performance is well documented and not a subject under investigation in this chapter. What is not known is the effect of a graded interphase on the performance of composite materials. **In this work, a graded interphase is defined as one that has a profile length of similar order of magnitude to the fiber diameter.** In essence, the subject of this research is to predict interphases that form on the micron scale. As such, the concentration profile that exists within a thin sizing film is inconsequential to the larger interphase existing in the bulk matrix. As such, the presence of the sizing phase can be neglected in terms of finding a separate concentration profile within it. In other words, a separate continuity equation for the sizing phase does not need to be solved. The nanoscale thickness of the film makes its solution trivial. However, the constitutive properties of the sizing phase greatly affects the formation of the

interphase. The boundary condition at the fiber/matrix interface is controlled by the constitutive properties of the sizing phase. Every phenomenological event that occurs within the sizing phase can be taken into account by adjusting the boundary condition at the fiber/matrix interface. Therefore, the sizing phase is treated as a planer source that occupies no mass. In addition, the fact that the swollen/relaxed sizing phase represents a small mass percent (<5.0 wt%) of the entire solution domain allows the interdiffusion to be modeled approximately as a pseudo-binary diffusion process. Negligible changes in stoichiometry of the matrix reactants occurs as a result of preferentially absorption into the sizing film. However, certain species of matrix may be preferential included or excluded due to equilibrium considerations at the interface. For this work, it is assumed that the matrix constituents (vinyl-ester oligomer, styrene, fillers, and additives) move as one material body and do not preferentially separate. These facts and assumptions allow the interdiffusion to be modeled as pseudo-binary. Without this assumption, the problem becomes almost impossible to solve due to the lack of constitutive theories for the multi-component relative mass transfer flux as a function of local gradients in chemical potential.

In this work, we are modeling the interdiffusion of the sizing and matrix in a typical dip-bath pultrusion process. In processes of this type, the typical time for wet-out and interdiffusion is approximately 15 minutes at ambient conditions due to typical line speed and pultruder dip bath dimensions. The thermosetting resin is rapidly cured (<1 minute) in the pultrusion die. Thus, it can be safely assumed that the majority of the sizing/matrix interdiffusion occurs in the dip bath and negligible interdiffusion occurs in the pultruder die *as long as* certain conditions are met. If the temperature variation of the dissolution diffusion coefficient and the sizing/matrix solubility can be represented by an Arrhenius expression, then negligible diffusion takes place in the pultruder die as long as $(E_s + E_d/2)$ is less than $5300R$ (44 kJ/mol). The E_s and E_d are the activation energies for solubility and diffusion respectively and R is the gas constant (derivation shown in section 4.8). If the sizing solubility is considered constant and not a function of temperature, then the required activation energy for diffusion, E_d , must be less than approximately $10,600R$ (88 kJ/mol) for negligible diffusion in the die. For the case of K-90 PVP diffusing into a pure vinyl-ester oligomer, Lao and co-workers [4.1] approximated the activation energy for the mutual diffusion coefficient of this system as approximately 95 kJ/mol or $11,000R$. Therefore, the assumption of negligible diffusion in the die is marginally acceptable. However, the model developed in this chapter can also account for diffusion in the die IF the

temperature versus time profile in the die is generated and the cure kinetics of the pultrudable Derakane™ matrix can be obtained.

For the modeling work presented in this thesis, it is also assumed that the sizing and matrix mix with constant volume and with constant overall density, i.e. $\Delta V_{\text{mixing}} = 0$ and $\rho = \text{Constant}$. The accuracy of these assumptions depends greatly upon the nature of the sizing and the matrix reactants used. As will be shown in Chapter 5, the mixing of K-90 PVP and Derakane™ 441-400 is not ideal. The density variation for Derakane™ 441-400/K-90 PVP blends varied from 1.065 to 1.150 g/cc for blends concentrations that varied from 0.0 to 5.0 wt% K-90 PVP. However, this density variation is not significant enough to invalidate the assumption of constant overall density. In addition, the interdiffusion of sizing and matrix is assumed to take place in a stationary liquid without the presence of bulk flow. Because the sizing phase represents a small percentage of the actual solution domain, the presence of this phase can be neglected as was discussed earlier. As sizing diffuses into the solution domain, it is assumed that an equal volume of matrix diffuses in the opposite direction in order to conserve system volume. Because the sizing and matrix components are assumed to have approximately the same density, this implies a zero mass average velocity and the liquid can be considered stationary. This assumption allows the bulk flow term in the mass balance equation to be eliminated.

The final assumption utilized in the work presented in this chapter is that every fiber in the composite has an identical interphase profile. Because there are typically several thousand carbon fibers in a composite cross-section, it would be impossible to predict a distinct interphase profile for each fiber. Therefore, the modeling task is simplified by assuming that each fiber is identical and forms into a regularly spaced packing array.

In summary, the assumptions used in the modeling work in this chapter are as follows.

- The relative mass transfer flux for the relaxed sizing diffusing into the matrix is assumed to follow Fick's First Law with a non-constant/concentration dependent diffusion coefficient.
- Movement of boundary between relaxed phase and bulk phase is neglected. The sizing phase is neglected and is treated as a plane source that occupies no mass.
- Matrix and initiator behave as a single component (i.e. Pseudo-binary).
- The cure/reaction occurs **rapidly** and after the diffusion is complete.

- Constant overall volume and ρ which implies a stationary liquid (bulk flow term negligible).
- Every fiber in the composite is considered identical (discussed in Section 4.1).

The rest of this chapter is organized into the following sections.

- 4.1– Geometry of Interdiffusion Domain
- 4.2 – Mass Transfer Theory
- 4.3 – Analytical Model for Interphase Formation
- 4.4 – Finite Element Simulation of Interphase Formation
- 4.5 – Results of Non-Fickian FEM Applied to the Theoretical Composite
- 4.6 – Summary
- 4.7 – Diffusion in Pultruder Die
- 4.8 – References

4.1 Geometry of Interdiffusion Domain

Before fundamental models can be utilized to predict the interdiffusion of the sizing and the matrix, the geometry over which the diffusion takes place must be defined. A typical cross-section of a continuously reinforced carbon fiber polymer matrix composite shows the randomness of the fiber packing (Figure 4.1-1). If fundamental models were to be applied to

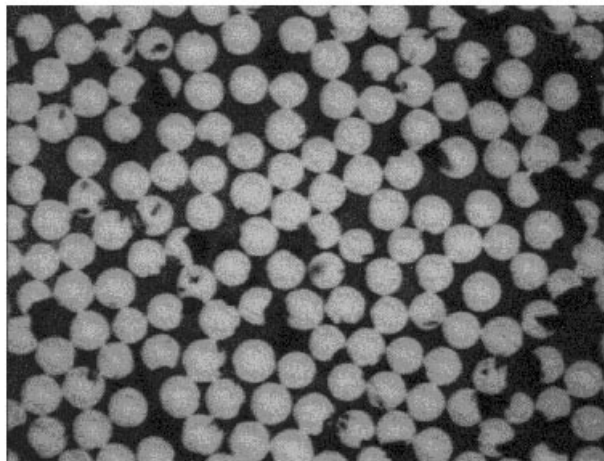


Figure 4.1-1 Optical Micrograph of a 65 volume % unidirectional pultruded Hexcel AS-4 G' carbon fiber/vinyl-ester composite cross-section

such a random arrangement, then the solution domain would be composed of an infinite number of fibers with distinct interphase profiles. The modeling effort would be greatly complicated by the fact that an infinite number of interphase profiles would have to be predicted. In modeling work of this type, it is customary to assume that the fibers arrange themselves into an ordered packing array. For instance, the hexagonal packing array has been used in previous work to simplify modeling efforts. In this work, it was decided that the hexagonal packing array would serve as the solution domain (Figure 4.1-2.a). With this assumption, each fiber in the composite has an identical interphase profile and modeling efforts are greatly simplified.

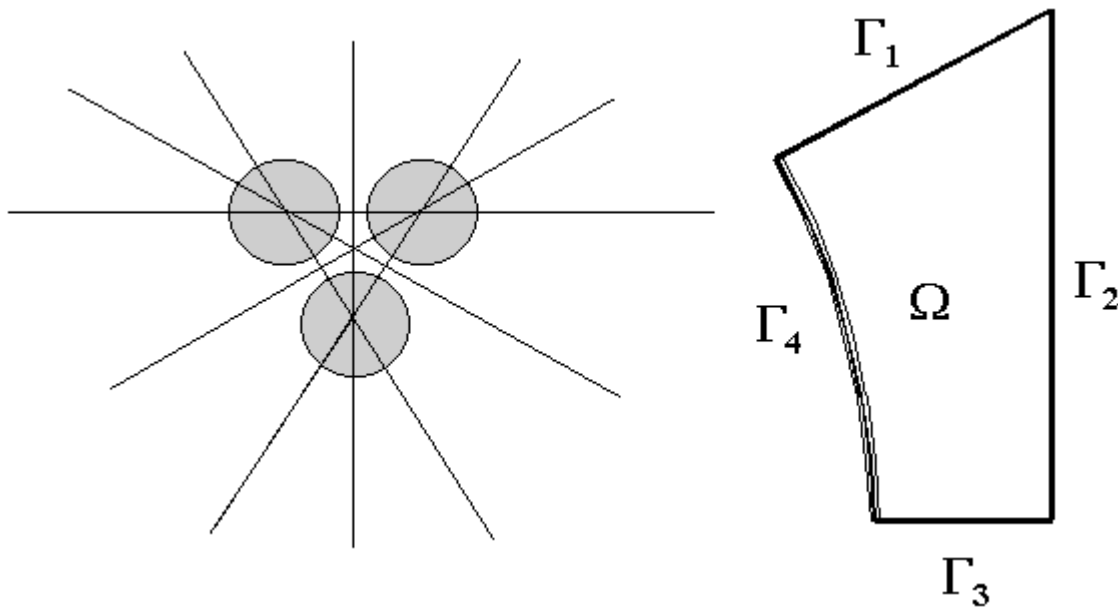


Figure 4.1-2 a.) Theoretical packing array: hexagonal packing array with lines drawn for the axis of symmetry b.) 60-30° triangular packing representing the fundamental unit of the theoretical composite.

The fundamental unit of an equally spaced hexagonal packing array is a 60°-30° right triangle with a circular section removed (Figure 4.1-2.b). The linear boundaries (Γ_1 , Γ_2 , and Γ_3) of this triangle represent axis of symmetry across which no mass is transferred. The lengths of these linear segments are related to the fiber volume fraction and fiber diameter by the following:

$$l_1 = R_f \left[2 \sqrt{\frac{\pi\sqrt{3}}{v_f} - 1} \right] \quad (4-1)$$

$$l_2 = R_f \left[\sqrt{\frac{\pi\sqrt{3}}{v_f}} \right] \quad (4-2)$$

$$l_3 = R_f \left[\sqrt{\frac{\pi\sqrt{3}}{6v_f} - 1} \right] \quad (4-3)$$

where R_f is the fiber radius and v_f is the composite fiber volume fraction. The circular arc (Γ_4) represents the sizing film. The length of the circular arc is the following:

$$l_4 = \frac{\pi}{6} R_f \quad (4-4)$$

The thickness of the sizing film, t_s , can be calculated from the sizing weight fraction by assuming the film is deposited in a homogeneous manner:

$$t_s = R_f \left(\sqrt{1 + \frac{\rho_f}{\rho_s} \left(\frac{1}{\omega_s} - 1 \right)} - 1 \right) \quad (4-5)$$

where ρ_f is the fiber density, ρ_s is the sizing density, and ω_s is the sizing weight fraction on the fiber surface.

At the beginning of the interdiffusion process, there exists two distinct phases. As was discussed in the introduction, the thickness of the sizing film allows for this phase to be neglected as long as the swelling diffusion coefficient is of similar or smaller magnitude than the dissolution diffusion coefficient. With the geometry of the solution domain being specified in this section, fundamental mass transfer theory can be utilized to accurately predict interphase composition.

4.2 Mass Transfer Theory

The equations governing the interdiffusion of the sizing/matrix under the assumptions discussed in the introduction will be presented in this section. The mass transfer theory utilized in this section was discussed in Chapter 2.

4.2.1 Governing Equations for Interphase Formation

For the case of binary Fickian diffusion with non-constant diffusion coefficient and the assumptions listed in the introduction to this chapter, equation (2.4) reduces to the following:

$$\frac{\partial \omega}{\partial t} = \nabla \cdot (D_d \nabla \omega) \quad (4-6)$$

where ω is the sizing weight fraction, D_d is the dissolution diffusion coefficient, t is the time, and ∇ is the gradient operator. Equation (4-6) is applicable to the bulk matrix phase where the relaxed/disentangled sizing is diffusing. This equation is utilized in the final non-fickian FEM code to compute the interphase concentration profile.

For the case of a constant dissolution diffusion coefficient, equation (4-6) reduces to the following:

$$\frac{\partial \omega}{\partial t} = D_d \nabla^2 \omega \quad (4-7)$$

The equation was utilized in proposal portion of this work to obtain approximate predictions of the interphase concentration profile.

4.2.1.1 Initial Condition

The applicable initial condition was that the solution domain contained no sizing initially.

$$\omega = 0.0 \quad (4-8)$$

4.2.1.2 Boundary Conditions

Two sets of boundary conditions apply to equations (4-6) and (4-7) either essential or natural/flux type. Along axis of symmetry, the prescribed sizing mass flux is zero. At the sizing/matrix interface, the boundary can be either essential or flux type depending upon the material properties of the sizing and the matrix. For the results presented in the proposal, the sizing was assumed to swell, relax, and disentangle instantaneously, thus establishing a thermodynamic equilibrium at the sizing/matrix interface. In addition, equation (4-7) was utilized to account for the fickian nature of the diffusion process. For the results presented in this chapter, the sizing/matrix interface can be successfully modeled with either thermodynamic equilibrium controlling and/or flux controlling. In addition, the results presented in this chapter account for the non-fickian diffusion process through application of equation (4-6).

The time required to completely dissolve the relaxed sizing material into the bulk matrix is called the dissolution time. Therefore, for times less than the dissolution time, the boundary condition at the sizing/matrix interface can be set equal to the thermodynamic equilibrium and/or a kinetically controlled flux. At times greater than the dissolution time, the boundary condition

at the sizing/matrix interface is of insulated flux type where the flux is set equal to zero sizing mass flux.

The time required for dissolution can be determined from the sizing weight fraction profile in the solution domain. Because the amount of sizing is known, the amount of sizing remaining on the surface of the fiber can be determined in two ways. The first is just a simple integration over the solution domain to determine the mass of sizing that has dissolved:

$$M_d = \rho \iiint_{\Omega} \omega d\Omega \quad (4-9)$$

where M_d is the dissolved sizing mass, ρ is the system density (assumed constant), ω is the sizing weight fraction, and Ω is the solution domain. When M_d is equal to the amount of sizing available on the fiber surface, the boundary condition at the sizing/matrix interface is switched to an insulated flux type. The mass of dissolved sizing can also be computed from the interfacial sizing mass fraction gradient as follows:

$$M_d = \int_t \left\{ \iint_{\Gamma} (\underline{n}_s \cdot \underline{n}) d\Gamma \right\} dt \quad (4-10)$$

At any time, the sizing mass flux, \underline{n}_s , can be computed from Fick's 1st Law. The value of the unit normal vector \underline{n} (into the solution domain) can be computed from the parameterization of the sizing/matrix interface:

$$\underline{n} = \left(\frac{1}{\sqrt{1 + \left(\frac{dx}{dy}\right)^2}} \right) \cdot \underline{\varepsilon}_x + \left(-\frac{dx}{dy} \cdot \frac{1}{\sqrt{1 + \left(\frac{dx}{dy}\right)^2}} \right) \cdot \underline{\varepsilon}_y \quad (4-11)$$

where the sizing/matrix interface is represented by $y = y(x)$ or $y = y(t)$ and $x = x(t)$. For the finite element solution, the first method for determination of the dissolution time was utilized. This method was most efficient because the do-loops necessary to complete the integration were already performed in the generation of the matrices to be discussed in section 4.4.1.

4.3 Analytical Models for Interphase Formation

As was discussed in section 4.1, the idealized composite solution domain is a 60-30° right triangle with a circular section removed. This geometry can be approximated with a simplified solution domain that will allow analytical solutions to be obtained to equation (4-7).

Two simplified solution domains exist for the idealized composite. The first simplified domain is two infinite parallel plates separated by a distance equal to the fiber-fiber spacing in the idealized composite. The second simplified solution domain is diffusion from a cylinder into an infinite medium. For the solutions presented in this section, the physical properties used are summarized later in Section 4.4.6 (Table 4.4.1).

The simplified solution domain for the first case can be generated (Figure 4.3-1). The boundary conditions as a function of time and the initial condition were specified in section 4.2.1.2. The solution to equation (4-7) for this simplified solution domain is the following for times less than the dissolution time [4.2]:

$$\omega = \omega_{eq} \left(1 - \operatorname{erf} \left\{ \frac{x}{2\sqrt{D_d t}} \right\} \right) \quad (4-12)$$

where ω_{eq} is the equilibrium sizing weight fraction in the matrix and D_d is the dissolution diffusion coefficient. This solution is rigorously accurate for a solution domain infinite in the x -direction. However, this solution is accurate in our simplified solution domain because the sizing diffusion front of one parallel plate never encroaches upon the diffusion front of the opposite parallel plate in the time period over which we are using this approximation ($t < t_d = \text{dissolution time}$). This will be apparent in the results presented later in this paragraph. The benefit of using this approximation is that it is a closed form solution that does not involve a series. The time required to completely dissolve the sizing can be determined by computing the

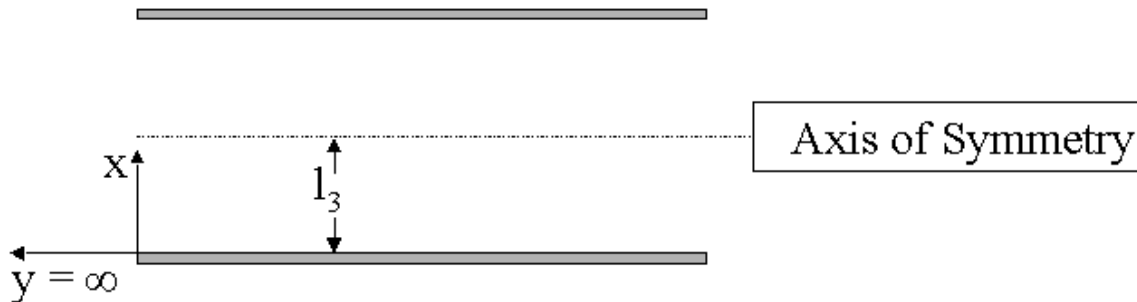


Figure 4.3-1 Planar source geometry utilized for simplification of the idealized composite.

flux of sizing and integrating over time [4.2]:

$$t_d = \left[\frac{M_t}{2C_{eq}} \right]^2 \frac{\pi}{D_d} \quad (4-13)$$

where t_d is the dissolution time, M_t is the mass of sizing per unit cross-sectional area, and C_{eq} is the thermodynamic equilibrium concentration (g/cm^3). M_t and C_{eq} can be computed from the following equations:

$$M_t = \rho_s \cdot t_s \quad (4-14)$$

$$C_{eq} = \frac{\omega_{eq}}{\left(\frac{\omega_{eq}}{\rho_s} + \frac{(1-\omega_{eq})}{\rho_m} \right)} \quad (4-15)$$

where ρ_m is the matrix density. Equation (4-15) assumes that the sizing and matrix mix ideally which was an assumption enumerated in the introduction section. The time required for sizing dissolution based upon the physical properties listed in Table 4.4.7 is summarized in the following equation:

$$t_d = \frac{5.9 \cdot 10^{-11} \text{ cm}^2}{D_d} \quad (4-16)$$

If the dissolution time t_d is greater than the processing time t_p , then the final interphase profile is equal to the profile generated from equation (4-12) with the time equal to the processing time t_p . If the dissolution time t_d is less than the processing time t_p , then the sizing mass fraction profile calculated from equation (4-12) at time t_d is used as the initial condition for the second stage of the solution where the interface boundary becomes impermeable. The solution to equation (4-7) for this time period is equal to the following [4.2]:

$$\omega = \frac{2}{l_3} \sum_{n=1}^{\infty} \left[\exp\left(-D_d n^2 \pi^2 \frac{t}{l_3^2}\right) \cdot \cos\left(\frac{n\pi x}{l_3}\right) \cdot \left\{ \int_0^{l_3} \omega_1(z) \cos\left(\frac{n\pi z}{l_3}\right) dz \right\} \right] + \frac{1}{l_3} \int_0^{l_3} \omega_1(z) dz \quad (4-17)$$

where z is a dummy integration variable and $\omega_1(z)$ is the solution generated from equation (4-12) at time equal to the dissolution time t_d . Interphase profiles can be generated from these equations as a function of the dissolution diffusion coefficient, D_d , and the spatial coordinate x (Figure 4.3-2). From Figure 4.3-2, it can be seen that for the physical properties and processing conditions listed in Table 4-1, a dissolution diffusion coefficient between 10^{-11} and $10^{-14} \text{ cm}^2/\text{sec}$ is needed for the formation of an interphase.

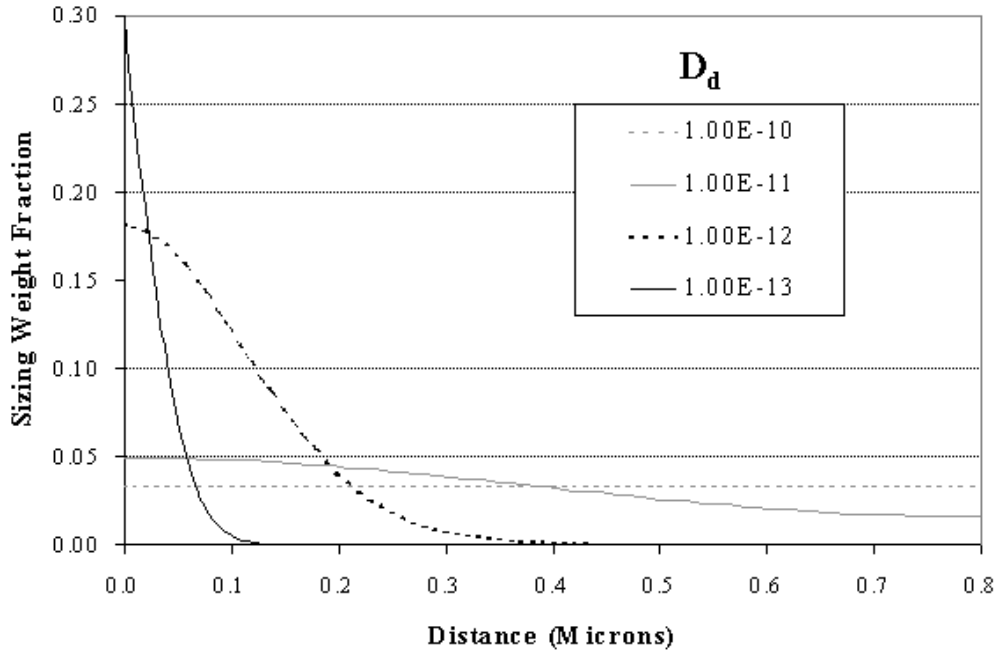


Figure 4.3-2 Planar source model interphase profile as a function of the dissolution diffusion coefficient, D_d . Note: Processing time equal to 15 minutes. Units on D_d are cm^2/s .

If the dissolution process is relaxation and/or disentanglement controlled, then the fiber/matrix interface boundary condition is of flux type and equation (4-12) is no longer valid for time less than the dissolution time. For a constant fickian diffusion coefficient, a flux-controlled dissolution process has an analytical solution for the simplified parallel-plate geometry. The sizing weight fraction as a function of time and position can be calculated from the following equation [4.2]:

$$\omega = \frac{f_s}{\rho_s} \cdot \frac{1}{D_d} \cdot \left[\frac{t}{l_3^2} + \frac{(3x^2 - l_3^2)}{6l_3^2} - \frac{2}{\pi^2} \cdot \left\{ \sum_{n=1}^{\infty} \left[\frac{(-1)^n}{n^2} \cdot \exp\left(\frac{-D_d n^2 \pi^2 t}{l_3^2}\right) \cdot \cos\left(\frac{n\pi x}{l_3}\right) \right] \right\} \right] \quad (4-18)$$

where $f_s = -(\mathbf{n} \cdot \mathbf{n}_s)$ is the sizing mass flux normal to the sizing/matrix interface. Equation (4-18) is valid as long as sizing remains at the fiber/matrix interface. The dissolution time can be calculated from the normal flux according to the following equation:

$$t_d = \frac{M_t}{f_s} \quad (4-19)$$

For times less than the dissolution time, equation (4-18) is utilized to obtain the concentration profile. At times greater than the dissolution time, the concentration profile is generated from equation (4-17) with $w_1(z)$ set equal to the concentration profile generated by equation (4-18) evaluated at a time equal to the dissolution time, t_d . This expression will be utilized later in section to verify the accuracy of the FEM code.

Another approximation to the solution domain is diffusion from a single cylinder. As long as the diffusion distance is less than one half the fiber-fiber separation (i.e. l_3), then this analytical solution should exactly match that obtained from the actual solution domain developed previously. Unfortunately, the solution to the diffusion equation under this simplified geometry is analytical but not simple. The solution is composed of integrals of Bessel's functions that are difficult to program. The time needed to program this solution was not justifiable considering the FEM model developed in the next section.

4.4 Finite Element Simulation of Interphase Formation

The Finite Element Method (FEM) is a powerful technique for solving differential equations over non-rectangular regions. It has several advantages over finite differencing schemes (FDS). First, the FEM method can be easily extended to any solution domain whereas the FDS can only be applied to a solution domain for which the program was designed. Once a program utilizing the FEM has been written, it is easily applied to any geometry by simply modifying the mesh. Second, the FEM method automatically insures continuity of fluxes across material boundaries that must be independently programmed in FDS. Third, the FEM method can more easily handle flux boundary conditions than the FDS.

Because equation (4-7) is analogous to the transient heat transfer equation, there are numerous commercial FEM packages that can be used to solve this problem for our solution domain. However, for reasons to be discussed in this paragraph, it was concluded that a stand alone FORTRAN 77 FEM code needed to be written to solve this problem. Commercial codes such as POLYFLOW readily solve the transient heat transfer equation but they severely limit the user's ability to post-process solutions into forms other than those designed into the package. For instance, POLYFLOW will solve the heat transfer equation for the case of equilibrium existing at the sizing/matrix interface but it will not integrate the surface flux to obtain the amount of sizing dissolved in as a function of time. The POLYFLOW solution would have to be

input into a separate FORTRAN program that would integrate the surface flux at each time domain. After the program had determined the time required to dissolve the sizing, the solution would have to be input into POLYFLOW as the initial condition for a 2nd solution where the sizing/matrix interface was impermeable. This would require more programming than would be required to write a stand alone FORTRAN code. Some commercial codes, such as POLYFLOW, give the user the flexibility to alter the source code to accomplish tasks not originally programmed. However, this would involve more work than the actual programming of the FEM method as was done in this case. In addition, POLYFLOW does not allow flexibility in assigning the functional dependence of the thermal conductivity and hence dissolution diffusion coefficient. Typically, thermal conductivity is a weak function of temperature. However, as will be discussed in Chapter 5, the dissolution diffusion coefficient can be a very strong function of concentration. Therefore, POLYFLOW could not successfully solve equation (4-6) for our case of highly non-fickian behavior. A stand along FORTRAN 77 code was written to solve the equations presented in section 4.2.1.

4.4.1 Derivation of Finite Element Equations

The method of weighted residuals was applied to equation (4-6). The diffusion equation was multiplied by a test function, ϕ , and integrated over the volume of the solution domain. The test function satisfies all homogeneous essential boundary conditions.

$$\iiint_{\Omega} \frac{\partial \omega}{\partial t} \phi d\Omega = \iiint_{\Omega} \phi \nabla \cdot (D_d \nabla \omega) d\Omega \quad (4-20)$$

$$\iiint_{\Omega} \frac{\partial \omega}{\partial t} \phi d\Omega = -\iiint_{\Omega} D_d \nabla \omega \cdot \nabla \phi d\Omega + \iiint_{\Omega} \nabla \cdot (\phi D_d \nabla \omega) d\Omega \quad (4-21)$$

After application of the Gauss-Divergence Theorem, the following equation was derived:

$$\iiint_{\Omega} \frac{\partial \omega}{\partial t} \phi d\Omega = -\iiint_{\Omega} D_d \nabla \omega \cdot \nabla \phi d\Omega - \iint \frac{\phi}{\rho} (\mathbf{n}_s \cdot \mathbf{n}) d\Gamma \quad (4-22)$$

where ρ was the bulk density, \mathbf{n}_s was the sizing mass flux, and \mathbf{n} was the outward unit normal. However, the test function is zero on all essential boundaries and the surface integral on the right can be simplified to the following:

$$\iiint_{\Omega} \frac{\partial \omega}{\partial t} \phi d\Omega = -\iiint_{\Omega} D_d \nabla \omega \cdot \nabla \phi d\Omega - \iint \frac{\phi}{\rho} (\mathbf{n}_s \cdot \mathbf{n}) d\Gamma_1 \quad (4-23)$$

where Γ_I represents the boundary between the fiber/matrix interface that can be either of essential or flux type.

If the fiber/matrix interface is controlled by a flux, then the surface integral in equation (4-23) cannot be neglected. In addition, the test function, ϕ , must be applied at every node because there are no essential boundary conditions present. If the fiber/matrix interface is controlled by thermodynamic equilibrium, then the boundary is of the essential type and the surface integral is zero.

Regardless of whether the fiber/matrix interface boundary condition is of the essential or flux type, it is helpful to break ω down into a part μ that satisfies the homogeneous portion of the essential boundary condition and a part η that satisfied the non-homogeneous portion of the essential boundary condition. This can be represented mathematically as the following:

$$\omega = \mu + \eta \quad (4-24)$$

If we approximate the values of the functions μ and ϕ as a linear combination of a series of finite element basis functions, ψ , then the following set of approximations is developed:

$$\mu = \sum_i \mu_i \psi_i \quad (4-25) \quad \phi = \sum_i d_i \psi_i \quad (4-26)$$

The summation is performed over all nodes that do not include the essential boundary. If the boundary is of the flux type and hence no essential boundary nodes are present, then the summation over i is performed over all the nodes present on the solution domain. If the fiber/matrix interface is controlled by thermodynamic equilibrium, then the essential boundary condition is satisfied by allowing η to equal the following:

$$\eta = s \sum_m \psi_m \quad (4-27)$$

The essential boundary is not a function of position along the boundary. The summation is performed over the essential boundaries only. If the fiber/matrix interface is of flux type, then the summation over m is not performed. The value of s is equal to the value of the boundary condition, which can be a function of time.

The shape functions, ψ_i , must be a subspace of \mathfrak{R}^3 and must also satisfy certain stability requirements represented by the following:

$$\iiint_{\Omega} \underline{\nabla} \psi_i \cdot \underline{\nabla} \psi_j d\Omega < \infty \quad (4-28)$$

Applying the approximations represented by equations (4-24) through (4-26), the following single equation results:

$$\begin{aligned}
& \sum_{i,j} \left[\frac{\partial \mu_i}{\partial t} d_j \iiint_{\Omega} \psi_i \psi_j d\Omega + \mu_i d_j \iiint_{\Omega} D_d \underline{\nabla} \psi_i \cdot \underline{\nabla} \psi_j d\Omega \right] = \\
& - \sum_j \left[d_j \iiint_{\Omega} \frac{\partial \eta}{\partial t} \psi_j d\Omega + d_j \iiint_{\Omega} D_d \underline{\nabla} \eta \cdot \underline{\nabla} \psi_j d\Omega \right] \\
& - \sum_j d_j \iint_{\Gamma_i} \frac{1}{\rho} (\underline{n}_s \cdot \underline{n}) \psi_j d\Gamma
\end{aligned} \tag{4-29}$$

Because the selection of the test function is arbitrary, the values for d_j are also arbitrary. For convenience, the values for d_j can be set equal to an arbitrary unit vector, which acts as a contraction on the summation:

$$d_j = \delta_{jp} \tag{4-30}$$

Applying equation (4-30) into equation (4-29) gives the following:

$$\begin{aligned}
& \sum_i \left[\frac{\partial \mu_i}{\partial t} \iiint_{\Omega} \psi_i \psi_p d\Omega + \mu_i \iiint_{\Omega} D_d \underline{\nabla} \psi_i \cdot \underline{\nabla} \psi_p d\Omega \right] = \\
& - \left[\iiint_{\Omega} \frac{\partial \eta}{\partial t} \psi_p d\Omega + \iiint_{\Omega} D_d \underline{\nabla} \eta \cdot \underline{\nabla} \psi_p d\Omega + \iint_{\Gamma_i} \frac{1}{\rho} (\underline{n}_s \cdot \underline{n}) \psi_p d\Gamma \right]
\end{aligned} \tag{4-31}$$

If the following substitutions are placed into equation (4-31), then the equation can be greatly simplified:

$$M_{ij} = \iiint_{\Omega} \psi_i \psi_j d\Omega \quad (4-32) \quad L_{ij} = \iiint_{\Omega} D_d \underline{\nabla} \psi_i \cdot \underline{\nabla} \psi_j d\Omega \quad (4-33)$$

This results in the following simplification:

$$\begin{aligned}
& \sum_i \left\{ \frac{\partial \mu_i}{\partial t} M_{ij} + \mu_i L_{ij} \right\} = - \left[\iiint_{\Omega} \frac{\partial \eta}{\partial t} \psi_j d\Omega + \iiint_{\Omega} D_d \underline{\nabla} \eta \cdot \underline{\nabla} \psi_j d\Omega \right. \\
& \left. + \iint_{\Gamma_i} \frac{1}{\rho} (\underline{n}_s \cdot \underline{n}) \psi_j d\Gamma \right]
\end{aligned} \tag{4-34}$$

If the approximation for η is now substituted into equation (4-34), the following equation results:

$$\begin{aligned}
& \sum_i \left\{ \frac{\partial \mu_i}{\partial t} M_{ij} + \mu_i L_{ij} \right\} = \\
& - \sum_m \left[\frac{\partial s}{\partial t} \iiint_{\Omega} \psi_m \psi_j d\Omega + s \iiint_{\Omega} D_d \underline{\nabla} \psi_m \cdot \underline{\nabla} \psi_j d\Omega \right] - \iint_{\Gamma_i} \frac{1}{\rho} (\underline{n}_s \cdot \underline{n}) \psi_j d\Gamma
\end{aligned} \tag{4-35}$$

The first integral on the right side of equation (4-35) represents the m^{th} row of the matrix M_{ij} and the second integral represents the m^{th} row of the matrix L_{ij} . Equation (4-35) can be simplified by making the following substitutions:

$$Q_j = \iiint_{\Omega} \sum_m \psi_m \psi_j d\Omega \quad (4-36) \quad R_j = \iiint_{\Omega} D_d \sum_m \underline{\nabla} \psi_m \cdot \underline{\nabla} \psi_j d\Omega \quad (4-37)$$

Substituting equations (4-36) and (4-37) into equation (4-35) gives the following:

$$\sum_i \left\{ \frac{\partial \mu_i}{\partial t} M_{ij} + \mu_i L_{ij} \right\} = - \left[\frac{\partial s}{\partial t} \cdot Q_j + s \cdot R_j \right] - \iint_{\Gamma_i} \frac{1}{\rho} (\underline{n}_s \cdot \underline{n}) \psi_j d\Gamma \quad (4-38)$$

The temporal approximations for equation (4-38) are generated from a finite-differencing scheme. Usually, a theta family of approximations is utilized such that solutions can be obtained at discrete time steps [4.3]. The approximations are as follows:

$$(1-\theta) \cdot \frac{\partial f_i^k}{\partial t} + \theta \cdot \frac{\partial f_i^{k+1}}{\partial t} = \frac{f_i^{k+1} - f_i^k}{\Delta t} \quad (4-39)$$

The θ is a parameter that can be varied from 0 to 1. If θ has a value of 0, then the finite differencing approximation is $O(\Delta t)$ accurate and conditionally stable. The condition for stability is the following [4.3]:

$$\Delta t_c < \frac{2}{(1-2\theta)\lambda} \quad (4-40)$$

where Δt_c is the critical time step and λ is the largest eigenvalue of matrices [A] and [B] defined later in this section. If the value of θ is 0.5, then the approximation is $O(\Delta t^2)$ accurate and is unconditionally stable. If θ has a value of 1, then the approximation is $O(\Delta t)$ accurate and unconditionally stable. Stability implies that the error in the approximation remains finite for all values of time. However, just because a solution is stable, this does not imply that the solution will be accurate. In order to obtain accurate solutions, the Δt utilized must be some fraction of the Δt calculated from equation (4-40). For the solutions presented in the following sections, the value of θ was chosen to be 0.5. This value of θ insures the solution will remain stable for all meshing schemes and values of Δt . The optimal way to determine the appropriate Δt for solution accuracy would be to compute the largest eigenvalue of [A] and [B] and use equation (4-40) to compute the maximum time step. The modeler would then select what fraction of the maximum time step to use. This technique was not utilized for the final FEM model. Accuracy was insured by selecting progressively smaller and smaller time steps until the predicted solution

domain did not deviate (within set limits) from one solution to the next. Equation (4-38) is valid at any time step k and this can be represented by the following:

$$\sum_i \left\{ \frac{\partial \mu_i^k}{\partial t} M_{ij} + \mu_i L_{ij}^k \right\} = - \left[\frac{\partial s^k}{\partial t} \cdot Q_j + s^k \cdot R_j^k \right] - \iint_{\Gamma_i} \frac{1}{\rho} (\underline{n}_s \cdot \underline{n}) \psi_j d\Gamma \quad (4-41)$$

The transient variables are given the superscript k to indicate that they are functions of time and their present value is for time step k. The matrices M_{ij} and Q_j are not functions of time because the shape functions are functions of spatial coordinates only. Because the matrices L_{ij} and R_j are functions of a non-constant dissolution diffusion coefficient, these matrices are functions of time. The sizing flux, \underline{n}_s , is assumed to be constant and not a function of time. Substituting equation (4-35) into equation (4-39) gives the following:

$$\begin{aligned} & \sum_i \left\{ \mu_i^{k+1} \left\{ \theta \cdot L_{ij}^{k+1} + \frac{M_{ij}}{\Delta t} \right\} \right\} = \\ & \sum_i \left\{ \mu_i^k \left\{ \frac{M_{ij}}{\Delta t} - (1-\theta) \cdot L_{ij}^k \right\} \right\} + s^k \left\{ \frac{Q_j}{\Delta t} - (1-\theta) \cdot R_j^k \right\} - s^{k+1} \left\{ \frac{Q_j}{\Delta t} + \theta \cdot R_j^{k+1} \right\} \\ & - \iint_{\Gamma_i} \frac{1}{\rho} (\underline{n}_s \cdot \underline{n}) \psi_j d\Gamma \end{aligned} \quad (4-42)$$

Equation (4-42) can be simplified by making the following substitutions:

$$A_{ij} = \theta \cdot L_{ij}^{k+1} + \frac{M_{ij}}{\Delta t} \quad (4-43) \quad B_{ij} = \frac{M_{ij}}{\Delta t} - (1-\theta) \cdot L_{ij}^k \quad (4-44)$$

$$P_j = \frac{Q_j}{\Delta t} - (1-\theta) \cdot R_j^k \quad (4-45) \quad G_j = \frac{Q_j}{\Delta t} + \theta \cdot R_j^{k+1} \quad (4-46)$$

Substituting these relationships into equation (4-42), gives the following:

$$\sum_i \left\{ \mu_i^{k+1} A_{ij} \right\} = \sum_i \left\{ \mu_i^k B_{ij} \right\} + \left\{ s^k P_j - s^{k+1} G_j \right\} - \iint_{\Gamma_i} \frac{1}{\rho} (\underline{n}_s \cdot \underline{n}) \psi_j d\Gamma \quad (4-47)$$

In matrix notation, equation (4-47) can be written as the following:

$$[\mu]^{k+1} \cdot [A] = [\mu]^k \cdot [B] + s^k [P] - s^{k+1} [G] - \iint_{\Gamma_i} \frac{1}{\rho} (\underline{n}_s \cdot \underline{n}) \psi_j d\Gamma \quad (4-48)$$

For the case of flux controlling the fiber/matrix interface, then equation (4-48) reduces to the following where the integrals are evaluated over all the nodes:

$$[\mu]^{k+1} \cdot [A] = [\mu]^k \cdot [B] - \iint_{\Gamma_i} \frac{1}{\rho} (\underline{n}_s \cdot \underline{n}) \psi_j d\Gamma \quad (4-49)$$

For the case of thermodynamic equilibrium controlling the fiber/matrix interface, then equation (4-48) reduces to the following where the integrals involving dummy variable i are evaluated at the nodes not on the fiber/matrix interface and the integrals involving dummy variable m are evaluated at the nodes on the fiber/matrix interface:

$$[\mu]^{k+1} \cdot [A] = [\mu]^k \cdot [B] + s^k [P] - s^{k+1} [G] \quad (4-50)$$

The value of μ at time step $k+1$, can be computed by solving the system of pseudo-linear equations represented by equation (4-49) or (4-50). The complexity created by solving equations (4-49) and (4-50) is that in order to obtain the value of μ at time step $k+1$, the value of L_{ij} and R_j must be known at time $k+1$. Therefore, the equations represented by (4-49) and (4-50) are not strictly linear. An approximate solution to equations (4-49) and (4-50) can be obtained by assuming that $L^{k+1} \approx L^k$ and $R^{k+1} \approx R^k$. After solving the equations for μ^{k+1} , the values for L^{k+1} and R^{k+1} can be computed and compared to the guess values of L^k and R^k . The new values for L^{k+1} and R^{k+1} can then be used to obtain a more accurate value for μ^{k+1} . This iterative scheme can be continued until certain error criteria are met or a pre-defined number of loops have been completed. The non-fickian FEM model presented in Appendix II allows the operator to input the number of iteration loops to perform. Utilizing this iterative scheme, the pseudo-linear equations represented by (4-49) and (4-50) can be solved efficiently by Gaussian elimination.

The model developed for the proposal assumed that the dissolution diffusion coefficient was constant and hence not a function of time and/or position. As was discussed in the proposal, this allowed equation (4-50) to be more efficiently solved by matrix inversion instead of Gaussian elimination. In addition, the non-linearities discussed previously were not present for the case of fickian diffusion.

4.4.1.1 Imposition of Boundary Condition at Sizing/Matrix Interface

After the sizing has completely dissolved into the matrix, the fiber/matrix interface boundary must be set equal to insulated flux type. Equation (4-49) generated in the previous section is valid for this situation with the flux \underline{n}_s set equal to zero:

$$[\mu]^{k+1} \cdot [A] = [\mu]^k \cdot [B] \quad (4-51)$$

The solution to equation (4-51) is again pseudo-linear. In order to obtain μ^{k+1} , L^{k+1} is needed. Therefore, the same iterative scheme discussed previously is utilized to obtain a solution to equation (4-51).

4.4.2 Mesh Generation for Idealized Composite Interphase

Before solutions to equations (4-49) and (4-50) can be produced, a mesh for the solution domain must be generated. The idealized composite was generated in section 4.1 and will be used in this section to generate the mesh. The meshes produced for the proposal were generated from a FORTRAN 77 program that utilized a constantly spaced angular grid with an equally divided radial definition. This program was modified to allow for greater mesh definition near the fiber/matrix interface. As will be discussed in Chapter 5, the highly non-fickian nature of the interdiffusion process dictates that large concentration gradients will exist near the fiber/matrix interface. In order to obtain accurate predictions of this gradient, the mesh needed to be more refined at nodes near the fiber/matrix interface.

For the final mesh generation program listed in Appendix I, the radial element length varies linearly with increasing radius while the angular subdivision is constant. The user inputs the number of angular elements (\mathcal{G}) and the number of radial elements (β) desired for the mesh. In addition, the user inputs the ratio of the initial radial length of the element to the final radial length of the element (dR_o/dR_f). Finally, the user inputs the fiber volume fraction, fiber diameter, fiber density, and the matrix density. From this information, the program generates the node numbering, the nodal coordinates, the boundary information, and the connectivity array.

The elements are generated by dividing the solution domain into quadrilaterals utilizing linear segments in both the angular and radial directions. The angular division is generated by subdividing the 30° angle into \mathcal{G} portions. $\mathcal{G}-1$ radially oriented linear segments are then placed from the center of the 30° - 60° triangle to the exterior linear boundary Γ_2 (Figure 4.4-1). The angle (α_n) between these linear segments and the exterior linear boundary Γ_3 is equal to $(30^\circ/\mathcal{G})(n)$ where n is the n^{th} angular segment and has values $0 \leq n \leq \mathcal{G}$. Each of these angular segments are then truncated at the intersection between them and the interface arc Γ_4 . Each of these angular segments has a length equal to the following:

$$\chi_n = \frac{R_f + l_3}{\cos\left(\frac{30^\circ \cdot n}{\mathcal{G}}\right)} - R_f \quad (4-52)$$

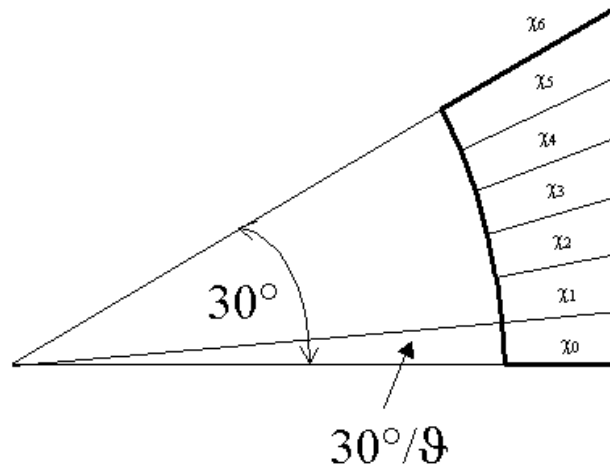


Figure 4.4-1 Schematic of angular subdivision of solution domain.

The elements are formed by dividing χ_n into β segments each having a specific length that varies linearly as a function of the radial position. This linear variation can be represented by the following equation:

$$dR_m = \frac{(dR_f - dR_o)}{\beta - 1} \cdot (m - 1) + dR_o \quad (4-53)$$

where dR_m is the m^{th} radial element length and m is the m^{th} radial segment and has values $0 \leq m \leq \beta$. Simplifying equation (4-53) gives the following:

$$dR_m = dR_o \left[\frac{\left(\frac{1}{F} - 1 \right)}{\beta - 1} \cdot (m - 1) + 1 \right] \quad (4-54)$$

where F is the user input ratio (dR_o/dR_f). The selection of dR_o and F are not independent do to the constraint that the sum of the total radial element lengths must be equal to the total radial length χ_n :

$$\chi_n = \sum_{m=1}^{\beta} dR_m \quad (4-55)$$

Substituting equation (4-54) into equation (4-55) and solving for dR_o gives the following.

$$dR_o = \frac{2\chi_n}{\beta(1 + \frac{1}{F})} \quad (4-56)$$

In summary, the radial element length as a function of the element position is the following:

$$dR_m = \frac{2\chi_n}{\beta(1+\frac{1}{F})} \left[\frac{\left(\frac{1}{F}-1\right)}{\beta-1} \cdot (m-1)+1 \right] \quad (4-57)$$

The elements are then formed by joining the angular segments and the corresponding radial segments (Figure 4.4-2).

The numbering scheme utilized for this program is to have node one located at position (0,0) (Figure 4.4-2) and increment sequentially along the angular subdivided arc. For instance, if there are ϑ elements in the angular direction and β elements in the radial direction, then nodes numbered 1 through $\vartheta+1$ would exist on the interface arc. Nodes numbered $\vartheta+2$ through $2\vartheta+2$ would exist on the next arc or radial subdivision. On the m^{th} arc where $1 \leq m \leq (\beta+1)$, nodes numbered $(m-1)\vartheta+m$ through $m \cdot (\vartheta+1)$ would exist. The total number of nodes will equal $(\vartheta+1)(\beta+1)$ while the total number of elements will equal $\vartheta \cdot \beta$.

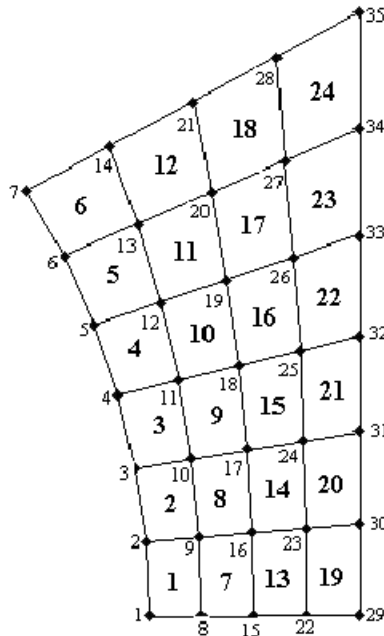


Figure 4.4-2 Finite Element mesh with angular subdivision, radial subdivision, element numbering, and node numbering shown.

Now having defined the numbering scheme utilized by the program, the determination of the nodal coordinates will be discussed. The nodal coordinates are easily specified because they reside on an arc of known center and radius. The center of the arc resides at the theoretical intersection of the linear boundary segments Γ_1 and Γ_3 . The radius is a function of the angle of the angular segment α_n and the position on the radial subdivision. The x and y coordinates for the node located on the n^{th} angular subdivision and the m^{th} arc or radial subdivision are as follows:

$$x = R_f (\cos \alpha_n - 1) \cdot \sum_{i=1}^m dR_i \cdot \cos \alpha_n \quad (4-58)$$

$$y = R_f (\sin \alpha_n) \cdot \sum_{i=1}^m dR_i \cdot \sin \alpha_n \quad (4-59)$$

where $0 \leq n \leq \vartheta$ and $0 \leq m \leq \beta$. This completes the specification of the nodal coordinates. The generation of the connectivity array will now be discussed.

The connectivity array is utilized to link the location of a global node to a master element node. As will be discussed in section 4.4.4, all integrations will be performed over a master element in s-t space. A mapping from x-y to s-t space will be generated. The connectivity array will allow this integration to be performed. The master element used in the FEM program is a simple four noded square with dimension 2X2 (Figure 4.4-3). The node numbering for this master element starts at the lower left node and progresses counterclockwise. Master element

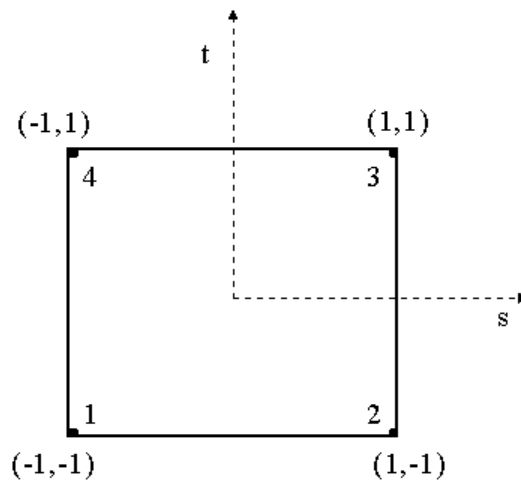


Figure 4.4-3 Schematic of four noded Master Element.

node one has coordinates (-1,-1). The syntax for the connectivity array is **ICON**(*ele,master_node*) where *ele* refers to the global element number and *master_node* refers to the master element node number. The value of **ICON**(*ele,master_node*) refers to the local node number. For instance, global node number 26 resides in global element numbers 16, 17, 22, and 23 (Figure 4.4-2). However, its position is different in all four. Its position in these elements can be specified in relation to the Master elements positioning. For instance, on element 16, global node 26 is in the 3 position of the Master element. On element 17, global node 26 is in the 2 position of the Master element. Therefore, **ICON**(16,3) = 26 and **ICON**(17,2) = 26. The specification of the connectivity array can be easily generated by inspecting the elements sequentially. The following expressions can be developed for the connectivity array. **ICON**(*ele*,1) = *ele* + *e*, **ICON**(*ele*,2) = *ele* + (*e* + 9) + 1, **ICON**(*ele*,3) = *ele* + (*e* + 9) + 2, and **ICON**(*ele*,4) = *ele* + *e* + 1 where *ele* is the element number and *e* is the largest integer less than or equal to the quotient *ele*/(9 + 1). This concludes the specification of the connectivity array. The specification of the interfacial boundary will now be discussed.

The nodes on the interfacial boundary must be specified so that the essential boundary conditions can be satisfied. The nodes appearing on the interfacial boundary are nodes numbered 1 through 9 + 1. If a flux were to be prescribed on the interfacial boundary, then a connectivity array for the boundary would need to be generated so that the corresponding line integrals could be computed. The specification of this connectivity array would be similar to that completed in the previous paragraph. This concludes the specification of the mesh needed for the Finite Element simulation. A listing of this program can be found in Appendix I.

4.4.3 Shape Function Used in FEM Approximation

Before solutions to equations (4-49) and (4-50) can be obtained, piecewise continuous polynomial expressions for the shape functions must be derived. In finite element work, the shape functions are chosen such that the following holds.

$\psi_i(x,y) = 1$ when *x,y* are evaluated at node *i* and $\psi_i(x,y) = 0$ when *x,y* are evaluated at any other node. However, all integrations are performed over the master element described in the previous section. Therefore, there are four master element shape functions (N_i) that must be derived to satisfy the following relationships.

For master node 1,

$N_1 = 1$ when $(s,t) = (-1,-1)$ $N_1 = 0$ when $(s,t) = (1,-1), (1,1),$ and $(-1,1)$

For master node 2,

$N_2 = 1$ when $(s,t) = (1,-1)$ $N_2=0$ when $(s,t) = (1,1), (-1,1),$ and $(-1,-1)$

For master node 3,

$N_3 = 1$ when $(s,t) = (1,1)$ $N_3 = 0$ when $(s,t) = (-1,1), (-1,-1),$ and $(1,-1)$

For master node 4,

$N_4 = 1$ when $(s,t) = (-1,1)$ $N_4 = 0$ when $(s,t) = (-1,-1), (1,-1),$ and $(1,1)$

The corresponding shape functions are as follows for the above specifications:

$$N_1 = \frac{1}{4}(t-1)(s-1) \quad \text{(4-60)} \quad N_2 = \frac{1}{4}(1-t)(s+1) \quad \text{(4-61)}$$

$$N_3 = \frac{1}{4}(s+1)(t+1) \quad \text{(4-62)} \quad N_4 = \frac{1}{4}(t+1)(1-s) \quad \text{(4-63)}$$

The mapping from s-t space to x-y space can be generated from these four shape functions, the global node position, and the connectivity array as follows:

$$x(ele, s, t) = \sum_{i=1}^{NPE} [NOD_x(ICON(ele, i)) \cdot N_i(s, t)] \quad \text{(4-64)}$$

$$y(ele, s, t) = \sum_{i=1}^{NPE} [NOD_y(ICON(ele, i)) \cdot N_i(s, t)] \quad \text{(4-65)}$$

where NPE is the number of nodes per element (equals 4), $NOD_x(node)$ is the x-coordinate of global node number $node$, $NOD_y(node)$ is the y-coordinate of global node number $node$, and $ICON(ele, i)$ is the connectivity array of global element number ele and master node number i .

4.4.4 Integrations over the Master Element

The matrices generated in section 4.4.1 involve the integration of the shape functions over the solution domain. As was discussed earlier, it is computationally more efficient to complete these integrations over a Master element. The element does not deform or change shape over the entire solution domain. The limits of integration remain constant. This allows the use of Gaussian quadrature for the numerical integration technique.

The matrix M_{ij} discussed earlier has the following definition where Ω is the solution domain in x-y space:

$$M_{ij} = \iiint_{\Omega} \psi_i \psi_j d\Omega \quad \text{(4-66)}$$

This integral can be evaluated element by element according to the following definitions:

$$M_{ij} = \sum^{nele} M^e_{ij} \quad (4-67)$$

$$M^e_{ij} = \iiint_{\Omega_e} \psi_i \psi_j d\Omega_e \quad (4-68)$$

where the values of i and j equal the number of nodes or the number of nodes minus the nodes on the essential boundary depending upon the state of the boundary condition. It should be noted that on each element, there exists only four non-vanishing shape functions. Therefore, the elemental matrix M^e_{ij} has 16 non-zero entries. These 16 non-zero entries can be represented by the following integral where the x - y space has been mapped into the s - t space:

$$M^e_{\alpha\beta} = \int_{-1}^1 \int_{-1}^1 N_\alpha N_\beta J(s,t) ds dt \quad (4-69)$$

where $1 \leq \alpha$ and $\beta \leq 4$, N_i and N_j are the master element shape functions, and J is the Jacobian of the transformation rule expressed by equation (4-70). The value of the Jacobian for the x - y to s - t mapping is the following:

$$J(ele, s, t) = \left\{ \frac{\partial x(ele, s, t)}{\partial s} \cdot \frac{\partial y(ele, s, t)}{\partial t} - \frac{\partial y(ele, s, t)}{\partial s} \cdot \frac{\partial x(ele, s, t)}{\partial t} \right\} \quad (4-70)$$

The value of the matrix M_{ij} can then be computed by properly summing the values of the elemental matrix $M^e_{\alpha\beta}$. The following FORTRAN 77 DO loop shows the proper way to assemble the elemental matrix into the global matrix. This program assumes that the matrix $[M]$ is available in its full storage mode (all entries are present) which is not the case in the final program presented in **Appendix II**.

```

DO 100 ELEMENT=1,NELEM
  DO 110 alpha=1,NPE
    DO 120 beta=1,NPE
      M(ICON(ELEMENT,alpha),ICON(ELEMENT,beta))=M(ICON(ELEMENT,alpha)
&      ,ICON(ELEMENT,beta))+ME(ELEMENT, alpha, beta)
120    CONTINUE
110    CONTINUE
100  CONTINUE

```

where NELEM is the number of elements in the mesh, NPE is the nodes per element (equal to 4), M is the matrix M_{ij} , ME is the matrix $M^e_{\alpha\beta}$ derived previously. The assembly of the $[M]$ matrix

is complicated by the fact that it will be stored in banded mode as will be discussed later. The details of the actual programming used to completely specify [M] will not be discussed.

The matrix L_{ij} is computed in a similar fashion. The elemental matrix $L_{\alpha\beta}^e$ is defined as follows:

$$L_{\alpha\beta}^e = \int_{-1}^1 \int_{-1}^1 D_{\alpha} \left\{ \left(\frac{\partial N_{\alpha}}{\partial s} \cdot \frac{\partial s}{\partial x} + \frac{\partial N_{\alpha}}{\partial t} \cdot \frac{\partial t}{\partial x} \right) \cdot \left(\frac{\partial N_{\beta}}{\partial s} \cdot \frac{\partial s}{\partial x} + \frac{\partial N_{\beta}}{\partial t} \cdot \frac{\partial t}{\partial x} \right) + \left(\frac{\partial N_{\alpha}}{\partial s} \cdot \frac{\partial s}{\partial y} + \frac{\partial N_{\alpha}}{\partial t} \cdot \frac{\partial t}{\partial y} \right) \cdot \left(\frac{\partial N_{\beta}}{\partial s} \cdot \frac{\partial s}{\partial y} + \frac{\partial N_{\beta}}{\partial t} \cdot \frac{\partial t}{\partial y} \right) \right\} J ds dt \quad (4-71)$$

In order to compute this integral, the derivatives of s and t with respect to x and y must be computed in terms of s and t. The derivation of these is presented in the following. The differential of x and y are as follows:

$$dx = \sum_{i=1}^4 \left[x_i \left\{ \frac{\partial N_i}{\partial s} \cdot ds + \frac{\partial N_i}{\partial t} \cdot dt \right\} \right] \quad (4-72)$$

$$dy = \sum_{i=1}^4 \left[y_i \left\{ \frac{\partial N_i}{\partial s} \cdot ds + \frac{\partial N_i}{\partial t} \cdot dt \right\} \right] \quad (4-73)$$

Solving these equations for ds and dt gives the following:

$$ds = \frac{\partial s}{\partial x} \cdot dx + \frac{\partial s}{\partial y} \cdot dy = \frac{1}{J} \left(\frac{\partial y}{\partial t} \cdot dx - \frac{\partial x}{\partial t} \cdot dy \right) \quad (4-74)$$

$$dt = \frac{\partial t}{\partial x} \cdot dx + \frac{\partial t}{\partial y} \cdot dy = \frac{1}{J} \left(-\frac{\partial y}{\partial s} \cdot dx + \frac{\partial x}{\partial s} \cdot dy \right) \quad (4-75)$$

Solving for the various derivatives gives the following:

$$\frac{\partial s}{\partial x} = \frac{1}{J} \cdot \frac{\partial y}{\partial t} \quad (4-76) \quad \frac{\partial t}{\partial x} = -\frac{1}{J} \cdot \frac{\partial y}{\partial s} \quad (4-77)$$

$$\frac{\partial t}{\partial y} = -\frac{1}{J} \cdot \frac{\partial x}{\partial s} \quad (4-78) \quad \frac{\partial s}{\partial y} = \frac{1}{J} \cdot \frac{\partial x}{\partial t} \quad (4-79)$$

Substituting these relationships into equation (4.69), gives the following:

$$L_{\alpha\beta}^e = \int_{-1}^1 \int_{-1}^1 \left[\left(\frac{\partial N_{\alpha}}{\partial s} \cdot \frac{\partial y}{\partial t} - \frac{\partial N_{\alpha}}{\partial t} \cdot \frac{\partial y}{\partial s} \right) \left(\frac{\partial N_{\beta}}{\partial s} \cdot \frac{\partial y}{\partial t} - \frac{\partial N_{\beta}}{\partial t} \cdot \frac{\partial y}{\partial s} \right) + \left(\frac{\partial N_{\alpha}}{\partial t} \cdot \frac{\partial x}{\partial s} - \frac{\partial N_{\alpha}}{\partial s} \cdot \frac{\partial x}{\partial t} \right) \left(\frac{\partial N_{\beta}}{\partial t} \cdot \frac{\partial x}{\partial s} - \frac{\partial N_{\beta}}{\partial s} \cdot \frac{\partial x}{\partial t} \right) \right] \left(\frac{1}{J} \right) ds dt \quad (4-80)$$

The same DO loop discussed earlier can be used to convert the elemental matrix $L_{\alpha\beta}^e$ into the global matrix L_{ij} . However, the actual assembly method utilized in the final program will not be discussed. Again, the final program generates [L] in band storage mode and the assembly program must take this into consideration.

The surface integral present in equation (4-48) must also be evaluated before solutions can be generated. The surface Γ_I can be parameterized by a single parameter, ξ . This can be represented by the following for each element on the fiber/matrix interface:

$$x = x_{n+1} \bar{N}_{n+1}(\xi) + x_n \bar{N}_n(\xi) \quad (4-81)$$

$$y = y_{n+1} \bar{N}_{n+1}(\xi) + y_n \bar{N}_n(\xi) \quad (4-82)$$

Where x_{n+1} and y_{n+1} are the end node positions on element n, x_n and y_n are the starting node positions on element n, \bar{N}_i are the shape functions utilized in the approximations, and ξ is the single parameter utilized in the approximation ($-1 \leq \xi \leq 1$). The numerical calculations are simpler for the FORTRAN code if the shape functions utilized to approximate the fiber/matrix boundary are set equal to the shape functions utilized to approximate the solution domain with s set equal to -1 . With this approximation, ξ is equivalent to t in the results generated previously. Utilizing this approximation, the surface integral can be approximated by the following integral over a 1-D master element:

$$\oint_{\Gamma_I} \left(\frac{1}{\rho} \right) (n_s \cdot n) \psi_j d\Gamma = \left(\frac{1}{\rho} \right) (n_s \cdot n) \sum_{elements} \int_{-1}^1 \psi_j(x(\xi), y(\xi)) \sqrt{\left(\frac{dx}{d\xi} \right)^2 + \left(\frac{dy}{d\xi} \right)^2} d\xi \quad (4-83)$$

where the flux and density have been factored out because they are considered constant.

The numerical integration scheme utilized to evaluate the elemental matrices [M] and [L], evaluate equation (4-48), and to integrate equation (4-9) to obtain the amount of sizing dissolved is Gaussian-Quadrature. Gaussian-Quadrature is very efficient at integrating polynomials or perturbations on polynomials. The quadrature approximation for an integral is as follows:

$$g(y) = \int_{-1}^1 f(x, y) dx \approx \sum_{i=1}^{quad} \omega_i f(x_i, y) \quad (4-84)$$

where *quad* is the number of quadrature points, ω_i is the weight for quadrature point i, and x_i is the value for the quadrature point. If the degree of the function $f(x,y)$ is n^{th} order in x then $\frac{1}{2} \cdot (n + 1)$ quadrature points are needed to exactly integrate equation (4-84) [4.4]. If $f(x,y)$ is not a polynomial or is a slight perturbation of a polynomial, then a higher number of quadrature points are needed to accurately integrate equation (4-84). A non-constant dissolution diffusion coefficient creates an instance where the $f(x,y)$ is a perturbation from a polynomial. For a

definite integral with limits equal to (-1,1), the first ten Gauss points and their weights are as follows [4.3]:

$x_1 = -0.973906528517172$	$\omega_1 = 0.066671344308688$
$x_2 = -0.865063366688985$	$\omega_2 = 0.149451349150581$
$x_3 = -0.679409568299024$	$\omega_3 = 0.219086362515982$
$x_4 = -0.433395394129247$	$\omega_4 = 0.269266719309996$
$x_5 = -0.148874338981631$	$\omega_5 = 0.295524224714753$
$x_6 = 0.973906528517172$	$\omega_6 = 0.066671344308688$
$x_7 = 0.865063366688985$	$\omega_7 = 0.149451349150581$
$x_8 = 0.679409568299024$	$\omega_8 = 0.219086362515982$
$x_9 = 0.433395394129247$	$\omega_9 = 0.269266719309996$
$x_{10} = 0.148874338981631$	$\omega_{10} = 0.295524224714753$

A double integral can be approximated by applying equation (4-84) twice as the following represents:

$$\int_{-1}^1 \int_{-1}^1 f(x, y) dx dy = \int_{-1}^1 g(y) dy \approx \sum_{j=1}^{quad} \omega_j g(y_j) \approx \sum_{j=1}^{quad} \sum_{i=1}^{quad} \omega_j \omega_i f(x_i, y_j) \quad (4-85)$$

where $g(y)$ is the function presented earlier in equation (4-84). This completes the specification of the matrices [M] and [L]. With this information, the vectors [Q] and [R] can be computed because they are merely the sum of certain terms in [M] and [L]. This completes the specifications needed to solve equations (4-49) and (4-50).

4.4.5 Storage of Matrices in Banded Form

For a well-defined mesh, equations (4-49) and (4-50) occupy an extremely large amount of computer memory. The matrices [A] and [B] are symmetric banded matrices with the half-bandwidth equal to the number of fiber/matrix boundary nodes plus 2. In other words, for a mesh containing 12 nodes and 4 nodes on the fiber/matrix boundary, the (12 X 12) matrices [A] and [B] can be represented by a (12 X 6) banded matrix (Figure 4.4-4). The band storage method saves 50% of the computer memory for this particular mesh. For meshes used later in the section 4.6 that contain 306 nodes and 6 fiber/matrix boundary nodes, the banded storage results in a 97% savings on computer memory. In addition, the computational times are greatly reduced. The storage of matrices in banded mode is not trivial. At first glance, it may seem rather simple to convert a symmetric banded matrix into a matrix stored in banded form. This is true if one has the symmetric banded matrix already generated and stored in full-form. However,

$$a) \quad [c] = \begin{bmatrix} \# & \# & 0 & 0 & \# & \# & 0 & 0 & 0 & 0 & 0 & 0 \\ \# & \# & \# & 0 & \# & \# & \# & 0 & 0 & 0 & 0 & 0 \\ 0 & \# & \# & \# & 0 & \# & \# & \# & 0 & 0 & 0 & 0 \\ 0 & 0 & \# & \# & 0 & 0 & \# & \# & 0 & 0 & 0 & 0 \\ \# & \# & 0 & 0 & \# & \# & 0 & 0 & \# & \# & 0 & 0 \\ \# & \# & \# & 0 & \# & \# & \# & 0 & \# & \# & \# & 0 \\ 0 & \# & \# & \# & 0 & \# & \# & \# & 0 & \# & \# & \# \\ 0 & 0 & \# & \# & 0 & 0 & \# & \# & 0 & 0 & \# & \# \\ 0 & 0 & 0 & 0 & \# & \# & 0 & 0 & \# & \# & 0 & 0 \\ 0 & 0 & 0 & 0 & \# & \# & 0 & 0 & \# & \# & \# & 0 \\ 0 & 0 & 0 & 0 & 0 & \# & \# & \# & 0 & \# & \# & \# \\ 0 & 0 & 0 & 0 & 0 & 0 & \# & \# & 0 & 0 & \# & \# \end{bmatrix}$$

$$b) \quad [c] = \begin{bmatrix} \# & \# & 0 & 0 & \# & \# \\ \# & \# & 0 & \# & \# & \# \\ \# & \# & 0 & \# & \# & \# \\ \# & 0 & 0 & \# & \# & 0 \\ \# & \# & 0 & 0 & \# & \# \\ \# & \# & 0 & \# & \# & \# \\ \# & \# & 0 & \# & \# & \# \\ \# & 0 & 0 & \# & \# & 0 \\ \# & \# & 0 & 0 & 0 & 0 \\ \# & \# & 0 & 0 & 0 & 0 \\ \# & \# & 0 & 0 & 0 & 0 \\ \# & 0 & 0 & 0 & 0 & 0 \end{bmatrix}$$

Figure 4.4-4 a). Schematic of a symmetric banded matrix of dimension 12X12. b.) Schematic of the same matrix stored in banded form with dimension now 12X6.

if one has to generate the matrix in banded form without having the full-form matrix available, then the computation is quite tedious. The final program listed in **Appendix II** successfully stores all matrices in banded form and performs calculations on these matrices. As was discussed earlier, the details of how the code generates the banded matrices without having the matrix in full-form will not be discussed. However, the complexities created in working entirely with banded matrices can be demonstrated for a simple matrix calculation. For instance, the simple matrix multiplication of $[A] \cdot [w]$ can easily be programmed by the following if $[A]$ is stored in its full form.

```
DO 100 J=1, NODES
  F(I) = F(I) + A(I,J)*W(J)
100 CONTINUE
```

However, if $[A]$ is stored in banded form, then the following code completes the same multiplication.

```
UP = NODES - I + 1
```

```

IF (UP.GE.BAND) THEN
  UPPER = BAND
ELSE
  UPPER = UP
ENDIF
DO 100 J=2-BAND,UPPER,1
  ACTUAL = I + J - 1
  IF (ACTUAL.GE.I) THEN
    F(I) = F(I) + A(I,J)*W(ACTUAL)
  ELSE
    IF (ACTUAL.GT.0) THEN
      COLUMN = I - ACTUAL + 1
      F(I) = F(I) + A(ACTUAL,COLUMN)*W(ACTUAL)
    ENDIF
  ENDIF
ENDIF
100 CONTINUE

```

Therefore, the code required to complete calculations involving matrices stored in banded mode is considerably more complex than the same code for fully stored matrices. However, the computational time is greatly reduced due to the fact that the total number of calculations has been reduced.

The resulting equations are solved by a linear equation solver developed specifically for symmetric matrices stored in banded mode [4.5]. For simulations involving the specification of a flux at the fiber/matrix interface, the code checks to verify that thermodynamic equilibrium is not violated. If thermodynamic equilibrium is violated, then thermodynamic equilibrium is enforced at the fiber/matrix interface. The final non-fickian FEM code is listed in **Appendix II**.

4.4.6 Verification of the FEM Code Against an Analytical Solution

For the proposal portion of this work, a FEM code was written that assumed fickian behavior and that the fiber/matrix interface was controlled by thermodynamic equilibrium. The validity of this model and the results developed with it have been discussed elsewhere [4.6]. The results of this model will be discussed in section 4.5.1.

The final interphase formation non-fickian FEM code will be verified against analytical models in this section. As was discussed earlier, the final non-fickian FEM code has numerous complexities that were not in the original fickian FEM model. First, the code can now accept non-fickian dissolution diffusion coefficients. Second, the code can accept a flux or relaxation/disentanglement rate at the fiber/matrix interface. In addition, the code now calculates, stores, and solves matrices that are stored in banded form.

Before the results generated by the non-fickian FEM code can be considered valid, the code must be verified for accuracy against analytical solutions for simplified solution domains. As was discussed in section 4.3, an analytical solution exists for the case of fickian diffusion between two infinite parallel plates. The solution generated in section 4.3 can be used to verify the non-fickian FEM code applied to a fickian dissolution diffusion coefficient. Even though this analytical solution was a one-dimensional solution and the FEM program was designed for a 2-D simulation, the two solutions can be compared. In order to compare the two results, a mesh applicable to the parallel plate geometry had to be created. A 2-D 1000 element mesh that had 5 vertical elements (y-axis) and 200 horizontal elements (x-axis) was used for the verification. Thermodynamic equilibrium was implemented at the $x=0$ boundary. The three other boundaries were set to zero-flux/impermeable. Only 5 vertical elements were selected because there should be no variation in sizing concentration in the y-direction due to axis of symmetry arguments. The time required to dissolve a certain amount of sizing was determined for both the 2-D FEM model and the 1-D analytical solution for a specified set of physical parameters. In addition, the sizing weight fraction as a function of time and position was generated. The predicted time for dissolution between the FEM solution and the analytical solution were 0.00640 and 0.00636 seconds. At a time of $1.0E-6$ seconds, which is below the dissolution time, the concentration profiles are identical (Figure 4.4-5). At a time of 0.008 seconds, which is slightly after the dissolution time, the solutions are again identical except at positions extremely close to the fiber/matrix interface (Figure 4.4-6). However, the maximum error between the analytical solution and the FEM solution was only 4% for this time period. At a time of 0.02 seconds, the solutions are essentially identical with a maximum difference of 0.3% (Figure 4.4-7). At a time of 0.125 seconds, the solutions are again identical with a maximum difference between the two solutions of 0.5% (Figure 4.4-8). Therefore, the non-fickian FEM code with a fickian dissolution diffusion coefficient accurately predicts the concentration profile for a thermodynamic

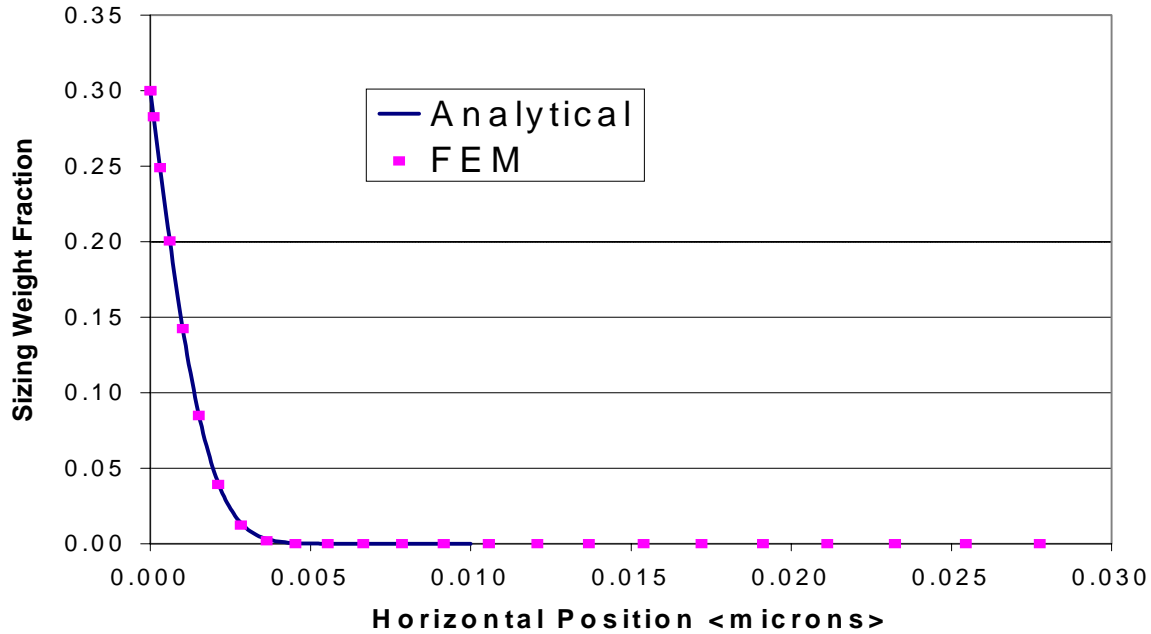


Figure 4.4-5 Comparison of Analytical Solution to Simplified Domain versus FEM Solution to Simplified Domain. ($D_d = 1.0 \mu\text{m}^2/\text{s}$, $w_s^{\text{eq}} = 0.3$, $M_s = 0.02$, $\theta = 0.5$, $dt = 0.0001$). Time = 0.000001 seconds.

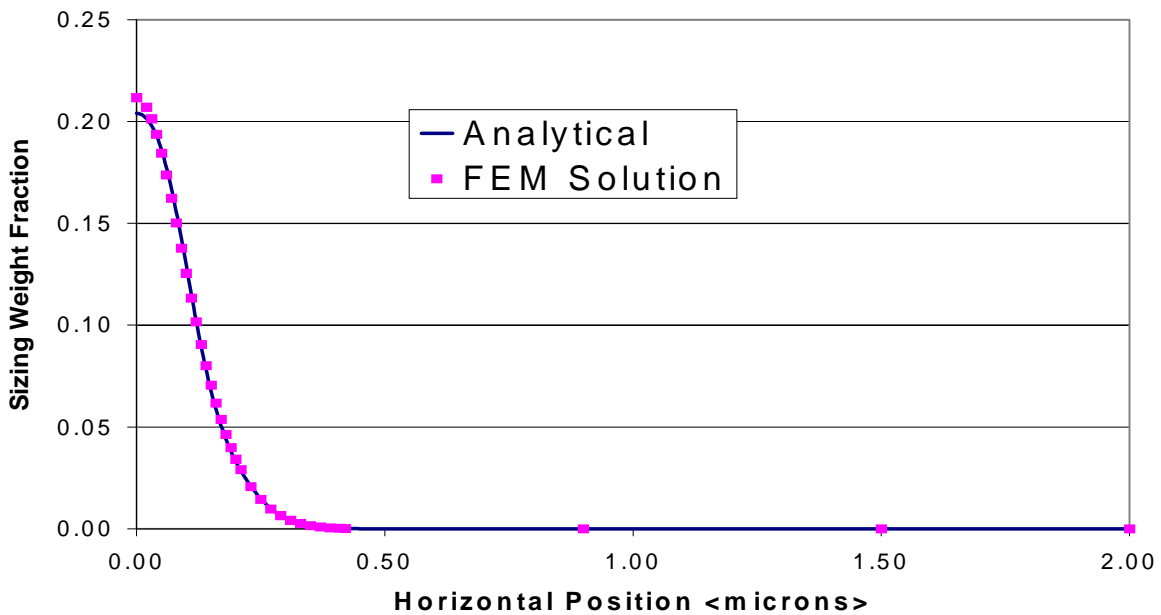


Figure 4.4-6 Comparison of Analytical Solution to Simplified Domain versus FEM Solution to Simplified Domain. ($D_d = 1.0 \mu\text{m}^2/\text{s}$, $w_s^{\text{eq}} = 0.3$, $M_s = 0.02$, $\theta = 0.5$, $dt = 0.0001$). a). Time = 0.008 seconds.

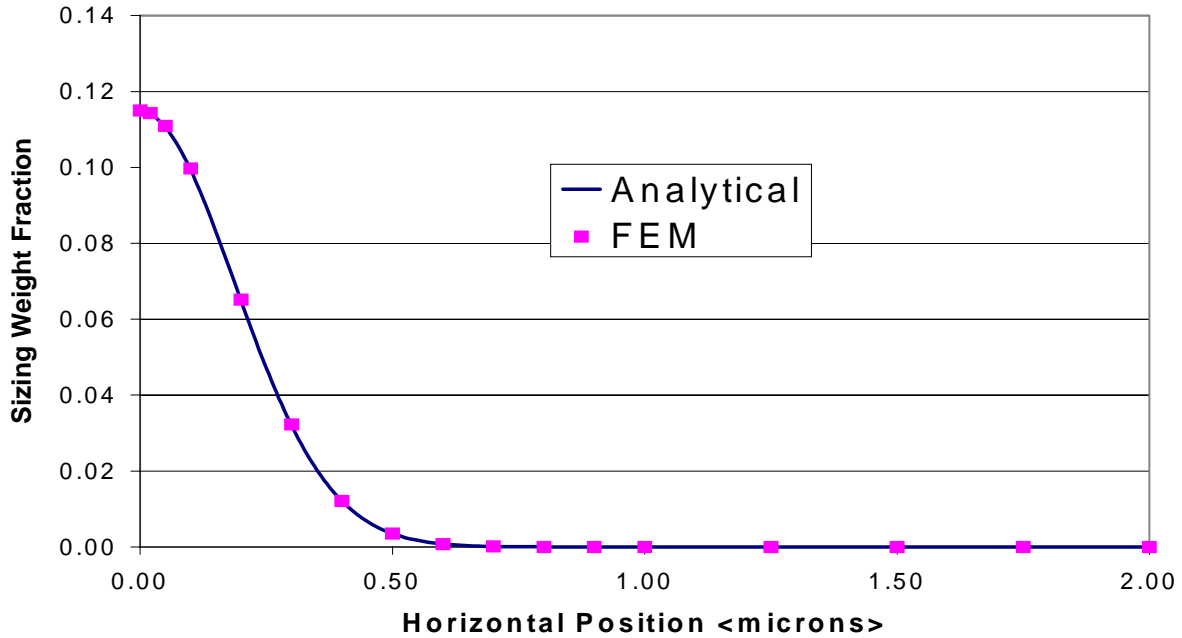


Figure 4.4-7 Comparison of Analytical Solution to Simplified Domain versus FEM Solution to Simplified Domain. ($D_d = 1.0 \mu\text{m}^2/\text{s}$, $w_s^{\text{eq}} = 0.3$, $M_s = 0.02$, $\theta = 0.5$, $dt = 0.0001$). a). Time = 0.02 seconds

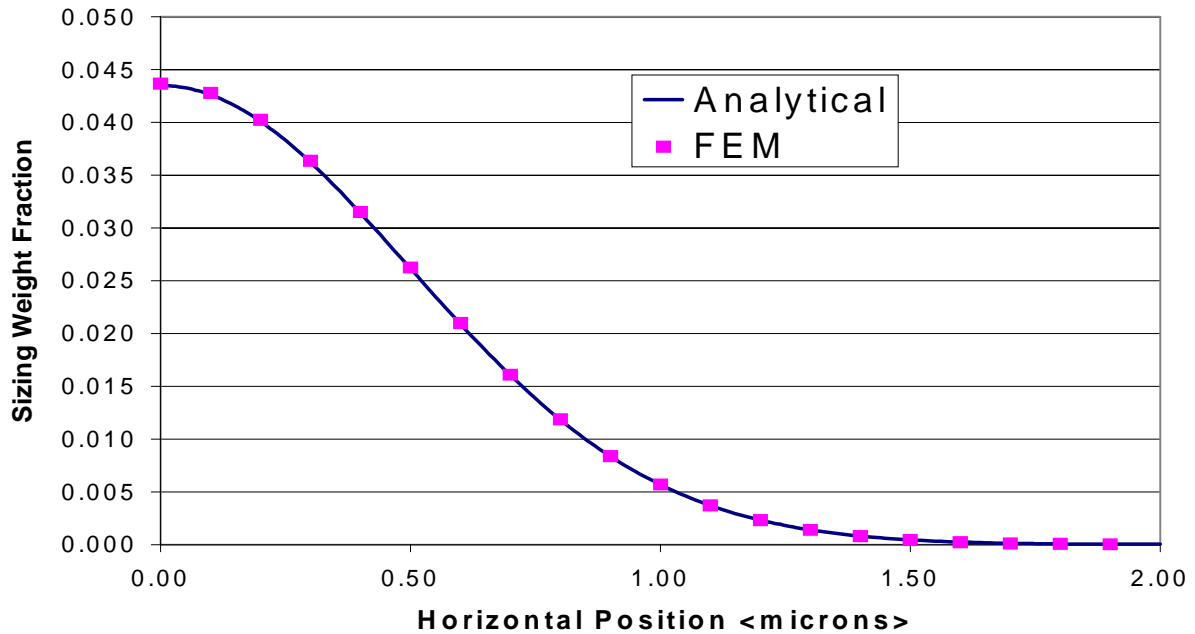


Figure 4.4-8 Comparison of Analytical Solution to Simplified Domain versus FEM Solution to Simplified Domain. ($D_d = 1.0 \mu\text{m}^2/\text{s}$, $w_s^{\text{eq}} = 0.3$, $M_s = 0.02$, $\theta = 0.5$, $dt = 0.0001$). Time = 0.125 seconds.

equilibrium controlled dissolution process. As further verification of the non-fickian FEM code's validity, a flux controlled dissolution process was tested. As was discussed in section 4.3, an analytical solution exists for the case of flux controlled diffusion between two parallel plates. For a flux of $1.0\text{E-}7 \text{ g/cm}^2/\text{s}$ implemented at the $x=0$ boundary, the concentration profile was calculated from equation (4-18) and compared to the FEM solution for times less than the dissolution time (Figure 4.4-9). The solutions are identical for the times selected. However, the times selected were less than 2% of the dissolution time. In order to more fully investigate the FEM model's accuracy, times closer to and beyond the dissolution time needed to be tested. Unfortunately, the flux utilized in these calculations was too small to allow the dissolution time to be reached in a reasonable computational time. Therefore, a second flux of higher value was selected for the second set of verifications. For a flux of $1.0\text{E-}5 \text{ g/cm}^2/\text{s}$ implemented at the $x=0$ boundary, the concentration profile was calculated from equation (4-18) and compared to the FEM solution for times less than the dissolution time (Figure 4.4-10). As was observed in the previous paragraph, the solutions are identical for the times selected. For times close to and beyond the dissolution time of 0.631 seconds, the solutions are again identical (Figure 4.4-11). Therefore, the non-fickian FEM code has been verified against analytical solutions for fickian diffusion processes controlled by thermodynamic equilibrium and relaxation/distentanglement.

The non-fickian portion of the non-fickian FEM code could not be verified due to a lack of analytical solutions for this case.

4.4.7 The Effect of Iterative Looping on the Solution

As was discussed earlier in this chapter, the non-constant dissolution diffusion coefficient creates non-linearity's that complicate the solution of the equations (4-48). The non-linearity's are removed by assuming the diffusion coefficient at time $k+1$ is approximately equal to the diffusion coefficient at time k . The concentration profile is then calculated and the diffusion coefficient at time $k+1$ can be determined. This diffusion coefficient can then be inserted back into the equations and a better estimate of the diffusion coefficient for time $k+1$ can be obtained. Therefore, the approximation should be improved with the completion of each iteration loop. The purpose of this section is to determine the effect of the number of iteration loops on solution convergence.

The mesh and physical parameters utilized for the simulations presented in this section

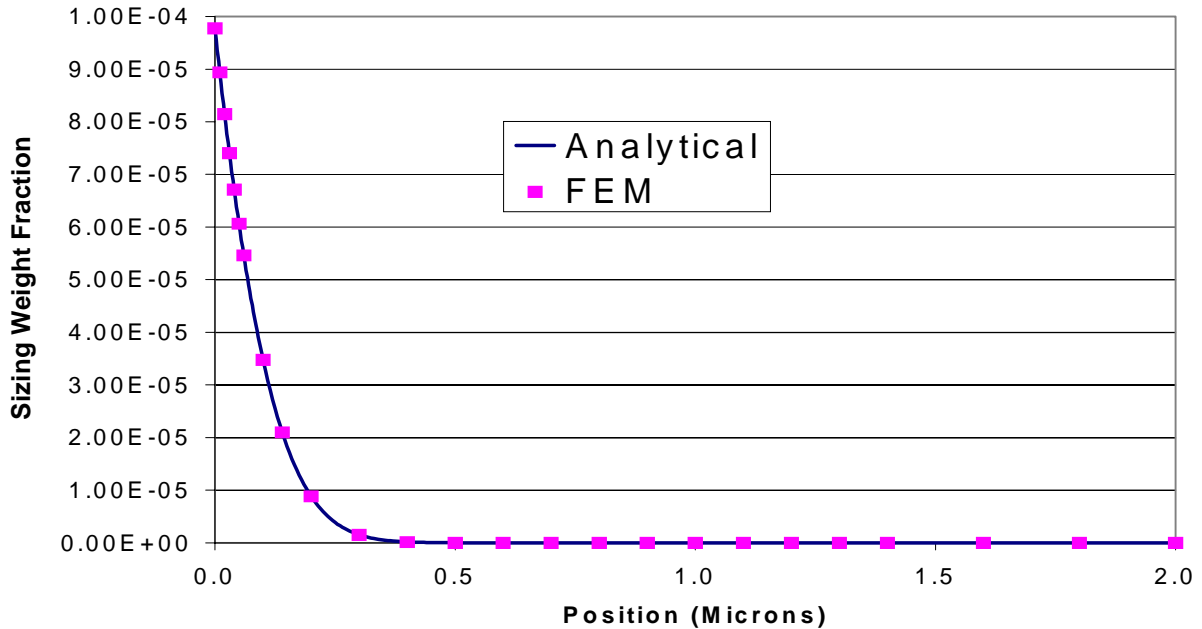


Figure 4.4-9 Comparison of Analytical Solution to Simplified Domain versus FEM Solution to Simplified Domain. ($f_s = 1.0E-7$ g/cm²/s, $D_d = 1.0$ μm²/s, $w_s^{eq} = 0.3$, $M_s = 0.02$, $\theta = 0.5$, $dt = 0.0001$). Time = 0.02 seconds (note: $t_d = 63.1$ seconds).

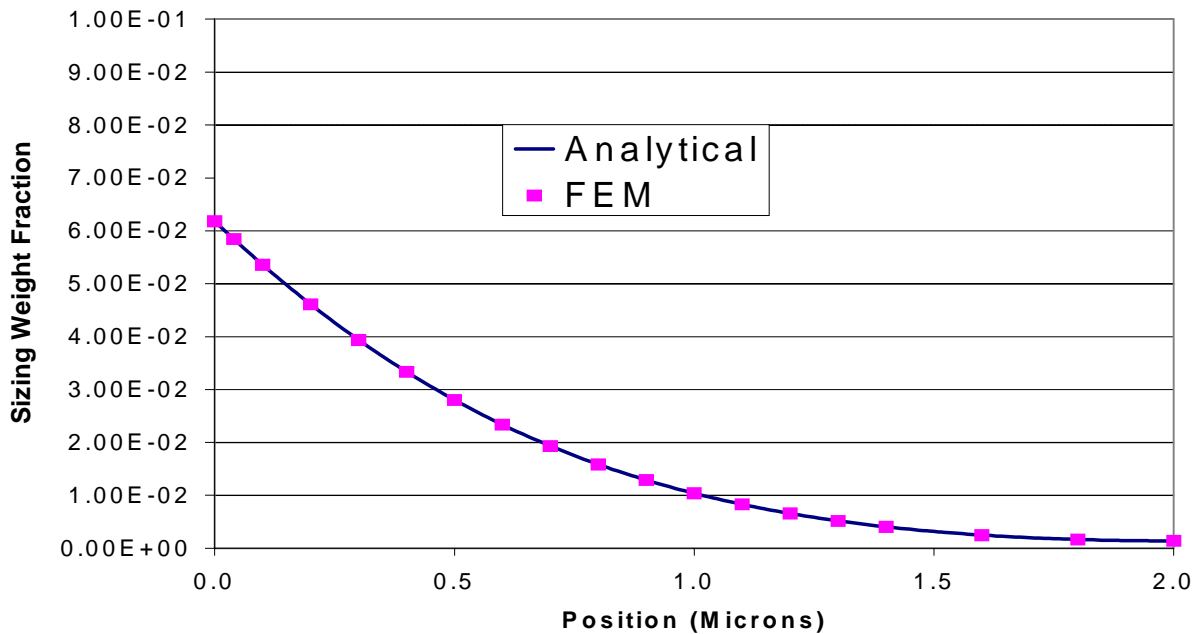


Figure 4.4-10 Comparison of Analytical Solution to Simplified Domain versus FEM Solution to Simplified Domain. ($f_s = 1.0E-5$ g/cm²/s, $D_d = 1.0$ μm²/s, $w_s^{eq} = 0.3$, $M_s = 0.02$, $\theta = 0.5$, $dt = 0.0001$). Note: time = 0.404 seconds < $t_d = 0.631$ seconds).

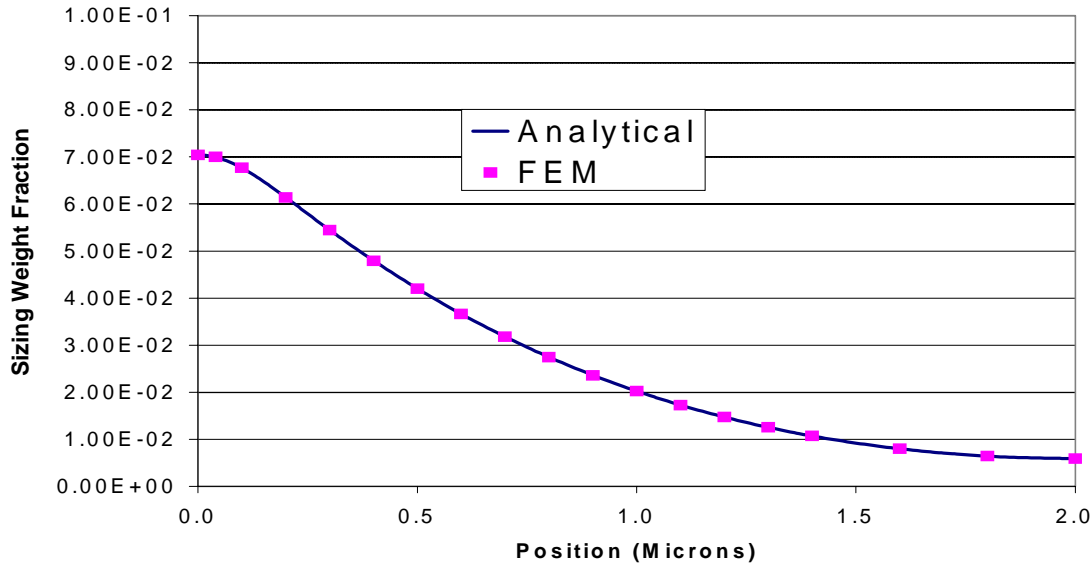


Figure 4.4-11 Comparison of Analytical Solution to Simplified Domain versus FEM Solution to Simplified Domain. ($f_s = 1.0E-5$ g/cm²/s, $D_d = 1.0$ μ²/s, $w_s^{eq} = 0.3$, $M_s = 0.02$, $\theta = 0.5$, $dt = 0.0001$). Time = 0.636 seconds > $t_d = 0.631$ seconds.

are identical to the ones to be discussed in more detail in section 4.4.9. The effect of looping was assessed by varying the number of iteration loops from 1 to 100 and comparing the solutions produced by each (Figure 4.4-12 and Figure 4.4-13). The solutions are essentially identical for the times investigated.

For simulations completed on systems that have thermodynamic equilibrium controlling the interdiffusion, the effect of looping is significant at times close to zero. The effect of looping dampens out at times remote from the initial time. In addition, the approximate solution generated by the FEM code is most erroneous at times close to the initiation time. This result seems paradoxical but does make sense based upon the initial condition input into a thermodynamically controlled interdiffusion problem. At a time equal to zero, the boundary nodes are set equal to the equilibrium value. This can be represented mathematically as a step function. This implies that only the boundary nodes should be equal to the equilibrium values and the solution domain should **not** have any sizing mass present at the initial time. However, the FEM model assumes that the concentration profile is a continuous function of position. For linear shape functions, the FEM code assumes that the sizing concentration profile on the essential boundary elements varies linearly from the equilibrium value to zero across the radial

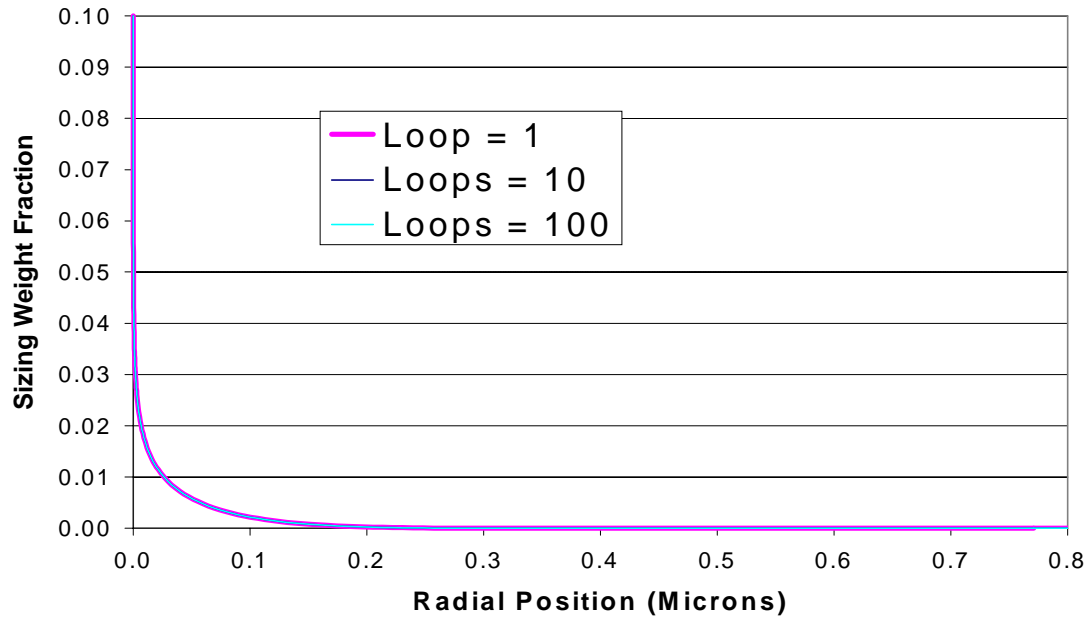


Figure 4.4-12 Non-fickian FEM Solution for 1, 10, and 100 iteration loops. Time equal to 0.5 seconds (Note: $dt = 0.001$ seconds).

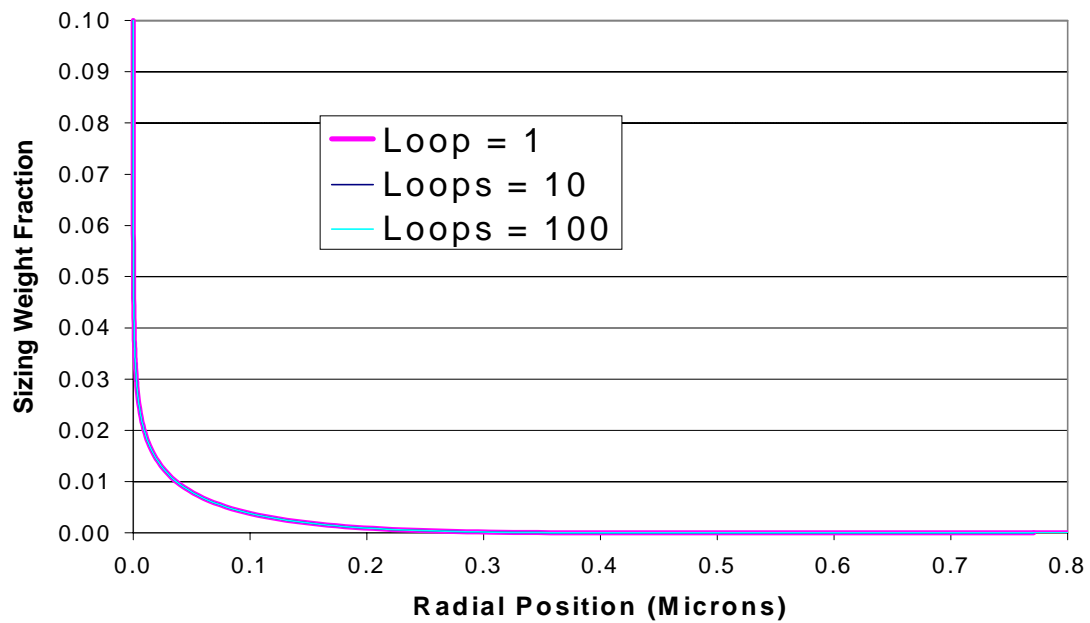


Figure 4.4-13 Non-fickian FEM Solution for 1, 10, and 100 iteration loops. Time equal to 1.0 seconds (Note: $dt = 0.001$ seconds).

length of the element. Therefore, the FEM solution does not start with zero sizing mass initially. At the first time step, the linearly varying concentration profile across the essential boundary element produces an extreme gradient in concentration at the boundary elements. The magnitude of this gradient increases with increasing mesh refinement near the interface. As a result, the predicted concentration profile close to the interface exceeds that allowed by thermodynamic equilibrium (Figure 4.4-14 Note: $\omega_{eq}=0.10$) for times close to the initiation time (time = dt). At times further away from the initiation time (time = 1000dt) (Figure 4.4-15), the solution is well behaved and does not exceed thermodynamic equilibrium. With increasing time, the solution converges to the real solution and the accuracy improves.

Physical reality dictates that no diffusion process initiates with thermodynamic equilibrium controlling the interfacial boundary. However, in systems where the time required to achieve thermodynamic equilibrium is small compared to the time required for the material to diffuse a significant distance away, these systems can be approximated as being equilibrium controlled. In actuality, no material can achieve instantaneous thermodynamic equilibrium even if the resistance to heat and mass transfer are zero. In actuality, all materials achieve thermodynamic equilibrium at a finite rate even though the rate may be negligible compared to the diffusion time. As such, the only physically meaningful initial boundary condition for an interdiffusion process is one that is of flux type. If the flux results in a boundary condition that violates thermodynamic equilibrium, then for the time frame and material system investigated, it is safe to conclude that equilibrium controls the diffusion process. Because all systems in reality are controlled by flux and not equilibrium at initiation, it is not surprising to find that mathematical solutions to flux controlled initiation are much better behaved. FEM solutions to flux controlled initiation are extremely accurate and well-behaved at all times including times close to zero (time = dt) (Figure 4.4-16).

4.4.8 The Effect of the Time Step Size

As expressed by equation (4-40), the size of the time step, dt, should greatly influence the stability and accuracy of the temporal finite difference approximations utilized in the FEM model. For all simulation results presented in this dissertation, the value for theta was chosen to be 0.5, which implies a stable solution for any time step value. A stable solution is one that does not uncontrollably oscillate [4.2]. However, this does not imply an accurate solution. For the

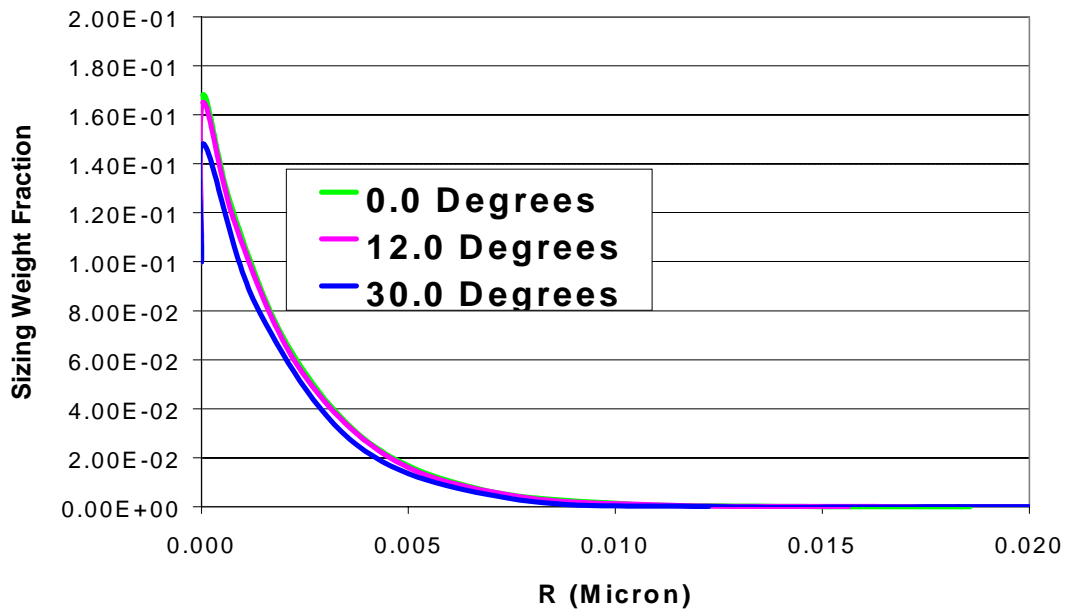


Figure 4.4-14 Non-fickian FEM Solution for time equal to 0.001 seconds or dt (note: overshoot above thermodynamic equilibrium of 0.10).

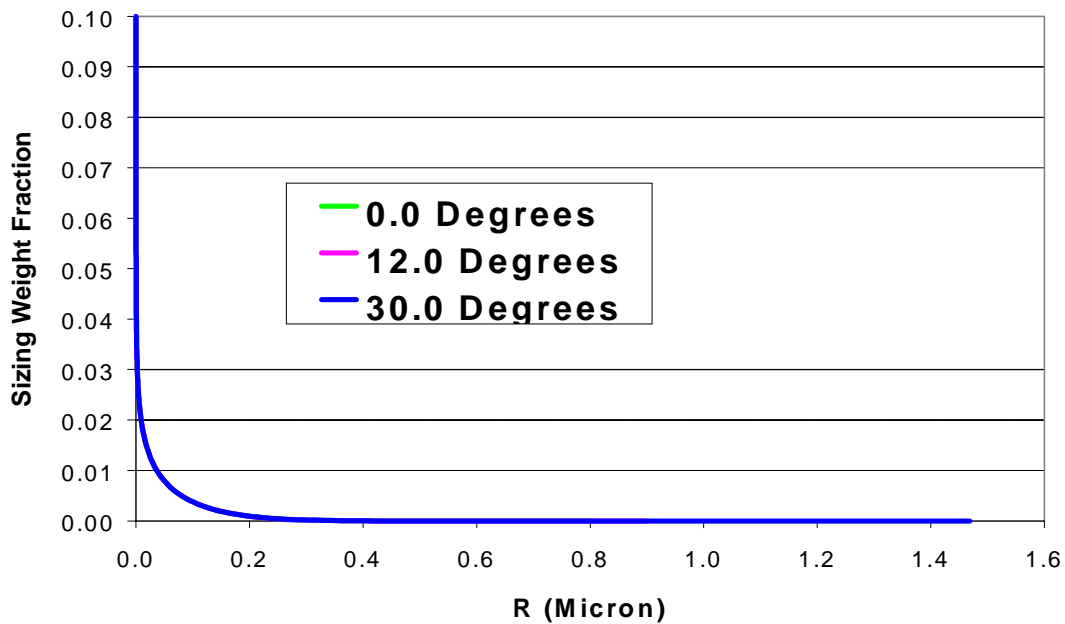


Figure 4.4-15 Non-fickian FEM Solution for Time equal to 1.0 seconds or 1000 dt (note: no overshoot).

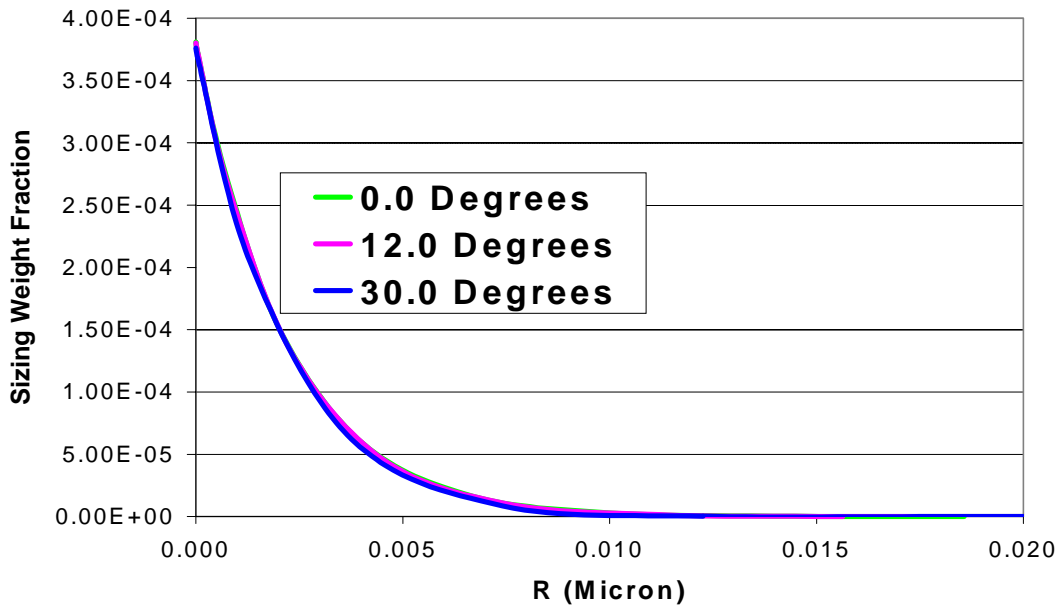


Figure 4.4-16 Non-fickian FEM solution for flux controlled dissolution (note: same conditions as Figure 4.4.6 but flux = $1.0E-7$ g/cm²/s). Time = 0.001 seconds.

simulation results presented in section 4.4.8, the theoretical composite mesh to be discussed in section 4.4.9 will be utilized. In addition, the physical parameters utilized will be discussed in more detail in section 4.5. To summarize, the dissolution diffusion coefficient was assumed to have the following concentration dependence:

$$D_d = 0.01 \exp(-128.41\omega_s) \quad (4-86)$$

where D_d is the dissolution diffusion coefficient in $\mu\text{m}^2/\text{sec}$ and ω_s is the sizing weight fraction. The thermodynamic equilibrium of the sizing in the matrix, ω_s^{eq} was assumed to equal 0.10.

The effect of time step size was investigated by varying the time step from $1.0E-4$ seconds to $1.0E-1$ seconds. At a time of 0.1 seconds, the FEM solutions for the different time steps are distinctly different (Figure 4.4-17). For the time steps of 0.1 and 0.01 seconds, the solution violates thermodynamic equilibrium, which is impossible. However, for the smaller time steps of 0.001 and 0.0001 seconds, the solution is well-behaved and does not violate thermodynamic equilibrium. In addition, there is negligible difference between the concentration profile predicted by the two smaller time steps. At a time of 5.0 seconds (Figure 4.4-18), the three smallest time steps produce a well-behaved solution. These three time steps also produce concentration profiles that are essentially identical. The largest time step of 0.1

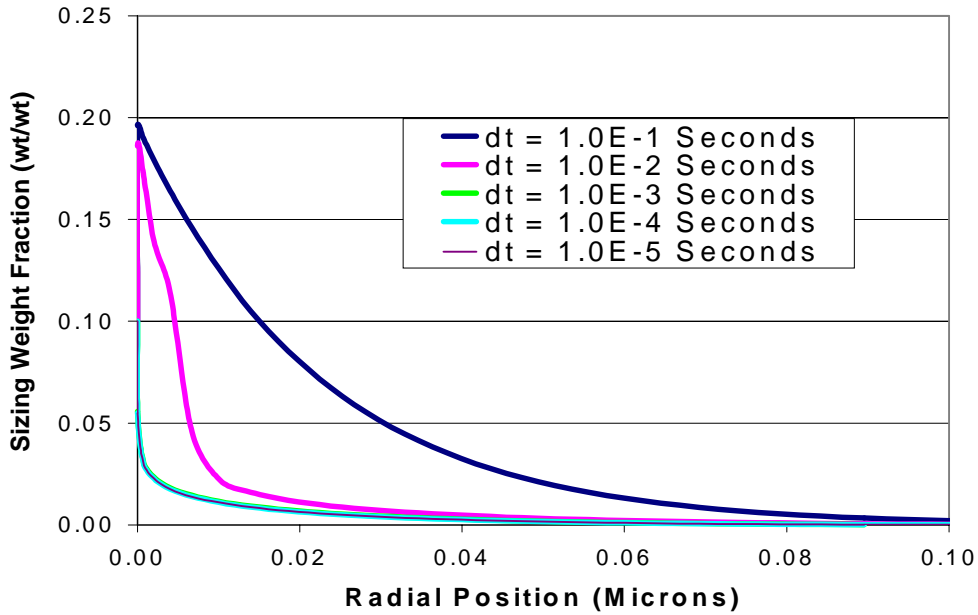


Figure 4.4-17 Non-fickian FEM solution to theoretical composite solution domain for various values of the time step. Time is equal to 0.1 seconds. (Note: $D_d <\mu\text{m}^2/\text{s}> = 0.01\exp(-128.41\omega_s)$, $\omega_s^{\text{eq}} = 0.10$, and $\nu_f = 0.60$).

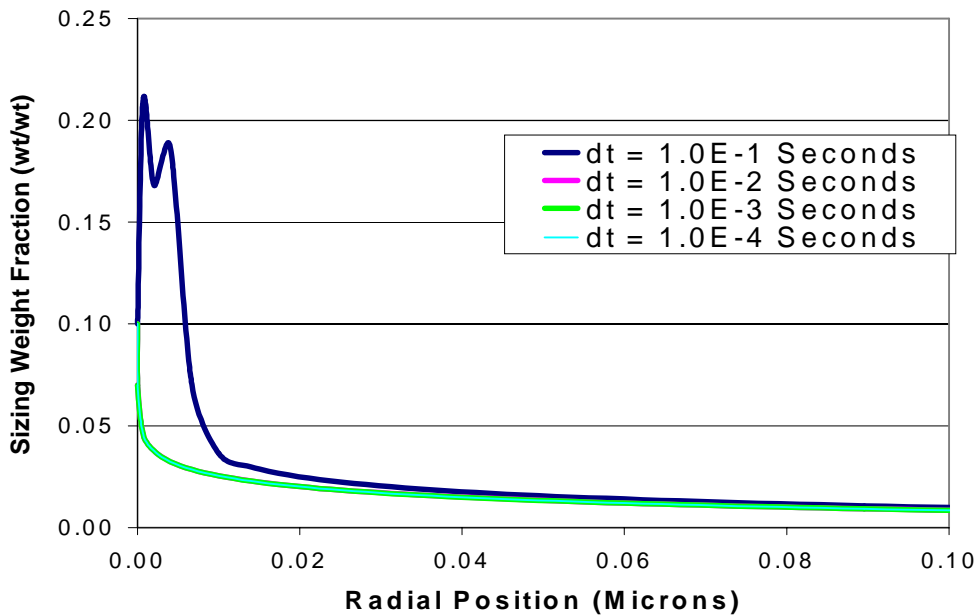


Figure 4.4-18 Non-fickian FEM solution to theoretical composite solution domain for various values of the time step. Time is equal to 5.0 seconds. (Note: $D_d <\mu\text{m}^2/\text{s}> = 0.01\exp(-128.41\omega_s)$, $\omega_s^{\text{eq}} = 0.10$, and $\nu_f = 0.60$).

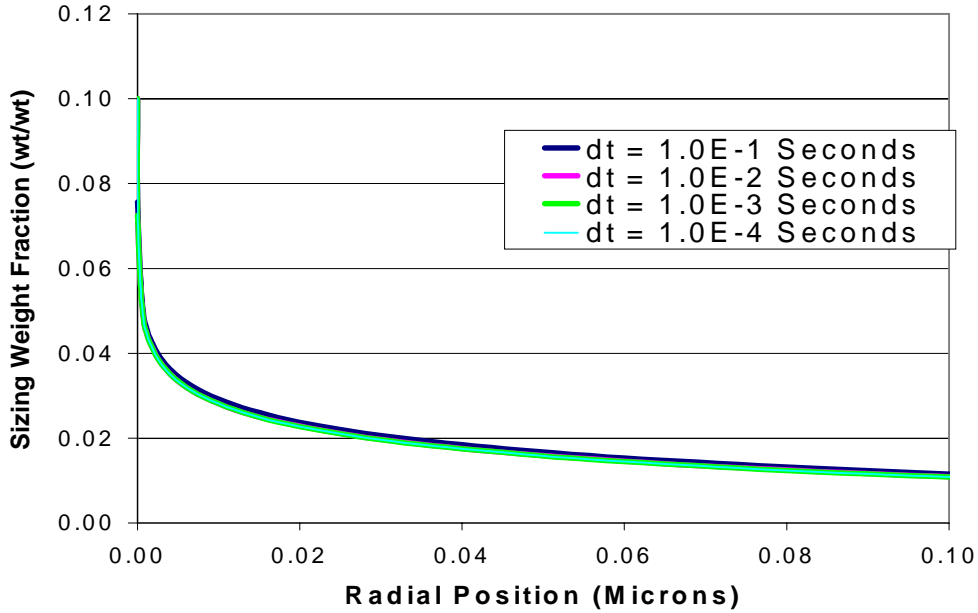


Figure 4.4-19 Non-fickian FEM solution to theoretical composite solution domain for various values of the time step. Time is equal to 10.0 seconds. (Note: $D_d <\mu\text{m}^2/\text{s}> = 0.01\exp(-128.41\omega_s)$, $\omega_s^{\text{eq}} = 0.10$, and $\nu_f = 0.60$).

seconds still produces a concentration that violates equilibrium. At a time of 10.0 seconds (Figure 4.4-19), all four time steps produce well-behaved solutions. In addition, there are negligible differences between the concentration profiles produced by each time step.

Therefore, for a theta of 0.5, the accuracy of the FEM solution is only dependent upon the time step for times similar in magnitude to the time step. This suggests that a small time step is needed for the early time solutions while a larger time step can be utilized for the later solutions. In order to take advantage of this observation and to minimize the time required to complete a simulation, the FEM code was modified to allow the user to input two different functional forms for a variable time step. The first functional form of the time step is a ramp and soak. The second is a linearly varying time step.

The linearly varying time step function present in the non-fickian FEM code was utilized to determine the effect of a variable time step. For an initial time step of 0.001 seconds and a final time step of 0.1 seconds, the concentration profiles produced were identical to that produced for a constant time step of 0.001 seconds for all times investigated (0.1 to 900

seconds). However, the total simulation time required for the variable time step simulation was approximately $1/50^{\text{th}}$ of the total simulation time required for the constant time step simulation.

4.4.9 The Effect of the Number of Elements in the Mesh

The mesh program discussed in section 4.4.2 was used to generate theoretical composite meshes for 60% fiber volume fraction composites. In order to investigate the effect of the number of elements on the predicted concentration, two different meshes were investigated. The first mesh had 50 elements in the radial direction and 5 elements in the angular direction for a total of 250 elements. The F ratio, dR_o/dR_f , was set equal to 0.001. In section 4.6, this mesh will be utilized to obtain predictions of the actual interphase for the K-90 and K-30 PVP systems. The second mesh had 150 radial elements and 20 angular elements for a total of 3000 elements. The F ratio, dR_o/dR_f , was set equal to equal 0.01. The second mesh was used to determine the effect of element number on the predicted concentration profile. The second mesh was not used to obtain interphase profiles for the K-90 and K-30 PVP systems due to the long computational time required to solve the equations for such a well-defined mesh. For a time of 5.0 seconds, the predicted concentration profiles are identical (Figure 4.4-20). Therefore, the 250 element mesh provides accurate predictions of the theoretical concentration profile.

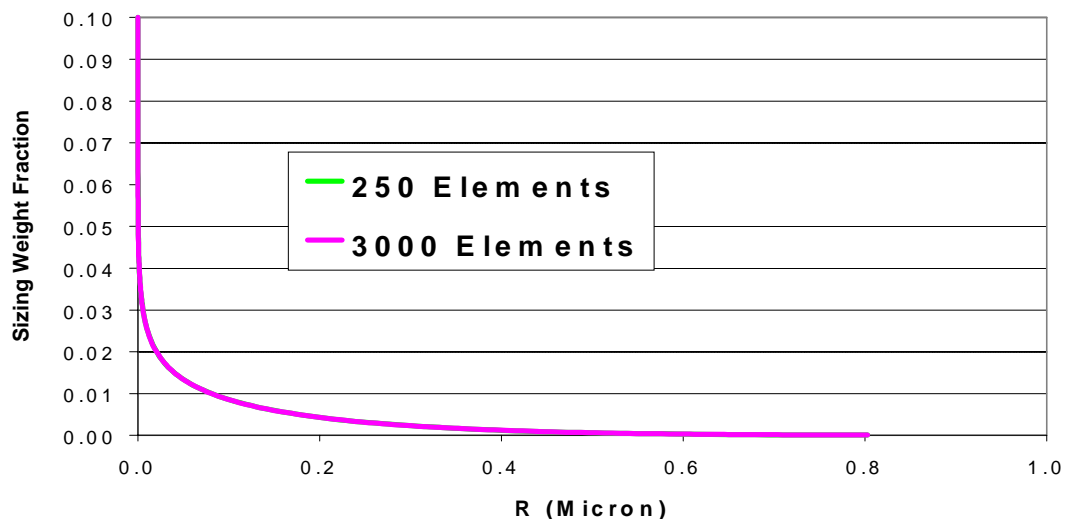


Figure 4.4-20 Non-fickian FEM solution to theoretical composite solution domain for two different meshes. Time is 5.0 seconds. (Note: $D_d <\mu\text{m}^2/\text{s}> = 0.01\exp(-128.41\omega_s)$, $\omega_s^{\text{eq}} = 0.10$, and $\upsilon_f = 0.60$).

4.5 Results of Fickian FEM Applied to the Theoretical Composite

The accuracy of the preliminary FEM was proven elsewhere [4.6]. The results from this model are restated in this section 4.5.1. The results for the fickian model with thermodynamic equilibrium controlling the interdiffusion process provided a range of dissolution diffusion coefficients for which interphase formation is possible. In section 4.6, the constitutive properties presented in Chapter 5 will be utilized along with the newly developed non-fickian FEM code to predict the interphase concentration profile for the K-90 and K-30 PVP systems.

4.5.1 Review of the Results for the Fickian FEM Code Applied to the Theoretical Composite

Utilizing the preliminary fickian diffusion model with thermodynamic equilibrium controlling interdiffusion, concentration profiles for the theoretical composite domain discussed in section 4.1 can be generated after certain physical and processing parameters applicable to the theoretical composite and the pultrusion process are input (Table 4-1). Several sizing weight fraction profiles were generated as a function of the dissolution diffusion coefficient and time (Figure 4.5-1 and Figure 4.5-2). The two figures represent two extremes of interphase formation. In Figure 4.5-1, an interphase is not present due to the lack of diffusion of the sizing into the matrix. In Figure 4.5-2, an interphase is also not present due to the large extent of sizing/matrix interdiffusion. Therefore, for the parameters listed in Table 4-1, a range of dissolution diffusion coefficients needed for the formation of an interphase can be determine from the two figures. For the simulation result shown in Figure 4.5-1, the dissolution diffusion coefficient was 10^{-8} cm^2/sec and the processing time was 0.001 seconds. Therefore, for a pultrusion processing time of 15 minutes, the dissolution diffusion coefficient needed to produce the profile depicted in Figure 4.5-1 is 1.1×10^{-14} cm^2/sec . For the simulation result shown in Figure 4.5-2, the dissolution diffusion coefficient was 10^{-8} cm^2/sec and the processing time was 0.05 seconds. Therefore, for a pultrusion processing time of 15 minutes, the dissolution diffusion coefficient needed to produce the profile depicted in Figure 4.5-2 is 5.6×10^{-13} cm^2/sec . In summary, for an idealized composite of 60% fiber volume fraction, a sizing level of 2.0 wt%, a processing time of 15 minutes, and a thermodynamic equilibrium of 30 wt% sizing in matrix, the range of dissolution diffusion coefficient needed for interphase formation is approximately 10^{-12} to 10^{-14} cm^2/sec . However, this range should be viewed very qualitatively. The existence of an

Table 4-1 Physical constants utilized for idealized composite FEM simulation. a.) Parameters utilized by the meshing program to generate the mesh. b.) Physical constants used by the FEM program. c.) Numerical parameters needed to approximate the temporal evolution.

a.)

Mesh Parameters

Composite Fiber Volume Fraction	0.60
Radius of the Fiber	3.5 μm

b.)

Physical Constants

Processing Time	15 minutes
Fiber Density (ρ_f)	1.78 g/cm ³
Radius of the Fiber	3.5 μm
Matrix Density (ρ_m)	1.16 g/cm ³
Sizing Density (ρ_s)	1.16 g/cm ³
Thermodynamic Equilibrium Weight Fraction of Sizing in Matrix (ω_s)	Varied according to sizing
Sizing Weight Fraction on Fiber	0.02
D_d (Dissolution Diffusion Coefficient)	Varied according to sizing

c.)

Numerical Parameters

θ	0.5
Δt_0 (seconds)	K-90: 1.0E-3 K-30: 5.0E-5
Δt_r (seconds)	K-90: 1.0E-3 K-30: 1.0E-1

interphase is dependent upon one's rigorous definition of an interphase.

These results compare somewhat favorably with the simplified analytical interphase formation model discussed in section 4.3. In that section, for the same physical and processing parameters, the range of dissolution diffusion coefficient needed for interphase formation was found to be between 10^{-11} and 10^{-14} cm²/sec. The discrepancy between the two models can be accounted for by the fact that the FEM model correctly accounts for the radial diffusion of the sizing material while the parallel plate model neglects it. The radial nature of the problem allows for the volumetric sink to increase with increasing radius. Therefore, as the diffusion front progresses from the fiber surface (note: r becomes larger), the radial position increases and the volumetric sink increases by $2\pi r \Delta r$ (note: $r \geq R_f$) while for a parallel plate increases by only

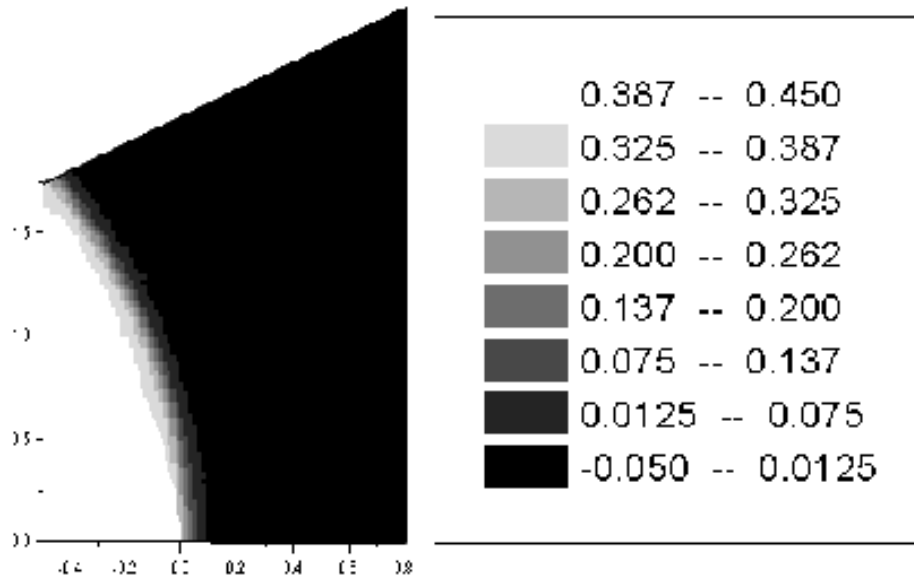


Figure 4.5-1 Sizing weight fraction profiles for $D_d = 10^{-8} \text{ cm}^2/\text{sec}$ and a time equal to 0.001 seconds or a $D_d = 10^{-11} \text{ cm}^2/\text{sec}$ and a time equal to 1.0 seconds.

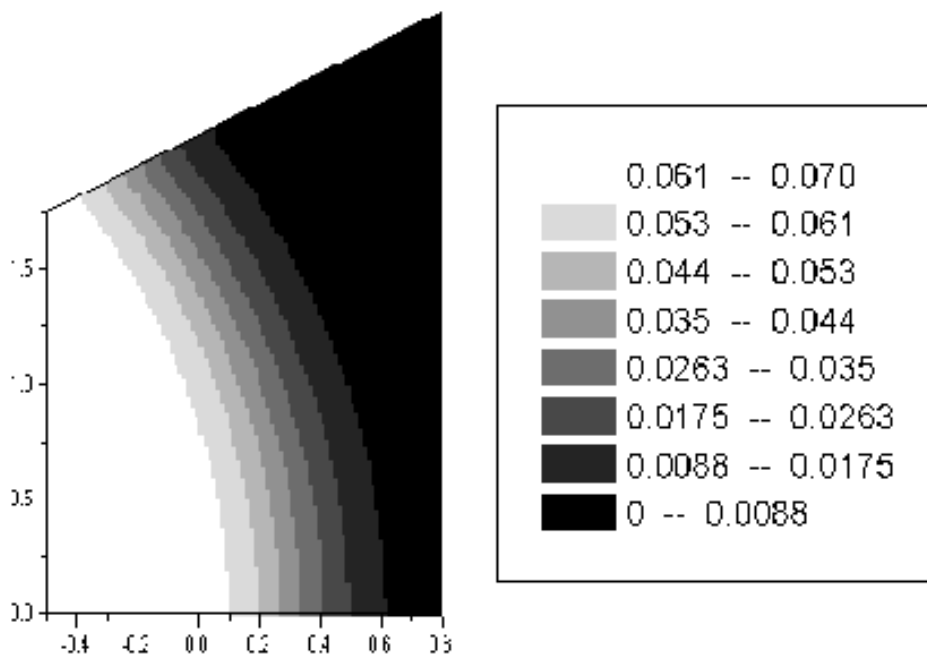


Figure 4.5-2 Sizing weight fraction profiles for $D_d = 10^{-8} \text{ cm}^2/\text{sec}$ and a time equal to 0.05 seconds or a $D_d = 10^{-11} \text{ cm}^2/\text{sec}$ and a time equal to 50 seconds.

$2\pi \cdot R_f \cdot \Delta r$. This increases the rate of mass transfer for the radial diffusion case and also decreases the maximum dissolution diffusion coefficient allowable for interphase formation. The minimum dissolution diffusion coefficient is identical for both models because of the small diffusion distances associated with a smaller D_d . The radial diffusion at regions close to the fiber/matrix interface is essentially identical to 1-D diffusion in a parallel plate region. It is not until the diffusion distance becomes on the same order of magnitude as the fiber radius does the effect of curvature become significant.

As will be discussed in Chapter 5, the dissolution diffusion coefficient was found to be highly non-fickian for both the K-90 PVP and K-30 PVP/Derakane systems. Therefore, the results presented in this section are not strictly applicable to the actual composite interphase. However, the range of dissolution diffusion coefficient needed for interphase formation that were generated from this simplified model can be used as a guide for determining whether a specific sizing material will result in the formation of an interphase.

4.6 Non-Fickian FEM Model Applied to the Theoretical Composite

In this section, the non-fickian FEM model and the composite mesh generation program developed in this chapter will be utilized to predict the interphase concentration profile as a function of the K-90 and K-30 PVP constitutive properties determined in Chapter 5. The constitutive properties of these two systems will be reviewed in the next two paragraphs. The mesh utilized for both the K-90 and K-30 PVP simulations will be the 250 element (note: 306 nodes) mesh discussed in section 4.4.8. The physical constants utilized for the simulations presented in this section are summarized in Table 4-1.

As will be discussed in more detail in Chapter 5, the K-90 PVP/Derakane system was found to be dissolution controlled. The swelling and relaxation portions of the K-90 PVP diffusion process are extremely fast compared to the dissolution portion. The K-90 PVP in Derakane™ dissolution diffusion coefficient was estimated to have the following concentration dependence:

$$D_d^{K-90} = 0.0071 \exp(-128.41\omega_{K-90}) \quad (4-87)$$

where D_d^{K-90} $\langle \mu\text{m}^2/\text{sec} \rangle$ is the K-90 PVP in Derakane™ dissolution diffusion coefficient and ω_{K-90} is the weight fraction of K-90 PVP in Derakane™ (wt K-90/wt Total). The thermodynamic

equilibrium weight fraction of K-90 PVP in Derakane™, ω_{k-90}^{eq} , was estimated to be 0.10 (wt K-90/wt Total) as will be discussed in chapter 5. From these constitutive data, the theoretical interphase concentration profile can be determined and will be discussed in section 4.6.1.

As will be discussed in more detail in Chapter 5, the K-30 PVP/Derakane system was found to be dissolution controlled. The swelling and relaxation portions of the K-30 PVP diffusion process are extremely fast compared to the dissolution portion. The K-30 PVP in Derakane dissolution diffusion coefficient was estimated to have the following concentration dependence:

$$D_d^{K-30} = 0.118 \exp(-37.27\omega_{K-30}) \quad (4-88)$$

where D_d^{K-30} $\langle \mu\text{m}^2/\text{sec} \rangle$ is the K-30 PVP in Derakane™ dissolution diffusion coefficient and ω_{K-30} is the weight fraction K-30 PVP in Derakane™ (wt K-30/wt Total). The thermodynamic equilibrium weight fraction of K-30 PVP in Derakane™, ω_{k-30}^{eq} , was estimated to be 0.25 (wt K-30/wt Total) as will be discussed in chapter 5. From these constitutive data, the theoretical interphase concentration profile can be determined and will be discussed in section 4.6.2.

4.6.1 Theoretical Prediction of the K-90 PVP Composite Interphase

The concentration profile for the K-90 PVP composite interphase was determined as a function of time (Figure 4.6-1) and (Figure 4.6-2). The exponential nature of the K-90 PVP/Derakane dissolution diffusion coefficient resulted in extreme gradients at the surface of the fiber. The extreme gradients flatten out quickly and the concentration profile becomes almost flat at regions remote from the fiber surface. Therefore, this suggests that a true graded interphase (gradients over the micron scale) is not possible in this system for typical pultrusion conditions. The K-90 PVP modifies the bulk matrix in almost a homogeneous fashion in regions not close to the interfacial zone. A non-zero sizing gradient at the fiber/matrix interface was present at all times, which suggested that the sizing phase still existed and had not completely dissolved. The percentage of dissolved sizing that had entered the solution domain was determined as a function of time (Figure 4.6-3). After the pultrusion processing time had been reached (i.e. 900 seconds), there was still 50% of the initial sizing mass left on the fiber surface. Therefore, the interfacial zone is composed of a swollen/relaxed K-90 PVP sizing phase and a region containing an extreme K-90 PVP/Derakane concentration gradient. The interphasial zone

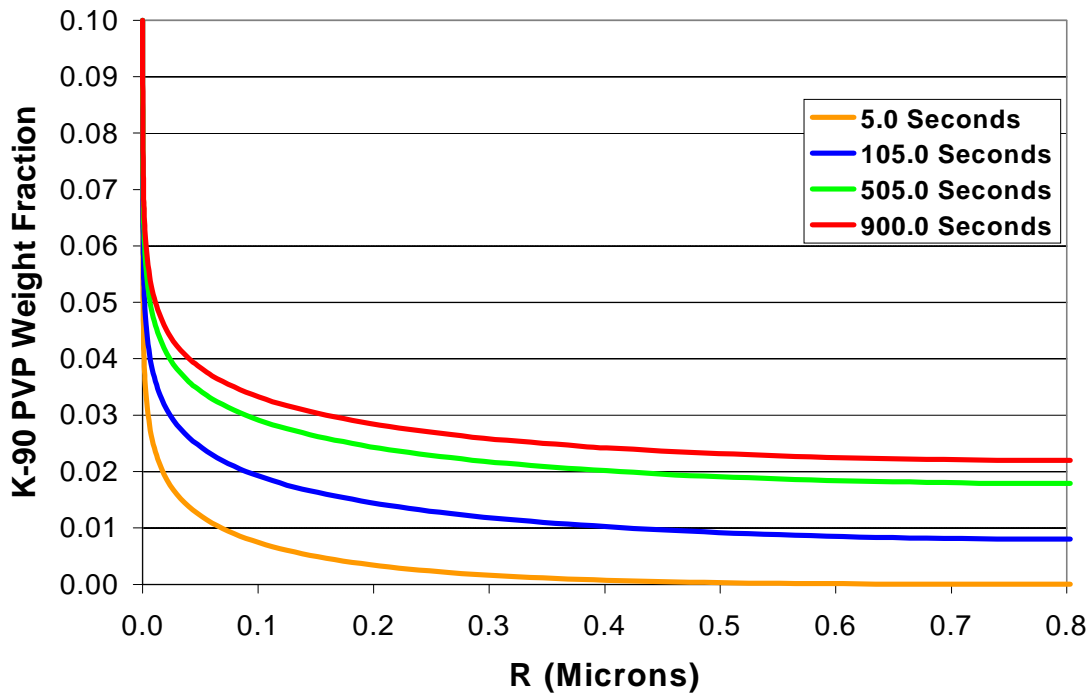


Figure 4.6-1 Non-fickian FEM solution to theoretical composite solution domain for K-90 PVP at various times. (Note: $D_d \langle \text{cm}^2/\text{s} \rangle = 0.0071 \exp(-128.41 \omega_s)$, $\omega_s^{\text{eq}} = 0.10$, and $\nu_f = 0.60$). Angle is 0° .

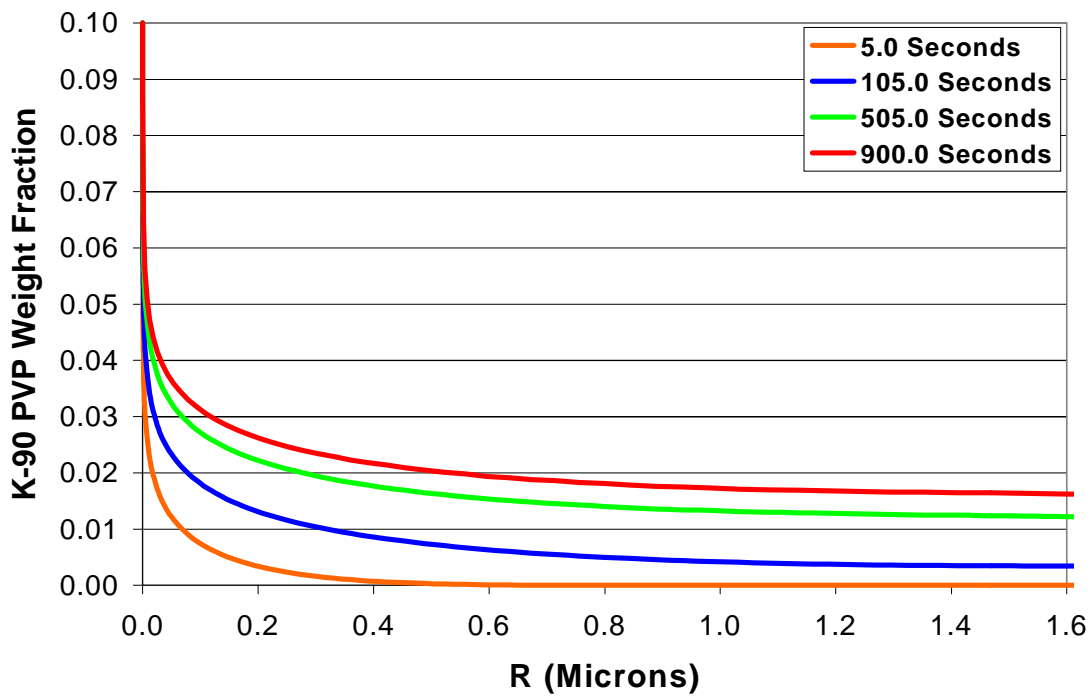


Figure 4.6-2 Non-fickian FEM solution to theoretical composite solution domain for K-90 PVP at various times. (Note: $D_d \langle \text{cm}^2/\text{s} \rangle = 0.0071 \exp(-128.41 \omega_s)$, $\omega_s^{\text{eq}} = 0.10$, and $\nu_f = 0.60$). Angle is 30° .

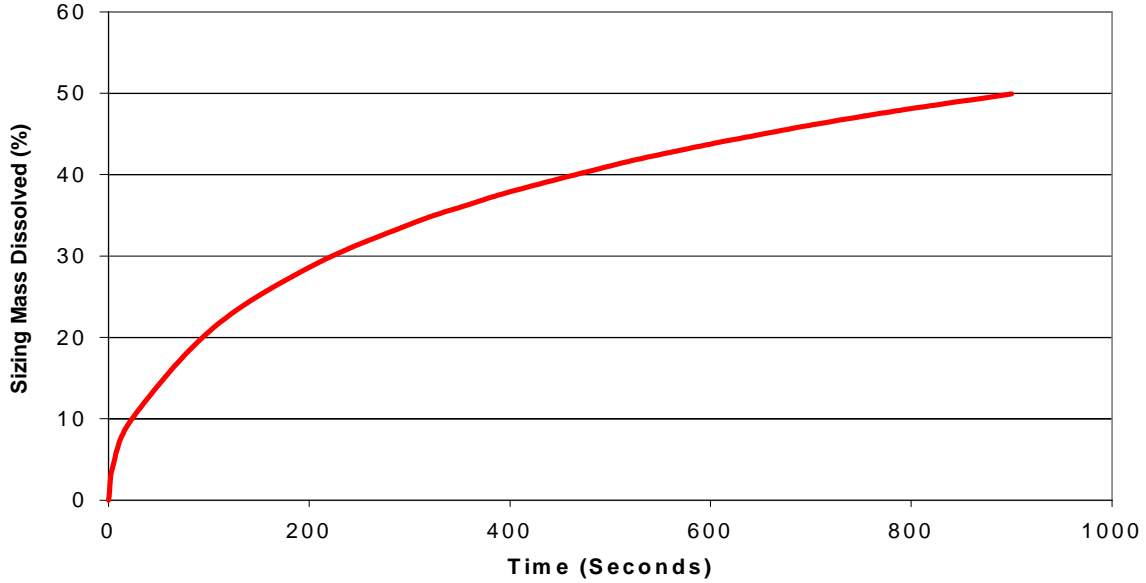


Figure 4.6-3 Non-fickian FEM predicted weight uptake of K-90 PVP as a function of time. (Note: $D_d < \text{cm}^2/\text{s} > = 0.0071 \exp(-128.41\omega_s)$, $\omega_s^{\text{eq}} = 0.10$, and $\upsilon_f = 0.60$).

is composed of a homogeneously modified matrix that contains very shallow K-90 PVP/Derakane gradients.

The K-90 PVP interphase concentration profile can be used to predict the interphase mechanical property profile. As will be discussed in Chapter 5, a series of K-90 PVP/Derakane blends were cured and tested for mechanical performance. The mechanical performance of these blends are summarized by the following equations:

For $0.000 \leq \omega_{K-90} \leq 0.0025$ the following holds,

$$\sigma_{K-90} = 1547.0\omega_{K-90} + 55.3 \quad (4-89)$$

$$STF_{K-90} = 336.0\omega_{K-90} + 1.9 \quad (4-90)$$

$$E_{K-90} = -92.0\omega_{K-30} + 3.44 \quad (4-91)$$

$$G_{K-90} = -35.1\omega_{K-30} + 1.31 \quad (4-92)$$

For $0.0025 \leq \omega_{K-90} \leq 0.1000$ the following holds,

$$\sigma_{K-90} = 77.7\omega_{K-90} + 70.8 \quad (4-93)$$

$$STF_{K-90} = 9.5\omega_{K-90} + 2.7 \quad (4-94)$$

$$E_{K-90} = 1.89\omega_{K-30} + 3.21 \quad (4-95)$$

$$G_{K-90} = 0.72\omega_{K-30} + 1.23 \quad (4-96)$$

where σ is the tensile strength in MPa, STF is the strain-to-failure in %, E is the tensile modulus in GPa, and G is the shear modulus in GPa. From these mechanical properties of K-90 PVP/Derakane blends, the interphase mechanical property profile was generated (Figure 4.6-4 through Figure 4.6-7). The mechanical property profile matches the trends observed in the concentration profile. The properties have the sharpest gradients near the fiber/matrix interface and flatten-out at regions remote from the fiber surface. The maximum change in tensile strength was observed to be approximately 10% across the entire solution domain (Figure 4.6-4). The strain-to-failure had a 20% decrease in its value from the fiber/matrix interface to the remote axis of symmetry (Figure 4.6-5). The moduli both tensile (Figure 4.6-6) and shear (Figure 4.6-7) only varied 4% over the entire solution domain. Therefore, for the K-90 PVP sizing system, there was not an interphase with steep mechanical property gradients. However, if the average mechanical properties of the K-90 PVP solution domain are compared to the average mechanical properties of the pure Derakane and hence unsized solution domain, then drastic differences are noted. For instance, the average K-90 PVP interphase tensile strength is approximately 34% higher than the unsized. The average K-90 PVP interphase strain-to-failure is approximately 68% higher than the unsized. However, the tensile and shear moduli of the K-90 PVP interphase is only 4% lower than the unsized. As was discussed in chapter 2, because the interphase shear modulus is unaffected by the addition of the K-90 PVP, the K-90 PVP and unsized systems would have the same or similar interfacial shear strengths. However, a higher interphase strength and strain-to-failure for a given modulus would allow a much greater interfacial shear stress to exist before transverse cracking and composite catastrophic failure resulted. As a result, the applied load at which interfacial debonding or transverse cracking initiated would be shifted to higher values. In addition, the K-90 PVP blends were characterized for shrinkage as a function of K-90 PVP concentration. The shrinkage as a function of K-90 PVP concentration was as follows:

For $0.00 \leq \omega_{K-90} \leq 0.05$, the following holds.

$$shrinkage(\%) = -134.0\omega_{K-90} + 8.37 \quad (4-97)$$

For $\omega_{K-90} \geq 0.05$, the following holds:

$$shrinkage(\%) = 1.88 \quad (4-98)$$

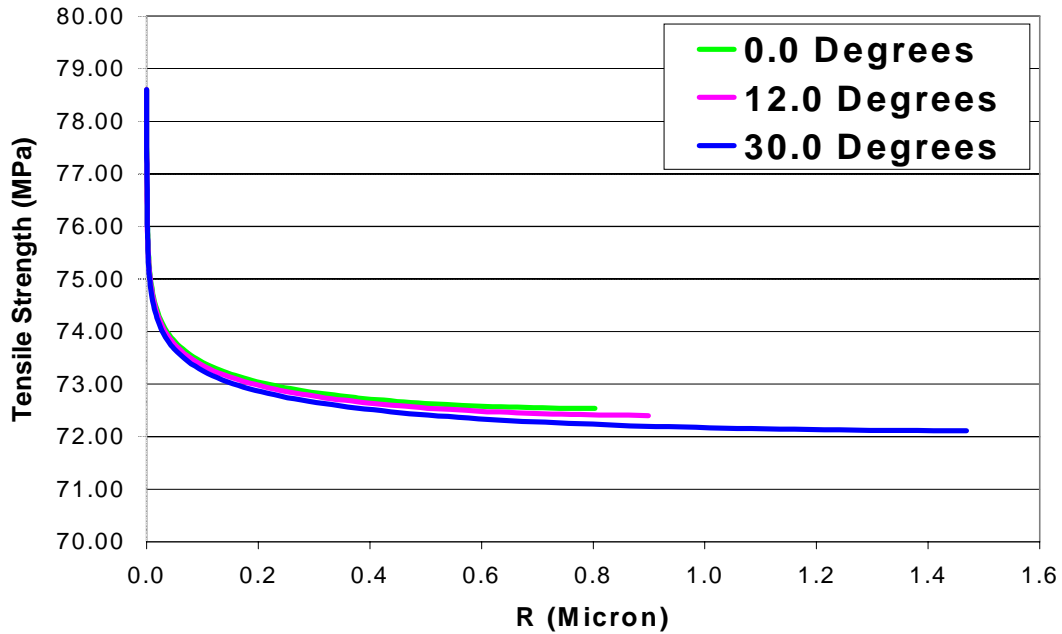


Figure 4.6-4 Theoretical interphase mechanical property profile for K-90 PVP sized composite. Static Tensile Strength (Note: Pure Derakane value is 55.3 MPa).

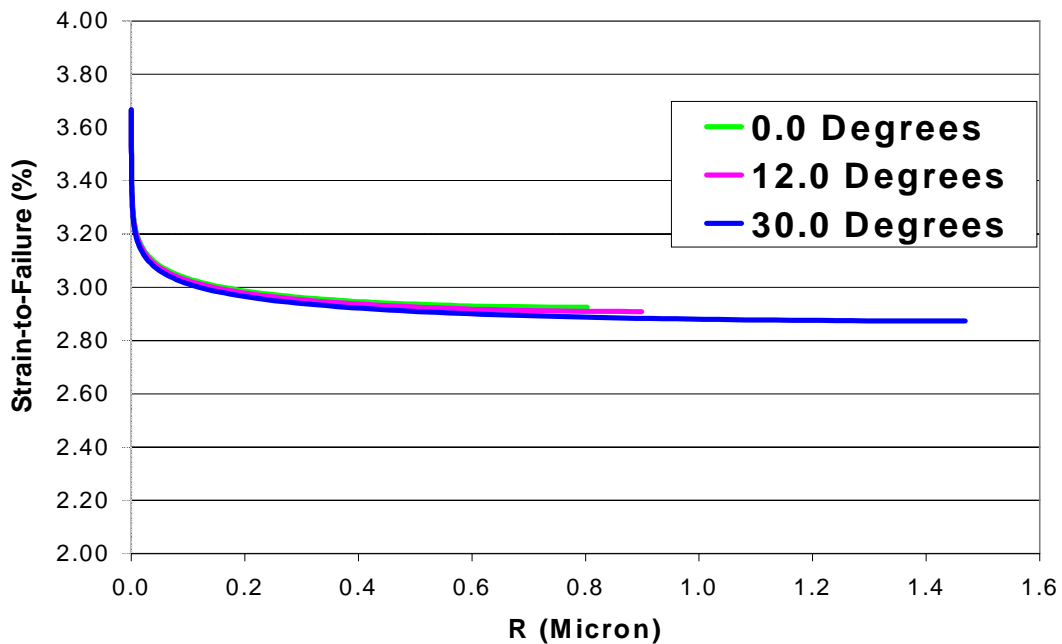


Figure 4.6-5 Theoretical interphase mechanical property profile for K-90 PVP sized composite. Strain-to-Failure (Note: Pure Derakane value is 1.9%).

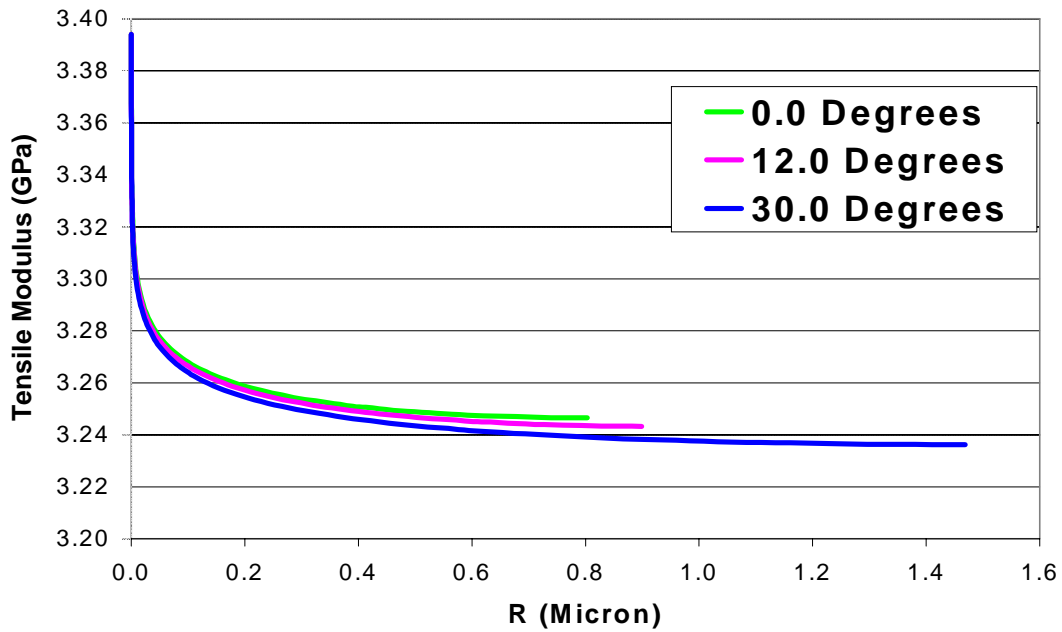


Figure 4.6-6 Theoretical interphase mechanical property profile for K-90 PVP sized composite. Static Tensile Modulus (Note: Pure Derakane value is 3.44 GPa).

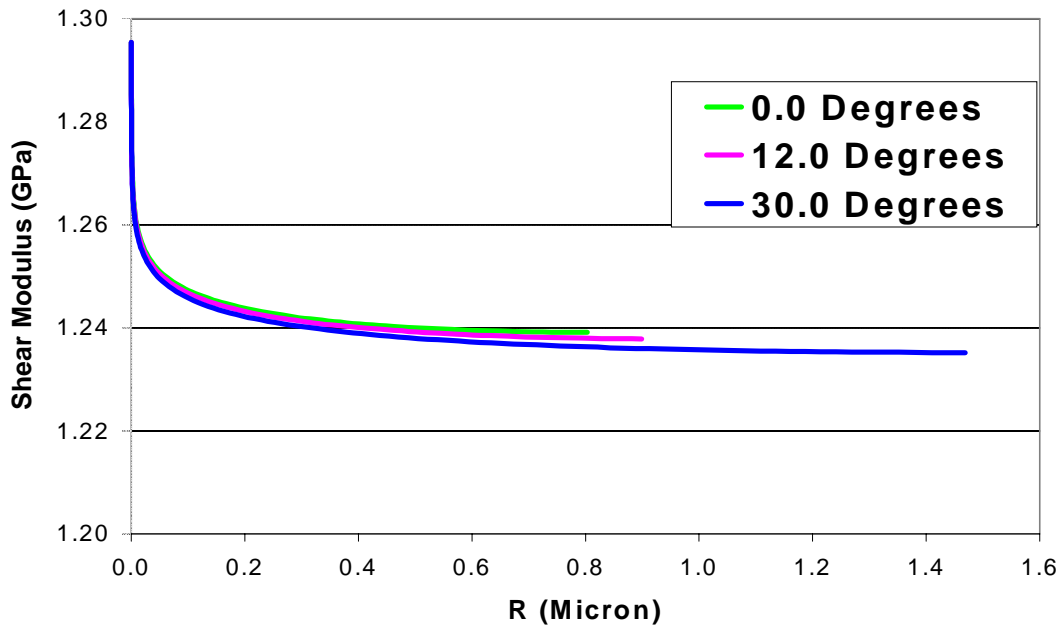


Figure 4.6-7 Theoretical interphase mechanical property profile for K-90 PVP sized composite. Static Shear Modulus (Note: Pure Derakane value is 1.31 GPa)

The K-90 PVP interphase shrinkage as a function of radial position was determined (Figure 4.6-8). The shrinkage was found to have the steepest gradients of all the interphase properties determined. In addition, the interphase shrinkage in all cases was significantly less than the pure Derakane value of 8.37%. Therefore, the residual stresses present at the fiber/matrix interface after cure will be significantly less for the K-90 PVP interphase as compared to the unsized system. The interphase property profiles and the unsized property profiles are summarized in Figure 4.6-9. The values for the specific property have been normalized against the maximum K-90 PVP property value existing in the interphase. The predicted interphase mechanical property profile can be used to partially explain the improvements in composite performance observed in the K-90 PVP sizing system. However, the processability improvements are still believed to dominate the on-axis mechanical property improvements observed in Chapter 3.

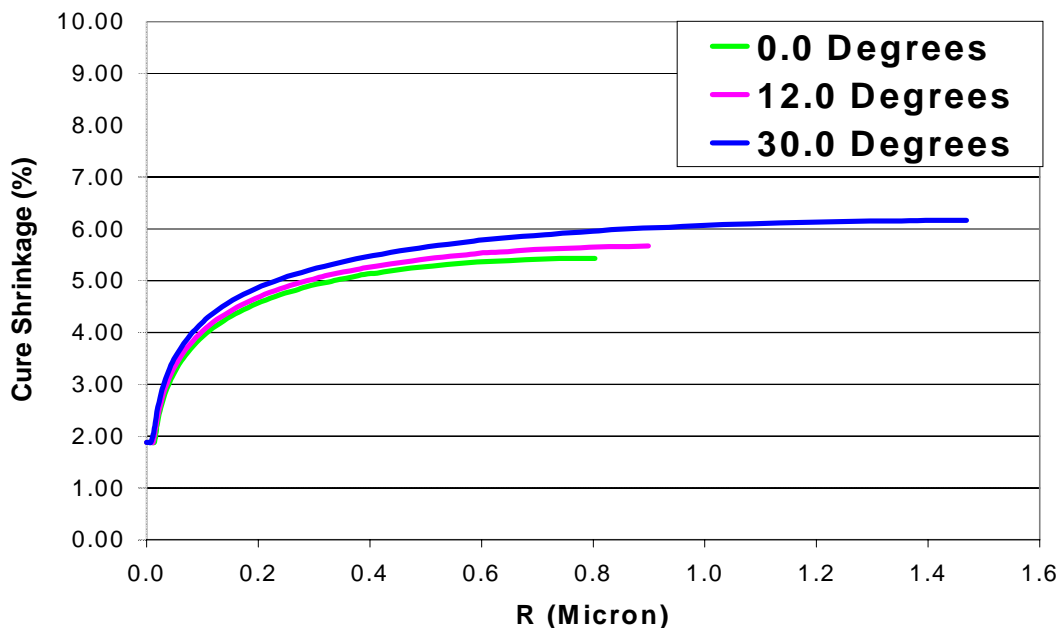


Figure 4.6-8 Theoretical interphase mechanical property profile for K-90 PVP sized composite. Cure shrinkage shown (Note: Pure Derakane value is 8.34%).

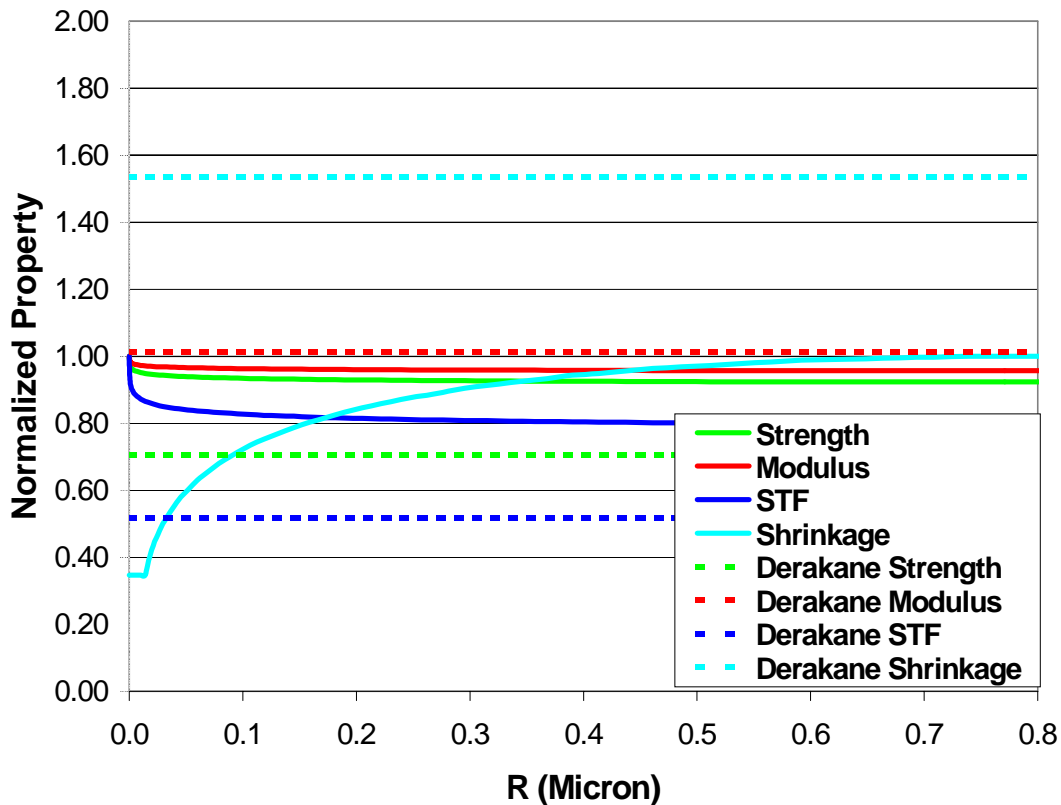


Figure 4.6-9 Theoretical interphase mechanical property profile for K-90 PVP sized composite. K-90 PVP interphase shown in solid lines. Unsized shown in dashed lines. Mechanical property values normalized to the maximum in that property existing in the K-90 PVP interphase profile.

4.6.2 Theoretical Prediction of the K-30 PVP Composite Interphase

The concentration profile for the K-30 PVP composite interphase was determined as a function of time (Figure 4.6-10 and Figure 4.6-11). At the times of practical interest, the exponential variation of dissolution diffusion coefficient with concentration did not produce the steep gradients observed with the K-90 PVP. At a time of 1.0 seconds, there exists a broad graded interphase in the composite solution domain (Figure 4.6-10). In addition, 29% of the sizing mass initially present on the fiber surface has dissolved into the solution domain after only 1.0 seconds. At a time of 10.0 seconds, 91% of the sizing mass initially present on the fiber surface has dissolved. Therefore, at the 100.0 second time frame, all the sizing has dissolved as is evident by the zero gradient at the fiber/matrix interface position of $R=0$ (Figure 4.6-11). At the end of the simulation or a time of 900 seconds, there is no gradient in the solution domain (Figure 4.6-12 and Figure 4.6-13). Therefore, the K-30 PVP sizing material does not form an

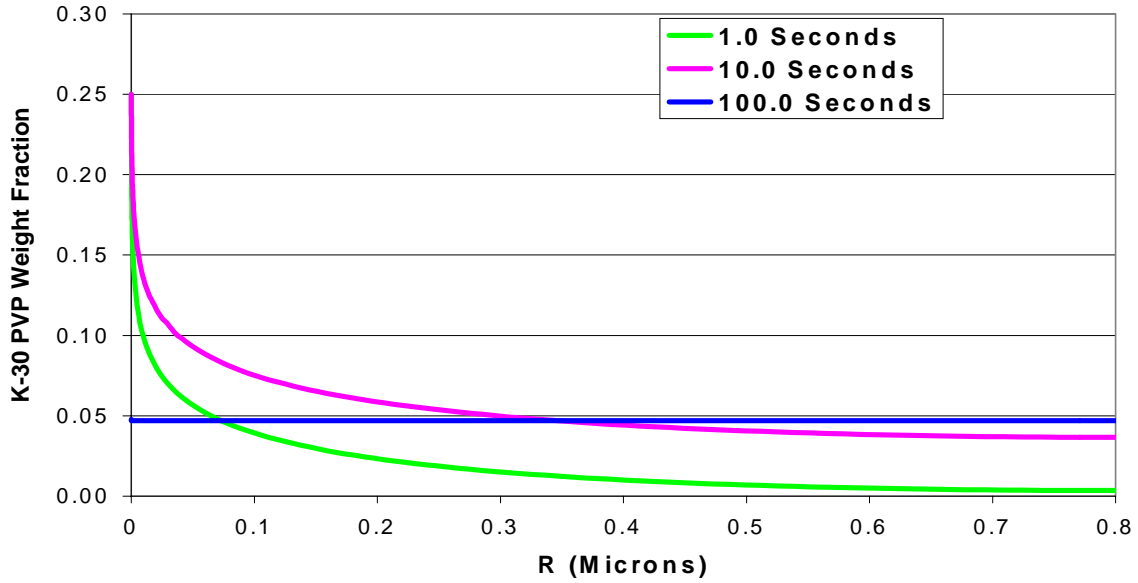


Figure 4.6-10 Non-fickian FEM solution to theoretical composite solution domain for K-30 PVP at various times. (Note: $D_d \langle \mu\text{m}^2/\text{s} \rangle = 0.118\exp(-37.27\omega_s)$, $\omega_s^{\text{eq}} = 0.25$, and $\nu_f = 0.60$). Angle is 0° .

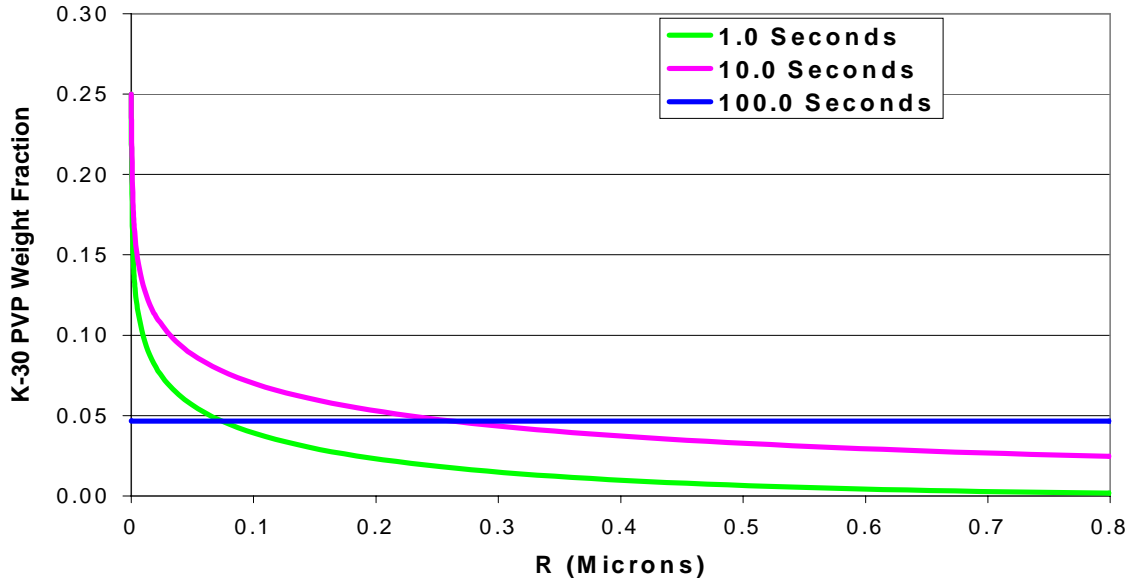


Figure 4.6-11 Non-fickian FEM solution to theoretical composite solution domain for K-30 PVP at various times. (Note: $D_d \langle \mu\text{m}^2/\text{s} \rangle = 0.118\exp(-37.27\omega_s)$, $\omega_s^{\text{eq}} = 0.25$, and $\nu_f = 0.60$). Angle is 30° .

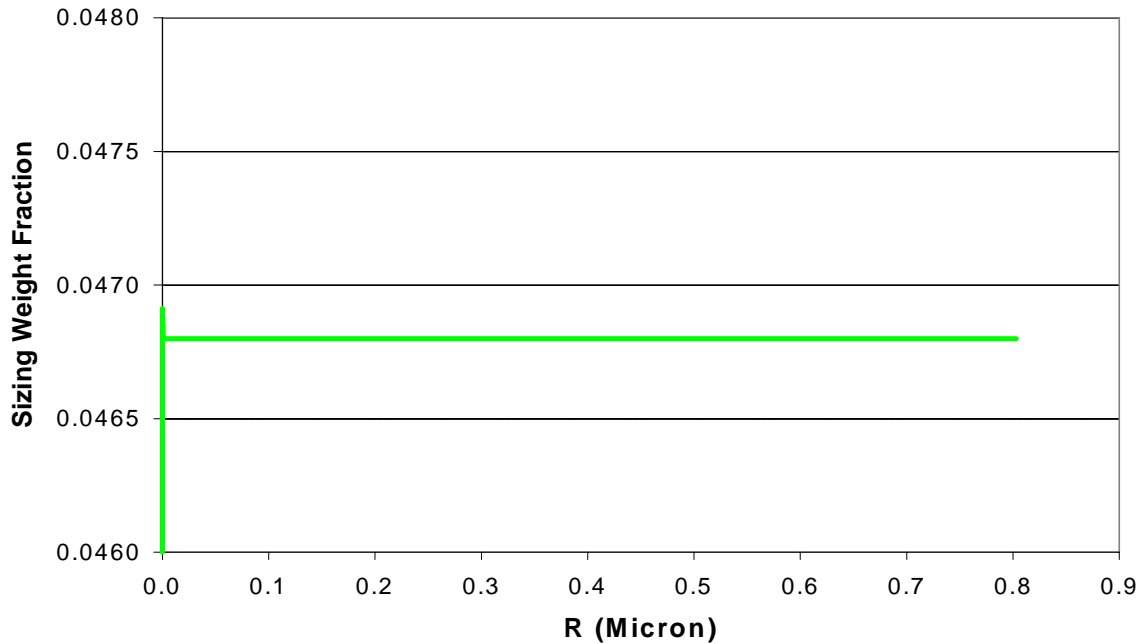


Figure 4.6-12 Non-fickian FEM solution to theoretical composite solution domain for K-30 PVP at a time of 900 seconds. (Note: $D_d <\mu\text{m}^2/\text{s}> = 0.118\exp(-37.27\omega_s)$, $\omega_s^{\text{eq}} = 0.25$, and $\nu_f = 0.60$). Angle is 0° .

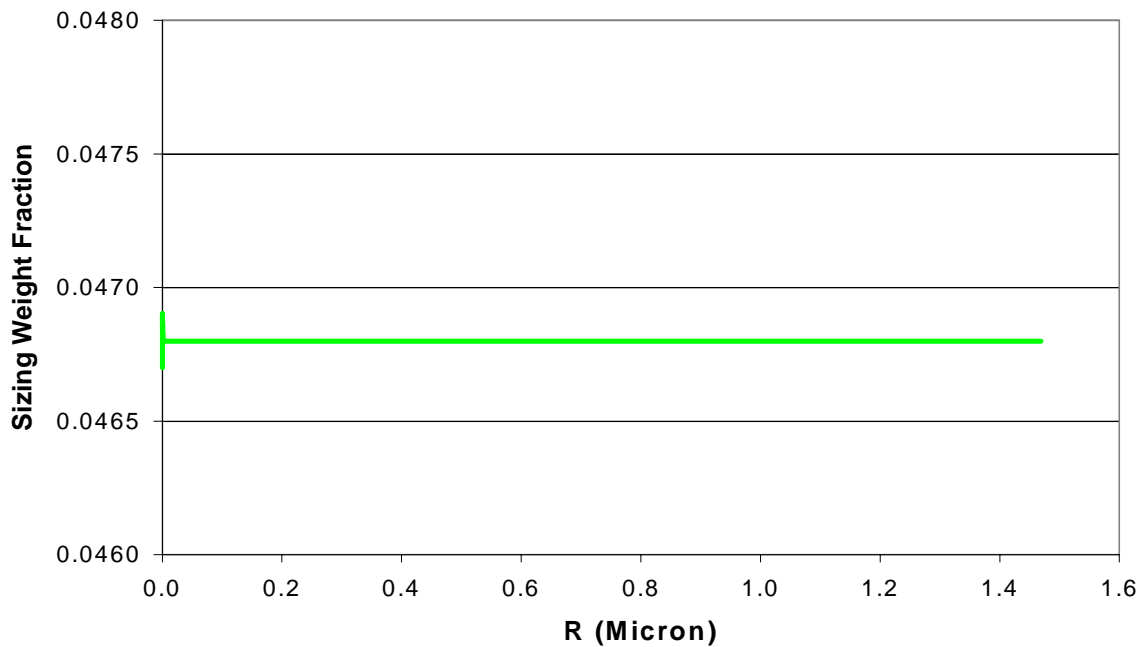


Figure 4.6-13 Non-fickian FEM solution to theoretical composite solution domain for K-30 PVP at a time of 900 seconds. (Note: $D_d <\mu\text{m}^2/\text{s}> = 0.118\exp(-37.27\omega_s)$, $\omega_s^{\text{eq}} = 0.25$, and $\nu_f = 0.60$). Angle is 30° .

interphase but can still homogeneously modify matrix properties such that improvements in composite mechanical performance could be expected. Unfortunately, K-30 PVP/Derakane blends were not tested for their mechanical performance. Therefore, a mechanical property profile similar to that generated for K-90 PVP could not be determined.

An interesting application for the K-30 PVP sizing material can be put forth based upon the K-90 PVP shrinkage data and the K-30 PVP interphase formation predictions. As will be discussed in chapter 5, the K-90 PVP significantly reduces the cure shrinkage of the Derakane™ due to strong hydrogen bonding interactions between the PVP and uncured/liquid Derakane™. However, this hydrogen bonding is not limited to the K-90 system and will also be prevalent in the K-30 system. Therefore, the K-30 PVP system should have the same affect on matrix shrinkage as the K-90 PVP. Due to the limited dissolution of the K-90 PVP sizing into the Derakane™ during the course of the pultrusion process, the reduction in shrinkage is only realized close to the fiber/matrix interface (Figure 4.6-8). One of the major problems with the application of the Derakane™ matrix in composites produced by any method is surface cracking at the part surface. The K-90 PVP cannot significantly reduce this cracking due to the limited dissolution. However, the K-30 PVP would significantly dissolve (homogeneously modifying the matrix for the case of dip bath pultrusion operations) and could effectively reduce surface cracking.

4.7 Summary

In this chapter, fundamental models were utilized to predict the interphase profile as a function of a dissolution diffusion coefficient, processing parameters, and physical properties of the sizing/matrix. In summary, for an idealized composite of 60% fiber volume fraction, a sizing level of 2.0 wt%, a processing time of 15 minutes, and a thermodynamic equilibrium of 30 wt% sizing in matrix, the range of dissolution diffusion coefficient needed for interphase formation is approximately 10^{-12} to 10^{-14} cm²/sec.

A non-fickian FEM model was developed that had several complexities added that were not in the original fickian FEM model. First, the non-fickian model can now accept non-constant/concentration dependent diffusion coefficients. Second, the model can now accept flux controlled dissolution problems. The non-fickian FEM model was applied to the constitutive properties determined for the K-90 PVP/Derakane system. The predicted K-90 PVP interphase

concentration profile displayed steep gradients at the fiber/matrix interface but essentially no gradients at points distant from the fiber surface. This was indicative of the exponential concentration dependence in the dissolution diffusion coefficient. The predicted mechanical property profile was essentially flat for the modulus but did show a steep gradient in the strain-to-failure and shrinkage properties. However, the K-90 PVP interphase compared to the unsized/pure Derakane interphase showed improvements in strength, strain-to-failure, and a reduction in cure shrinkage without significantly affecting the interphase tensile or shear moduli. Because the interphase shear modulus is unaffected by the addition of the K-90 PVP, the K-90 PVP and unsized systems will have the same or similar interfacial shear strengths. However, a higher interphase strength and strain-to-failure for a given modulus will allow a much greater interfacial shear stresses to exist before transverse cracking and composite catastrophic failure resulted. As a result, the applied load at which interfacial debonding or transverse cracking initiated will be shifted to higher values. The presence of K-90 PVP in the Derakane matrix resulted in a reduction in cure shrinkage. As a result, the residual stresses present at the fiber/matrix interface after cure will be significantly less for the K-90 PVP interphase as compared to the unsized system. The predicted interphase mechanical property profile can be used to partially explain the improvements in composite performance observed in the K-90 PVP sizing system. However, the processability improvements are still believed to dominate the on-axis mechanical property improvements observed in Chapter 3.

The non-fickian FEM model predicted that the K-30 PVP interphase is flat. The K-30 PVP swells, relaxes, disentangles, and diffuses so rapidly that no sizing remains on the surface of the fiber and no concentration gradient exist. Therefore, the K-30 PVP sizing material can only affect composite mechanical performance through homogeneous modification of the matrix. However, the effect of K-30 PVP in the Derakane matrix was not determined.

4.8 Diffusion in Pultruder Die

As was discussed in the introduction section of this chapter, diffusion in the pultruder die can be neglected as long as the sum of the activation energies for diffusion and solubility are less than approximately $2000 \cdot R$. The method by which this estimation was obtained is presented in this section.

It was assumed that the dissolution diffusion coefficient and the sizing and matrix solubility's could be represented by an Arrhenius expression:

$$D = D_o \exp\left[\frac{-E_d}{RT}\right] \quad (4-99)$$

$$\rho_s = \rho_o \exp\left[\frac{-E_s}{RT}\right] \quad (4-100)$$

where D is the dissolution diffusion coefficient at absolute temperature T, D_o is the pre-exponential dissolution diffusion coefficient, E_d is the activation energy for the dissolution process, R is the gas constant, ρ_s is the sizing/matrix solubility expressed as a density function at absolute temperature T, ρ_o is the pre-exponential sizing/matrix solubility, and E_s is the activation energy of the solubility process. The amount of sizing material that has left the carbon fiber surface can be *approximated* through the use of equation (4-13). The amount of sizing dissolved in the dip bath and die can be *approximated* by the following:

$$M_{DB} \cong 2\rho_o \cdot \exp\left[\frac{-E_s}{RT_A}\right] \cdot \sqrt{\frac{t_{db} \cdot D_o \exp\left(\frac{-E_d}{RT_A}\right)}{\pi}} \quad (4-101)$$

$$M_{Die} \cong \frac{1}{\sqrt{\pi}} \int_{t_{db}}^{t_{db}+t_g} \rho_o \exp\left[\frac{-E_s}{RT}\right] \cdot \sqrt{\frac{D_o \exp\left(\frac{-E_d}{RT}\right)}{t}} dt \quad (4-102)$$

where M_{DB} is the mass of sizing per unit area dissolved in the dip bath, t_{DB} is the time for interdiffusion in the dip bath, and T_A is the temperature of the dip bath, M_{Die} is the mass of sizing per unit area dissolved in the die, t_{gel} is the time required for the matrix to typically gel, and T(t) is the temperature profile experience by the composite part in the die. Taking the ratio of these two masses and gives the following:

$$\frac{M_{Die}}{M_{DB}} \cong \frac{1}{2\sqrt{t_{db}}} \int_{t_{db}}^{t_{db}+t_g} \frac{1}{\sqrt{t}} \cdot \exp\left[\frac{\left(E_s + \frac{1}{2}E_d\right)}{R} \cdot \left(\frac{1}{T_A} - \frac{1}{T(t)}\right)\right] dt \quad (4-103)$$

Assuming a linear variation of temperature with time in the die or T(t) = M·(t-t_{db}) + T_{AMB}, equation (4-103) can be integrated numerically to give the ratio of diffusion in the die versus diffusion in the dip bath. Assuming the composite gels almost instantaneously upon reaching

75°C (the approximate initiation temperature of the organic peroxide utilized in the pultrudable vinyl-ester resin) and that the composite takes approximately 30 seconds to reach this temperature, the ratio of diffusion in the die to diffusion in the dip bath can be computed as a function of the $(E_s + E_d/2)/R$. With these assumptions, the values for the variables in equation (4-103) are as follows: $T_A = 293.15\text{K}$, $t_{db} = 900 \text{ sec}$, $M = 11/6$, and $t_{gel} = 30 \text{ sec}$. If negligible die diffusion is assumed to take place when the ratio of diffusion in the die to diffusion in the dip bath is less than 10%, then equation (4-103) can be integrated numerically to give the necessary $(E_s + E_d/2)/R$. The resulting solution is that $E/R = (E_s + E_d/2)/R$ must be less than 5300 for the ratio to be less than 10%. If the sizing solubility is assumed to be constant and not a strong function of temperature, then the required activation energy for diffusion must be less than approximately 10,600R for diffusion in the die to be neglected.

4.9 References

- 4.1 C. M. Laot, 'Spectroscopic Characterization of Molecular Interdiffusion at a Poly(vinylpyrrolidone)/Vinyl-Ester Interface', M.S. Thesis, Department of Chemical Engineering, Virginia Polytechnic Institute and State University, Blacksburg, VA, August 1997.
- 4.2 J. Crank, *The Mathematics of Diffusion*, (Second Edition), Clarendon Press (1975).
- 4.3 J. N. Reddy, *An Introduction to the Finite Element Method*, (Second Edition), McGraw-Hill (1993).
- 4.4 R. Batra, Class notes for introduction to finite elements class. Department of Engineering Science and Mechanics, Virginia Polytechnic Institute and State University.
- 4.5 Cook, Malkus, and Plesha, 'Concepts and Applications of Finite Element Analysis', 3rd Edition, Wiley and Sons.
- 4.6 N. S. Broyles, 'Thermoplastic Sizings: Effects on Processing and Mechanical Properties of Pultruded Carbon Fiber/Vinyl-Ester Composites', Ph.D. proposal, May, 1996, Department of Chemical Engineering, VPI&SU.

Chapter 5

Measurements of the Constitutive Properties Relevant to Sizing/Matrix Interdiffusion

5 Introduction

In the previous chapter, a fundamental FEM model was developed that predicts interphase formation as a function of a dissolution diffusion coefficient, sizing/matrix interface relaxation and/or distentanglement rate, sizing/matrix thermodynamic equilibrium, and other processing parameters. This model had a series of assumptions made about the constitutive nature of sizing/matrix interdiffusion. The purpose of this chapter is two-fold: 1). To determine the constitutive properties needed to apply the model and 2). To determine the accuracy of the assumptions made about the constitutive nature of sizing/matrix interdiffusion.

In this chapter, dielectric experimental results are presented that reveal some of the constitutive properties of sizing/matrix interdiffusion. Microdielectric sensors were used to monitor the swelling, relaxation, and dissolution of the sizing material into the vinyl-ester matrix. In addition, sizing/matrix blend properties were generated that included static tensile strength, strain-to-failure, and modulus, un-cured and cured blend density, shrinkage upon cure, and the cured blend glass transition temperature. In addition, the zero shear viscosity of sizing/matrix blends were determined and utilized to estimate the non-fickian dissolution diffusion coefficient. The constitutive data obtained from these experiments was to serve as an input into the mass transport models developed in Chapter 4 to obtain accurate predictions of interphase formation and interphase mechanical properties.

This chapter is organized into the following sections.

- 5.1 – Theory of Dielectric Spectroscopy
- 5.2 – Experimental
- 5.3 – Results and Discussion
- 5.4 – Estimation of Constitutive Properties Needed in FEM Model
- 5.5 – Conclusions
- 5.6 – References

5.1 Theory of Dielectric Spectroscopy

The micro-dielectric sensors and the relevant theory utilized for the experiments presented in this chapter are described here [2.28]. The micro-dielectric sensors (Figure 5.1-1) utilized in these experiments were ½" X 1" glass rectangles coated with a gold interdigitized array. A complex voltage was input to the array according to the following equation:

$$V(t) = V_o \exp(\omega t i) \quad (5-1)$$

where V_o was the peak voltage, ω was the frequency, and t was the time. A sample of the material to be analyzed was uniformly coated on the sensor's surface. As the voltage was cycled, the material acted as a capacitor that stored and then correspondingly released the charge. This generated a complex current that was monitored and recorded:

$$I(t) = I_l(t) + I_c(t) i \quad (5-2)$$

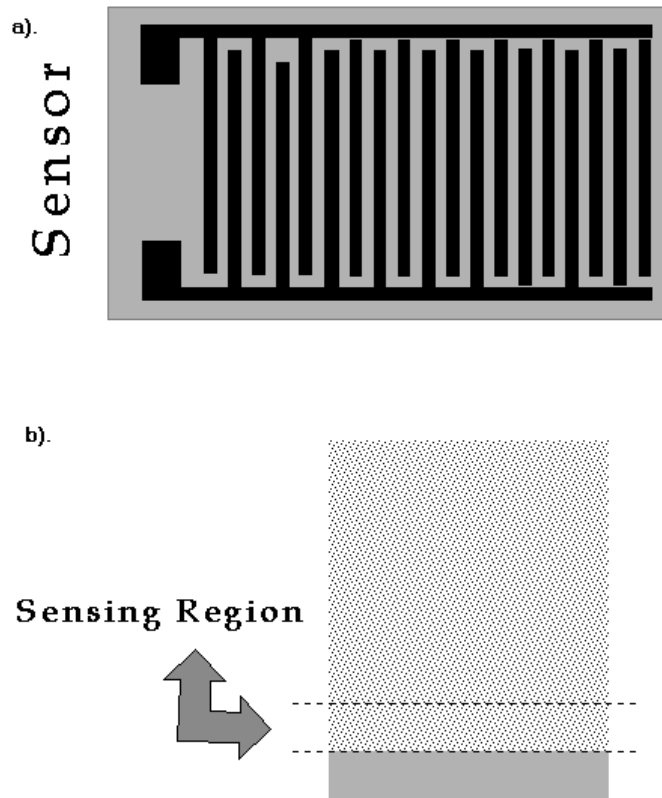


Figure 5.1-1 Schematic of micro-dielectric sensor utilized for interdiffusion studies. a). Top view of sensor showing interdigitized gold grid. b). Side view of sensor showing sensing region or the penetration depth. Note: Any material outside of the sensing region does not contribute to the measurement.

where I is the total current, I_l is the out of phase current, and I_c is the in-phase current. From the in-phase current and out of phase current, the in-phase (ϵ') and out of phase (ϵ'') permittivity could be determined from the following equations [5.1]:

$$\epsilon'(t) = \frac{I_c(t)}{\omega C_o V(t)} \quad (5-3)$$

$$\epsilon''(t) = \frac{I_l(t)}{\omega C_o V(t)} \quad (5-4)$$

where C_o is the capacitance of the uncoated sensor. For simple/non-polar fluids, the ϵ' will be frequency independent and the ϵ'' will equal zero. If the sample being analyzed is polymeric in nature, then the ϵ' versus frequency will have a typical form (Figure 5.1-2). At high frequencies, the potential field applied to the sample can only distort the electron clouds and dipoles but does not affect the bulk macromolecule. At low frequencies, the potential field is applied long enough to distort the electron clouds, dipoles, and the bulk macromolecule. At intermediate frequencies,

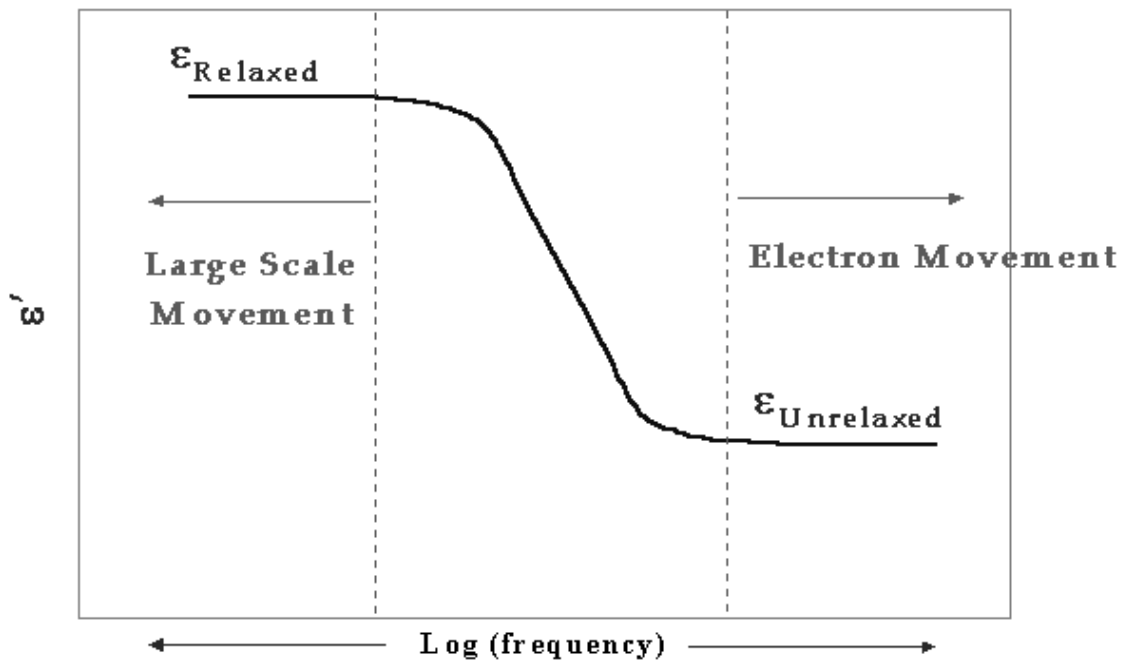


Figure 5.1-2 Typical ϵ' vs. $\log(\omega)$ plot for a polymeric sample. At low frequencies, the value of ϵ' levels off to the relaxed permittivity or ϵ_r . At high frequencies, the value of ϵ' levels off to the un-relaxed permittivity or ϵ_u .

a mixture of electron cloud, dipoles, and bulk macromolecular movement occurs. At both the high and low frequency extremes, the ϵ' approaches a finite and constant value. At the high frequencies, the value at which the ϵ' levels out is denoted as ϵ_u or the un-relaxed permittivity. The un-relaxed permittivity is given this distinction because the bulk macromolecular segments are unaffected at the high frequencies and therefore the segments remained un-relaxed. At the low frequencies, the value at which the ϵ' levels out is denoted as ϵ_r or the relaxed permittivity. The relaxed permittivity is given this distinction because the bulk macromolecular segments are affected at the low frequencies and therefore the segments relax [5.1]. It is difficult in an experimental setup to obtain both the ϵ_u and ϵ_r due to a limitation in accessible frequencies. For instance, if the polymeric sample being analyzed is well *below* T_g , then only the right hand portion of the typical curve may be obtained which includes the ϵ_u . If the polymeric sample being analyzed is well *above* T_g , then only the left-hand portion of the typical curve may be obtained which includes the ϵ_r . Therefore, monitoring ϵ' as a function of frequency can be utilized to track changes in the T_g of the sample being analyzed. One major advantage to utilizing the dielectric sensors over traditional mechanical methods is that the method is applicable to testing liquids at any temperature.

The grid spacing (i.e. the distance between the parallel grids on the sensor) directly determines the distance that the electric field penetrates into the sample (Figure 5.1-1.b). This penetration is not a function of the dielectric properties of the material coating the sensor. The material closer to the sensor surface will contribute more to the overall sensing region permittivity than material further away from the surface. The average in-phase permittivity, ϵ' , can be computed from the following expression:

$$\epsilon'_{ave} = \frac{\int_0^l w(x)\epsilon'(x)dx}{\int_0^l w(x)dx} \quad (5-5)$$

where ϵ'_{ave} is the average in-phase permittivity in the sensing region (note: this is what the experiment determines), l is the penetration depth of the sensing region, $w(x)$ is the weight function that is a function of the sensing distance (note: $w(x)$ also affected by the material

composition to a certain extent but this is neglected in the analysis), and ϵ' is the in-phase permittivity.

The penetration depth and the weight function, $w(x)$, can be determined from a separate set of experimental trials. These trials involve coating the sensor with the bulk material at various coating levels below and above the suspected sensing distance, l . From the in-phase permittivity versus bulk material thickness data, the l and maximum in-phase permittivity, ϵ'_{\max} can be determined (Figure 5.1-3). Because air has a negligible in-phase permittivity and the $\epsilon'(x)$ is constant and equal to ϵ'_{\max} for this particular case, equation (5-5) simplifies to the following expression:

$$\frac{\epsilon'_{ave}(x)}{\epsilon'_{\max}} = \frac{1}{1 + \int_x^l w(x)dx} \quad (5-6)$$

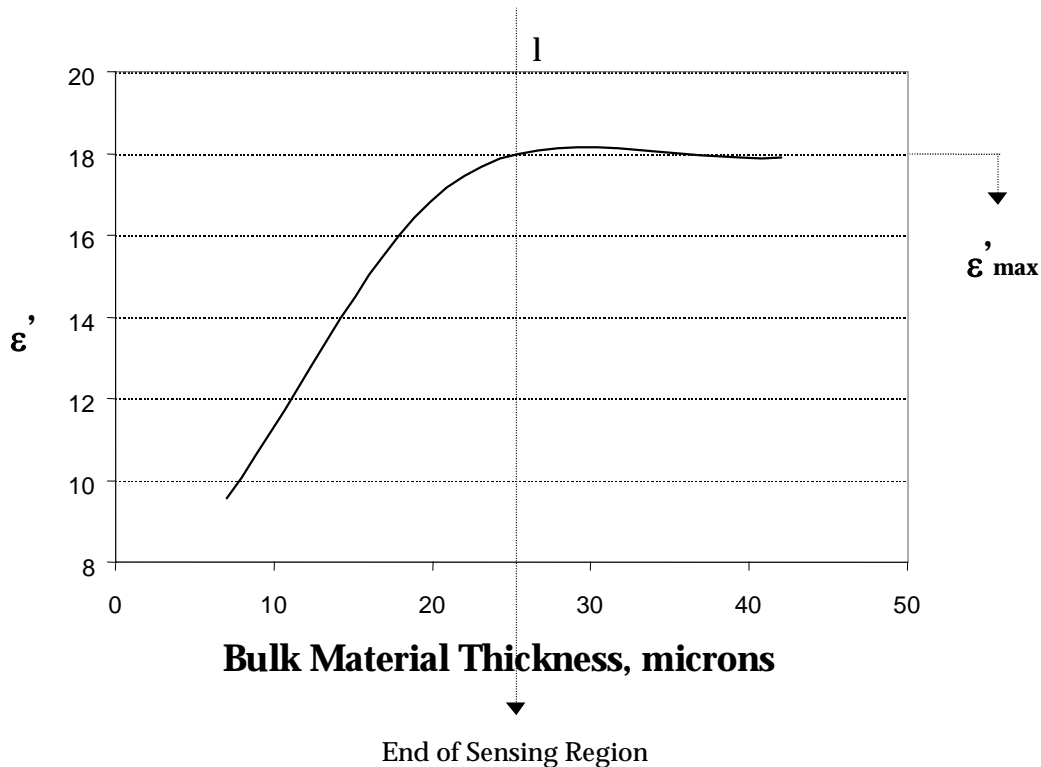


Figure 5.1-3 In-phase permittivity (ϵ') at a certain frequency versus bulk material thickness. End of sensing region noted where ϵ' remains constant. l , ϵ'_{\max} , and $d\epsilon'(x)/dx$ can be easily determined from graph. Weight function $w(x)$ can be determined from equation (5-7).

This expression can be solved for $w(x)$ and can be represented by the following:

$$w(x) = \frac{\varepsilon'_{\max}}{\{\varepsilon'_{ave}(x)\}^2} \cdot \frac{d\varepsilon'_{ave}(x)}{dx} \quad (5-7)$$

where $d\varepsilon'_{ave}(x)/dx$ is computed from the ε' versus bulk material thickness plot (Figure 5.1-3). Because the sensing distance or penetration distance remains essentially constant, changes in the experimentally measured dielectric response can be utilized to track changes in the composition of the material occupying the sensing region. Therefore, a sensing region permittivity versus time experiment can be utilized to estimate the average diffusion coefficient for the permeant into the bulk material (i.e. matrix into sizing for our case). There are two ways that the diffusion coefficient of the permeant can be estimated from a permittivity versus time experiment.

The first and most quantitatively accurate method is to utilize blend permittivity data and fundamental mass transport models to compute an average fickian diffusion coefficient, which was the method employed by Larson et. al. [2.57]. Numerous blends of the penetrant and bulk material are made and analyzed at several frequencies to generate an in-phase permittivity (ε') versus concentration plot (Figure 5.1-4.a). Utilizing fundamental mass transport models and the maximum penetrant in bulk material concentration, the *theoretical concentration* profile versus time and position can be predicted within the sensing region as a function of an average diffusion coefficient. The results of the calibration experiments (Figure 5.1-4.a.) can be used to convert the *theoretical concentration* profile into a *theoretical in-phase permittivity* profile (Figure 5.1-4.b) versus time and as a function of an average diffusion coefficient. However, only the average permittivity across the sensing region can be experimentally determined as a function of time. Because $w(x)$ had been determined from equation (5-7), the *theoretical in-phase permittivity* profile discussed earlier can be converted into an *average in-phase permittivity* as a function of time and a diffusion coefficient. However, the *average in-phase permittivity* as a function of time is experimentally accessible as was discussed earlier (Figure 5.1-4.b). Therefore, an average diffusion coefficient can be calculated that minimizes the difference between the *theoretical permittivity* and that measured experimentally. If the average theoretical value does not closely match the experimental value, then the constitutive model selected for the fundamental transport equation must be inapplicable. This method neglects the effects of bulk material relaxation and transport and also assumes Fickian-behavior. This method was not utilized in the preliminary experimental work presented in this chapter.

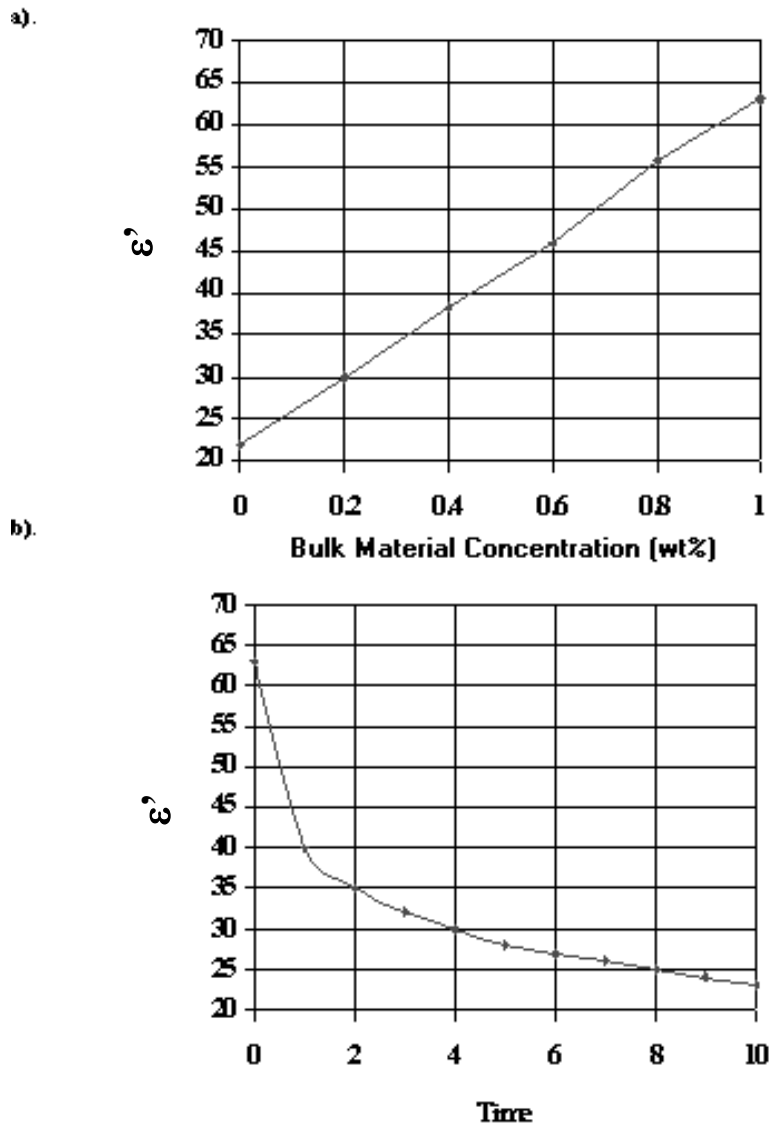


Figure 5.1-4 In-phase permittivity (ϵ') at a certain frequency versus a). concentration of bulk material in the penetrant. b). time as the penetrant diffuses into the bulk material which has an initial thickness greater than the thickness of the sensing region. Note: Data fabricated for illustration purposes.

The second method allows one to qualitatively estimate the penetrant diffusion coefficient by determining the time required for the penetrant to enter the sensing region. This method does not provide a quantitative value of the penetrant diffusion coefficient but does produce an order of magnitude estimate of its value. As with the previous method, the sensor's sensing distance is determined by coating a sensor with bulk material thicknesses below and above the suspected sensing distance (Figure 5.1-3). After the sensing distance has been

determined, the sensor is then coated with a known thickness of the bulk material that is greater than the sensing distance, l . The penetrant material is then allowed to diffuse into the bulk material. The ϵ' versus time data is collected (Figure 5.1-4.b). When the ϵ' begins to change from its original value, the penetrant has been transported to the sensing region. This time can be used to determine the order of magnitude diffusion coefficient from the following equation:

$$\xi = 1 - \operatorname{erf} \left[\frac{l}{2\sqrt{D \cdot t_s}} \right] \quad (5-8)$$

where ξ is the ratio of the penetrant concentration at the sensing region boundary to the maximum concentration of the penetrant in the bulk material. ξ is a small number that is used to indicate when the interface concentration has changed enough to influence the experimentally measured ϵ' value (Note: D does not strongly depend upon ξ for small values of ξ : see Figure 5.3-13). This method only provides a qualitative estimate of the penetrant diffusion coefficient and does not take into account bulk material relaxation, bulk material transport, or non-Fickian diffusion. However, this method does eliminate the need to have the dielectric response of penetrant/bulk material blends.

5.2 Experimental

5.2.1 Materials

The K-90 PVP sizing material (LUVISKOL lot # 20421501) (Figure 3.1.1.b) was obtained from BASF. The M_w of this material was 1,250,000 g/mol and it had a T_g of 180°C [3.1]. This material was dried at 110°C for 18 hours before being used.

The K-30 PVP material (LUVISKOL lot # G40107PO0) (Figure 3.1.1.b) was obtained from BASF. The M_w of this material was 49,000 g/mol and it had a T_g of 168°C [3.1]. This material was not dried before it was used.

The Phenoxy™ sizing material (PKHW-35 lot # 217013) (Figure 3.1.1.a) was obtained from Phenoxy Associates, Rock Hill, SC. This material was obtained as a 30wt% dispersion of approximately 1-micron diameter particles in 57wt% water [3.1.13]. The balance of the suspension contained 10 wt% of a cosolvent, butoxyethanol, and 3 wt% of a neutralant, dimethylethanolamine. In order to make the hydrophobic Phenoxy™ shown in Figure 3.1.1.a

water dispersible, the commercially available Phenoxy™ suspension contained a modified version of the Phenoxy™ backbone shown in Figure 3.1.1.a. For every ten repeat units, a single carboxylic acid functionality had been added to the diglycidyl ether functionality [3.1.13]. The M_n of the Phenoxy™ was 19,000 g/mol (GPC) and it had a T_g of 97°C (DSC) [1.8].

The methanol used to prepare the K-90 PVP dip coating solutions was HPLC grade (lot # 37099) obtained from EM Science.

The isopropanol used to break the Phenoxy™ emulsion was HPLC grade (lot # B5417) obtained from Burdick and Jackson.

The THF used to prepare the Phenoxy™ dip coating solution was HPLC grade (lot # AU779) obtained from Baxter.

The vinyl-ester oligomer was obtained from the Dow Chemical Company (Figure 3.1.1.c) (lot # MD10018PS1). The M_n of the vinyl-ester oligomer was 690 g/mol, which was equivalent to the vinyl-ester oligomer, utilized in the Dow 441 vinyl-ester resin (70wt% vinyl-ester, 30wt% styrene monomer).

The styrene monomer utilized to prepare the vinyl-ester oligomer/styrene blends was obtained from Aldrich Chemical (cat. # 5497-2 lot. # 03520PQ) with stabilizers.

The Dow 441-400 vinyl-ester resin (Figure 3.1.1.c&d) was obtained from the Dow Chemical Company. The resin consisted of 70wt% vinyl-ester oligomer and 30wt% styrene monomer.

The sizing/Derakane™ blends were cured with benzoyl peroxide (BPO). The BPO utilized for this purpose was obtained from Aldrich. The material was 97% pure (lot # ES 03918CS).

Whatman Qualitative filter paper (Cat. # 1001 070) was used to filter the separated Phenoxy™ particles from the broken suspension. The separation procedure utilized is discussed in the next section.

5.2.2 Equipment

5.2.2.1 Dielectric Equipment

5.2.2.1.1 Sensors

The micro-dielectric sensors were obtained from Prof. David Kranbuehl at the College of William and Mary.

5.2.2.1.2 Impedance Analyzer

5.2.2.2 Profileometer

The profileometer utilized in these experiments was a Dektak³ manufactured by Sloan Technology Corporation. The model number for the profileometer was 20084.

5.2.3 Separation of Phenoxy™ particles from suspension

The Phenoxy™ sizing material was supplied in the form of a 35wt% emulsion of 1-micron particles. Before these particles could be used to prepare a dip coating solution or a Phenoxy™/Dow 441-400 blend, the particles had to be separated from the emulsion. Both of these end use applications required the particles to be dissolved into a solvent (either THF or the Dow 441-400 vinyl-ester resin), therefore, a small particle size was desired to minimize the resistance to dissolution (i.e. $< 75\mu\text{m}$).

The Phenoxy™ suspension was broken by adding isopropanol to the as-received suspension. Approximately 350g of Phenoxy™ suspension and 1150g of isopropanol were added to a 2000ml erlenmeyer flask. After the flask was capped, it was vigorously shaken for 2 minutes. The particles were then allowed to settle to the bottom of the flask. The clear liquid was then decanted off leaving a dense liquid of the separated particles. This dense liquid was then added to a large vacuum-assisted filter funnel where the liquid was removed from the separated particles. While still in the filter funnel, the Phenoxy™ particles were washed with approximately 250g of water and then allowed to partially dry for 30 minutes. The partially dried Phenoxy™ particles were then spread on a paper towel where final drying was allowed to take place. As the drying proceeded, the particles tended to coalesce. To counteract this, the particles were ground in a large mortar and pestle **every** two hours. After approximately eight

hours of drying and grinding, the particles were allowed to dry overnight without further grinding. After drying overnight, the particles were ground one last time. At this point, the Phenoxy™ particles were completely dried and separated from the original suspending liquid. This separation process usually resulted in at least 95% theoretical recovery of Phenoxy™.

The resulting Phenoxy™ particles were separated into their fundamental particle size by a mechanical separator that consisted of a series of sieve trays and a tapper. The tapper was fitted with sieve trays that ranged from a course to very fine sieve size. The last three sieve trays had 150, 75, and 35 μ m sieve sizes. The separated particles were placed in the coarse sieve tray and the tapper was allowed to tap for a period of three hours. As the particles passed through the progressively smaller and smaller sieve sizes, the particles were separated and collected in the various trays. The sieve trays were emptied and the particles were placed into four separate containers. The particle size distribution was determined by weighing the particles present in each tray. Approximately 85 wt% of the Phenoxy™ particles had a fundamental particle size greater than 150 μ m. Due to concerns about the time required for dissolution of the Phenoxy™ particles in the Derakane™, only particles with a diameter less than 75 μ m were used for the experimental work presented in this chapter. The remaining 15 wt% of the Phenoxy™ particles had the following particle size distribution: 34% --> 75 μ m < d < 150 μ m, 46% --> 35 μ m < d < 75 μ m, 20% --> d < 35 μ m. These particles were utilized for the dip coating solutions and the Phenoxy™ in the Dow 441-400 blends.

5.2.4 Preparation of sizing/solvent dip coating solutions

The sensors were coated by dipping them into a concentrated solution of the sizing in a volatile solvent. The dipping solution's concentration directly determined the final thickness of the coated sensor. The K-90 PVP sizing material was chosen as the primary system of interest in this constitutive property study. Therefore, the bulk of the data presented describes this system. However, limited data were developed for the Phenoxy™ sizing system.

Coating solutions of K-90 PVP in methanol were prepared at 10, 25, and 32 wt% K-90 PVP. These three solutions were selected based upon the solubility of the K-90 PVP in the methanol. In addition, an attempt was made to prepare solutions that had noticeably different viscosities. The solutions were stirred overnight to allow the high molecular weight PVP to fully dissolve into the methanol.

A coating solution of 25wt% Phenoxy™ in THF was prepared. Only one solution was prepared due to the difficulty in dissolving the Phenoxy™ into the THF. The separated Phenoxy™ particles ($d < 75\mu\text{m}$) were added directly to the THF and rapid stirring was accomplished with an Arrow 850 high torque stirrer. The mixture was allowed to stir for approximately eight hours.

5.2.5 Profilometry to determine sensor flatness

Before the sensors could be dip coated with the sizing solutions, the flatness of the uncoated sensors was determined via profilometry. The profilometer used a small stylus to rub across the surface to be analyzed. As the stylus moves up and down, the instrument computed the deflection and generated a topographical map (Figure 5.2-1). In order to insure that the profilometer generated an accurate profile, the surface of the instrument was leveled (Figure 5.2-2). The zero reference plane was established by zeroing the instrument at the two ends of the sensor (i.e. at the sensor leads and the opposing sensor end). A surface scan at the low speed setting was completed at the left, center, and right front of each uncoated sensor to be used in the experiments that follow. Because the final coating thickness was desired to be between 7 and $42\mu\text{m}$ depending upon the experiment, the sensors needed to be extremely flat. Therefore, any uncoated sensor that had more than a 0.5, 1.0, $2.0\mu\text{m}$ deviation from flatness was not used for an experiment requiring a 7, 22, $42\mu\text{m}$ coating, respectively.

5.2.6 Preparing the sensors to be coated

Before sensor coating was attempted, the sensors were covered completely (front, back, and sides) with parafilm. The parafilm was then carefully removed from the sensor front, leaving the sides and back protected by the film. If the coated sensor was to be used in an actual dielectric experiment, then a small portion of the parafilm was also left covering the leads of the interdigitized gold array (Figure 5.2-3.a). The purpose of this was two-fold. First, this facilitated the attachment of the electrical leads to the sensor once the coating had been applied. Second, the uncovered portion served as a zero height and a leveling reference for the thickness measurement discussed in the next section. In order to determine the processing parameters needed to produce a consistent and repeatable coating, a dipping calibration experiment was conducted for each sizing/solvent combination. If a dipping calibration experiment was being

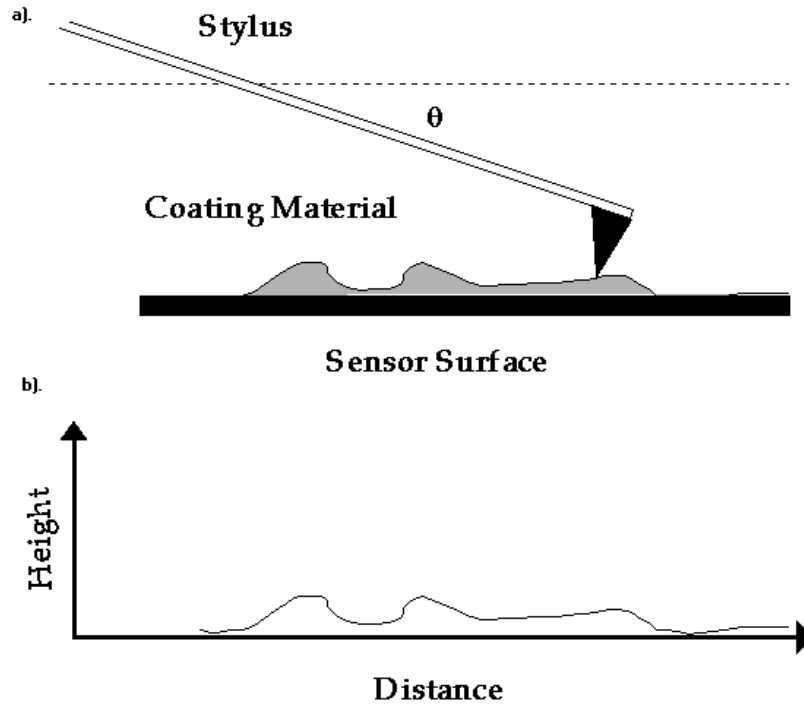


Figure 5.2-1 a). Schematic of profileometer utilizing stylus to scan the surface of the sensor. Note: Sensor detects changes in the angle θ per change in the horizontal scanning position b). Output of profileometer scan showing surface topography.

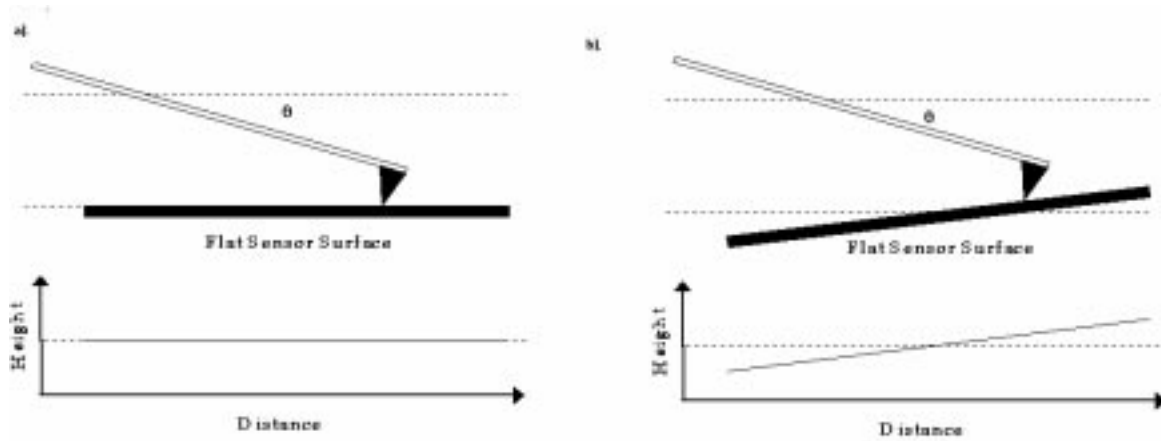


Figure 5.2-2 Schematic of profileometer leveling process. a). A perfectly flat sensor that is level with the stylus scanning direction. b). A perfectly flat sensor that is not level with the stylus scanning direction.

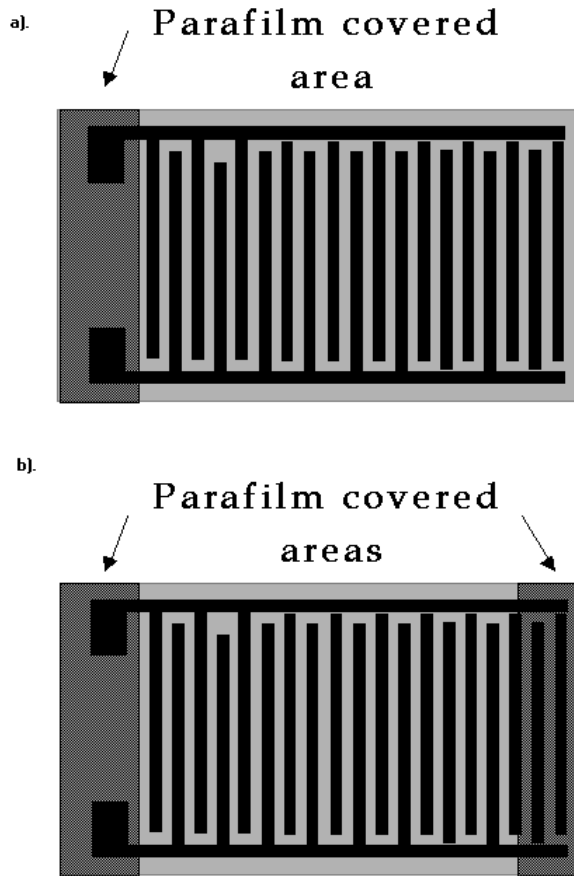


Figure 5.2-3 Schematic of micro-dielectric sensor coated with parafilm (Top view shown). Note: Bottom and sides covered also. a). Parafilm coating sensor leads, sides, and bottom. Note: This is the typical configuration for sensors to be tested in a dielectric experiment. b). Parafilm coating sensor leads, end, sides, and bottom. Note: This is the configuration utilized for coating thickness calibrations.

conducted on the sensor, then a small portion of the parafilm was also left covering the front end of the sensor (Figure 5.2-3.b). After the final coating had been applied, this left two uncoated areas on the sensor surface; one on each end of the sensor. Because the two front ends of the sensor were left uncovered, the profilometer could be accurately leveled. Because the sensor was left uncoated at the end remote from the leads, a portion of the interdigitized grid was also left uncovered. Because the sensors having this final coating configuration would not be used for an actual dielectric experiment, this configuration did not compromise the accuracy of the calibration experiment.

5.2.7 Dip coating of the micro-dielectric sensors

After the sensor had been prepared for dip coating, it was connected to a string via an alligator clip. The string was then placed in the grips of an Instron 4104 test frame and suspended approximately one foot from the bottom of the machine. A small 20-ml glass container filled with the dipping solution was placed below the suspended sensor. The sensor was then carefully lowered into the dipping solution. After the sensor was completely immersed, the sensor was pulled from the solution at a slow-controlled rate. The sensor was then placed in a convection oven at 100°C for 15 minutes. The sensor was then ready for coating thickness determination.

The concentration of the dipping solution and the rate at which the sensor was pulled from the solution determined the coating thickness and its uniformity. In order to determine the coating parameters and dipping solution concentration necessary to achieve the three target K-90 PVP thicknesses of 7, 22, and 42 μm , a dipping calibration experiment was conducted utilizing the sensors protected on both ends by the parafilm. The removal speed of the sensor from the dipping solution was varied from 0.25 mm/min to 1.50 mm/min while the dipping solution concentration was varied from 10 to 32 wt% K-90 PVP in methanol. After the optimal removal speed and dipping solution concentrations had been determined for the K-90 PVP in methanol system, this line speed was utilized for the other coating systems. For the other coating systems, the dipping solution concentration was chosen such that its viscosity closely matched that of the optimal PVP concentration.

After the optimal coating conditions had been determined for the materials to be analyzed, the sensors to be utilized for the actual dielectric experiments were coated using the optimized parameters. The sensors with only the leads protected were utilized for this purpose.

5.2.8 Profilometry to determine coating thickness

After the sensors had been coated with the materials to be analyzed, the coating thickness was determined by profilometry. Before the thickness profile could be determined, the profilometer had to be leveled and zeroed. The procedure utilized for this leveling and zeroing depended upon whether the remote end of the sensor was coated or not.

If both sensor ends were uncoated (Figure 5.2-3.a) (i.e. sensor utilized in a dipping calibration procedure), then the leveling was completed by zeroing the profilometer at the two

sensor ends. This established a very wide reference plain that enabled the profilometer to accurately measure the thickness across the entire sensor.

If only the lead end of the sensor was uncoated (Figure 5.2-3.b) (i.e. sensor utilized in an actual dielectric experiment), then the leveling was completed by zeroing the profilometer at the uncoated end and adjusting the leveling until the initial thickness profile followed a horizontal line. Because the leveling plane in this case was narrow, the accuracy of the level could not be guaranteed at regions remote from the uncoated portion. Therefore, this method only allowed the determination of the coating thickness at regions close to the sensor leads and didn't allow the determination of an actual profile as was the case with the other sensor preparation technique. However, the other sensor preparation technique would have left a portion of the interdigitized grid uncovered and this would have compromised the accuracy of the dielectric experiment.

5.2.9 Preparing blends for dielectric and mechanical property determination

Two sets of K-90 PVP/Derakane™ 441-400 vinyl-ester blends were prepared. The first set had blend compositions of 0.25, 1.00, 3.00, and 5.00 wt% K-90 PVP. The second set had blend compositions of 0.25, 1.00, 2.58, 5.27, 11.11 wt% K-90 PVP. The Derakane™ was added to a one-quart mason jar. An Arrow 850 high torque stirrer was placed into the Derakane™ and stirring was set at the maximum speed. The K-90 PVP was slowly added to the Derakane™ at a point where the vorticity appeared to be the greatest. If the K-90 PVP was added too quickly, then the PVP would clump and not dissolve. However, if the K-90 PVP was added too slowly, then the PVP would start to significantly dissolve before all the PVP had been added. This greatly increased the solution viscosity and made the adding of additional PVP impossible. After all the K-90 PVP had been added to the Derakane™, the mixture was allowed to rapidly stir until all of the K-90 PVP had been dissolved (approximately 24 hours for the 5.0 wt%). Some of the resulting K-90/Derakane™ blends were utilized for dielectric analysis and density determination (note: after the blend had been catalyzed then the density was determined). In addition, the zero shear viscosity as a function of K-30 PVP blend concentration was determined. The zero shear viscosity was used to estimate the dissolution diffusion coefficient from the Stokes-Einstein Equation. Some of the blends were also used for the preparation of cured K-90 PVP/Derakane blends. The curing procedure is discussed later in this chapter.

Utilizing the same procedure listed above, K-30 PVP/Derakane™ blends were also prepared. The blends had concentrations of 0.26, 1.00, 3.00, 7.50, and 15.00wt% K-30 PVP in Derakane™. The zero shear viscosity as a function of K-30 PVP blend concentration was determined and will be discussed later. The zero shear viscosity was used to estimate the dissolution diffusion coefficient from the Stokes-Einstein Equation. A 6.95 wt% Phenoxy™ in Derakane™ blend was prepared. Approximately 360g of the Derakane™ was added to a quart size mason jar. An Arrow 850 high torque stirrer was placed into the Derakane™ and stirring was set at the maximum speed. The Phenoxy™ was slowly added to the Derakane™. After several hours of rapid stirring, the optical appearance of the mixture remained very turbid. In addition, the viscosity of the mixture did not change significantly during the process. This was a strong indication that the Phenoxy™ was not dissolving into the Derakane™. Because the Phenoxy™ would not dissolve in the Derakane™, neither dielectric properties nor the density could be obtained on this blend. However, this blend was cured and tested for cured blend density and other mechanical properties.

5.2.10 Static dielectric experiments on blends

Electrical leads were attached to an uncoated dielectric sensor. The sensor was then secured to the bottom of a 500ml beaker. After being secured, the in-air capacitance of the sensor was determined by applying a potential and measuring the output current. After the in-air capacitance had been determined, the blends were slowly added to the beaker until the entire sensor was covered with at least ½ cm of the material.

The dielectric response of the blend was then determined. The dielectric impedance analyzer input a potential at the following frequencies and the output current was determined: 0.05 kHz, 0.125 kHz, 0.25 kHz, 0.50 kHz, 5.0 kHz, 25.0 kHz, 50.0 kHz, 250.0 kHz, 500.0 kHz, and 1000.0 kHz. From equations (5-2), (5-3), and (5-4), the in-phase, ϵ' , and out-of-phase, ϵ'' , permittivity were determined as a function of frequency and time. For this set of experiments, the experiment was allowed to proceed for a period of approximately 60 minutes.

5.2.11 Static dielectric properties of K-90 PVP films

Electrical leads were attached to a dielectric sensor that had been coated and characterized for coating thickness. The sensor was then secured to the top of an ordinary lab

bench. The in-air capacitance of the coated sensor could not be determined in this case due to the coating. Therefore, a typical in-air capacitance for an uncoated sensor was input into the software.

The transient dielectric response of the film was then determined as a function of frequency. The dielectric impedance analyzer input a potential at the following frequencies and the output current was determined: 0.05 kHz, 0.125 kHz, 0.25 kHz, 0.50 kHz, 5.0 kHz, 25.0 kHz, 50.0 kHz, 250.0 kHz, 500.0 kHz, and 1000.0 kHz. From equations 2, 3, and 4, the in-phase, ϵ' , and out-of-phase, ϵ'' , permittivity were determined as a function of frequency and time. For this set of experiments, the experiment was allowed to proceed until steady state was achieved.

5.2.12 Transient dielectric experiments of interdiffusion

Electrical leads were attached to a dielectric sensor that had been coated and characterized for coating thickness. The sensor was then secured to the bottom of a 500ml beaker. The in-air capacitance of the coated sensor could not be determined in this case due to the coating. Therefore, a typical in-air capacitance for an uncoated sensor was input into the software. The penetrant material (usually Dow™ 441-400 vinyl-ester) was slowly added to the beaker until the entire sensor was covered with at least ½ cm of the material.

The transient dielectric response of the blend was then determined. The dielectric impedance analyzer input a potential at the following frequencies and the output current was determined: 0.05 kHz, 0.125 kHz, 0.25 kHz, 0.50 kHz, 5.0 kHz, 25.0 kHz, 50.0 kHz, 250.0 kHz, 500.0 kHz, and 1000.0 kHz. From equations (5-2), (5-3), and (5-4), the in-phase, ϵ' , and out-of-phase, ϵ'' , permittivity were determined as a function of frequency and time. For this set of experiments, the experiment was allowed to proceed for as long as possible or until steady state was achieved.

5.2.13 Density determination of the un-cured blends

The density of the un-cured K-90 PVP/Derakane™ blends was determined utilizing a Fisher Scientific grease pycnometer. The assembled pycnometer was weighed empty and then full of deionized water at ambient temperature. The pycnometer was carefully dried. The K-90 PVP/Derakane™ blend was added to the pycnometer base while insuring that no air bubbles were

trapped. The pycnometer was reassembled and weighed. The density of the blend was determined from the following equation:

$$\rho_u = \frac{(m_{blend} - m_{pyc})}{(m_{water} - m_{pyc})} \quad (5-9)$$

where ρ_u was the density of the un-cured blend, m_{blend} was the mass of the pycnometer filled with the blend, m_{pyc} was the mass of the pycnometer, m_{water} was the mass of the pycnometer filled with the water (note: all at the ambient temperature).

5.2.14 Curing of the blends

The K-90 PVP/Derakane™ and the Phenoxy™/Derakane™ were cured utilizing benzoyl peroxide. In past work here at Virginia Tech [1.8], a BPO concentration of 1.1 wt% in Derakane™ was utilized (or a .011:1 ratio of BPO to Derakane™). In order to keep the material systems somewhat similar, the same ratio of BPO to Derakane™ was utilized in these experiments. However, because the amount of sizing material varied from blend to blend, so did the actual concentration of BPO. The blend was added to a suitable glass container. An Arrow 850 high torque stirrer was placed into the blend and stirring was set at the medium speed. The BPO was slowly added to the stirring mixture. After the BPO had dissolved (approximately 1 hour), the blend was degassed utilizing approximately 24 inHg vacuum. The blend was allowed to degas for approximately 30 minutes. The catalyzed K-90 PVP/Derakane™ blend was used for the density determination.

The catalyzed K-90 PVP/Derakane™ and Phenoxy™/Derakane™ blends were cured utilizing the following procedure. A 8" X 6" X ¼" vertical mold was utilized for the curing process to prevent the formation of air voids. The mold was treated with mold release and then assembled. The blend was added very slowly to the mold. Because the viscosity of some of the blends was so high, it was difficult preventing air from being trapped in the mold. In addition, the high viscosity prevented some of the blends from flowing into the corners of the mold. This was counteracted by heating the mold to a temperature above room temperature but below the initiation temperature of the Derakane™ and holding it there for a period of time. After the top had been secured to the mold, it was then placed in a Fisher Isotemp forced convection oven. The material was cured utilizing the following cure cycle: 1 hour hold at 65°C → heating at

10°C/min to 150°C → 20 minute hold at 150°C. After the mold had cooled to room temperature, the cured blend was removed.

5.2.15 Density determination of the cured blends

The density of the cured blends was determined by applying Archimedes' principle. Approximately 6 grams of the cured blend was weighed. The sample was then immersed in isopropyl alcohol and weighed again. The density of the cured blend was calculated using Archimedes' principle using the following equation:

$$\rho_c = \frac{\rho_{IPA} \cdot W_{air}}{W_{air} - W_{IPA}} \quad (5-10)$$

where ρ_c = density of the cured blend, ρ_{IPA} = density of Isopropyl alcohol, W_{air} = weight of blend in air and W_{IPA} = weight of sample in isopropyl alcohol (note: all at ambient temperature).

5.2.16 Shrinkage of Blends upon Cure

As the free-radical polymerization of the Derakane™ network progresses, the density of the system correspondingly increases due to a decrease in system volume. The degree of volumetric shrinkage can be determined from the cured and un-cured blend densities utilizing the following equation:

$$\beta = 100 \cdot \left[1 - \frac{\rho_u}{\rho_c} \right] \quad (5-11)$$

where β is the percent blend shrinkage, ρ_u is the un-cured blend density computed from equation (5-9), and ρ_c is the cured blend density computed from equation (5-10).

5.2.17 Glass transition temperature determination of the cured blends

The glass transition temperature of the blends was determined through the use of Differential Scanning Calorimetry (DSC). First and second heat data were generated for pure Derakane™ and the K-90 PVP/Derakane™ blends. The second heat data was generated by holding the system isothermally at 250°C for 10 minutes. These experiments were completed by Dr. Chris Robertson.

5.2.18 Rheological Experiments on K-90 and K-30 Blends

The zero shear viscosity of the K-90 and K-30 PVP blends was determined with a Bohlin VOR rheometer. A cone and plate fixture was utilized for both steady shear and oscillatory experiments. The plate had a fixed diameter of 254mm and the cone angle was fixed at 5.44°. Due to the volatile nature of the styrene portion of the Derakane matrix, the sample and fixture were enclosed in a solvent trap that prevented excessive loss of the styrene component. The sample was placed between the cone and plate fixture. After the instrument had been zeroed, the instrument was operated in steady shear mode. For each blend, the range of shear rates tested had to be different to account for the large functional dependence of the viscosity on K-90 PVP concentration. The VOR rheometer can accurately measure torque on the upper plate only within a certain range. In other words, the VOR is torque limited. The instrument's torque range can be altered by varying the torque bar or the shear rate. For the experiments discussed in this chapter, the torque range was adjusted by varying both the torque bar and the shear rate range for each of the materials. For each blend tested, the shear rate was varied over at least one order of magnitude. The shear rates utilized ranged from 0.00187 to 11.7 1/s. The zero shear viscosity was estimated from two or three shear rates per sample. In addition, the blends were tested for their oscillatory response at a fixed frequency of 1 Hz. The instrument was set in the auto-strain mode such that the output torque did not fall below a critical value.

5.2.19 Static tensile property determination of cured blends

The static tensile properties were determined in accordance with ASTM D-690. These experiments were conducted by Dr. Nikhil Verghese.

5.3 Results and Discussion (Note: Basis for all error bars was 1- σ)

In section 5.3.1, the results of the micro-dielectric experiments are presented and discussed. In section 5.3.2, the results of the mechanical properties of the sizing/matrix blends are presented and discussed.

5.3.1 Microdielectric Results and Discussion

Section 5.3.1 details the experimental results associated with the micro-dielectric experiments. The purpose of these experiments was to both qualitatively and quantitatively evaluate the interdiffusion of the sizing and the matrix.

5.3.1.1 Profilometry to determine sensor flatness

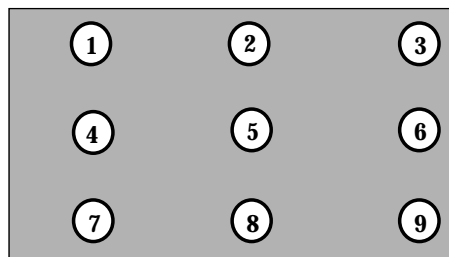
Seventeen dielectric sensors were received from Prof. Kranbuehl's group. The as-received sensors were determined for flatness (Table 5-1). Only eight of the seventeen sensors were found to be flat enough for any type of dielectric experiment. In addition, only three were found to be flat within $0.5\mu\text{m}$. Therefore, the remaining nine sensors were discarded and not utilized in any experimental results presented in this chapter.

5.3.1.2 Dip coating of the micro-dielectric sensors

After the sensors had been characterized for flatness, a calibration experiment for the K-90 PVP in methanol solution was completed in order to determine the optimal coating parameters. In order to determine the optimal withdrawal speed for the sensor, the K-90 PVP in

Table 5-1 Flatness of sensors utilized for dielectric experiments. Nine positions on the sensor surface (see schematic below for position on sensor) were tested. Numeric value shown indicates the deviation from flatness. Note: * indicates sensors that had an acceptable flatness level and were used in the experiments. The other sensors were discarded.

Sensor ID #	1 (um)	2 (um)	3 (um)	4 (um)	5 (um)	6 (um)	7 (um)	8 (um)	9 (um)
F1*	2.40	2.00	1.50	2.00	1.50	0.50	1.75	1.50	0.75
F2	8.00	10.4	7.50	8.00	10.00	7.00	8.00	10.40	8.00
F3*	1.50	1.00	0.25	1.50	1.00	0.50	1.25	0.75	0.25
F4*	0.25	0.50	0.25	0.20	0.00	0.00	0.10	-0.20	-0.40
F5*	1.00	1.00	0.75	0.70	0.60	0.30	0.80	0.80	0.40
F6	n.a.	n.a.	n.a.	5.00	8.00	6.00	n.a.	n.a.	n.a.
F7*	0.40	0.60	0.40	0.30	0.40	0.10	0.40	0.30	0.00
F8*	-0.20	-0.20	-0.10	-0.20	-0.30	-0.30	-0.40	-0.60	-0.40
F9	n.a.	n.a.	n.a.	5.00	7.00	5.00	n.a.	n.a.	n.a.
F10*	0.40	0.30	0.20	0.30	0.30	0.20	0.40	0.30	0.00
F11	n.a.								
F12	n.a.	n.a.	n.a.	6.00	8.00	6.00	n.a.	n.a.	n.a.
S11	n.a.	n.a.	n.a.	-3.50	-5.00	-3.50	n.a.	n.a.	n.a.
S12	n.a.	n.a.	n.a.	-3.50	-5.00	-4.00	n.a.	n.a.	n.a.
S13	n.a.	n.a.	n.a.	-4.00	-5.00	-4.00	n.a.	n.a.	n.a.
S14*	0.00	-0.50	-1.50	-0.50	0.50	0.00	n.a.	n.a.	n.a.
S15	n.a.	n.a.	n.a.	3.60	4.50	3.50	n.a.	n.a.	n.a.



methanol dipping solution concentration was kept constant at a value of 25wt% while the withdrawal speed was varied from 0.25 to 1.5 mm/min. For withdrawal speeds equal to or less than 0.75 mm/min, the final K-90 PVP coating was found to be extremely non-uniform (Figure 5.3-1). In addition, the coating was found to be unrepeatably from dip coating to dip coating (Figure 5.3-2). However, for withdrawal speeds greater than 0.75 mm/min, the coating was both uniform and repeatable (Figure 5.3-3). In order to minimize the coating time, a withdrawal speed of 1.5 mm/min was selected for the remainder of the experimental results presented in this chapter. Sensors were dip coated with the four different K-90 PVP in methanol solutions to test the effect of dipping concentration (Figure 5.3-4). In addition, one set of replicate experiments were conducted to verify that the final coating was repeatable. Because the 1.5 mm/min withdrawal speed was utilized for the calibration experiments, the coating was found to be very uniform across the sensor surface (uniform to within 15%). The coating thickness varied linearly with concentration for concentrations that ranged from 20 to 33.2 wt% K-90 PVP in methanol. The coating thickness at the 10 wt% K-90 PVP concentration did not follow this linear trend. In addition, the coating thickness were not very repeatable and had typical variations of 10 to 30%. Therefore, the calibration experiments were only used as a guide for selecting the dipping concentration needed to achieve a target coating thickness.

5.3.1.3 Penetration depth for micro-dielectric sensors

The penetration depth was determined by coating the sensor with varying amounts of K-90 PVP. Unfortunately, due to a limitation in flat sensor availability, only three K-90 PVP coated sensors were utilized for this determination. From past work completed by this author and Prof. Kranbuehl, the penetration depth was suspected to be approximately 17 μ m. Therefore, it was desired to coat the three flat dielectric sensors with at least one thickness below and one above the suspected 17 μ m sensing distance. After inspecting the results of the calibration experiments (Figure 5.3-4), the following K-90 PVP in methanol dip solution concentrations were utilized: 20, 25, and 33.2 wt%. The resulting coated sensors were characterized for initial thickness utilizing the procedure discussed in the experimental section. Because the coating conditions utilized for this set of experiments were identical to those utilized for the calibration experiments, it was assumed that the coating thickness would again be uniform. This could not be verified due to the inability to accurately level the profilometer with only one end of the

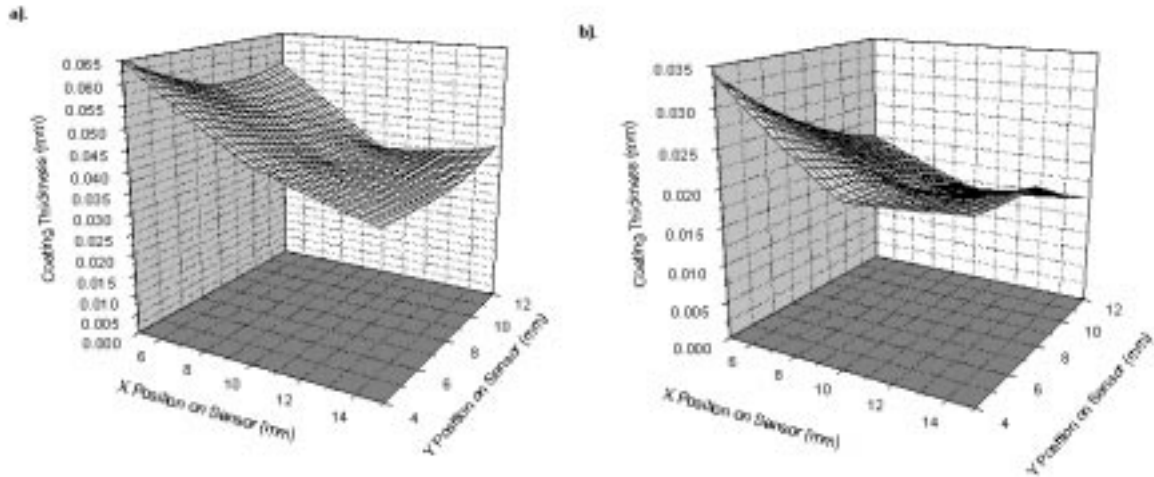


Figure 5.3-1 Coating thickness versus sensor position for 25wt% K-90 PVP in methanol dipping solution and a sensor withdrawal speed of a). 0.25 mm/min. b). 0.75 mm/min.

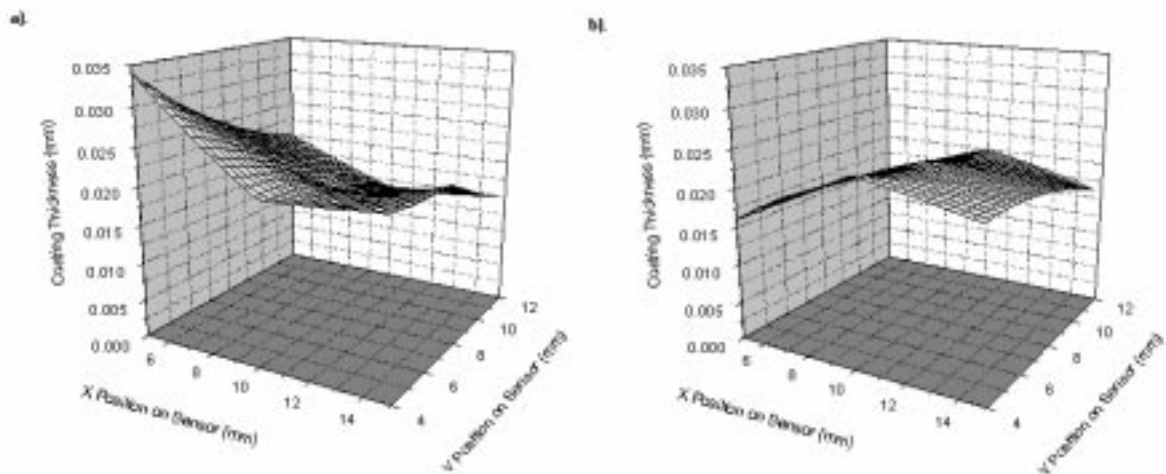


Figure 5.3-2 Coating thickness versus sensor position for 25wt% K-90 PVP in methanol dipping solution and a sensor withdrawal speed of 0.75 mm/min. a). Sensor F1 b). Sensor F3.

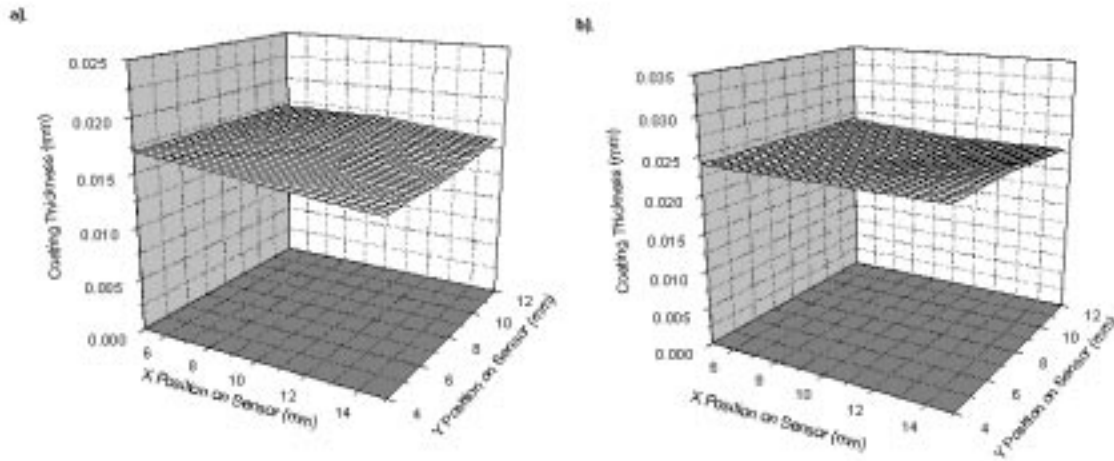


Figure 5.3-3 Coating thickness versus sensor position for 25wt% K-90 PVP in methanol dipping solution and a sensor withdrawal speed of a). 1.50 mm/min b). 3.00 mm/min.

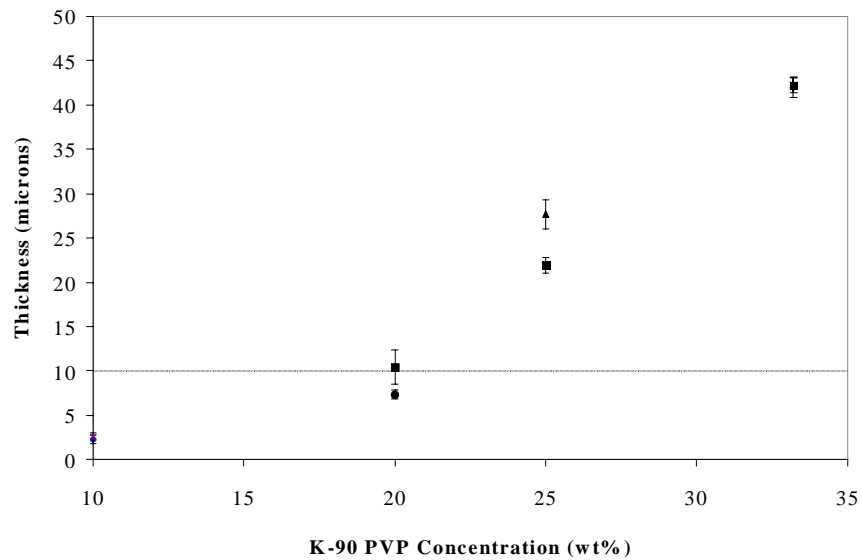


Figure 5.3-4 K-90 PVP coating thickness for 1.5 mm/min withdrawal rate versus K-90 PVP in methanol dipping solution concentration.

sensor uncoated. The coating thicknesses (note: near the uncoated sensor leads) that resulted were 7, 22, and 42 μm for the dipping solution concentrations of 20, 25, and 33.2 wt% respectively.

The dielectric properties of these coated sensors were measured in order to determine the penetration or sensing distance, l . The in-phase permittivity was determined as a function of the K-90 PVP thickness (Figure 5.3-5). The sensing distance, l , was between 7 and 22 μm . Unfortunately, a more quantitative estimate of the sensing distance could not be obtained due to a lack of data points. In addition, the weight function, $w(x)$, could not be determined for the same reason. For the remaining results presented in this chapter, the sensing distance, l , was assumed to have the 17 μm value determined earlier.

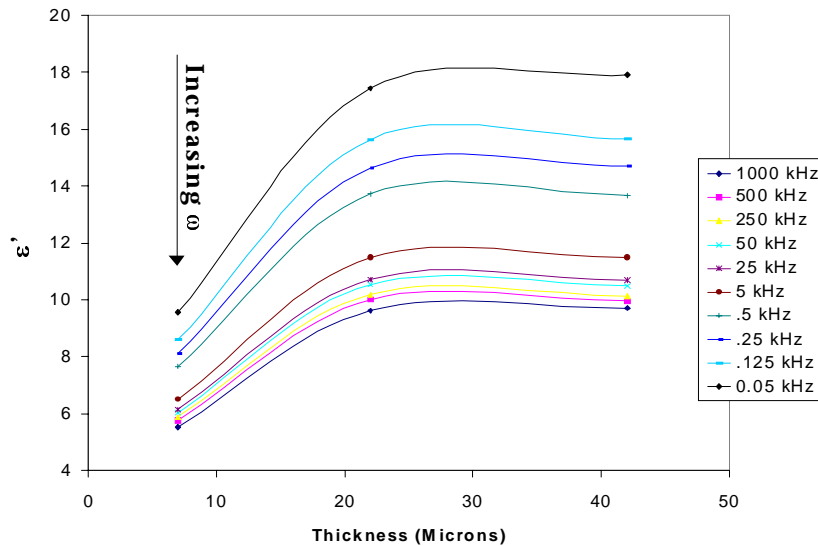


Figure 5.3-5 In-phase permittivity versus K-90 PVP coating thickness. Note: Sensing distance is between 7 and 22 μm .

5.3.1.4 Static dielectric experiments on K-90 PVP film

The dielectric properties (ϵ' , ϵ'' , and $\tan \delta$) of the K-90 PVP film were already determined during the penetration depth experiments just discussed (Figure 5.3-6). The in-phase permittivity showed typical high T_g polymeric behavior (Figure 5.3-6.a). At high frequencies, the ϵ' remains essentially constant indicative of the un-relaxed permittivity, ϵ_u . However, the

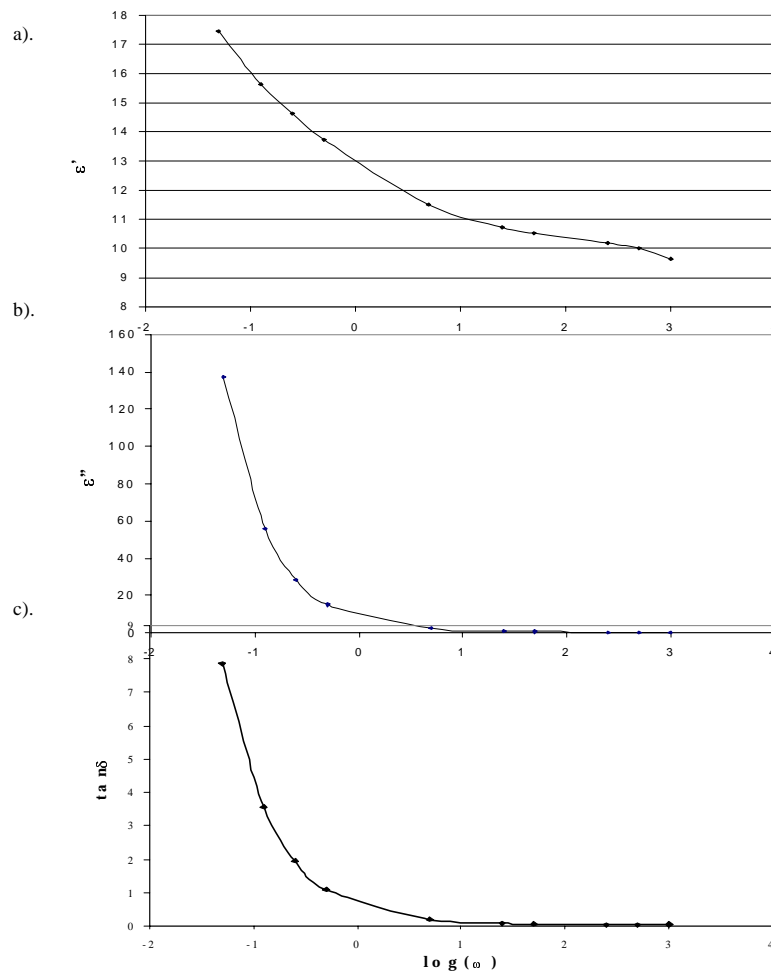


Figure 5.3-6 Dielectric response of 22 μ m thick K-90 PVP film versus $\log(\omega)$ where ω is in kHz. a). In-phase permittivity b). Out-of-phase permittivity c). Loss tangent.

corresponding relaxed permittivity, ϵ_r , was not present at the low frequencies due to the high T_g of the K-90 PVP material ($T_g = 180^\circ\text{C}$).

5.3.1.5 Static dielectric experiments on K-90 PVP/Derakane Blends

Dielectric properties (ϵ' , ϵ'' , and $\tan \delta$) of the K-90 PVP/Derakane blends were measured as a function of frequency (Figure 5.3-7) for a period of approximately 60 minutes. The dielectric properties for the pure Derakane, 0.25wt%, and the 1.0wt% K-90 PVP in DerakaneTM display a 40% variation over the course of the experiment. The true dielectric properties of these

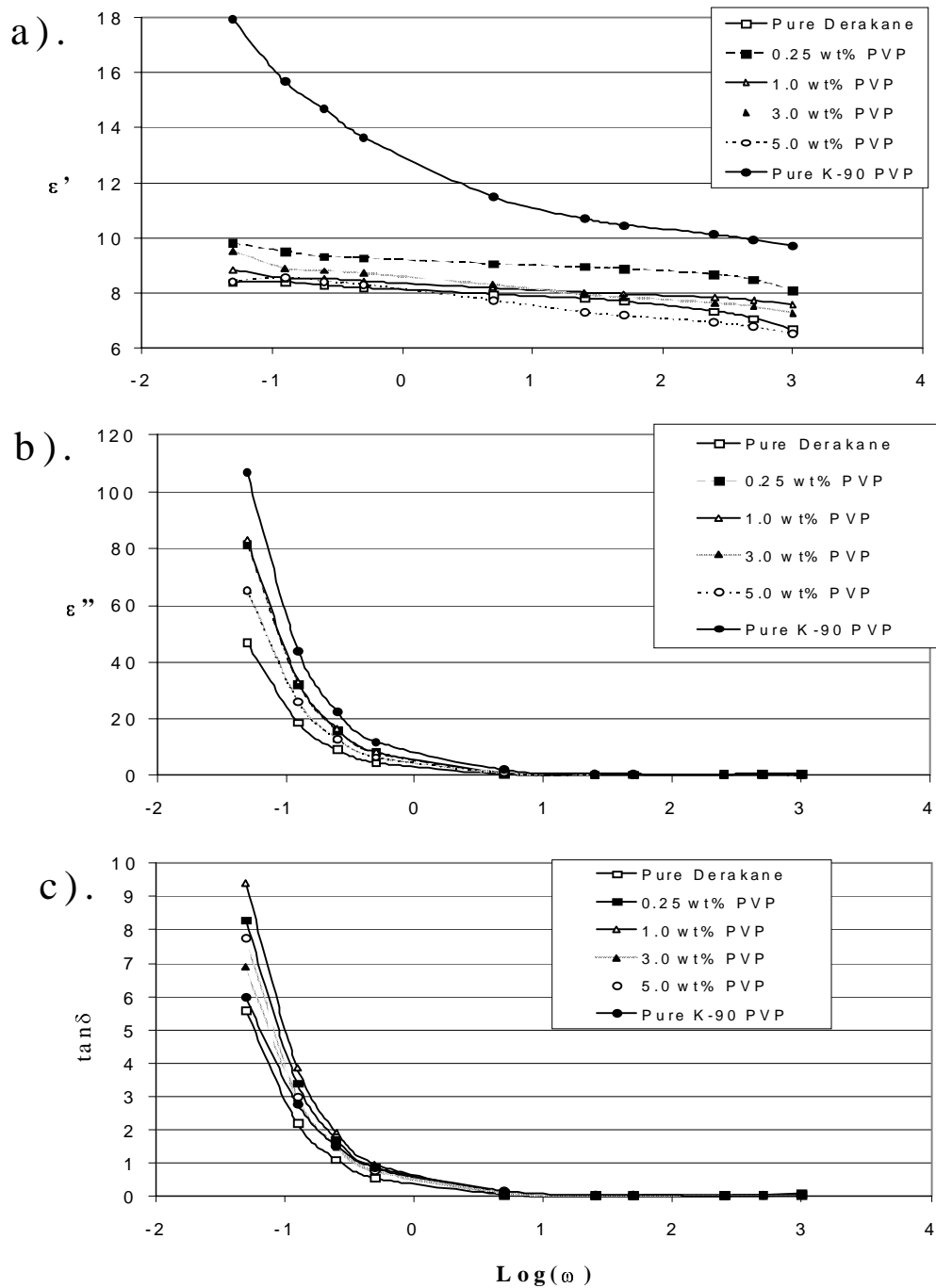


Figure 5.3-7 Dielectric properties versus $\log(\omega)$ for K-90 PVP/Derakane blends. a). ϵ' b). ϵ'' and c). $\tan \delta$.

materials should not change over the time period investigated. Therefore, this transient in dielectric properties was probably the result of liquid flowing off the sensor during the course of the experiment.

The dielectric properties did not follow a monotonically increasing or decreasing pattern with respect to changes in concentration. It was felt that the values of ϵ' at high frequencies should directly correlate to electron density and be approximately linear with respect to concentration (over the concentration range where miscible). The values of ϵ' at 1000.0 kHz did follow this trend between the concentration range of 0.25 and 5.0 wt% (Figure 5.3-8). The values of ϵ' at 1000.0 kHz for the pure Derakane and the pure K-90 PVP did not fall on a line drawn through the 0.25, 1.0, 3.0, and 5.0 wt% values. We postulate that this might be explained by the phenomena discussed in the previous paragraph. The pure K-90 PVP was not expected to fall on the same line because of its solid and extremely viscous nature.

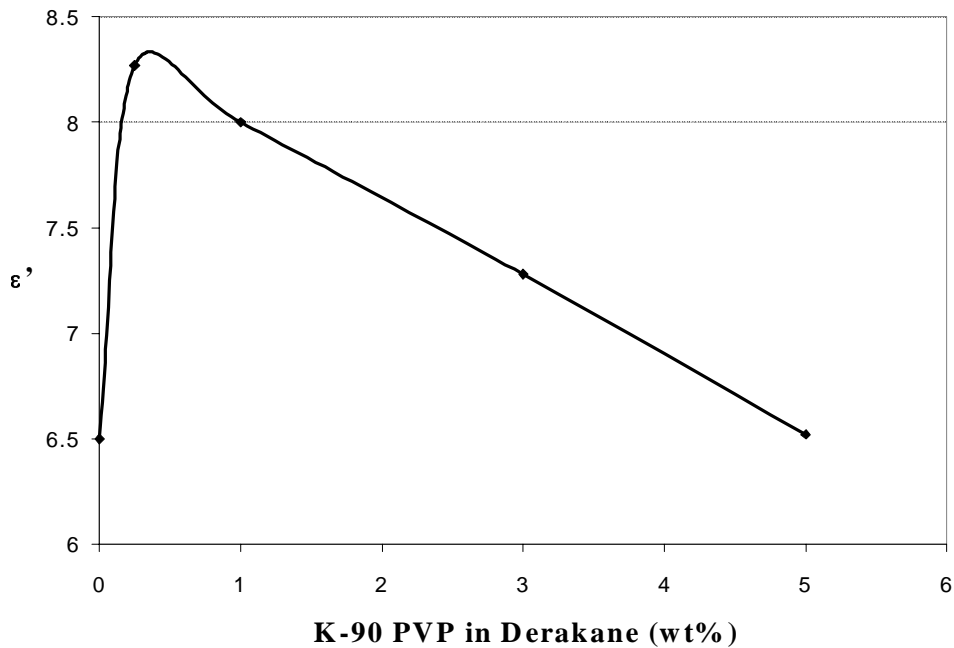


Figure 5.3-8 In-phase permittivity (ϵ') at 1000kHz versus K-90 PVP in Derakane concentration.

5.3.1.6 Transient dielectric experiments of interdiffusion

5.3.1.6.1 Transient K-90 PVP Diffusing into Derakane

Dried K-90 PVP was coated onto a flat dielectric sensor via methanol. The thickness of this K-90 PVP coated sensor was found to be $42\mu\text{m}$ by profilometry. This sensor was then coated with an infinite bath of the Derakane™ 441-400. Dielectric properties were measured as a function of the same frequencies utilized previously for a time period equal to approximately 1344 minutes (Figure 5.3-9 and Figure 5.3-12). At the start of the experiment, the dielectric properties exactly matched those measured earlier for the pure K-90 PVP coated sensor. The dielectric properties remained constant until the first change in the properties was observed at approximately 70 minutes. Therefore, it took the Derakane™ approximately 70 minutes to travel $25\mu\text{m}$ (note: $42 - 17\mu\text{m}$). Utilizing equation (5-8), the swelling diffusion coefficient was calculated as a function of the parameter ξ (Figure 5.3-13) for x and t equal to $25\mu\text{m}$ and 70 minutes, respectively. As was mentioned in the theoretical section, ξ was the ratio of the Derakane™ in K-90 PVP concentration at the sensing region boundary divided by the maximum Derakane™ in K-90 PVP concentration. The value of the Derakane™ concentration at the boundary when the ϵ' initially changes is very small. Therefore, ξ is very small (<0.01) at the point when the ϵ' initially changes. From Figure 5.3-13, the value of the swelling diffusion coefficient can be approximated to be on the order of $10^{-10} \text{ cm}^2/\text{sec}$.

For early times (<404 minutes) the material in the sensing region was far below T_g (noted by the presence of ϵ_u and absence of ϵ_r in the ϵ' experiment). As the transient experiment progressed, the ϵ' values continued to drop and an inflection point appeared at approximately 808 minutes. This inflection point progressively moved to the right, which was an indication of macromolecular relaxation and a drop in T_g . At long times (>808 minutes), the ϵ_r was now clearly present indicating the material in the sensing region was near T_g . The ϵ' at high frequencies was well below the expected steady state ϵ' value shown for pure Derakane (Figure 5.3-12). This was an indication that at some time in the future, the high frequency ϵ' values should start increasing to the steady state Derakane™ values. The $\tan \delta$ went through a relative maximum at times greater than approximately 808 minutes indicating a shift to lower T_g and hence a more relaxed material in the sensing region.

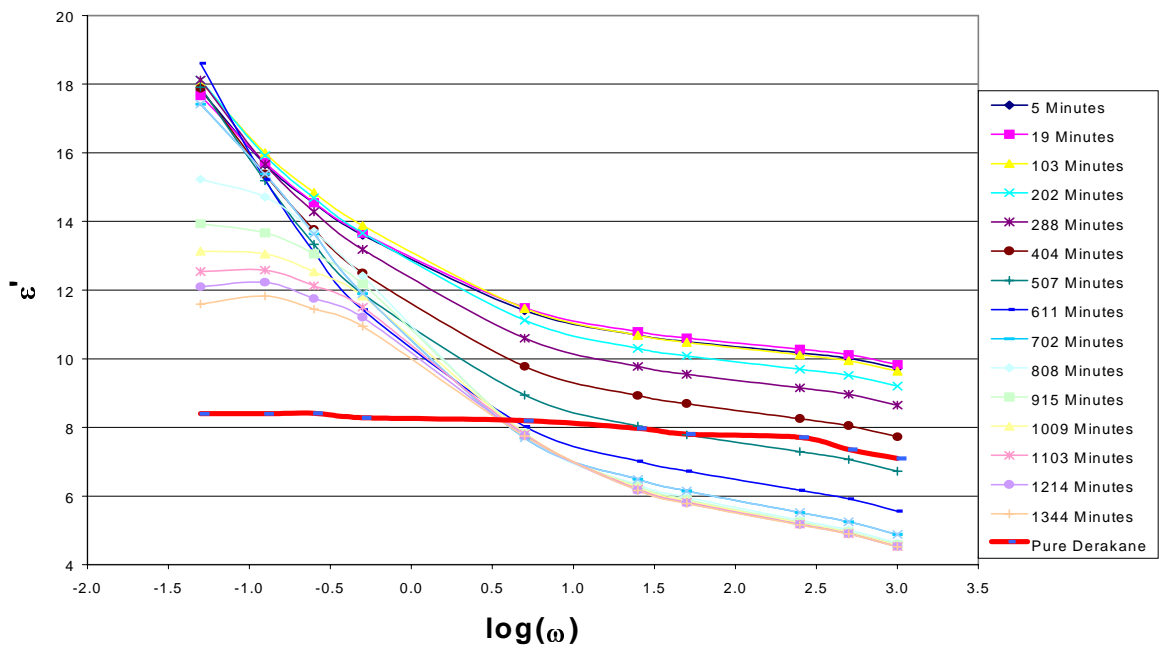


Figure 5.3-9 Derakane™ 441-400 vinyl-ester resin diffusing into 42μm thick K-90 PVP film. ϵ' versus $\log(\omega)$ at various times.

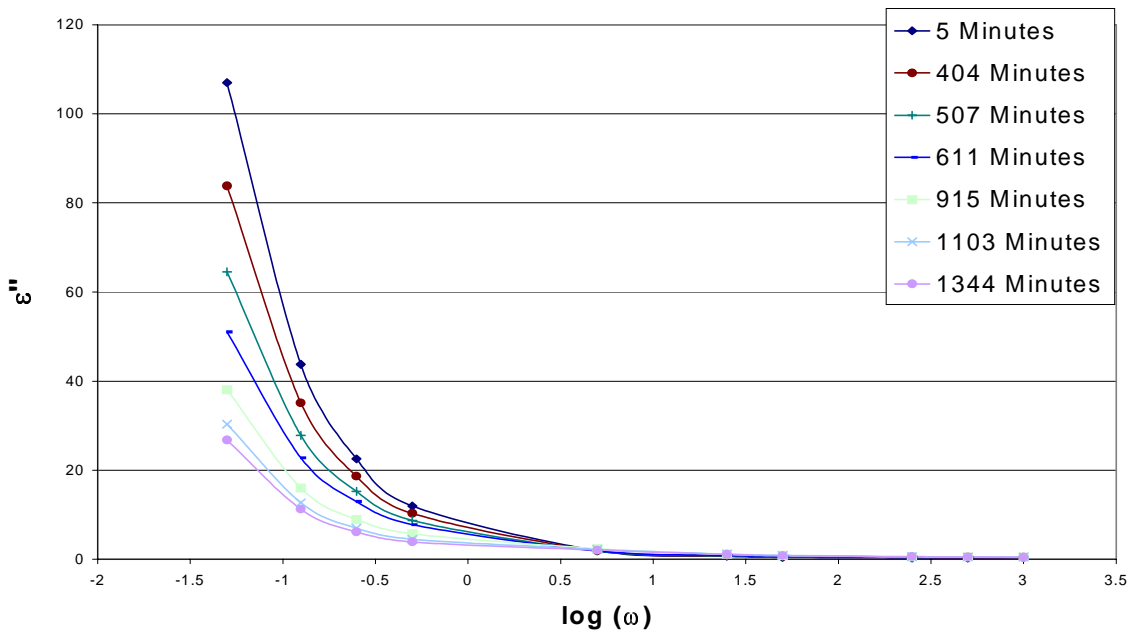


Figure 5.3-10 Derakane™ 441-400 vinyl-ester resin diffusing into 42μm thick K-90 PVP film. ϵ'' versus $\log(\omega)$ at various times.

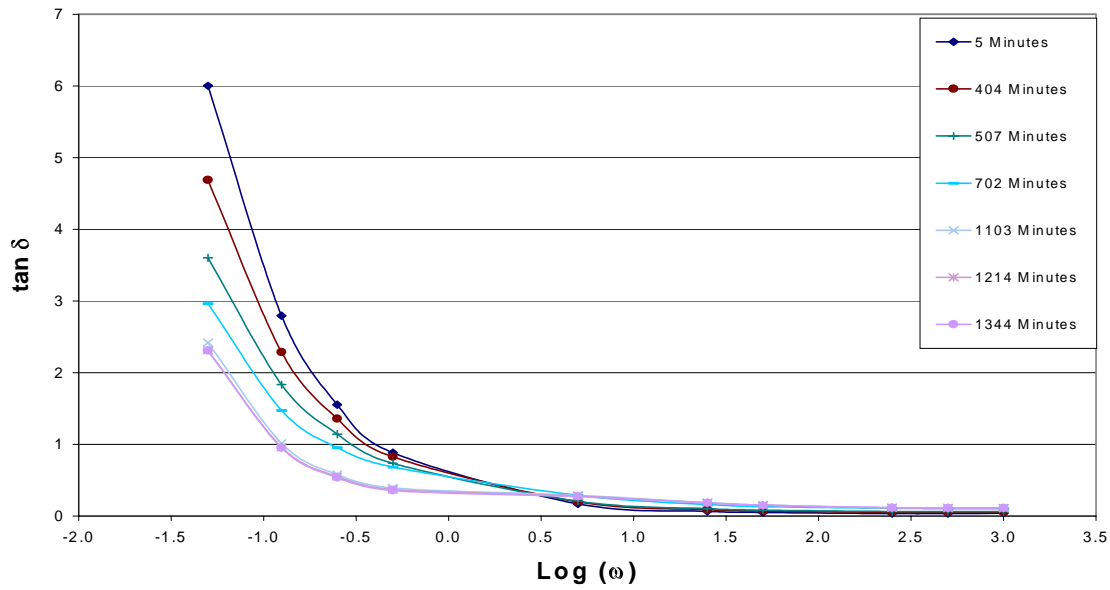


Figure 5.3-11 Derakane™ 441-400 vinyl-ester resin diffusing into 42μm thick K-90 PVP film. $\tan \delta$ versus $\log(\omega)$ at various times.

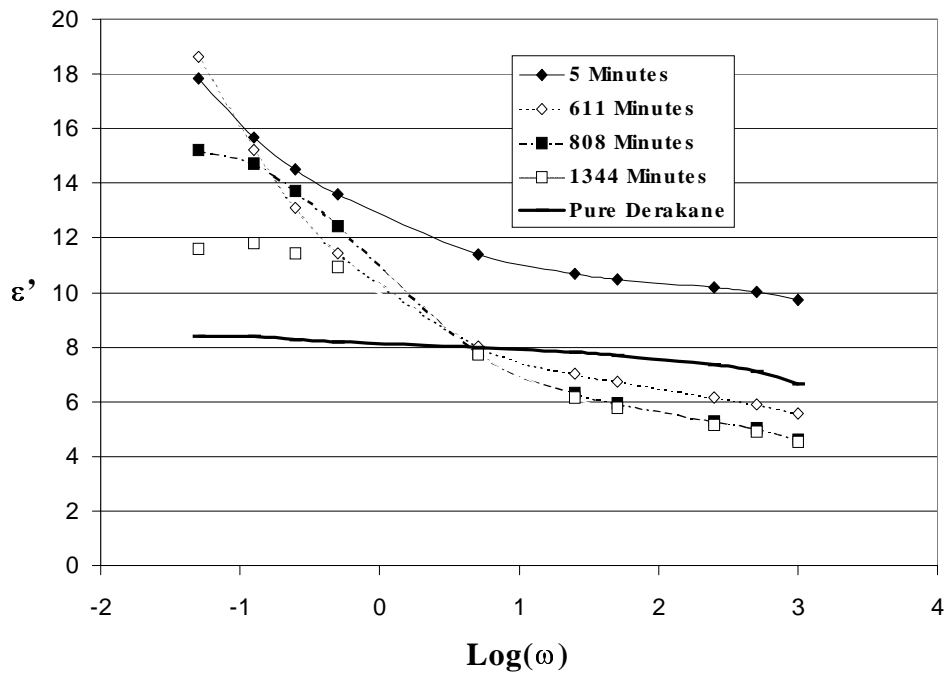


Figure 5.3-12 Derakane™ 441-400 vinyl-ester resin diffusing into 42μm thick K-90 PVP film. In-phase permittivity, ϵ' , versus $\log(\omega)$ at various times. Note: fewer times shown for clarity.

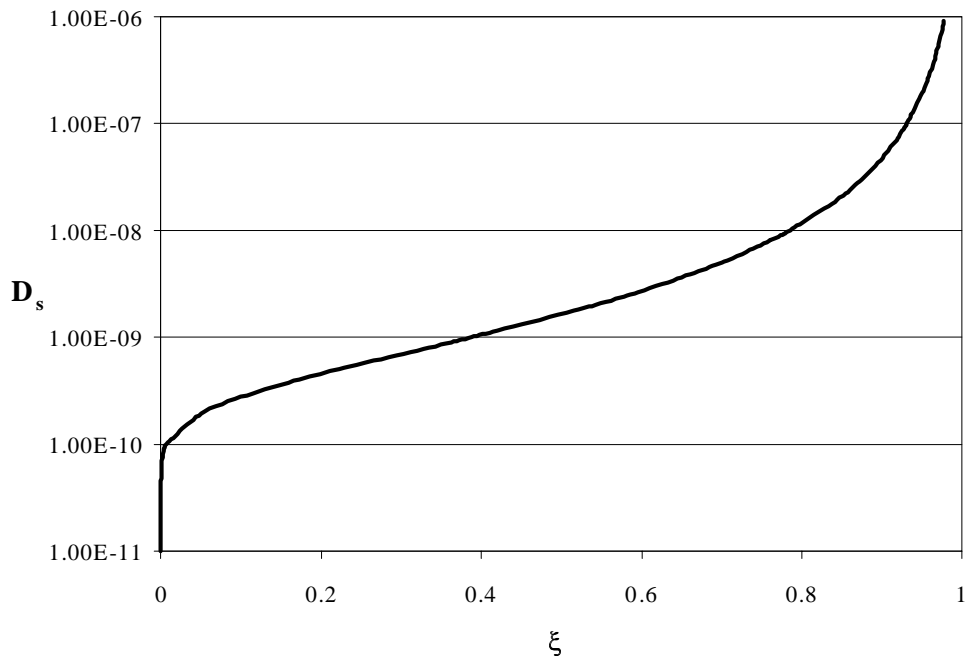


Figure 5.3-13 Theoretical prediction of swelling diffusion coefficient, D_s , versus parameter ξ calculated from equation III.5. Note: value of x was $25\mu\text{m}$ and value of t was 70 minutes.

After 1344 minutes, the ε' at high frequencies reached a relative minimum and the rate of decrease of the ε' at low frequencies had decreased. The system appeared to approach a “psuedo-steady state”. This “psuedo-steady state” is believed to be the completion of the relaxation portion of the interdiffusion process. If the dissolution process were slower than the relaxation process, then the material in the sensing region would have attained a “psuedo steady-state” until such time as the relaxed-material/bulk-material interface encroached upon the sensing region. At that time, the ε' would slowly collapse upon the pure Derakane™ values. However, if the dissolution process were much faster than the relaxation process, then the material in the sensing reach would not reach a “psuedo-steady state” and would only reach the true steady-state when the material in the sensing region was pure Derakane™. The former case was observed in this set of experiments. It was therefore concluded that for the case of K-90 PVP diffusing into Derakane™, the interdiffusion process was dissolution controlled, which was the assumption utilized in the previous chapter. Unfortunately, no quantitative value for the dissolution diffusion coefficient could be obtained from the data collected in this set of experiments. If the experiment had been allowed to progress for a much longer period of time,

then the dissolution diffusion coefficient could have been approximated from the time required to reach steady state. As will be discussed later in section 5.4.1, the dissolution diffusion coefficient can be approximated from the Stokes-Einstein equation.

5.3.1.6.2 Transient K-90 PVP Diffusing into Styrene

Dried K-90 PVP was coated onto a flat dielectric sensor via methanol. This sensor was then coated with an infinite bath of styrene monomer. Dielectric properties were measured as a function of the same frequencies utilized previously for a time period equal to approximately 360 minutes (Figure 5.3-14 and Figure 5.3-15). The ϵ' vs. $\log(\omega)$ data seemed to indicate that the K-90 PVP material may be swelled very slowly by the styrene but no relaxation was occurring since the shape of the curve remains the same. The data also indicated that the material in the sensing region was well below T_g (noted by the presence of ϵ_u and absence of ϵ_r). This data indicated that the K-90 PVP was not readily soluble in the styrene monomer but may be swellable by it. The time required for the dielectric properties to change was again approximately 70 minutes. This was an indication that the styrene component of the Derakane™ matrix was responsible for the swelling behavior observed in the previous experiment because the predicted D_s were the same. However, because the styrene was shown to be unable to relax and dissolve the K-90 PVP in this experiment, it can be concluded that the vinyl-ester portion of the Derakane™ matrix was responsible for the relaxation and dissolution observed in the previous experiment. The vinyl-ester portion was transported with the styrene during the swelling portion of the interdiffusion process.

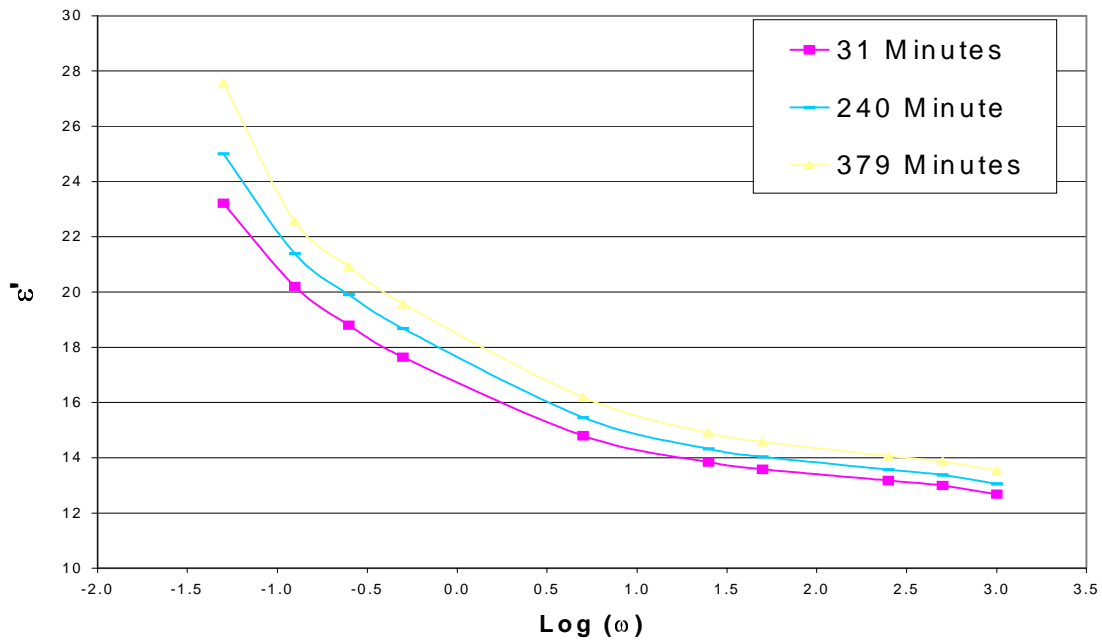


Figure 5.3-14 Monomeric styrene diffusing into 42 μ m thick K-90 PVP film. ϵ' versus $\log(\omega)$.

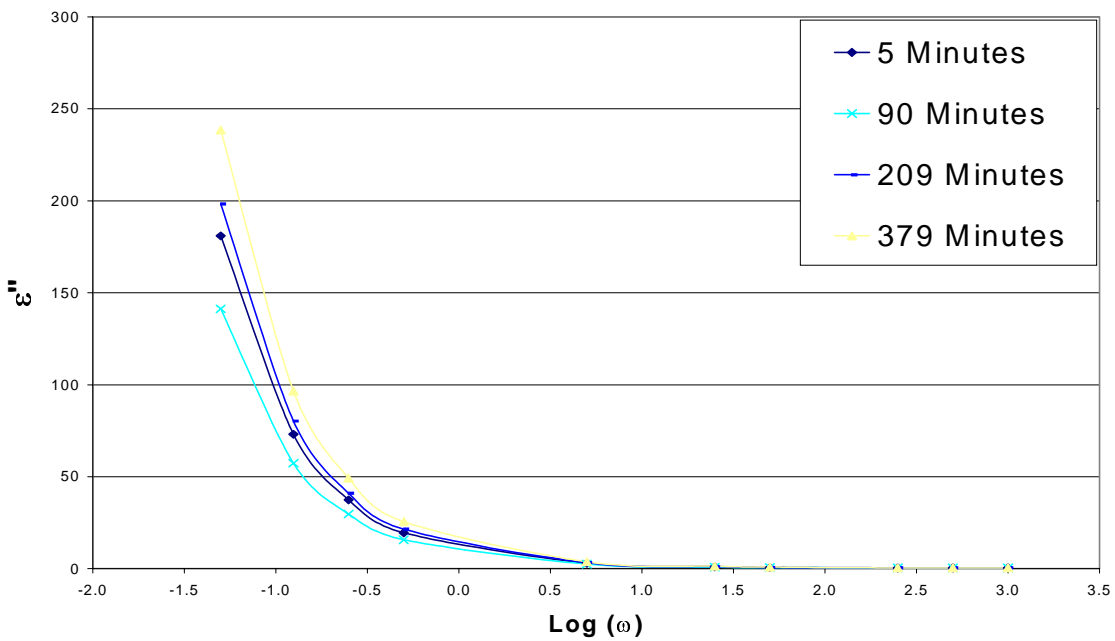


Figure 5.3-15 Monomeric styrene diffusing into 42 μ m thick K-90 PVP film. ϵ'' versus $\log(\omega)$.

5.3.2 Mechanical Properties Results and Discussion

This section details the experimental results associated with the mechanical properties of sizing/matrix blends. The sizing/matrix blend properties that were determined included static tensile strength, strain-to-failure, and modulus, un-cured and cured blend density, shrinkage upon cure, and the cured blend glass transition temperature. The data generated from these properties were to serve as an input into the model developed in Chapter 4 such that an accurate prediction of interphase mechanical property profile could be obtained.

5.3.2.1 Density determination of the un-cured blends

The density of the un-cured K-90 PVP/Derakane™ were determined as a function of K-90 PVP concentration in the Derakane™ (Figure 5.3-16.a). The density followed a linear behavior versus concentration over the range studied, 0-5wt%. If the K-90 PVP/Derakane™ system were to have behaved ideally over the entire concentration range, then the theoretical pure K-90 PVP density should have been approximately 2.67 g/ml. The pure K-90 PVP density is approximately 1.20 g/ml which is an indication of a positive deviation from ideal mixing due to strong hydrogen bonding interactions. Li and co-workers [1.9] showed similar trends with K-90 PVP and Derakane™. They attributed this non-ideality to the hydrogen bonding between the K-90 PVP and the vinyl-ester portion of the Derakane™.

5.3.2.2 Density determination of the cured blends

The density of the cured K-90 PVP/Derakane™ were determined as a function of K-90 PVP concentration in the Derakane™ (Figure 5.3-16.b). The cured blend density was found to be constant and not a function of K-90 PVP in Derakane™ concentration. This result was surprising considering the fact that the un-cured blend density showed a strong dependence on K-90 PVP concentration. Assuming the same degree of matrix cure, this would imply a decrease in matrix shrinkage as a function of increasing K-90 PVP in Derakane™ composition as will be discussed in the next section.

5.3.2.3 Shrinkage of Blends upon Cure

The shrinkage of the blends upon cure was computed from equation (5-11) (Figure 5.3-17). The results showed that the shrinkage decreased with increasing K-90 PVP in

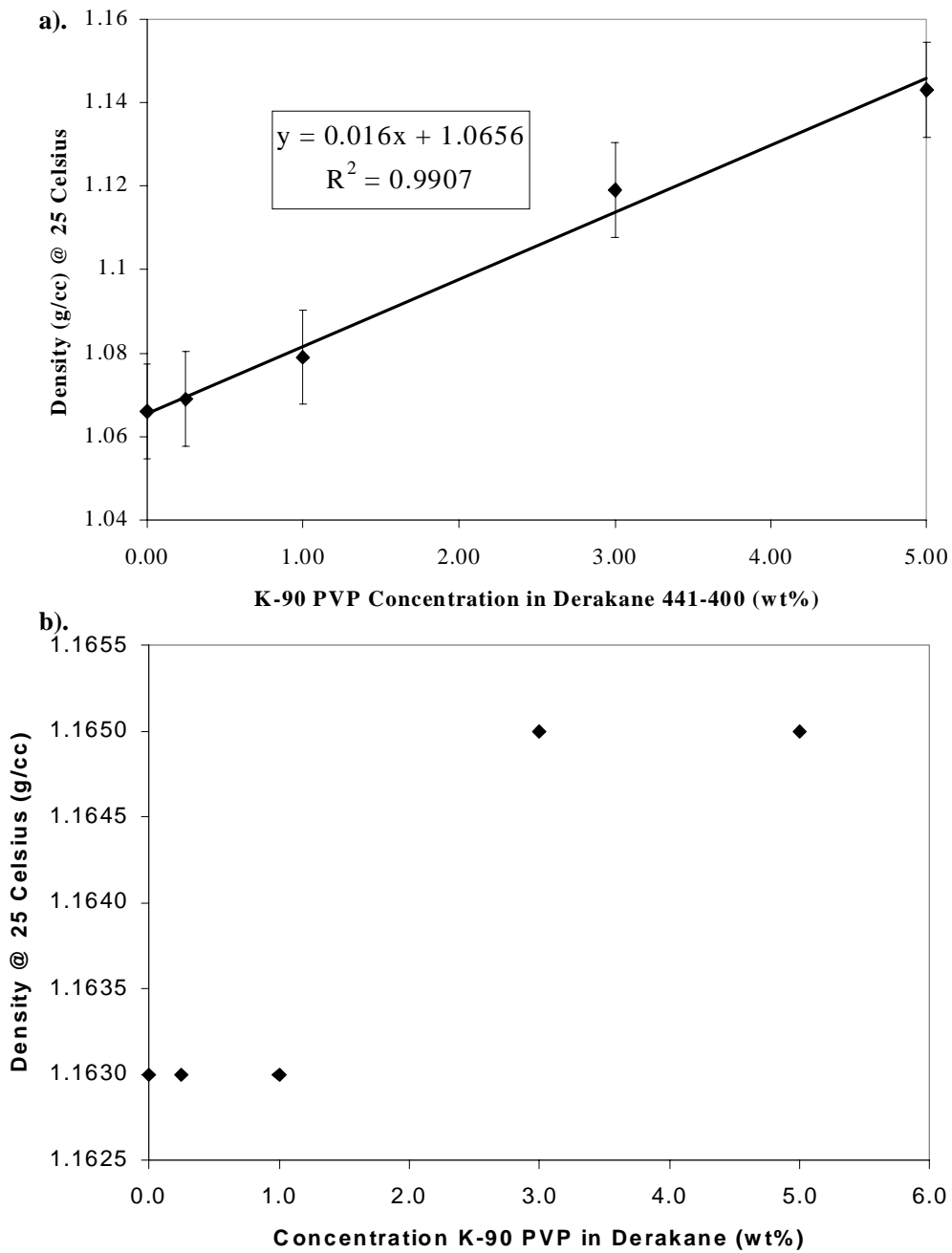


Figure 5.3-16 Density at 25°C for K-90 PVP in Derakane™ blends. a). un-cured b). cured.

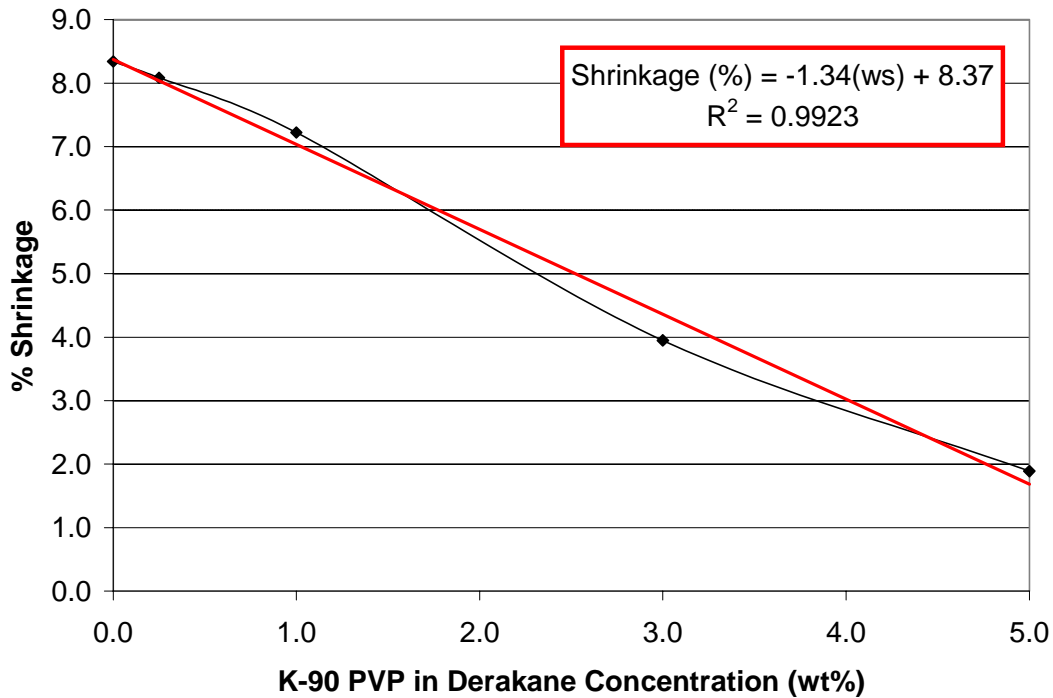


Figure 5.3-17 Percentage blend shrinkage as a function of K-90 PVP in Derakane™.

Derakane™ concentration. The shrinkage showed a 4-fold decrease from the pure Derakane™ value of 8.3% to 1.9% for the 5.0wt% K-90 PVP. As was discussed in Chapter 4, this has positive implications for the interphase region where shrinkage induced fiber/matrix interface cracking is known to be a problem with the Derakane™ system.

The matrix shrinkage as a function of K-90 PVP concentration was quantified by fitting the experimental values to a straight line. For the 0.0 to 5.0wt% K-90 PVP in Derakane™ concentration range, the shrinkage data closely followed a straight line as was evident by the R^2 value of 0.9923. The shrinkage function was as follows:

$$shrinkage(\%) = -134.0\omega_{K-90} + 8.37 \quad (5-12)$$

For K-90 PVP in Derakane™ concentrations greater than 5.0wt%, the shrinkage was assumed to be equal to the shrinkage at the 5.0wt% level (value obtained from experimental data point and not equation (5-12)) and constant at that value:

$$shrinkage(\%) = 1.88 \quad (5-13)$$

where ω_{K-90} is the K-90 PVP in Derakane™ weight fraction. Equations (5-12) and (5-13) were utilized in Chapter 4 to obtain the shrinkage profile existing in the K-90 PVP sized composite interphase.

5.3.2.4 Glass transition temperature determination of the cured blends (Completed by Dr. Chris Robertson)

The glass transition temperature of the cured blends was determined by DSC (Figure 5.3-18 and Figure 5.3-19). There was a single T_g for all the K-90 PVP/Derakane™ blend compositions tested, which was an indication of miscibility. The Fox equation can be used to predict the blend glass transition as a function of the pure component glass transitions and is accurate for miscible systems without strong secondary bonding or interactions [5.3]:

$$\frac{1}{T_g^{blend}} = \frac{\omega_1}{T_{g,1}} + \frac{(1-\omega_1)}{T_{g,2}} \quad (5-14)$$

where T_g^{blend} is the blend glass transition, ω_1 is the weight fraction of component one in the blend, $T_{g,1}$ is the pure glass transition of component one, and $T_{g,2}$ is the pure glass transition of component two. The first and second heat glass transition temperatures were compared to those predicted by the Fox equation (Figure 5.3-18 and Figure 5.3-19). The data showed a deviation from the Fox equation that was indicative of the hydrogen bonding present in this system. Between the first and second DSC heats, there was a consistent difference of approximately 9°C in the blend glass transition temperatures for all blend compositions. This was an indication that all the K-90 PVP in Derakane™ blends had the same degree of cure and that none of the variations in matrix shrinkage discussed previously were due to differences in matrix cure between the blend compositions.

5.3.2.5 Rheological Experiments on K-90 and K-30 PVP Blends

5.3.2.5.1 K-90 PVP in Derakane™ Blends

The zero shear viscosities of the K-90 PVP/Derakane™ blends discussed earlier were determined. The five blends were analyzed at different shear rate ranges due to the concentration dependence of the viscosity. The pure Derakane™ was analyzed at the following shear rates: 0.117, 1.1170, and 11.700 1/s (Figure 5.3-20). The viscosity did not show any statistically

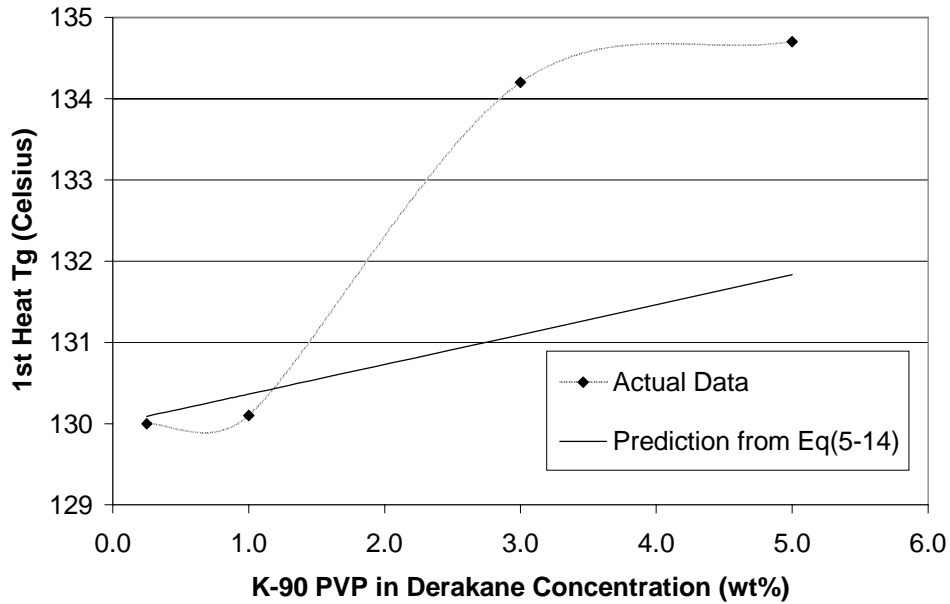


Figure 5.3-18 Glass transition temperature of cured K-90 PVP in Derakane™ 441-400 blends as measured by DSC (10°C/min). 1st heat.

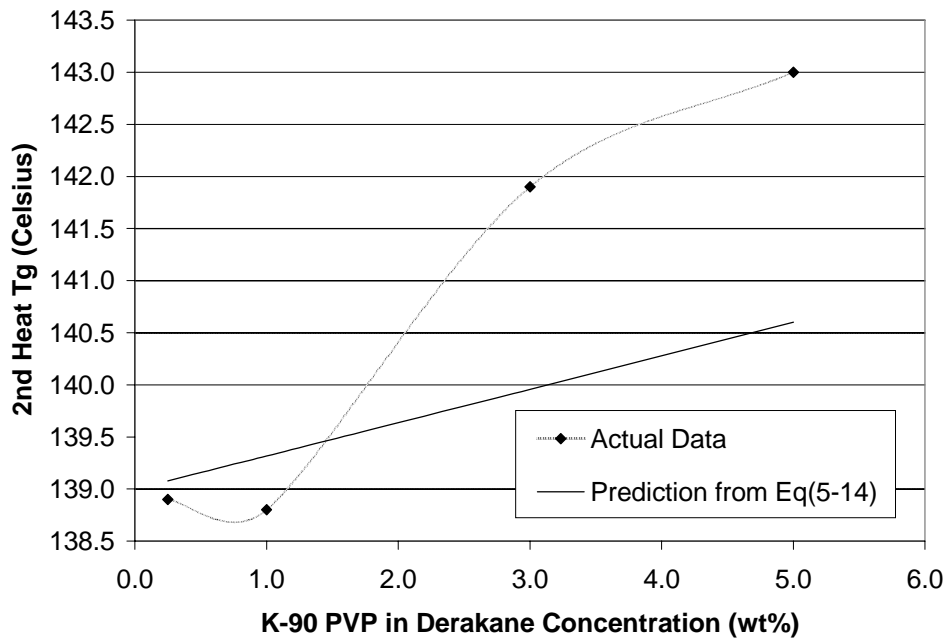


Figure 5.3-19 Glass transition temperature of cured K-90 PVP in Derakane™ 441-400 blends as measured by DSC (10°C/min). 2nd heat (isothermal hold at 250°C for 10 minutes).

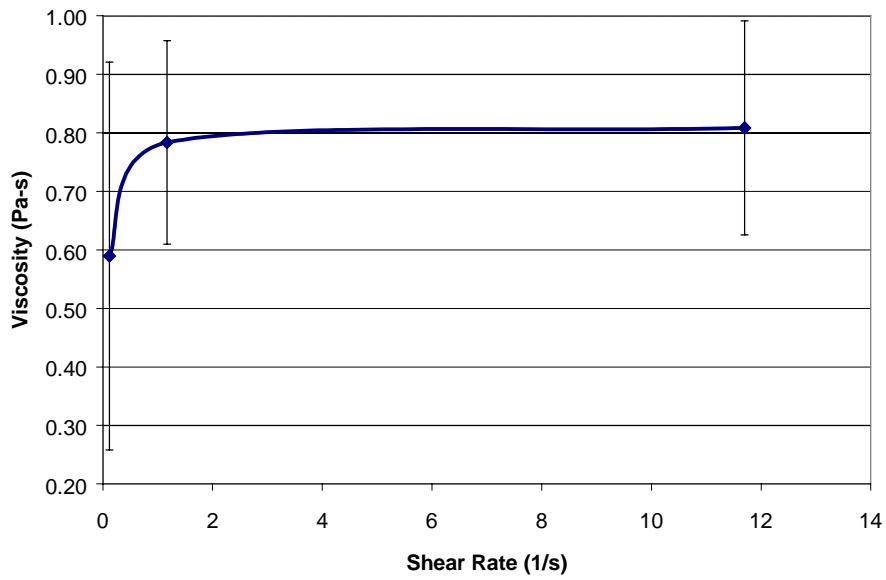


Figure 5.3-20 Shear viscosity as a function of shear rate for the pure Derakane™ vinyl-ester matrix material. Temperature = 25°C.

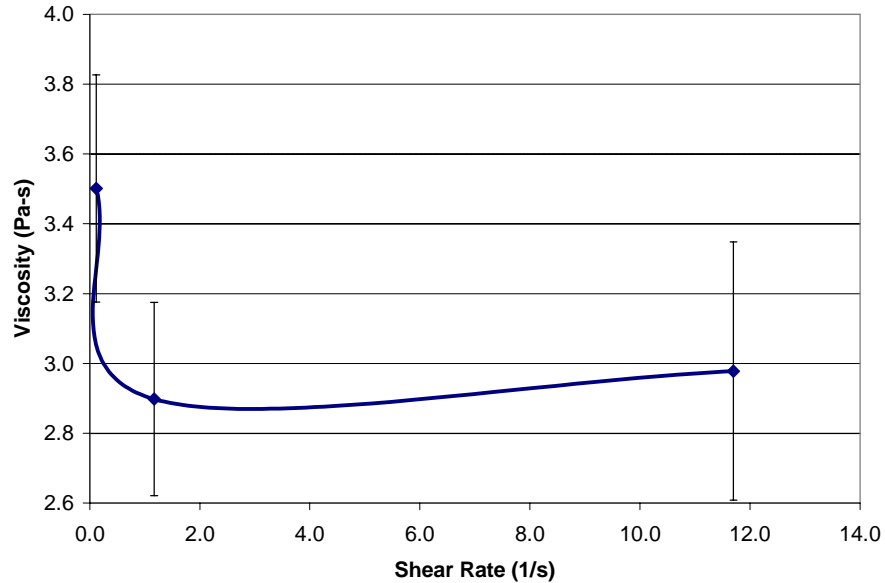


Figure 5.3-21 Shear viscosity as a function of shear rate for the 0.25wt% K-90 PVP in Derakane™ vinyl-ester matrix material. Temperature = 25°C.

significant shear rate dependence over the range tested. The oscillatory response of this material confirmed its Newtonian behavior. The phase angle was 90° . The zero shear viscosity was estimated by averaging the shear viscosity at the three shear rates tested ($\eta_o \approx 0.73 \pm 0.12$ Pa·s).

The 0.25 wt% K-90 PVP in Derakane™ was analyzed at the following shear rates: 0.117, 1.1170, and 11.700 1/s (Figure 5.3-21). As was the case for the pure Derakane™ material, the viscosity did not show a statistically significant shear rate dependence. However, the oscillatory response did indicate the initiation of some non-Newtonian behavior. The phase angle was approximately 87° . The zero shear viscosity was estimated by averaging the shear viscosity at the three shear rates tested ($\eta_o \approx 3.13 \pm 0.33$ Pa·s).

The 1.00 wt% K-90 PVP in Derakane™ was analyzed at the following shear rates: 0.117, 1.1170, and 11.700 1/s (Figure 5.3-22). This blend viscosity did show a slight shear rate dependence. However, the shear viscosity at 0.117 1/s was only 18% higher than the shear viscosity at 11.7 1/s. The oscillatory response indicated a further progression into non-Newtonian behavior with a phase angle of approximately 82° . The zero shear viscosity was estimated by averaging the shear viscosity at the three shear rates tested ($\eta_o \approx 6.22 \pm 0.52$ Pa·s).

The 3.00 wt% K-90 PVP in Derakane™ was analyzed at the following shear rates: 0.0117, 0.1117, and 1.17000 1/s (Figure 5.3-23). This blend viscosity did not show a statistically significant shear rate dependence despite the higher concentration of K-90 PVP. The oscillatory response was more consistent with the increased K-90 PVP concentration indicating a further progression into non-Newtonian behavior. The phase angle was determined to be $72 \pm 12^\circ$. The zero shear viscosity was estimated by averaging the shear viscosity at the three shear rates tested ($\eta_o \approx 48.3 \pm 3.6$ Pa·s).

The 5.00 wt% K-90 PVP in Derakane™ was analyzed at the following shear rates: 0.0117, 0.1117, and 1.17000 1/s (Figure 5.3-24). This blend viscosity did show a distinct shear-thinning region but a Newtonian plateau region was not observed. The oscillatory response was highly non-Newtonian with a phase angle of $60 \pm 7^\circ$. The zero shear viscosity determination was complicated by the fact that the viscosity was highly shear-dependent and Newtonian plateau was not present. The zero shear viscosity was estimated to be the viscosity at the lowest measured shear rate ($\eta_o \approx 900 \pm 300$ Pa·s).

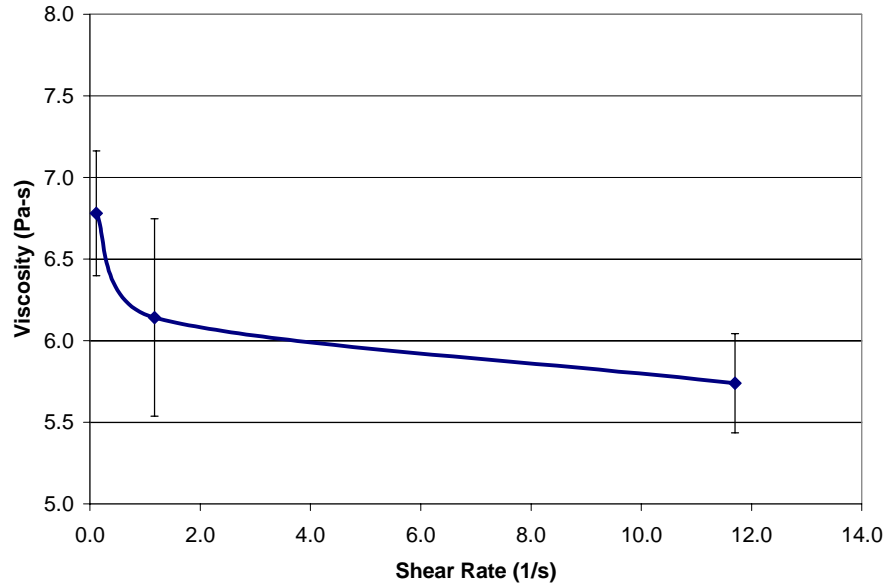


Figure 5.3-22 Shear viscosity as a function of shear rate for the 1.00wt% K-90 PVP in Derakane™ vinyl-ester matrix material. Temperature = 25°C.

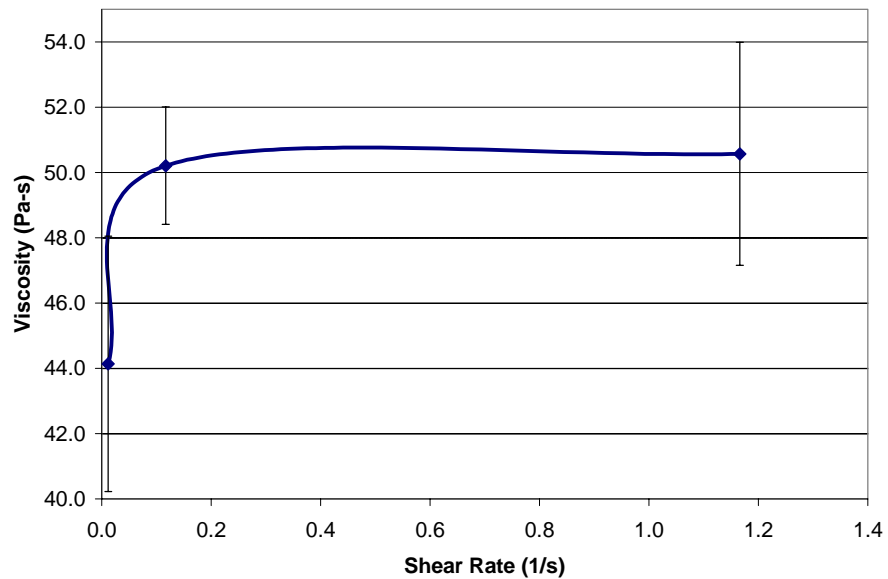


Figure 5.3-23 Shear viscosity as a function of shear rate for the 3.00wt% K-90 PVP in Derakane™ vinyl-ester matrix material. Temperature = 25°C.

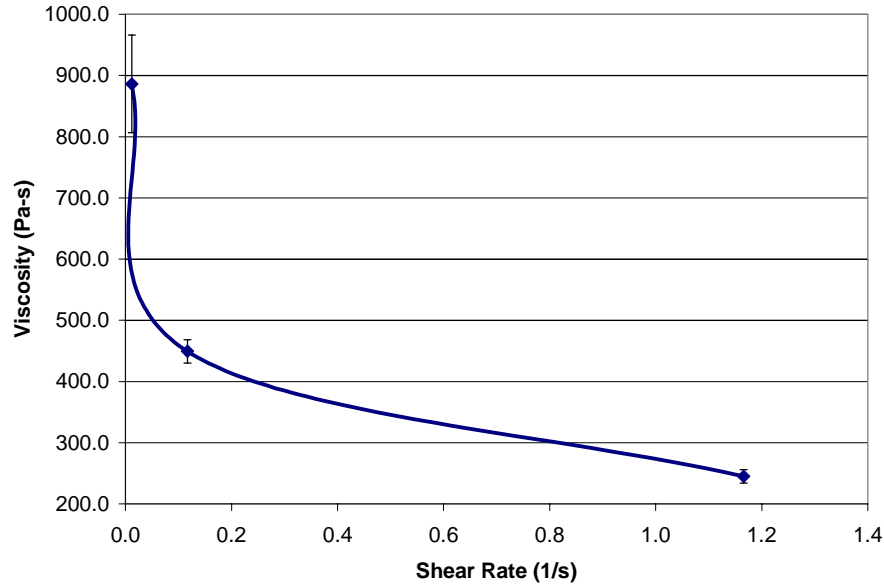


Figure 5.3-24 Shear viscosity as a function of shear rate for the 5.00wt% K-90 PVP in Derakane™ vinyl-ester matrix material. Temperature = 25°C.

The zero shear viscosity as a function of K-90 PVP in Derakane™ was estimated to have the following functional dependence (Figure 5.3-25):

$$\eta_o = 1.33 \exp(128.4\omega_{K-90}) \quad (5-15)$$

where η_o is in Pa·s. Equation (5-15) will be utilized in Section 5.4.1.1 estimate the dissolution diffusion coefficient for the K-90 PVP/Derakane™ system.

5.3.2.5.2 K-30 PVP in Derakane™ Blends

The zero shear viscosities of the K-30 PVP/Derakane™ blends discussed earlier were determined. The five blends were analyzed at different shear rate ranges due to the concentration dependence of the viscosity. The pure Derakane™ was analyzed at the following shear rates: 1.17 and 11.70 1/s (Figure 5.3-26). The viscosity did not show any statistically significant shear rate dependence over the range tested. The oscillatory response of this material confirmed its Newtonian behavior. The phase angle was $88 \pm 1^\circ$. The zero shear viscosity was estimated by averaging the shear viscosity at the two shear rates tested ($\eta_o \approx 0.38 \pm 0.03$ Pa·s).

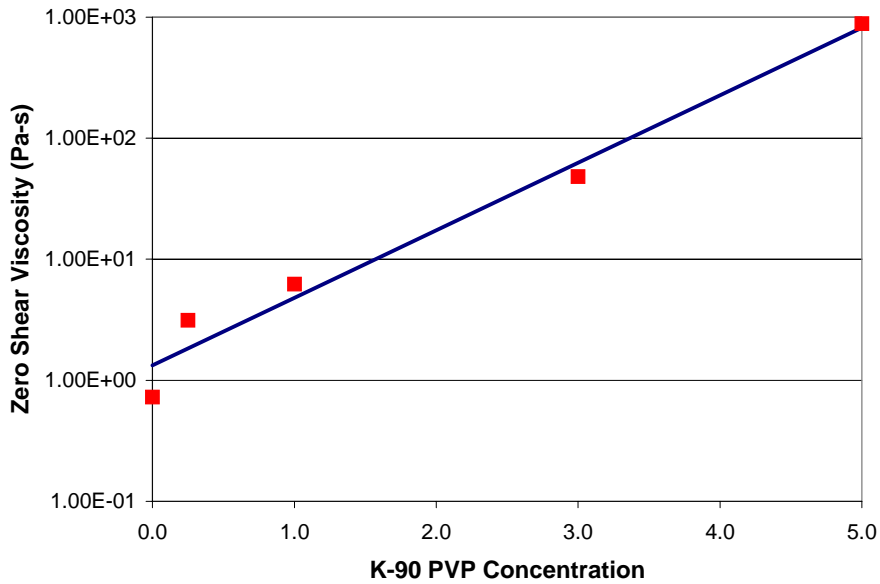


Figure 5.3-25 Zero shear viscosity as a function of K-90 PVP in Derakane™ concentration. $\eta_0 = 1.33 \exp(128.4 \omega_{K-90})$ shown in blue. Actual data shown in red.

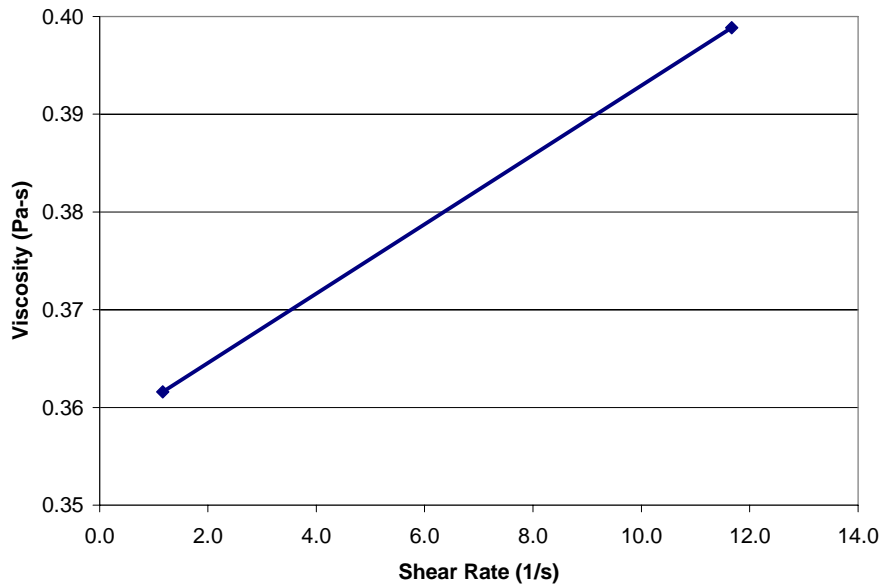


Figure 5.3-26 Shear viscosity as a function of shear rate for the pure Derakane™ vinyl-ester matrix material. Temperature = 25°C.

The 1.10 wt% K-30 PVP in Derakane™ was analyzed at the following shear rates: 1.17 and 11.7 1/s (Figure 5.3-27). This blend exhibited Newtonian behavior. The oscillatory response also indicated Newtonian behavior with a phase angle of $89 \pm 1^\circ$. The zero shear viscosity was estimated by averaging the shear viscosity at the two shear rates tested ($\eta_o \approx 0.53 \pm 0.05$ Pa·s).

The 4.30 wt% K-30 PVP in Derakane™ was analyzed at the following shear rates: 0.117 and 1.17 1/s (Figure 5.3-28). This blend exhibited Newtonian behavior. The oscillatory response also indicated Newtonian behavior with a phase angle of $89.3 \pm 0.1^\circ$. The zero shear viscosity was estimated by averaging the shear viscosity at the two shear rates tested ($\eta_o \approx 2.15 \pm 0.34$ Pa·s).

The 8.60 wt% K-30 PVP in Derakane™ was analyzed at the following shear rates: 0.117, 1.17, and 3.69 1/s (Figure 5.3-29). The viscosity was not statistically a function of shear rate. The oscillatory response also indicated Newtonian behavior with a phase angle of $88.6 \pm 0.1^\circ$. The zero shear viscosity was estimated by averaging the shear viscosity at the two shear rates tested ($\eta_o \approx 12.9 \pm 1.5$ Pa·s).

The 17.50 wt% K-30 PVP in Derakane™ was analyzed at the following shear rates: 0.117 and 1.17 (Figure 5.3-30). Again, the viscosity was not statistically a function of shear rate. However, the oscillatory response indicated a shift toward non-Newtonian behavior with a phase angle of $81.0 \pm 0.1^\circ$. The zero shear viscosity was estimated by averaging the shear viscosity at the two shear rates tested ($\eta_o \approx 239.6 \pm 4.6$ Pa·s).

The zero shear viscosity as a function of K-30 PVP in Derakane™ was estimated to have the following functional dependence (Figure 5.3-31):

$$\eta_o = 0.404 \exp(37.27 \omega_{K-30}) \quad (5-16)$$

where η_o is in Pa·s. Equation (5-16) will be utilized in Section 5.4.1.2 to estimate the dissolution diffusion coefficient for the K-30 PVP/Derakane™ system.

5.3.2.6 Static tensile property determination of cured blends

The static tensile properties of the cured K-90 PVP in Derakane™ blends were determined (Figure 5.3-32 through Figure 5.3-35). The static tensile strength was a strong function of the amount of K-90 PVP present in the blend (Figure 5.3-32). The initial increase in

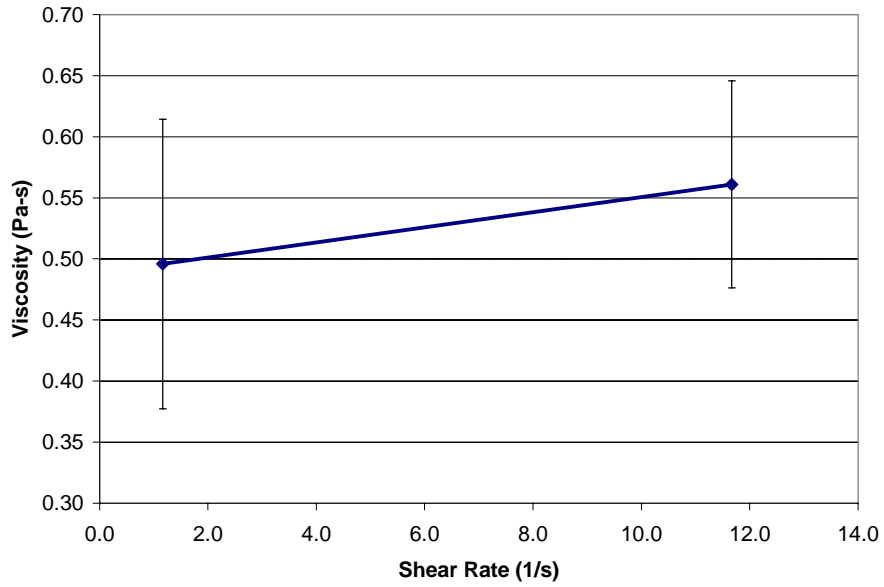


Figure 5.3-27 Shear viscosity as a function of shear rate for the 1.10wt% K-30 PVP in Derakane™ vinyl-ester matrix material. Temperature = 25°C.

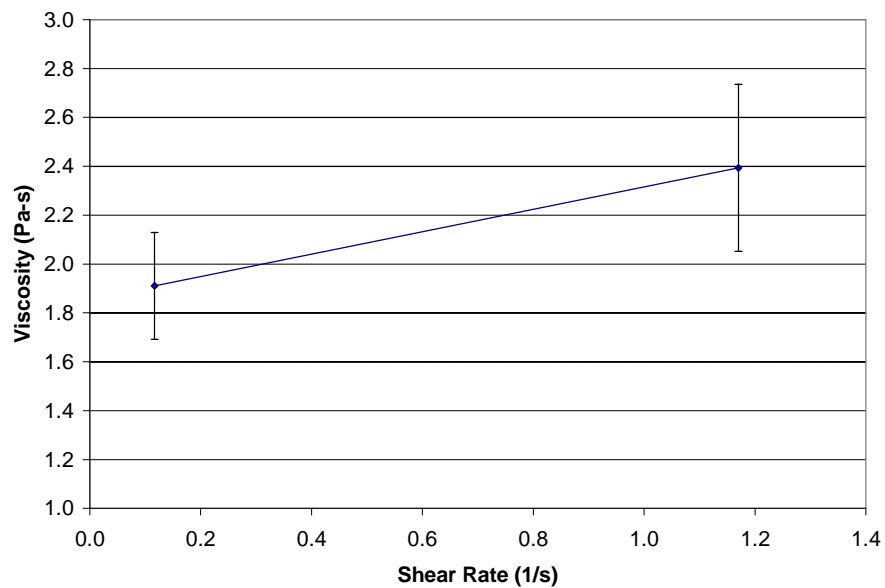


Figure 5.3-28 Shear viscosity as a function of shear rate for the 4.30wt% K-30 PVP in Derakane™ vinyl-ester matrix material. Temperature = 25°C.

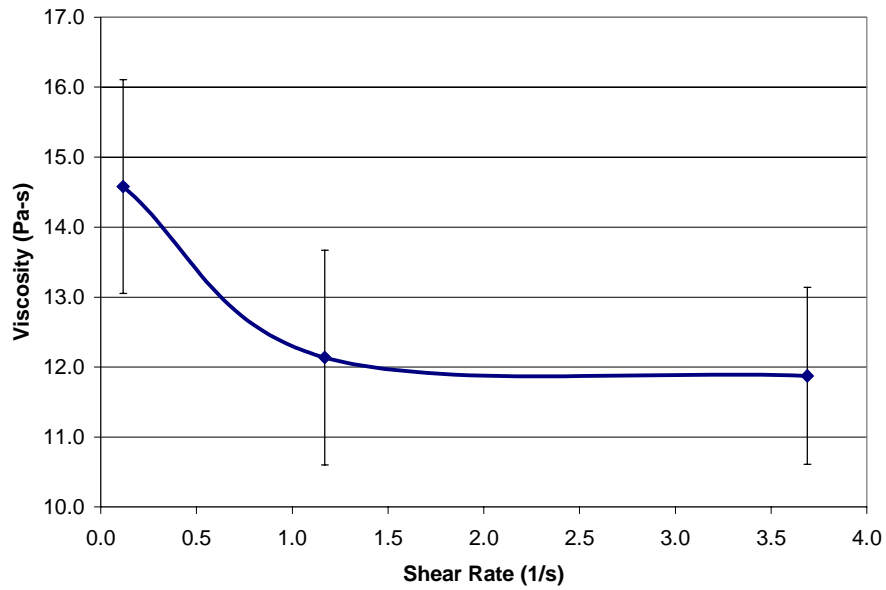


Figure 5.3-29 Shear viscosity as a function of shear rate for the 8.60wt% K-30 PVP in Derakane™ vinyl-ester matrix material. Temperature = 25°C.

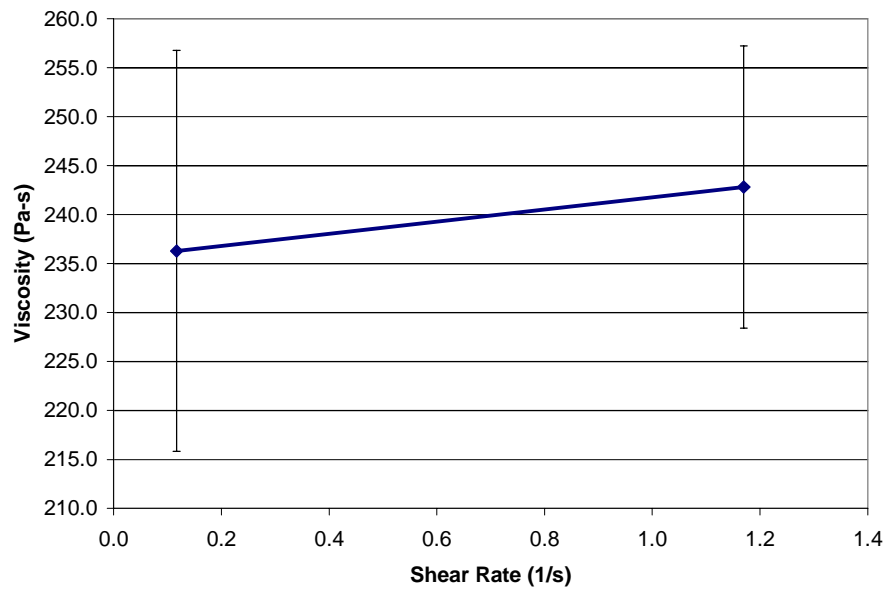


Figure 5.3-30 Shear viscosity as a function of shear rate for the 17.5wt% K-30 PVP in Derakane™ vinyl-ester matrix material. Temperature = 25°C.

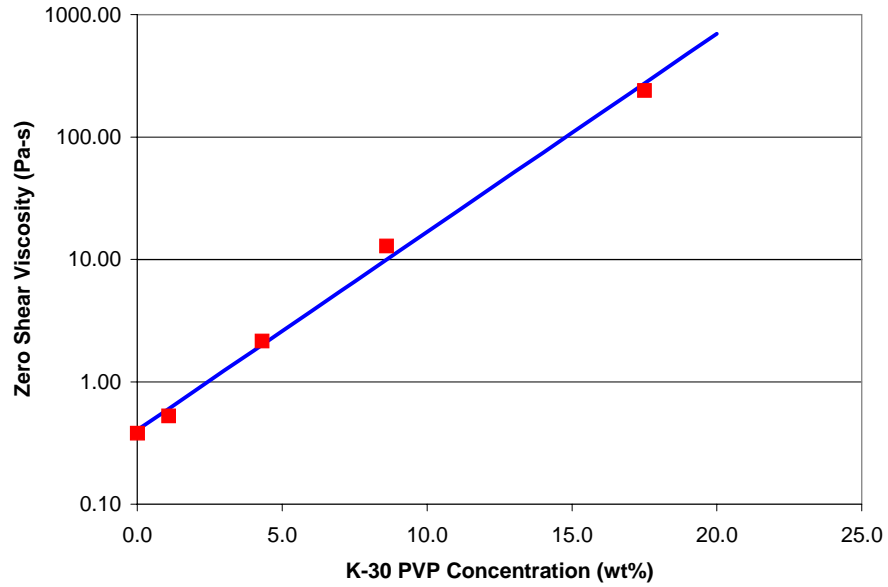


Figure 5.3-31 Zero shear viscosity as a function of K-90 PVP in Derakane™ concentration. $\eta_0 = 0.404 \exp(37.27 \omega_{K-30})$ shown in blue. Actual data shown in red.

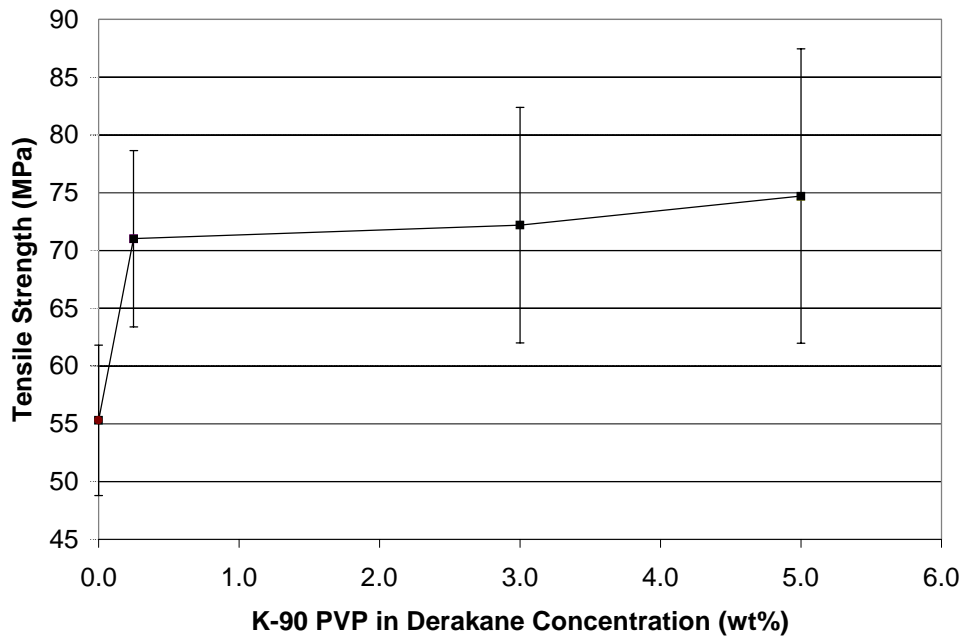


Figure 5.3-32 Static tensile strength of K-90 PVP in Derakane™ blends.

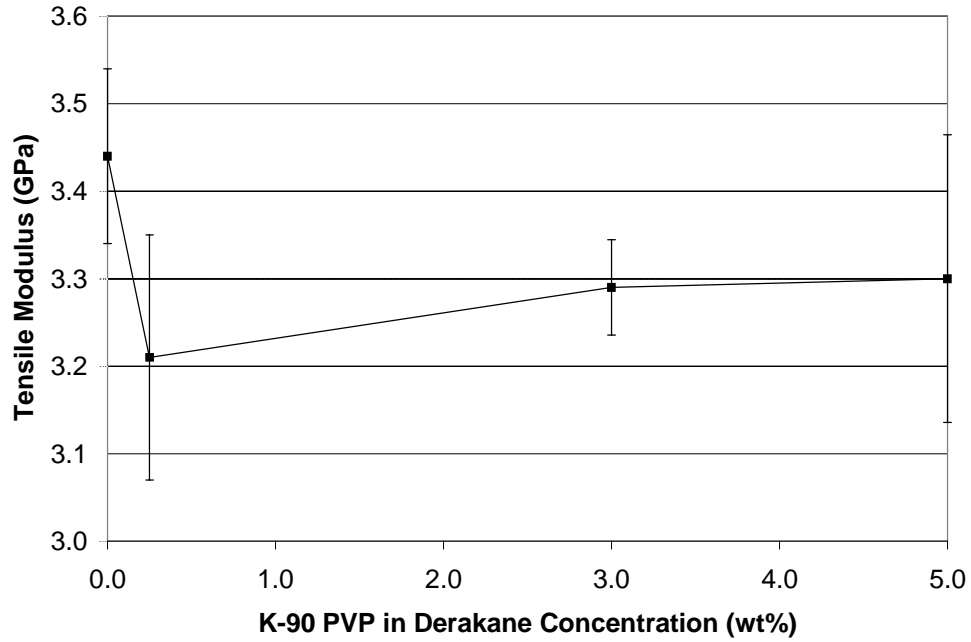


Figure 5.3-33 Static tensile modulus of K-90 PVP in Derakane™ blends.

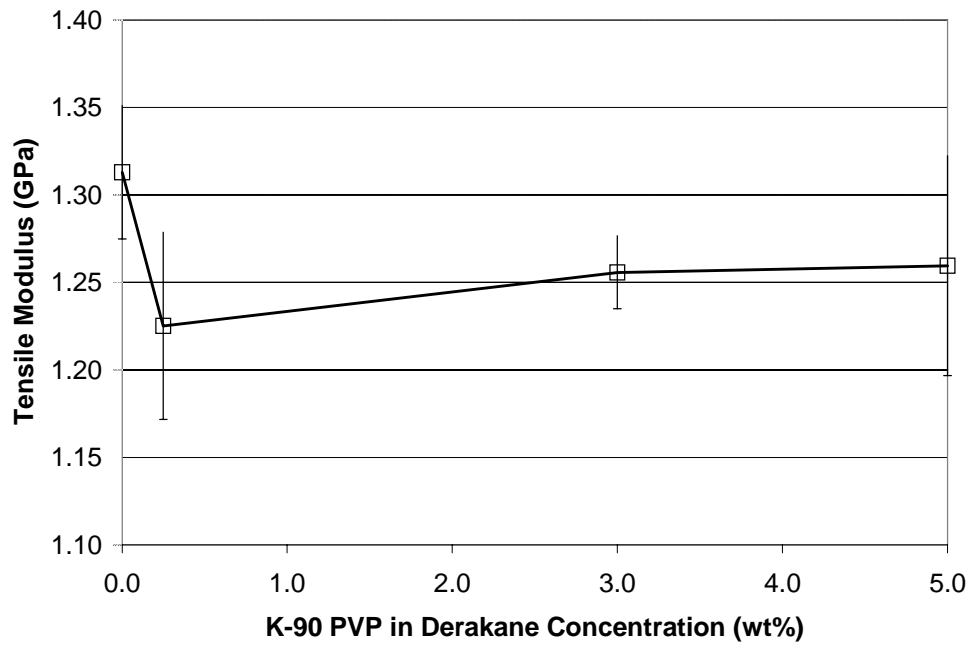


Figure 5.3-34 Static tensile shear modulus of K-90 PVP in Derakane™ blends.

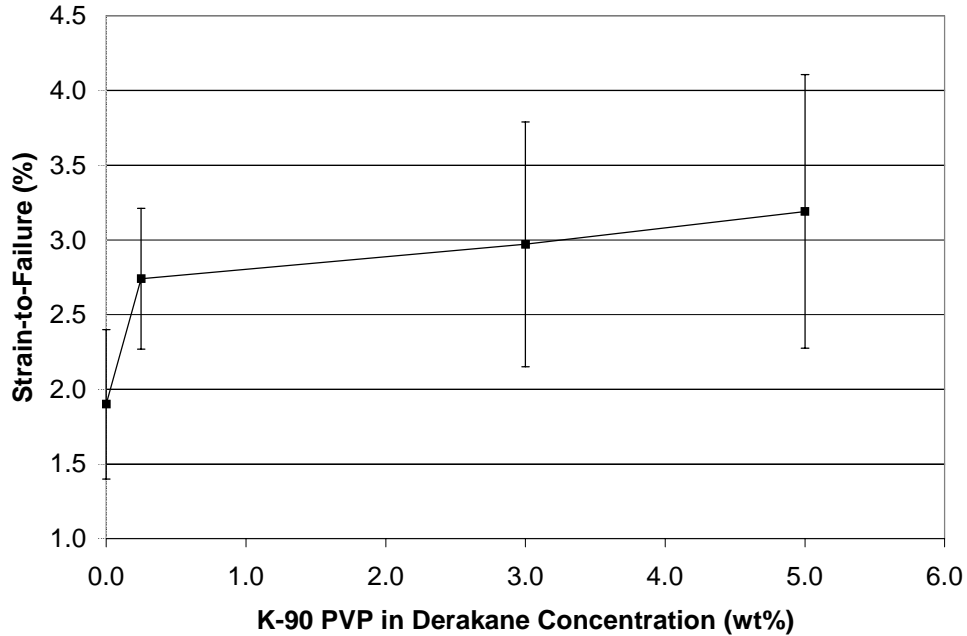


Figure 5.3-35 Static tensile strain-to-failure of K-90 PVP in Derakane™ blends.

strength was the greatest at nearly 30% (55 MPa for pure Derakane™ compared to 71 MPa for 0.25wt% K-90 PVP). The increase in strength at higher K-90 PVP amounts was less dramatic increasing only 5% over the 0.25 to 5.00 wt% K-90 PVP concentrations.

The K-90 PVP concentration dependence of the tensile strength was quantified by fitting the data into two linear regions. For K-90 PVP in Derakane™ concentrations below 0.25 wt%, the two experimental data points (0.00, 55.3 MPa) and (0.0025, 71.02 MPa) were utilized to generate the following line:

$$\sigma_{K-90} = 6288.0\omega_{K-90} + 55.3 \quad (5-17)$$

For K-90 PVP in Derakane™ concentrations above 5.00 wt%, the two experimental data points (0.0025, 71.02 MPa) and (0.050, 74.71 MPa) were utilized to generate the following line:

$$\sigma_{K-90} = 77.7\omega_{K-90} + 70.8 \quad (5-18)$$

The tensile modulus was found to be essentially constant over the range of K-90 PVP amounts tested (maximum variation was 7%: 3.44 GPa for the pure Derakane™ and 3.21 GPa for the 0.25 wt% K-90 PVP)(Figure 5.3-33).

Again, the K-90 PVP concentration dependence of the tensile modulus was quantified by fitting the data into two linear regions. For K-90 PVP in Derakane™ concentrations below 0.25 wt%, the two experimental data points (0.00, 3.44 GPa) and (0.0025, 3.21 GPa) were utilized to generate the following line:

$$E_{K-90} = -92.0\omega_{K-90} + 3.44 \quad (5-19)$$

For K-90 PVP in Derakane™ concentrations above 5.00 wt%, the two experimental data points (0.0025, 3.21 GPa) and (0.050, 3.30 GPa) were utilized to generate the following line:

$$E_{K-90} = 1.89\omega_{K-90} + 3.21 \quad (5-20)$$

The matrix shear modulus was also found to be insensitive to variations in K-90 PVP concentration (Figure 5.3-34). The K-90 PVP concentration dependence of the matrix shear modulus was quantified by fitting the data into two linear regions. For K-90 PVP in Derakane™ concentrations below 0.25 wt%, the two experimental data points (0.00, 1.313 GPa) and (0.0025, 1.225 GPa) were utilized to generate the following line:

$$G_{K-90} = -35.1\omega_{K-90} + 1.31 \quad (5-21)$$

For K-90 PVP in Derakane™ concentrations above 5.00 wt%, the two experimental data points (0.0025, 1.225 GPa) and (0.050, 1.260 GPa) were utilized to generate the following line:

$$G_{K-90} = 0.72\omega_{K-90} + 1.23 \quad (5-22)$$

The matrix strain-to-failure was a strong function of the amount of K-90 PVP present in the blend (Figure 5.3-35). The initial increase was the highest (1.9% strain for pure Derakane™ and 2.75% strain for 0.25wt% K-90) and peaked at a value of 3.2% strain for 5.0wt% K-90 PVP. The K-90 PVP concentration dependence of the matrix strain-to-failure was quantified by fitting the data into two linear regions. For K-90 PVP in Derakane™ concentrations below 0.25 wt%, the two experimental data points (0.00, 1.9%) and (0.0025, 2.74%) were utilized to generate the following line:

$$STF_{K-90} = 336.0\omega_{K-90} + 1.9 \quad (5-23)$$

For K-90 PVP in Derakane™ concentrations above 5.00 wt%, the two experimental data points (0.0025, 2.74%) and (0.050, 3.19%) were utilized to generate the following line:

$$STF_{K-90} = 9.5\omega_{K-90} + 2.7 \quad (5-24)$$

From this limited set of data, it can be concluded that even small additions of K-90 PVP to the Derakane™ significantly increases static tensile strength and strain-to-failure without significantly affecting the modulus. The quantification of the blend mechanical properties was utilized in Chapter 4 to obtain the interphase mechanical property profile existing in a K-90 PVP sized composite. The significance of this interphase was discussed in Chapter 4.

5.4 Estimation of Constitutive Properties Needed in FEM Model

The non-fickian FEM model discussed in Chapter 4 needed a dissolution diffusion coefficient to be input before solutions to dissolution controlled interphase formation could be generated. In addition, for dissolution controlled interphase formation, a thermodynamic equilibrium for the sizing material in the Derakane™ matrix needed to be determined. In this section, the dissolution diffusion coefficient is estimated from the Stokes-Einstein equation. Also in this section, the thermodynamic equilibrium is estimated from the blends discussed previously.

5.4.1 Estimation of Dissolution Diffusion Coefficient

Once the sizing material has become relaxed and disentangled, Narasimhan and co-workers [2.33] proposed that Brownian motion controls the diffusion. The diffusion coefficient for systems undergoing Brownian motion can be determined from the Stokes-Einstein relationship:

$$D = \frac{k \cdot T}{6\pi\eta \cdot r_h} \quad (5-25)$$

where k is Boltzman's constant, η is the solvent viscosity, T is the absolute temperature, and r_h is the mean hydrodynamic radius of the species involved in the diffusion. For polymer solutions, the mean hydrodynamic radius can be approximated from the radius of gyration. Therefore, the dissolution diffusion coefficient can be approximated from the following equation [2.53]:

$$D_d = \frac{kT}{6\pi\eta_s \cdot r_g} \quad (5-26)$$

The dissolution diffusion coefficient expressed by equation (5-26) is a function of concentration due to the concentration dependence of the solvent viscosity, η_s , and the radius of gyration, r_g . The solvent viscosity as a function of concentration was determined for the K-90 (Section

5.3.2.5.1) and K-30 (Section 5.3.2.5.2) PVP. Therefore, the radius of gyration needed to be determined before equation (5-26) could be applied.

The radius of gyration for the polymer sizing in the Derakane™ can be obtained from light scattering experiments. However, these experiments could not be completed during the course of this work. Therefore, approximations for the radius of gyration involving chain statistics were utilized.

The average end-to-end distance, $\langle R^2 \rangle_f^{0.5}$, of a freely-jointed statistical chain can be expressed as follows [5.4]:

$$\langle R^2 \rangle_f^{0.5} = l\sqrt{n} \quad (5-27)$$

where l is the segment length and n is the number of statistical segments. The approximation expressed by equation (5-27) can be improved by inserting a correction factor for chain stiffness and restricted rotation called the characteristic ratio, C_∞ . This results in the following approximation for the end-to-end distance [5.4]:

$$\langle R^2 \rangle = l\sqrt{n \cdot C_\infty} \quad (5-28)$$

The C_∞ for most polymer materials lies between 4 and 10. The radius of gyration, r_g , can be approximated from the $\langle R^2 \rangle$ as follows [5.4]:

$$r_g = l\sqrt{\frac{n \cdot C_\infty}{6}} \quad (5-29)$$

For the PVP materials, the value for l is approximately 0.154 nm. The value for the number of statistical segments can be approximated from the following:

$$n = \frac{2 \cdot MW_n}{MW_{repeat}} \quad (5-30)$$

where MW_n is the number average molecular weight and MW_{repeat} is the repeat unit molecular weight for PVP, which is 111g/mol. The PVP materials utilized in these experiments were commercially available and were not supplied with values for MW_n . However, the weight average molecular weight, MW_w was provided with the PVP materials. The MW_n can be calculated from MW_w and the polydispersity, α , which is treated as a parameter in the approximations that follow:

$$MW_w = MW_n \cdot \alpha \quad (5-31)$$

The polydispersity, α , for most commercially available polymers lies in the range from 1.5-2.0 [5.4].

5.4.1.1 K-90 PVP

The approximations discussed in section 5.4.1 will now be utilized for the K-90 PVP sizing system to obtain predictions of the dissolution diffusion coefficient. The commercially available K-90 PVP sizing material had a weight average molecular weight, MW_w , of 1,200,000 g/mol. If the polydispersity, α , is assumed to be equal to 1.67, then the number of statistical segments, n , was found to equal 13,000 from equations (5-30) and (5-31). Literature values for the characteristic ratio, C_∞ , of PVP were found to range from 9.3 – 12.3 in various solvents at room temperature [5.5]. Therefore, the C_∞ was assumed to be concentration and molecular weight independent and equal to 10. The approximated radius of gyration, r_g , was calculated to be equal to 0.0226 μm . Applying this approximated radius of gyration into equation (5-26) and utilizing the viscosity/concentration function expressed by equation (5-15) gives the following approximation for the dissolution diffusion coefficient, D_d :

$$D_d = 0.0071 \exp(-128.41\omega_{K-90}) \quad (5-32)$$

where D_d is the K-90 PVP dissolution diffusion coefficient in units of $\mu\text{m}^2/\text{s}$. This equation was utilized in Chapter 4 to obtain the predicted interphase concentration profile discussed in that chapter (Figure 5.4-1).

5.4.1.2 K-30 PVP

The approximations discussed in section 5.4.1 will now be utilized for the K-30 PVP sizing system to obtain predictions of the dissolution diffusion coefficient. The commercially available K-30 PVP sizing material had a weight average molecular weight, MW_w , of 49,000 g/mol. If the polydispersity, α , is assumed to be equal to 1.67 as was the case with the K-90 PVP, then the number of statistical segments, n , was found to equal 530 from equations (5-30) and (5-31). Utilizing an assumed C_∞ of 10, the approximated radius of gyration, r_g , was calculated to be equal to 0.0046 μm . Applying this approximated radius of gyration into equation (5-26) and utilizing the viscosity/concentration function expressed by equation (5-16) gives the following approximation for the dissolution diffusion coefficient, D_d :

$$D_d = 0.118 \exp(-37.27\omega_{K-30}) \quad (5-33)$$

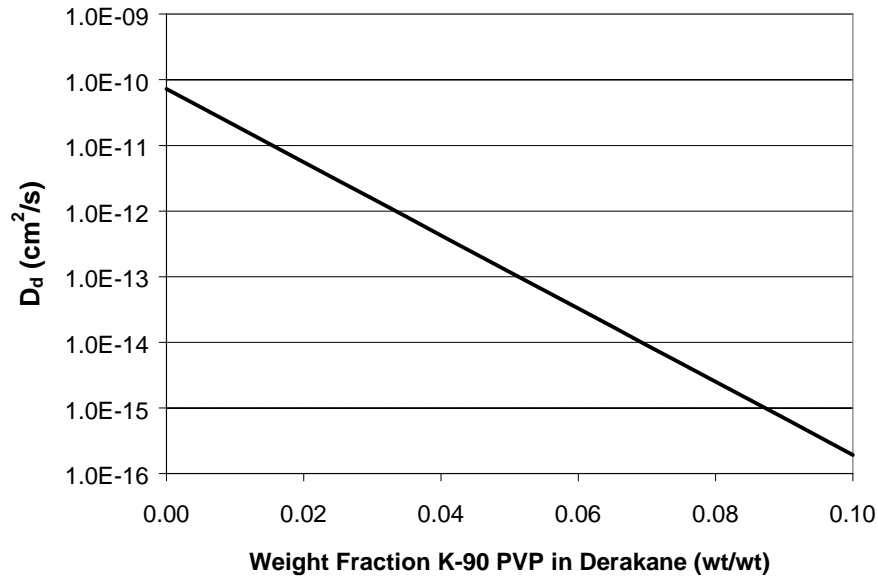


Figure 5.4-1 Dissolution diffusion coefficient, D_d , for the K-90 PVP/Derakane™ system predicted by equation (5-26).

where D_d is the K-30 PVP dissolution diffusion coefficient in units of $\mu\text{m}^2/\text{s}$. This equation was utilized in Chapter 4 to obtain the predicted interphase concentration profile discussed in that chapter (Figure 5.4-2).

5.4.2 Estimation of Fiber/Matrix Interface Boundary Condition

Before the model developed in Chapter 4 could be utilized for interphase predictions, the boundary condition at the fiber/matrix interface had to be determined. In this section, methods for theoretically determining this boundary condition is discussed along with a discussion of its application to the K-90 and K-30 PVP/Derakane™ systems.

As was discussed in chapter 4 and proved in this chapter, the interdiffusion of the K-90 PVP was dissolution controlled. The K-30 PVP was assumed to be dissolution controlled. The swelling and relaxation stages were proven to be very fast compared to the dissolution stage where the highly non-fickian dissolution diffusion coefficient controlled the interphase formation. In addition, it was assumed but not proven that the rate of chain disentanglement was also negligible compared to the dissolution stage. The combination of the proven facts and assumptions allowed the solution domain interface boundary (Γ_4) to be specified completely by a

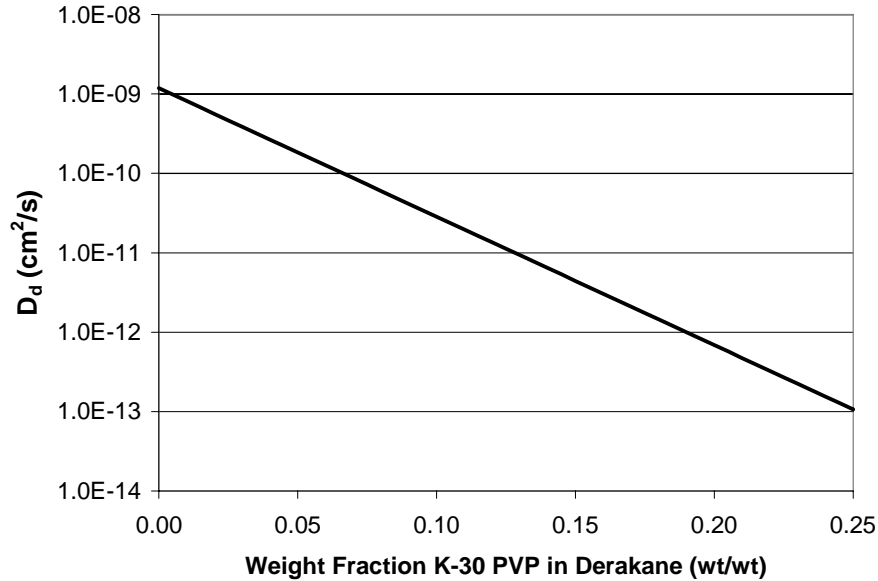


Figure 5.4-2 Dissolution diffusion coefficient, D_d , for the K-30 PVP/Derakane™ system predicted by equation (5-26).

thermodynamic equilibrium. For this special case, the value of the thermodynamic equilibrium was determined by a phase transition in the disentangled sizing phase. The change in Gibbs free energy of mixing, ΔG_m , determines the value of this phase transition and can be approximately represented by the following [5.6]:

$$\frac{\Delta G_m}{N_T RT} = x_s \ln \phi_s + (1 - x_s) \ln \phi_m + \phi_s (1 - x_s) \chi \quad (5-34)$$

where N_T is the total number of moles, x_s is the sizing mole fraction, ϕ_s is the sizing volume fraction, ϕ_m is the matrix volume fraction, and χ is the Flory-Huggins interaction parameter. However, equation (5-34) is not accurate for systems with a large extent of hydrogen bonding, which is the case for the PVP/Derakane™ system. Therefore, the thermodynamic equilibrium existing at the fiber/matrix interface was estimated from the blend data discussed earlier. The thermodynamic equilibrium was assumed to be approximately equal to the maximum amount of sizing material that could be added to the Derakane™ without creating two phases. For both the K-90 and K-30 PVP materials, PVP could be added to the Derakane™ without the creation of two-phases for the experimentally accessible concentrations. Both PVP materials had a limited range of experimentally accessible blend concentrations due to the increase in viscosity with

increasing PVP concentration. Therefore, thermodynamic equilibrium was assumed to exist at the first concentration where the PVP/Derakane™ blend was essentially a solid. For the K-90 PVP/Derakane™ system, the thermodynamic equilibrium existing in the Derakane™ rich phase was estimated to be 0.10 weight fraction K-90 PVP. For the K-30 PVP/Derakane™ system, the thermodynamic equilibrium existing in the Derakane™ rich phase was estimated to be 0.25 weight fraction K-30 PVP. These values were utilized in the simulation results presented in chapter 4.

The non-fickian FEM code developed in chapter 4 can also be utilized for interdiffusion processes where the rate of sizing disentanglement is not significantly smaller than the rate of dissolution (note: the swelling and relaxation are still negligible). For this special case, both the disentanglement rate and thermodynamic equilibrium at the fiber/matrix interface must be specified. Narasimhan and co-workers [2.53] developed a chain reptation model for the dissolution of glassy polymers. These researchers concluded that the rate at which relaxed material becomes available for dissolution is related to the reptation time of the relaxed polymer. Because the polymer segment travels approximately one radius of gyration during one reptation time, the researchers concluded that the rate at which relaxed material enters the bulk phase was approximately equal to the following [2.53]:

$$k_d = \frac{r_g}{t_{rep}} \quad (5-35)$$

where k_d is the relaxation velocity, r_g is the polymer radius of gyration, and t_{rep} is the reptation time. Once the disentanglement velocity is determined, then the flux, $\underline{n}_s \cdot \underline{n}$, can be determined from the following equation:

$$\underline{n}_s \cdot \underline{n} = \omega_s^d \rho k_d \quad (5-36)$$

where ω_s^d is thermodynamic equilibrium weight fraction of the sizing existing in the entangled sizing phase (note: not equal to ω_s^{eq}) and ρ is the bulk density existing in the entangled sizing phase. The r_g was approximated in section 5.4.1 for the K-90 and K-30 PVP sizing systems. However, the reptation time could not be approximated and equation (5-35) could not be applied to either of our systems. If the reptation time could be determined, then equation (5-35) could be used to determine the accuracy of the dissolution controlled assumption utilized in chapter 4. In addition, a flux-controlled simulation could be completed once the thermodynamic equilibrium

had been specified by equation (5-34). For example, the disentanglement flux and thermodynamic equilibrium would be input into the FEM model. The model would then calculate the interphase profile as a function of time. If thermodynamic equilibrium were surpassed at the interface, then the FEM model would switch from interface flux controlled to interface equilibrium controlled. From the interface concentration as a function of time, the user could then determine whether the interdiffusion was flux (i.e. interface concentration less than thermodynamic equilibrium) or equilibrium controlling (i.e. interface concentration equal to thermodynamic equilibrium).

5.5 Conclusions

The dielectric experimental results presented in section 5.3.1 clearly showed two of the four stages associated with the interdiffusion of a polymer and a compatible solvent: swelling and relaxation. The swelling diffusion coefficient for Derakane™ in K-90 PVP was estimated to be on the order of 10^{-10} cm²/sec. The styrene component of the Derakane™ was found to be responsible for the swelling stage while this component did not relax the K-90 PVP. The vinyl-ester portion was found to be responsible for the relaxation of the K-90 PVP which allowed for its dissolution into the Derakane™ phase.

The dielectric results for the K-90 PVP diffusing into pure Derakane™ indicated that a “psuedo steady-state” was reached. This was an indication that the relaxation portion of the interdiffusion process had been completed. Because the dielectric properties had not reached the pure Derakane™ values, the dissolution process was still in its early stages. Therefore, K-90 PVP diffusing into Derakane™ was dissolution controlled, which was the assumption used in the modeling presented in Chapter 4. In addition, it was assumed that the K-30 PVP diffusing into Derakane™ was also dissolution controlled. No conclusions about the disentanglement rate could be reached. However, it was assumed that the disentanglement rate was very fast compared to the dissolution rate for both the K-90 and K-30 PVP sizing systems.

The addition of small amounts of K-90 PVP to the pure Derakane™ matrix had profound affects on the matrix shrinkage, tensile strength, and tensile strain-to-failure. The matrix shrinkage was found to be a strong function of K-90 PVP concentration. There was a four fold decrease in shrinkage from pure Derakane™ to 5.0wt% K-90 PVP in Derakane™. As was

discussed in chapter 4, this will have profound effects on the residual stress distribution at the fiber/matrix interface due to a reduction in cure shrinkage. The blend glass transition temperature was not found to follow the Fox equation due to strong hydrogen bonding interactions.

The tensile strength was found to increase approximately 30% between the pure Derakane™ and the 0.25wt% K-90 PVP in Derakane without significantly affecting the modulus. The strain-to-failure was found to increase approximately 45% between the pure Derakane™ and the 0.25wt% K-90 PVP in Derakane™.

As was discussed in chapter 4, if the K-90 PVP sized composite interphase had similar properties to those observed in the K-90 PVP/Derakane™ blends, then substantial effects on composite performance would be expected. The quantitative implications of these effects cannot be determined. However, the large effects on on-axis composite properties (longitudinal tension, longitudinal flexure, and compression) discussed in chapter 3 section 3.1 are still believed to be **mainly** attributable to changes in fiber processability and not changes in interphase properties and/or fiber/matrix adhesion. The smaller effects on on-axis composite properties (longitudinal flexure) discussed in chapter 3 section 3.2 may be attributable to the alterations in interphase properties discussed in this chapter.

5.6 References

- 5.1 N. G. McCrum, B. E. Read, and G. Williams, *Anelastic and Dielectric Effects in Polymeric Solids*, John Wiley & Sons Ltd., 1967.
- 5.2 Personal communication with Mrs. Maggie Bump, VPI&SU, Dept. of Chemistry.
- 5.3 S. L. Rosen, *Fundamental Principles of Polymeric Materials*, John Wiley & Sons, 1982.
- 5.4 R. J. Young and P. A. Lovell, *Introduction to Polymers*, 2nd edition, Chapman & Hall, 1991.
- 5.5 J. Brandrup and E. H. Immergut, *Polymer Handbook*, John Wiley & Sons, 1989.
- 5.6 J. M. Prausnitz, R. N. Lichtenthaler, E. Gomes de Azevedo, *Molecular Thermodynamics of Fluid-Phase Equilibria*, 2nd Edition, Prentice-Hall, Englewood Cliffs, NJ.

Guide to the Appendices

This section details the three appendices referenced in the main body of this thesis. Appendix I is a listing of the mesh generation program utilized to simulate composite interphases. Appendix II is a listing of the non-fickian FEM program discussed in chapter 4. Finally, Appendix III is a data-sorting program that was not discussed in the main body of this thesis.

The numerical approach utilized by the mesh generation program was discussed in chapter 4 section 4.4.2 and the actual FORTRAN code is listed in Appendix I. This paragraph details the user interface details needed to utilize the program to obtain composite meshes for various physical situations. The program is stored on the 1.44MB floppy enclosed with this thesis. The mesh program is stored in an executable file called *mesh*. Upon running the mesh program, the following input is requested:

1. Enter fiber volume fraction

The value of this input must be between 0 and 1.

2. Enter number of arc elements

This is the number of elements on the interface arc. For the mesh shown in Figure 4.4-2, the number of arc elements was equal to 6.

3. Enter number of radial elements

This is the number of elements on the radial subdivision. For the mesh shown in Figure 4.4-2, the number of radial elements was equal to 4.

4. Enter value for dR_o/dR_f

This is the value of the initial radial length of the element divided by the final length of the radial element. For non-fickian simulations, this mesh refinement is necessary for accurate interphase concentration profiles.

With this information, the program generates the following output files.

1. *Nelem.mes*

This file contains the number of elements existing in the mesh.

2. *Nodes.mes*

This file contains the number of nodes existing in the mesh.

3. *Nodx.mes*

This file contains the x-coordinate of the nodes existing in the mesh. The nodes are input sequentially from 1 to the number of nodes. For instance, the first x-coordinate in the *Nodx.mes* data file is for node #1. The second corresponds to node #2.

4. *Nody.mes*

This file contains the y-coordinate of the nodes existing in the mesh. The nodes are input sequentially from 1 to the number of nodes. For instance, the first y-coordinate in the *Nodx.mes* data file is for node #1. The second corresponds to node #2.

5. *Essbc.mes**

This file contains the number of boundary nodes existing on the fiber/matrix interface arc.

6. *Icon.mes*

This file contains the connectivity array discussed in section 4.4.2.

7. *Data.mes**

This file contains the connectivity array for the fiber/matrix interface arc.

*Not utilized by the non-fickian FEM program in any calculations but is still needed before the simulation will run properly.

The numerical approach utilized by the non-fickian FEM program was discussed in chapter 4 and the actual FORTRAN code is listed in Appendix II. This paragraph details the user interface details needed to utilize the program to obtain interphase formation predictions for various physical situations. The program is stored on the 1.44MB floppy enclosed with this thesis. The mesh program is stored in an executable file called *non-fickian_flux*. As was discussed previously, the *non-fickian_flux* code must have the seven *.mes files stored in the same directory as the *non-fickian_flux* code before the simulation can be completed. Upon running the non-fickian program with the mesh files properly in place, the following input is requested:

1. Enter final time

This is the total simulation time in seconds. For most interphase formation simulations discussed in chapter 4, the total simulation time was set equal to 900 seconds.

2. Enter <1> if you want a constant dt

Enter <2> if you want a ramp on dt

This determines whether the simulation will have a constant time step, dt , or a variable time step. A variable time step is utilized to take advantage of the fact that a smaller time step is needed at early times. The effect is to reduce the computational time without reducing accuracy. If <1> is selected, then the time step, dt , is constant and sub-option 2a is presented. If <2> is selected, then sub-option 2b is presented.

2a. dt is constant

Enter value for dt (Seconds)

The time step, dt , was chosen to be constant and not a function of the total time. The time step, dt , is entered in seconds.

2b. Enter <1> if you want a linear variation on dt

Enter <2> if you want a step variation on dt

This determines whether the simulation will have a linear variation on the time step, dt , as a function of processing time or a step variation. If <1> is selected, then a linear variation is selected and sub-option 2b.a is presented. If <2> is selected, then a step variation is selected and sub-option 2b.b is presented.

2b.a Linear variation on dt

Enter initial value of dt

Enter final value of dt

A linear variation on the time step, dt , is selected. The initial value of the time step, dt_o , is input in seconds. The final value of the time step, dt_f , or the value of the time step at the end of the simulation in seconds is input.

2b.b Step variation of dt

Enter # of steps (Maximum of 10)

Enter dt for step #

Enter end time for step #

A step variation on the time step, dt , is selected. The number of different steps is input. The program allows a maximum of 10 steps. For each step variation, the user must input the time step, dt , for that step in seconds. In addition, the user must input the end time for each step number in seconds.

3. Enter time step for saving data (seconds)

Because the amount of data generated by the simulation is large, it becomes necessary to store data at selected time intervals. This is the time step, t_s , in which data is to be saved in seconds. The data is saved at times equal to $n \cdot t_s$ where n is an integer ≥ 1 .

4. Enter value for theta

This is the value for theta, θ , shown in equation (4.39). θ is a parameter that can be varied from 0 to 1. If θ has a value of 0, then the finite differencing approximation is $O(\Delta t)$ accurate and conditionally stable. If the value of θ is 0.5, then the approximation is $O(\Delta t^2)$ accurate and is unconditionally stable. If θ has a value of 1, then the approximation is $O(\Delta t)$ accurate and unconditionally stable. For all simulation results presented in this thesis, the value for θ was selected to be 0.5.

5. Enter the mass fraction of sizing on carbon fiber

This is the value for the sizing level on the carbon fiber in sizing weight per total weight (sizing + carbon fiber). For all simulation results presented in this thesis, the sizing level was set equal to 0.02.

6. Enter the density of the sizing (g/cm^3)

The sizing density is input in g/cm^3 .

7. Diffusivity = $A \exp(E_a \cdot \omega_s)$

Enter A ($\mu\text{m}^2/\text{sec}$)

Enter E_a (unitless)

This input is utilized to specify the exponential concentration dependence of the dissolution diffusion coefficient, D_d in $\mu\text{m}^2/\text{s}$. The pre-exponential, A, in $\mu\text{m}^2/\text{sec}$ is input. The activation energy, E_a , is also input. The ω_s is the sizing weight fraction (wt sizing/ wt total) existing in the interphase region (note: $0 \leq \omega_s \leq 1$).

8. Enter initial ws

The initial sizing weight fraction in the solution domain is input. For all simulations discussed in this thesis, the value for the initial sizing weight fraction was 0.

9. Enter thermodynamic equilibrium of sizing in matrix (wt/wt)

The thermodynamic equilibrium value for the sizing in the matrix is entered (wt/wt). This value was calculated in chapter 5 section 5.4.2.

10. Enter # of iteration loops to perform

As was discussed in chapter 4 section 4.4.7, the non-linearity's created by the non-constant dissolution diffusion coefficient were approximated with an iterative solution. The number of iteration loops performed per time step is input in this step.

11. For dissolution controlled interdiffusion please enter <1>

For relaxation/disentanglement controlled please enter <2>

If it is known apriori that the interdiffusion process is dissolution controlled, then <1> is input. If it is not known apriori whether dissolution or relaxation/disentanglement controls the interdiffusion process, the <2> is input and sub-option 11a is presented.

11a. Enter value for flux <g/cm²/sec> Note: this should be greater than 0

The relaxation/disentanglement flux at the fiber/matrix interface is input here in g/cm²/sec.

With this information, the non-fickian FEM code solves for the concentration profile at every time step and stores it for certain time steps. The user input data and the output data is stored in a file named *data.dat*. An example of a *data.dat* file is shown below:

```
DIFF= A*EXP(EA*WS)
A = 1.0000000000000000E-002
EA = -128.4100000000000000
DT= 1.0000000000000000E-003
THETA= 5.0000000000000000E-001
PROCESS IS DISSOLUTION CONTROLLED
THERMODYNAMIC EQUILIBRIUM AMOUNT OF SIZING <WT/WT> 1.0000000000000000E-001
MASS FRACTION SIZING ON FIBER <WT/WT> 2.0000000000000000E-002

1.0000000000000001E-001 ← This is the time in seconds
.10000E+00 ← This is the sizing weight fraction at node #1
.10000E+00 ← This is the sizing weight fraction at node #2
.10000E+00 ← This is the sizing weight fraction at node #3
.10000E+00 ← This is the sizing weight fraction at node #4
.10000E+00 ← etc ....
.10000E+00
.55774E-01
.55535E-01
.54850E-01
.53838E-01
.21554E-01 ← Data cut-off to conserve space
-.21515E-26
-.11205E-26
.25991E-28 ← This is the sizing weight fraction at the final node

8.135683448771003E-001 ← This is the mass % sizing dissolved in
```

```

2.0000000000000002E-001 ← This is the next time
.10000E+00
.10000E+00
.10000E+00
.10000E+00
.10000E+00
.10000E+00
.10000E+00
.57961E-01
.57729E-01
.57065E-01
.56084E-01
.54703E-01
.53225E-01 ← etc ....

```

The first few lines of data are the user-input data just discussed. The first line containing a number represents the time in seconds. The data that follows is the concentration of sizing in the matrix (wt/wt) that exists at nodes numbered 1 through the total number of nodes. After all the concentrations for all the nodes have been specified for this time, the percentage of the starting sizing that has dissolved into the matrix is displayed for this time. After the percent sizing dissolved has been displayed, the next time, the corresponding concentration data, and the percent sizing dissolved are displayed. This pattern continues until the final time is reached.

The data file, *data.dat*, just discussed needed to be filtered before efficient presentation of the results could be accomplished. The most efficient way to display a concentration profile over a two-dimensional area is with a contour plot as long as steep gradients are not present. Unfortunately, the steep concentration gradients present at the fiber/matrix interface did not allow the use of contour plots. The most efficient method of displaying the non-fickian interphase data generated was to utilize two-dimensional plots of concentration versus radial position. The radial subdivision of the mesh discussed in section 4.4.2 was used to generate the radial positioning. A data sorter program was compiled that allows the user to select which radial subdivision to display. The actual FORTRAN code utilized for this sorting is displayed in Appendix III. This paragraph details the user interface details needed to utilize the program to obtain interphase formation predictions for various physical situations. The program is stored on the 1.44MB floppy enclosed with this thesis. The data sorter program is stored in an executable file called *multi-sort*. The *multi-sort* program needs the *nodes.mes*, *essbc.mes*, *nodx.mes*, and *nody.mes* files in order to complete the data sorting. In addition, the user must select the concentration data at a particular time period from the *data.dat* file and store it in a new file

called *ws.dat*. For instance, if the user wanted to sort the previously listed data for time equal to 0.1 seconds, then the *ws.dat* file should contain the following:

```
.10000E+00← This is the sizing weight fraction at node #1
.10000E+00← This is the sizing weight fraction at node #2
.10000E+00← This is the sizing weight fraction at node #3
.10000E+00← This is the sizing weight fraction at node #4
.10000E+00← etc ....
.10000E+00
.55774E-01
.55535E-01
.54850E-01
.53838E-01
.21554E-01 ← Data cut-off to conserve space
-.21515E-26
-.11205E-26
.25991E-28← This is the sizing weight fraction at the final node
```

After *ws.dat* has been created and stored in the same directory as *multi-sort* and the **.mes* files, the program can be run. The following user input information will be requested:

1. There are # iso-angles to select

How many iso-angles do you wish to generate

For each node on the fiber/matrix interface arc, a radial line from the interface to the axis of symmetry can be drawn. Each of these radial lines represents an iso-angle. The program tells the user how many there are available and asks the user to input the number he/she wishes to display. For instance, if there are 20 nodes on the fiber/matrix boundary, then 20 iso-angles exist. The program labels the iso-angles in a particular manner. The first iso-angle is always located at an angle of 0° or at the Γ_3 interface listed in Figure 4.1.2. The last iso-angle, 20th in this case, is always located at 30° or at the Γ_1 interface. The user can select how many of the available iso-angles to sort.

2. Enter iso-angle line for selection

The user is then asked to select the iso-angle lines to sort. If the user inputs that he/she wants to display three of the 20 available iso-angles, then the user now has to define which three of the 20 he/she wants to sort.

The program then produces a data file called *wsn.dat* and *R.dat* that store the concentration and radial position data for each iso-angle line that had been selected. This data can then be converted into a two-dimensional plot of concentration versus radial position at various angles in the solution domain.

APPENDIX I

```
*****
*****
*****
```

PROGRAM MAKER

```
*****
*****THIS VERSION OF MAKER HAS NON-CONSTANT SPACING*****
*****THE GRID SPACING IS LINEAR*****
*****
```

INTEGER NELEMMAX, NODESMAX, ESSBCMAX, NPE

```
*****
```

PARAMETER (NPE=4)
PARAMETER (NELEMMAX=2500, NODESMAX=5000, ESSBCMAX=100)

```
*****
```

DIMENSION NODX(NODESMAX), NODY(NODESMAX),
&ICON(NELEMMAX, NPE), DATA1(ESSBCMAX)

```
*****
```

REAL LY, LX, DY, DX, NODX, NODY, DXO, DYO, DXF, DYF

INTEGER YELE, XELE, NELEM, ESSBC, DATA1, NODE, ELEMENT

INTEGER SKIPX, SKIPPY

```
*****
*****USER SPECIFIED MESH DATA*****
*****
```

PRINT*, 'ENTER LENGTH OF X'
READ*, LX

PRINT*, 'ENTER LENGTH ON Y'
READ*, LY

PRINT*, 'ENTER NUMBER OF ELEMENTS ON X'
READ*, XELE

PRINT*, 'ENTER NUMBER OF ELEMENTS ON Y'
READ*, YELE

```
*****
*****ENTER INITIAL LENGTHS FOR THE SEGMENTS*****
*****
```

PRINT*, 'ENTER INITIAL LENGTH FOR DX <ENTER 0.0 IF EQUAL SPACING>'
READ*, DXO

```

PRINT*, 'ENTER INITIAL LENGTH FOR DY <ENTER 0.0 IF EQUAL SPACING>'
READ*, DY0

*****
*****DETERMINE IF EQUAL SPACING OR NOT AND ADJUST*****
*****

IF (DX0.EQ.0.0) THEN

    DX0 = LX/XELE

    DXF = DX0

    SKIPX = 1

ELSE

    DXF = 2*LX/XELE - DX0

ENDIF

IF (DY0.EQ.0.0) THEN

    DY0 = LY/YELE

    DYF = DY0

    SKIPPY = 1

ELSE

    DYF = 2*LY/YELE - DY0

ENDIF

*****
*****COMPUTE NUMBER OF ELEMENTS*****
*****

NELEM=YELE*XELE

*****
*****GENERATE NODES*****
*****

*****
*****INITIALIZE THE POSITION INDICATORS*****
*****

    POSX=1
    POSY=1

*****
*****INITIALIZE ELEMENT AND NODE NUMBER*****
*****

```

```

ELEMENT=1
NODE=1

*****
***DETERMINE NUMBER OF ESSENTIAL BOUNDARY CONDITIONS***
*****

ESSBC=YELE+1

*****
**START GENERATING CONNECTIVITY ARRAY AND NODAL POSITIONS**
*****

DO 110 WHILE (POSX.LE.(XELE+1))

    POSY=1

    DO 100 WHILE (POSY.LE.(YELE+1))

        IF (POSY.LE.YELE) THEN

            IF (POSX.EQ.1) THEN

                ICON(ELEMENT,1)=NODE
                ICON(ELEMENT,4)=NODE+1

            ENDIF

            IF (POSX.EQ.(XELE+1)) THEN

                ICON((ELEMENT-YELE),2)=NODE
                ICON((ELEMENT-YELE),3)=NODE+1

            ENDIF

            IF (POSX.GT.1) THEN

                IF (POSX.LT.(XELE+1)) THEN

                    ICON((ELEMENT-YELE),2)=NODE
                    ICON((ELEMENT-YELE),3)=NODE+1
                    ICON(ELEMENT,1)=NODE
                    ICON(ELEMENT,4)=NODE+1

                ENDIF

            ENDIF

        ENDIF

    END IF

*****
*****DETERMINE X POSITION*****
*****

    IF (POSX.EQ.1) THEN

        NODX(NODE)=0.0

```

```

ELSE

*****
*****DETERMINE DX FOR THE NODE POSITION*****
*****

DX = (DXF-DXO)/(XELE-1)*(POSX-2)+DXO

*****
*****DETERMINE NODX POSITION*****
*****

NODX(NODE)=NODX(NODE-ESSBC) + DX

ENDIF

*****
*****DETERMINE Y POSITION*****
*****

IF (POSY.EQ.1) THEN

NODY(NODE)=0.0

ELSE

*****
*****DETERMINE DY FOR THE NODE POSITION*****
*****

DY = (DYF-DYO)/(YELE-1)*(POSY-2)+DYO

*****
*****DETERMINE NODY POSITION*****
*****

NODY(NODE)=NODY(NODE-1) + DY

ENDIF

POSY=POSY+1

NODE=NODE+1

ELEMENT=ELEMENT + 1

100 CONTINUE

POSX=POSX+1
ELEMENT=ELEMENT-1

110 CONTINUE

NODE=NODE-1
ELEMENT=ELEMENT-YELE-1

```

```

*****
*****GENERATE ESSENTIAL BOUNDARY*****
*****

      DO 200 I=1,(YELE+1)
        DATA1(I)=YELE+2-I
200    CONTINUE

*****
*****OPEN DATA1 FILES*****
*****

      OPEN(300,FILE='NELEM.MES',STATUS='NEW')
      OPEN(310,FILE='NODES.MES',STATUS='NEW')
      OPEN(320,FILE='ESSBC.MES',STATUS='NEW')
      OPEN(330,FILE='ICON.MES',STATUS='NEW')
      OPEN(340,FILE='NODX.MES',STATUS='NEW')
      OPEN(350,FILE='NODY.MES',STATUS='NEW')
      OPEN(360,FILE='DATA.MES',STATUS='NEW')

*****
*****WRITE THE DATA1*****
*****

      WRITE(300,*) ELEMENT
      CLOSE(300)
      WRITE(310,*) NODE
      CLOSE(310)
      WRITE(320,*) ESSBC
      CLOSE(320)

      DO 400 I=1,NELEM
        DO 410 J=1,NPE
          WRITE(330,*) ICON(I,J)
410    CONTINUE
400    CONTINUE

      CLOSE(330)

      DO 500 I=1,NODE
        WRITE(340,*) NODX(I)
        WRITE(350,*) NODY(I)
500    CONTINUE
      CLOSE(340)
      CLOSE(350)

      DO 600 I=1,ESSBC
        WRITE(360,*) DATA1(I)
600    CONTINUE
      CLOSE(360)

      END

*****
*****
*****

```

APPENDIX II

```
*****
*****THIS PROGRAM HAS LOOPING, FLUX, AND VARIABLE DT*****
*****

PROGRAM DIFFUSION

*****
*****VARIABLE DECLARATION FOR PARAMETERS*****
*****

INTEGER NODESMAX, NELEMAX, ESSBCMAX, BANDMAX

INTEGER GAUSSPTS, NPE, NPLE, STEPMAX

*****
*****PARAMETER SPECIFICATION*****
*****

*****PARAMETER FOR NUMBER OF NODES*****

PARAMETER (NODESMAX=5000)

*****PARAMETER FOR NUMBER OF ELEMENTS*****

PARAMETER (NELEMAX=5000)

*****PARAMETER FOR # OF NODES THAT ARE ESS. B.C.'S*****

PARAMETER (ESSBCMAX=1000)

*****PARAMETER FOR # OF ELEMENTS ON NAT. B.C.'S*****

PARAMETER (BANDMAX=200)

*****PARAMETER FOR NUMBER OF GAUSS POINTS*****

PARAMETER (GAUSSPTS=10)

*****PARAMETER FOR NUMBER OF NODES PER ELEMENT*****

PARAMETER (NPE=4)

*****PARAMETER FOR NUMBER OF NODES PER LINEAR ELEMENT**

PARAMETER (NPLE=2)

*****PARAMETER FOR MAXIMUM NUMBER OF DIFFERENT DT'S*****

PARAMETER (STEPMAX=10)

*****
*****DIMENSIONALIZATION OF VARIOUS ARRAYS*****
```

```

*****
*****DIMENSIONALIZE STIFFNESS MATRIX*****

    DIMENSION LS(NODESMAX,BANDMAX)
    DIMENSION LSF(NODESMAX,BANDMAX)
    DIMENSION MS(NODESMAX,BANDMAX)
    DIMENSION A(NODESMAX,BANDMAX)
    DIMENSION B(NODESMAX,BANDMAX)

*****DIMENSIONALIZE LOAD VECTOR*****

    DIMENSION F(NODESMAX)
    DIMENSION Q(NODESMAX)
    DIMENSION R(NODESMAX)
    DIMENSION RFUT(NODESMAX)
    DIMENSION FSUR(ESSBCMAX)
    DIMENSION FMUL(NODESMAX)

*****DIMENSIONALIZE GAUSS POINT ARRAY*****

    DIMENSION GAUSS(GAUSSPTS)

*****DIMENSIONALIZE WEIGHT ARRAY*****

    DIMENSION WEIGHT(GAUSSPTS)

*****DIMENSIONALIZE SHAPE FUNCTION ARRAYS*****

    DIMENSION NS(NPE)

*****DIMENSIONALIZE DERIVATIVES SHAPE FUNCTION ARRAYS

    DIMENSION DSNS(NPE)
    DIMENSION DTNS(NPE)

*****DIMENSIONALIZE CONNECTIVITY ARRAY*****

    DIMENSION ICON(NELEMMAX,NPE)

*****DIMENSIONALIZE NODAL COORDINATES*****

    DIMENSION NODX(NODESMAX)
    DIMENSION NODY(NODESMAX)

*****DIMENSIONALIZE ARRAY THAT GIVES THE NODES ON THE ESS****
*****BOUNDARY CONDITION BOUNDARY*****

    DIMENSION DATA1(ESSBCMAX)

*****DIMENSIONALIZE WEIGHT FRACTIONE DATA1 ARRAY*****

    DIMENSION WS(NODESMAX),WSFUTURE(NODESMAX)

*****DIMENSIONALIZE TIME STEP ARRAY (MAY NOT BE USED)*****

    DIMENSION DTSTEP(STEPMAX)

```

*****DIMENSIONALIZE TIME TO STEP UP ARRAY (MAY NOT BE USED)*****

DIMENSION ENDTIME(STEPMAX)

*****VARIABLE DECLARATION*****

DOUBLE PRECISION WEIGHT, GAUSS, NODX, NODY, TF, S, NS, DSNS,
&DTNS, DYS, DYT, DXS, DXT, DT, TS, MF, PS, THETA, DIFF, COUNTER, WSI, DUMB

DOUBLE PRECISION JACOB, ME, X, Y, LE, F, WS, A, LS, B,
&MS, T, TIME, MASSE, WSP, MASSF, THICK, MASS, Q, R, PREEXP, EA, FMUL

DOUBLE PRECISION WSF, LEF, LSF, RFUT, FSUR, DTO, DTF, DTSTEP

DOUBLE PRECISION WSFUTURE, SIZFLUX, ENDTIME

INTEGER M, N, I, J, ICON, ELEMENT, NODES, NELEM, ESSBC, INFO, INFO_2

INTEGER DATA1, SKIP, DONG, BAND, COLUMN, ACTUAL, UP, UPPER, NSURELE

INTEGER K, TODISK, ITER, UNCLE, LOOP, MAXLOOP, ANSW, SHIT, DOME

INTEGER STEPS

*****IF SKIP IS ZERO THEN SIZING STILL REMAINS*****
***** & *****
*****STIFFNESS MARIX AND LOAD VECTOR MUST BE NORMALIZED*****

*****COLUMN IS THE COLUMN POSITION IN THE BANDED MATRIX*****

*****SPECIFY SOME PHYSICAL PARAMETERS*****

DOUBLE PRECISION PI, RF, PF, WSEQ

PARAMETER (PI=3.141592654D0, RF=3.5D0, PF=1.78D-12)

*****FUNCTIONS USED IN MAIN PROGRAM*****

*****NON-FICKIAN DIFFUSION FUNCTION*****

DIFF(DUMB)=PREEXP*EXP(EA*DUMB)

*****INPUT VARIOUS GAUSS POINTS AND THEIR WEIGHTS*****

WEIGHT(1)=.066671344308688D0
WEIGHT(2)=.149451349150581D0
WEIGHT(3)=.219086362515982D0

WEIGHT(4)=.269266719309996D0
WEIGHT(5)=.295524224714753D0
WEIGHT(6)=.066671344308688D0
WEIGHT(7)=.149451349150581D0
WEIGHT(8)=.219086362515982D0
WEIGHT(9)=.269266719309996D0
WEIGHT(10)=.295524224714753D0

GAUSS(1)=-.973906528517172D0
GAUSS(2)=-.865063366688985D0
GAUSS(3)=-.679409568299024D0
GAUSS(4)=-.433395394129247D0
GAUSS(5)=-.148874338981631D0
GAUSS(6)=.973906528517172D0
GAUSS(7)=.865063366688985D0
GAUSS(8)=.679409568299024D0
GAUSS(9)=.433395394129247D0
GAUSS(10)=.148874338981631D0

*****DEFINE THE MESH*****

*****OPEN MESH FILES*****

OPEN(10,FILE='NELEM.MES',STATUS='OLD')

OPEN(11,FILE='NODES.MES',STATUS='OLD')

OPEN(12,FILE='ESSBC.MES',STATUS='OLD')

*****NUMBER OF ELEMENTS*****

READ(10,*) NELEM

*****NUMBER OF NODES*****

READ(11,*) NODES

*****NUMBER OF ESSENTIAL BOUNDARY CONDITIONS*****

READ(12,*) ESSBC

*****CLOSE UP MESH FILES*****

```

CLOSE (10)

CLOSE (11)

CLOSE (12)

*****
*****OPEN CONNECTIVITY ARRAY FILE*****
*****

OPEN(10,FILE='ICON.MES',STATUS='OLD')

*****
*****RETRIEVE CONNECTIVITY ARRAY*****
*****

DO 130 I=1,NELEM

DO 131 J=1,NPE

READ(10,*) ICON(I,J)

131 CONTINUE

130 CONTINUE

*****
*****CLOSE CONNECTIVITY ARRAY FILE*****
*****

CLOSE (10)

*****
*****OPEN MESH POSITION INDICATOR FILES*****
*****

OPEN(10,FILE='NODX.MES',STATUS='OLD')

OPEN(11,FILE='NODY.MES',STATUS='OLD')

*****
*****READ IN THE MESH POSITIONS*****
*****

DO 132 I=1,NODES

READ(10,*) NODX(I)

READ(11,*) NODY(I)

132 CONTINUE

*****
*****CLOSE MESH POSITION INDICATOR FILES*****
*****

CLOSE (10)

```

```

CLOSE (11)

*****
***OPEN ESSENTIAL BOUNDARY CONDITION CONNECTIVITY ARRAY***
*****

OPEN(10,FILE='DATA.MES',STATUS='OLD')

*****
***GENERATE ESSENTIAL BOUNDARY CONDITION CONNECTIVITY ARRAY***
*****

DO 135 I=1,ESSBC

    READ(10,*) DATA1(I)

135 CONTINUE

*****
****CLOSE ESSENTIAL BOUNDARY CONDITION CONNECTIVITY ARRAY****
*****

CLOSE (10)

*****
*****CALCULATE NUMBER OF SURFACE ELEMENTS*****
*****THIS MUST BE CHANGED IF THE SHAPE FUNCTIONS ARE CHANGED*****
*****

NSURELE = ESSBC - 1

*****
*****TIME TO INITIALIZE DATA FILES*****
*****

OPEN(10,FILE='DATA.DAT',STATUS='NEW')

*****
*****TIME TO INPUT TRANSIENT INFORMATION*****
*****

PRINT*,'ENTER FINAL TIME (Seconds) '

READ*,TF

*****
*****TIME TO INPUT SPECIFICATION FOR DT*****
*****

777 PRINT*,'ENTER <1> IF YOU WANT A CONSTANT DT'
PRINT*,'ENTER <2> IF YOU WANT A RAMP ON DT'

READ*,INFO

IF ((INFO.NE.1).AND.(INFO.NE.2)) GOTO 777

```

```

IF (INFO.EQ.2) THEN
778  PRINT*, 'ENTER <1> IF YOU WANT A LINEAR VARIATION ON DT'
    PRINT*, 'ENTER <2> IF YOU WANT A STEP VARIATION ON DT'

    READ*, INFO_2

    IF ((INFO_2.NE.1).AND.(INFO_2.NE.2)) GOTO 778

    IF (INFO_2.EQ.1) THEN

        PRINT*, 'LINEAR VARIATION OF DT'
        PRINT*, 'ENTER INITIAL VALUE OF DT'

        READ*, DTO

        PRINT*, 'ENTER FINAL VALUE OF DT'

        READ*, DTF

    ELSE

        PRINT*, 'STEP VARIATION OF DT'
        PRINT*, 'ENTER # OF STEPS (MAXIMUM OF 10)'

        READ*, STEPS

        DO 999 I=1, STEPS

            PRINT*, 'ENTER DT FOR STEP#', I

            READ*, DTSTEP(I)

            IF (I.LT.STEPS) THEN

                PRINT*, 'ENTER END TIME FOR STEP#', I

                READ*, ENDTIME(I)

            ENDIF

999    CONTINUE

        ENDTIME(STEPS)=1.1D0*TF

    ENDIF

ELSE

    PRINT*, 'DT IS CONSTANT'
    PRINT*, 'ENTER VALUE FOR DT (SECONDS)'
    READ*, DT

ENDIF

PRINT*, 'ENTER TIME STEP FOR SAVING DATA1 (Seconds)'

```

```

READ*,TS

PRINT*, 'ENTER VALUE OF THETA (0-1)'

READ*,THETA

*****
*****INPUT OF PHYSICAL DATA1*****
*****

PRINT*, 'ENTER MASS FRACTION OF SIZING ON CARBON FIBER'

READ*,MF

PRINT*, 'ENTER DENSITY OF SIZING (g/cm3)'

READ*,PS

PRINT*, 'DIFFUSIVITY = A*EXP(EA*WS)'

PRINT*, 'ENTER A <MICRON^2/S>'

READ*,PREEXP

PRINT*, 'ENTER EA'

READ*,EA

PRINT*, 'ENTER INITIAL WS'

READ*,WSI

*****
*****EQUILIBRIUM SIZING AMOUNT IN MATRIX*****
*****

PRINT*,
&'ENTER THERMODYNAMIC EQUILIBRIUM OF SIZING IN MATRIX (WT/WT)'

READ*,WSEQ

*****
*****ENTER ITERATIVE PARAMETERS*****
*****

PRINT*, 'ENTER # OF ITERATION LOOPS TO PERFORM'

READ*,MAXLOOP

*****
*****ENTER IF PROCESS IS GOING TO BE RELAXATION OR*****
*****DISENTANGLEMENT CONTROLLED*****
*****

PRINT *,
&'FOR DISSOLUTION CONTROLLED INTERDIFFUSION PLEASE ENTER <1>'

```

```

PRINT*,
&'FOR RELAXATION/DISENTANGLEMENT CONTROLLED PLEASE ENTER <0>'

READ*,ANSW

IF (ANSW.NE.1) THEN

    ANSW=0

    PRINT*,
    &'ENTER VALUE FOR FLUX <G/CM^S/S> NOTE: THIS SHOULD BE >0.0'

    READ*,SIZFLUX

ENDIF

*****
*****STORE PHYSICAL DATA*****
*****

WRITE(10,*) 'DIFF= A*EXP(EA*WS)'

WRITE(10,*) 'A =',PREEXP

WRITE(10,*) 'EA =',EA

IF (INFO.EQ.1) THEN

    WRITE(10,*) 'DT=',DT

ELSE

    IF (INFO_2.EQ.1) THEN

        WRITE(10,*) 'DT=(DTF-DTO)/TF+DTO'
        WRITE(10,*) 'DTO=',DTO
        WRITE(10,*) 'DTF=',DTF

    ELSE

        DO 888 I=1,STEPS

            WRITE(10,*) 'DT=',DTSTEP(I)
            WRITE(10,*) 'FOR TIME LESS THAN',ENDTIME(I)

888        CONTINUE

    ENDIF

ENDIF

WRITE(10,*) 'THETA=',THETA

IF (ANSW.EQ.1) THEN

    WRITE(10,*) 'PROCESS IS DISSOLUTION CONTROLLED'

```

```

ELSE

    WRITE(10,*)
    & 'PROCESS IS RELAXATION/DISENTANGLEMENT CONTROLLED'
    WRITE(10,*) 'FLUX <G/CM^2/S> =',SIZFLUX

ENDIF

WRITE(10,*) 'THERMODYNAMIC EQUILIBRIUM AMOUNT OF SIZING <WT/WT>'
& ',WSEQ
WRITE(10,*) 'MASS FRACTION SIZING ON FIBER <WT/WT>',MF

*****
*****CONVERT TO MICRONS*****
*****

PS=PS*1.0D-12
SIZFLUX=SIZFLUX*1.0D-8

*****
*****CALCULATIONS INVOLVING PHYSICAL DATA1*****
*****

THICK=RF*((1.0+PF/PS*MF/(1.0-MF))**.5-1.0)

MASS=PI*(2.00*RF*THICK+THICK**2.00)/12.0

*****
*****CALCULATE BANDWIDTH*****
*****

BAND = ESSBC + 2

PRINT*, 'CALCULATED BANDWIDTH =',BAND

*****
*****IMPLEMENTING INITIAL CONDITION*****
*****
*****WSF IS THE INITIAL GUESS FOR THE FINAL CONCENTRATION AT*****
*****TIME K+1. THIS IS SET EQUAL TO THE INITIAL CONDITION*****
*****

DO 136 I=1,NODES

    WS(I)=WSI
    WSFUTURE(I)=WSI

136 CONTINUE

*****
*****IMPLEMENTING ESSENTIAL BOUNDARY CONDITION IF NEEDED*****
*****

IF (ANSW.EQ.1) THEN

    DO 1007 I=1,ESSBC

```

```

      WS(DATA1(I))=WSEQ
      WSFUTURE(DATA1(I))=WSEQ

1007   CONTINUE

      ENDIF

*****
*****INITIALIZING TIME TO ZERO*****
*****

      TIME=0.0D0

*****
*****WHEN UNCLE IS ZERO M HAS NOT BEEN CALCULATED*****
*****IT ONLY NEEDS TO BE COMPUTED ONCE!!!*****
*****IT IS NOT A FUNCTION OF TIME*****
*****FSUR IS ALSO NOT A FUNCTION OF TIME*****
*****

      UNCLE=0

*****
*****WHEN DOME IS ZERO Q HAS NOT BEEN CALCULATED YET*****
*****

      DOME=0

*****
*****WHEN ITER IS ZERO*****
*****L, R, B, AND P ARE CALCULATED*****
*****THEY ONLY NEED TO BE COMPUTED ONCE PER ITERATION!!!*****
*****

      ITER=0

*****
*****INITIALIZING LOOP COUNTER TO ZERO*****
*****

      LOOP=0

*****
*****IF SKIP IS ZERO THEN SIZING STILL REMAINS*****
*****& *****
*****STIFFNESS MARIX AND LOAD VECTOR MUST BE NORMALIZED*****
*****COLUMN IS THE COLUMN POSITION IN THE BANDED MATRIX*****
*****

      SKIP=0

*****
*****IF DONG IS ZERO THEN WS(X,Y) IS NOT*****
*****STORED IN FILE*****
*****

```

```

DONG=0

*****
****TODISK DETERMINES WHEN TO WRITE MASS DISSOLVED TO DISK*****
*****

TODISK = 0

*****
*****COUNTER DETERMINES WHEN TO WRITE DATA TO DISK *****
*****

COUNTER=0.0D0

*****
*****SHIT DETERMINES WHEN TO PUT IN THE ESSENTIAL BOUNDARY*****
*****DO TO CALCULATED BOUNDARY BEING GREATER THAN EQUILIBRIUM***
*****

SHIT=0

*****
****INITIALIZE ARRAYS THAT ARE NOT FUNCTIONS OF TIME TO ZERO****
***ALSO INITIALIZING F(I) TO ZERO FOR THE INITIAL CALCULATION***
*****

DO 80 I=1,NODES

DO 90 J=1,BAND

MS(I,J)=0.0D0

90 CONTINUE

Q(I)=0.0D0

80 CONTINUE

*****
****DETERMINE VALUE OF DT TO UTILIZE FOR THIS TIME STEP*****
*****

2 IF (INFO.EQ.2) THEN

IF (INFO_2.EQ.1) THEN

DT = (DTF - DTO)/TF*TIME + DTO

ELSE

I=1

779 IF (TIME.LT.ENDTIME(I)) THEN

DT=DTSTEP(I)

ELSE

```

```

                I=I+1

                GOTO 779

            ENDIF

        ENDIF

    ENDIF

*****
*****INITIALIZE ARRAYS TO ZERO THAT ARE A FUNCTION OF TIME****
*****BUT AREN'T CHANGED DURING AN ITERATION*****
*****

    DO 81 I=1,NODES

        DO 91 J=1,BAND

            LS(I,J)=0.0D0

91         CONTINUE

            R(I)=0.0D0

81        CONTINUE

*****
*****INITIALIZE ARRAYS TO ZERO THAT ARE A FUNCTION OF TIME****
*****BUT DO CHANGE DURING AN ITERATION*****
*****

    DO 77 LOOP=1,MAXLOOP

        PRINT*, 'THIS IS LOOP NUMBER', LOOP

    DO 82 I=1,NODES

        DO 92 J=1,BAND

            LSF(I,J)=0.0D0

92         CONTINUE

            RFUT(I)=0.0D0

82        CONTINUE

*****
*****INITIALIZE MASS ELEMENT TO ZERO*****
*****

*         IF (SKIP.EQ.0) THEN

            MASSE=0.0D0

```

```

*      ENDIF

*****
*****ASSEMBLE THE STIFFNESS MATRIX*****
*****AND THE LOAD VECTOR*****
*****ASSEMBLE ELEMENT STIFFNESS MATRIX*****
*****DO VOLUME INTEGRAL PARTS FIRST*****
*****

      DO 100 ELEMENT=1,NELEM

*****
*****BEGIN 10 POINT GAUSSIAN INTEGRATION*****
*****INTEGRATE OVER S AND T IF 2-D INTEGRATION*****
*****

      DO 150 M=1,GAUSSPTS

          DO 160 N=1,GAUSSPTS

              T=GAUSS(M)

              S=GAUSS(N)

              CALL SHAPFUN(S,T,NS,DSNS,DTNS)

*****
*****INITIALIZE VARIABLES TO ZERO*****
*****

          X=0.0D0

          Y=0.0D0

          DXS=0.0D0

          DYS=0.0D0

          DXT=0.0D0

          DYT=0.0D0

          WSP=0.0D0

          WSF=0.0D0

*****
*****CALCULATE VALUES OF X,Y, AND WS AT GAUSS POINTS*****
*****

          DO 1010 K=1,NPE

              X=X+NODX(ICON(ELEMENT,K))*NS(K)

              Y=Y+NODY(ICON(ELEMENT,K))*NS(K)

              WSP=WSP+WS(ICON(ELEMENT,K))*NS(K)

```

```

      WSF=WSF+WSFUTURE ( ICON ( ELEMENT , K ) ) *NS ( K )

*****
*****CALCULATE DERVIATIVES OF X AND Y W/R TO S AND T*****
*****

      DXS=DXS+NODX ( ICON ( ELEMENT , K ) ) *DSNS ( K )

      DYS=DYS+NODY ( ICON ( ELEMENT , K ) ) *DSNS ( K )

      DXT=DXT+NODX ( ICON ( ELEMENT , K ) ) *DTNS ( K )

      DYT=DYT+NODY ( ICON ( ELEMENT , K ) ) *DTNS ( K )

1010      CONTINUE

*****
*****CALCULATE JACOBIAN*****
*****

      JACOB=DXS*DYT-DYS*DXT

*****
*****DETERMINE MASS OF SIZING DISSOLVED IN AT PREVIOUS TIME STEP**
*****

*****
*****CALCULATE MASS OF SIZING IN THIS ELEMENT*****
*****

*          IF ( SKIP.EQ.0 ) THEN

          IF ( ITER.EQ.0 ) THEN

              MASSE=WSP*JACOB*WEIGHT ( M ) *WEIGHT ( N ) +MASSE

*          ENDIF

          ENDIF

*****
*****NOW GENERATE MATRICES OVER THIS ELEMENT*****
*****

      DO 110 I=1,NPE

          DO 120 J=1,NPE

*****
*****IF TRUE COLUMN IS LESS THAN ROW THEN DON'T CALCULATE*****
*****

              IF ( ICON ( ELEMENT , J ) .LT. ICON ( ELEMENT , I ) ) GOTO 120

*****
*****IF TRUE COLUMN IS LESS THAN ROW THEN DON'T CALCULATE*****

```

```

*****
          COLUMN = ICON(ELEMENT,J) - ICON(ELEMENT,I) + 1
*****
*****VOLUME INTEGRAL PART OF STIFFNESS MATRIX*****
*****
155          IF (UNCLE.EQ.0) THEN

              ME=NS(I)*NS(J)*JACOB*WEIGHT(M)*WEIGHT(N)

              MS(ICON(ELEMENT,I),COLUMN)=MS(ICON(ELEMENT,I)
&              ,COLUMN) + ME

              ENDIF

              IF (ITER.EQ.0) THEN

                  LE=(DIFF(WSP)*((DSNS(I)*DYT-DTNS(I)*DYS)*
&                  (DSNS(J)*DYT-DTNS(J)*DYS)
&                  +(DTNS(I)*DXS-DSNS(I)*DXT)*(DTNS(J)*
&                  DXS-DSNS(J)*DXT))/JACOB
&                  )*WEIGHT(M)*WEIGHT(N)

                  LS(ICON(ELEMENT,I),COLUMN)=LS(ICON(ELEMENT,I)
&                  ,COLUMN) + LE

                  ENDIF

                  LEF=(DIFF(WSF)*((DSNS(I)*DYT-DTNS(I)*DYS)*
&                  (DSNS(J)*DYT-DTNS(J)*DYS)
&                  +(DTNS(I)*DXS-DSNS(I)*DXT)*(DTNS(J)*
&                  DXS-DSNS(J)*DXT))/JACOB
&                  )*WEIGHT(M)*WEIGHT(N)

                  LSF(ICON(ELEMENT,I),COLUMN)=LSF(ICON(ELEMENT,I)
&                  ,COLUMN) + LEF

*****
*****
*****
120          CONTINUE

110          CONTINUE

160          CONTINUE

150          CONTINUE

100          CONTINUE

*****
*****ASSEMBLE SURFACE INTEGRAL FOR FLUX CALCULATION*****
*****DO NOT DO IF PROCESS IS DISSOLUTION CONTROLLED*****
*****IF NOT DO ONLY ONCE. THIS TERM IS NOT A*****

```

```

*****FUNCTION OF TIME MATRIX*****
*****

      IF ((ANSW.EQ.0).AND.(UNCLE.EQ.0)) THEN

        DO 200 ELEMENT=1,NSURELE

          DO 210 M=1,GAUSSPTS

*****NOTE: FOR THIS BOUNDARY S IS ALWAYS GOING TO BE -1*****
*****

            S=-1.0D0

            T=GAUSS(M)

            CALL SHAPFUN(S,T,NS,DSNS,DTNS)

*****
*****INITIALIZE VARIABLES TO ZERO*****
*****

            X=0.0D0

            Y=0.0D0

            DXDPSI=0.0D0

            DYDPSI=0.0D0

*****
*****CALCULATE VALUES OF X,Y,DXDPSI, AND DYDPSI AT GAUSS POINTS**
*****

            DO 5000 K=1,NPLE

*****
*****MUST NOW DETERMINE WHICH ONE TO USE*****
*****NOTE: THIS ONE MUST BE MODIFIED IF SHAPE FUNCTIONS*****
*****ARE CHANGED*****
*****

                IF (K.EQ.1) I=1
                  IF (K.EQ.2) I=4

*****

                X = X + NODX(ICON(ELEMENT,I))*NS(I)

                Y = Y + NODY(ICON(ELEMENT,I))*NS(I)

                DXDPSI=DXDPSI+NODX(ICON(ELEMENT,I))*DTNS(I)

                DYDPSI=DYDPSI+NODY(ICON(ELEMENT,I))*DTNS(I)

5000          CONTINUE

```

```

*****
*****GENERATE THE SURFACE INTEGRAL PORTION OF LOAD VECTOR*****
*****

```

```

DO 5010 I=1,NPLE

```

```

*****
*****MUST NOW DETERMINE WHICH ONE TO USE*****
*****NOTE: THIS ONE MUST BE MODIFIED IF SHAPE FUNCTIONS*****
*****ARE CHANGED*****
*****

```

```

IF (I.EQ.1) K=1
IF (I.EQ.2) K=4

```

```

*****

```

```

& FSUR(ICON(ELEMENT,K))=FSUR(ICON(ELEMENT,K)) +
& SIZFLUX/PS*NS(K)*WEIGHT(M)*((DXDPSI)**(2.0D0)+
& (DYDPSI)**(2.0D0)
& )**(0.5D0)

```

```

5010 CONTINUE

```

```

210 CONTINUE

```

```

200 CONTINUE

```

```

ENDIF

```

```

*****
*****SUM UP MASS AND SEE IF IT IS GREATER THAN THE MASS*****
*****AVAILABLE*****
*****

```

```

IF (ITER.EQ.0) THEN

```

```

MASSF=100.0*MASSE/MASS

```

```

IF (MASSF.LT.100.0) THEN

```

```

SKIP=0

```

```

ELSE

```

```

*****
*****NOW SET SKIP=1 SO THAT ZERO FLUX IS IMPLEMENTED*****
*****

```

```

SKIP=1

```

```

ENDIF

```

```

ENDIF

```

```

*****

```

```

*****CALCULATE A & B*****
*****

DO 460 I=1,NODES

DO 470 J=1,BAND

A(I,J)=DT*THETA*LSF(I,J) + MS(I,J)

IF (ITER.EQ.0) B(I,J)=MS(I,J) - (1-THETA)*LS(I,J)*DT

470 CONTINUE

460 CONTINUE

*****
*****LOAD VECTOR TERMS*****
*****

*****SKIP IF ALL THE SIZING IS GONE AND THUS A MATRIX DOES NOT*****
*****NEED MODIFICATION. IF NOT SKIP, THEN IMPLEMENTATION OF ESSBC*****
*****IS INVOKED*****
*****

IF ((SKIP.EQ.1).OR.(ANSW.EQ.0)) GOTO 451

*****

DO 350 I=1,NODES

DO 370 J=1,ESSBC

*****
*****CALCULATE Q AND R*****
*****
*****DETERMINE WHICH TERMS ON BANDED MATRIX TO ADD*****
*****

IF (J.GE.I) THEN

*****
*****IF ESSBC NODE IS GREATER THAN ROW THEN ACCESS BAND*****
*****

COLUMN = J - I + 1

IF (DOME.EQ.0) Q(I)=MS(I,COLUMN)+Q(I)

IF (ITER.EQ.0) R(I)=LS(I,COLUMN)+R(I)

RFUT(I)=LSF(I,COLUMN)+RFUT(I)

ELSE

*****

```

```

*****IF ESSBC NODE IS LESS THAN ROW THEN ACCESS BAND WITH*****
*****ROW AND COLUMN INTERCHANGED*****
*****BE CAREFUL THAT THE COLUMN ACTUAL EXISTS!!!*****
*****

```

```

      COLUMN = I - J + 1

```

```

*****
*****CHECK TO SEE IF COLUMN ACTUALLY EXISTS*****
*****IF IT DOESN'T THEN IT IS ZERO!*****
*****

```

```

      IF (COLUMN.LE.BAND) THEN

```

```

          IF (DOME.EQ.0) Q(I)=MS(J,COLUMN)+Q(I)

```

```

          IF (ITER.EQ.0) R(I)=LS(J,COLUMN)+R(I)

```

```

          RFUT(I)=LSF(J,COLUMN)+RFUT(I)

```

```

      ENDIF

```

```

    ENDIF

```

```

370     CONTINUE

```

```

350     CONTINUE

```

```

*****
****SET ROWS AND COLUMNS ON ESSENTIAL BOUNDARY EQUAL TO ZERO****
*****MUST TAKE INTO ACCOUNT BANDED FORM OF LS AND MS*****
*****

```

```

      DO 400 J=1,ESSBC

```

```

          DO 410 I=1,NODES

```

```

*****
*****NULLIFY BY ROWS ON ESSENTIAL NODES*****
*****

```

```

          IF (I.LE.BAND) THEN

```

```

              A(J,I)=0.0D0

```

```

              IF (ITER.EQ.0) B(J,I)=0.0D0

```

```

          ENDIF

```

```

*****
*****NULLIFY BY COLUMNS ALL ENTRIES ABOVE THE DIAGONAL*****
*****

```

```

          IF (J.GE.I) THEN

```

```

              COLUMN = J - I + 1

```

```

A(I,COLUMN)=0.0D0

IF (ITER.EQ.0) B(I,COLUMN)=0.0D0

ENDIF

410     CONTINUE

400     CONTINUE

*****
*****NORMALIZATION OF A*****
*****

DO 450 I=1,ESSBC

*****
*****NOTE: REAL DIAGONAL ALWAYS ENDS UP IN COLUMN 1*****
*****

A(I,1)=1.0D0

450     CONTINUE

*****
*****WE CAN NOW TELL THE PROGRAM NOT TO CALCULATE Q ANYMORE*****
*****IF IT HAS CALCULATED IT ALREADY*****
*****

DOME=1

*****
*****WE CAN NOW TELL THE PROGRAM NOT TO CALCULATE M AND FSUR*****
*****ANYMORE SINCE IT HAS CALCULATED IT ALREADY*****
*****

451     UNCLE=1

*****
*****INITIALIZE LOAD VECTOR TO ZERO*****
*****IF NEEDED*****
**F(I) DOES NOT CHANGE DURING THE COURSE OF AN ITERATION IF**
*****THE FLUX IS BEING IMPLEMENTED*****
*****

*****
**F(I) DOES NOT CHANGE IF WE ARE IN THE MIDDLE OF AN ITERATION**
*****AND A FLUX IS BEING IMPLEMENTED*****
*****

IF ((ITER.EQ.1).AND.((ANSW.EQ.0).OR.((ANSW.EQ.1).AND.
&(SKIP.EQ.1)))) GOTO 524

*****
*****START CALCULATING F(I)*****
*****

```

```

DO 515 I=1,NODES

    F(I)=0.0D0

*****
*****NULLIFY FMUL(I) IF ITER IS EQUAL TO ZERO*****
*****THEN CALCULATE THE VALUE OF FMUL(I)*****
*****

    IF (ITER.EQ.0) THEN

        FMUL(I)=0.0D0

*****
*****DO THE WS*B MULTIPLICATION IF NEEDED*****
*****

*****CORRECT FOR THE FACT THAT NOT ALL COLUMNS ARE PRESENT*****
*****

        UP = NODES - I + 1

        IF (UP.GE.BAND) THEN

            UPPER = BAND

        ELSE

            UPPER = UP

        ENDIF

        DO 510 J=2-BAND,UPPER,1

*****
*****DETERMINE ACTUAL COLUMN THAT WS CORRESPONDS TO*****
*****

            ACTUAL = I + J - 1

            IF (ACTUAL.GE.I) THEN

*****
*****MULTIPLY TERMS ON AND ABOVE DIAGONAL UTILIZING*****
*****

                FMUL(I)=WS(ACTUAL)*B(I,J) + FMUL(I)

            ELSE

                IF (ACTUAL.GT.0) THEN

*****
*****DETERMINE COLUMN POSITION IN BANDED MATRIX*****
*****

```

```

        COLUMN = I - ACTUAL + 1

        FMUL(I)=WS(ACTUAL)*B(ACTUAL,COLUMN) + FMUL(I)

    ENDIF

    ENDIF

510     CONTINUE

    ENDIF

*****
*****ADD THE B*W MULTIPLICATION TO F*****
*****

    F(I) = F(I) + FMUL(I)

*****
*****NOW ADD THE ESSENTIAL BOUNDARY CONDITION IF NEEDED*****
*****

    IF ((ANSW.EQ.1).AND.(SKIP.EQ.0)) THEN

        F(I) = F(I) + WSEQ*(Q(I)-DT*(1.0D0-THETA)*R(I))-WSEQ*
&      (Q(I)+DT*THETA*RFUT(I))

    ENDIF

*****
*****NOW ADD THE FLUX BOUNDARY CONDITION IF NEEDED*****
*****

    IF (((ANSW.EQ.0).AND.(SKIP.EQ.0)).AND.(I.LE.ESSBC)) THEN

        F(I) = F(I) + DT*FSUR(I)

    ENDIF

*****
*****NORMALIZE THE LOAD VECTOR IF NEEDED*****
*****

    IF (((ANSW.EQ.1).AND.(SKIP.EQ.0)).AND.(I.LE.ESSBC)) THEN

        F(I)=WSEQ

    ENDIF

*****
*****NOW DO THE NEXT VALUE OF I*****
*****

515     CONTINUE

*****

```

```

*****RENAME THE LOAD VECTOR TO WSFUTURE TO PRESERVE THE VALUE*****
*****
524   DO 5005 I=1,NODES
      WSFUTURE(I)=F(I)
5005  CONTINUE
*****
*****TIME TO SOLVE THE EQUATIONS*****
*****
      CALL SOLVE(A,WSFUTURE,BAND,NODES)
      ITER=1
77    CONTINUE
*****
*****DETERMINE IF THERMODYNAMIC EQUILIBRIUM HAS BEEN VIOLATED*****
*****
      IF ((ANSW.EQ.0).AND.(SKIP.EQ.0)) THEN
          DO 987 I=1,ESSBC
              IF (WSFUTURE(I).GT.WSEQ) SHIT=1
987    CONTINUE
          IF (SHIT.EQ.1) THEN
              DO 2031 I=1,NODES
                  WSFUTURE(I)=WS(I)
                  IF (I.LE.ESSBC) THEN
                      WSFUTURE(I)=WSEQ
                      WS(I)=WSEQ
                  ENDIF
2031  CONTINUE
          ANSW=1
          ITER=0
          GOTO 2
      ENDIF
ENDIF

```

```

*****
*****TIME TO GET READY FOR THE NEXT TIME INCREMENT*****
***WIPE OUT PAST VALUES OF WS AND SET INITIAL GUESS FOR WSFUTURE**
*****EQUAL TO PRESENT VALUES*****
*****

      DO 527 I=1,NODES

          WS(I)=WSFUTURE(I)

527    CONTINUE

      ITER=0

*****
*****INCREMENT TIME LOCATORS*****
*****

      TIME = TIME + DT

      COUNTER = COUNTER + DT

*****
*****PRINT WHAT TIME WE JUST CALCULATED*****
*****

      PRINT*,'FINISHED CALCULATING RESULTS FOR TIME = ',TIME

*****
*****MUST WRITE MASS IF PREVIOUS STEP INVOLVED DATA STORAGE*****
*****

      IF (TODISK.EQ.1) THEN

          WRITE(10,*)

          WRITE(10,*) MASSF

          TODISK = 0

      ENDIF

      IF (COUNTER.LT.TS) GOTO 3

      COUNTER = 0.0D0

      TODISK = 1

      WRITE(10,*)

      WRITE(10,*) TIME

      DO 800 I=1,NODES

          WRITE(10,3000) WS(I)

          PRINT*,'WS(',I,')=',WS(I)

```

```

800  CONTINUE

3000  FORMAT(E15.5)

      PRINT*, '% MASS DISSOLVED IN=', MASSF

*****
*****TIME TO DO IT AGAIN IF NESSESARY*****
*****

3    IF (TIME.LT.TF) GOTO 2

*****
*****FINISH UP*****
*****

3027  PRINT*, 'I AM DONE DAMMIT'

      CLOSE(10)

*****
*****END OF MAIN PROGRAM*****
*****

      END

*****
*****SUBROUTINES USED IN MAIN PROGRAM*****
*****

      SUBROUTINE SHAPFUN(S,T,NS,DSNS,DTNS)

*****

*****DECLARE VARIABLE USED AS PARAMETERS*****

      INTEGER NPE

*****SET PARAMETERS*****

      PARAMETER (NPE=4)

*****DIMENSIONALIZE VARIOUS ARRAYS*****

      DIMENSION NS(NPE),DSNS(NPE),DTNS(NPE)

*****

*****VARIABLE DECLARATION*****

      DOUBLE PRECISION S,T,NS,DSNS,DTNS

*****INPUT THE SHAPE FUNCTIONS FOR QUADRILATERALS*****
*****NOTE: IF YOU CHANGE THESE THEN THE SURFACE INTEGRAL*****
*****SUBROUTINE NEEDS TO BE MODIFIED*****

```

```

NS(1)=.25D0*(T-1.0D0)*(S-1.0D0)
NS(2)=-.25D0*(T-1.0D0)*(S+1.0D0)
NS(3)=.25D0*(S+1.0D0)*(T+1.0D0)
NS(4)=-.25D0*(T+1.0D0)*(S-1.0D0)

```

*****INPUT THE DERIVATIVES OF THE VARIOUS SHAPE FUNCTIONS*****

```

DSNS(1)=.25D0*(T-1.0D0)
DTNS(1)=.25D0*(S-1.0D0)
DSNS(2)=-.25D0*(T-1.0D0)
DTNS(2)=-.25D0*(S+1.0D0)
DSNS(3)=.25D0*(T+1.0D0)
DTNS(3)=.25D0*(S+1.0D0)
DSNS(4)=-.25D0*(T+1.0D0)
DTNS(4)=-.25D0*(S-1.0D0)

```

RETURN

END

*****BANDED EQUATION SOLVER*****
*******NOTE: BANDED EQUATION SOLVER OBTAINED FROM REFERENCE 4.5*******
*******Cook, Malkus, and Plesha, 'Concepts and Applications of Finite*******
*******Element Analysis', 3rd Edition, Wiley and Sons.*******

SUBROUTINE SOLVE(AP,FP,BANDP,NODESP)

INTEGER NODESMAX,BANDMAX

PARAMETER (NODESMAX=5000,BANDMAX=200)

DIMENSION AP(NODESMAX,BANDMAX),FP(NODESMAX)

DOUBLE PRECISION AP,FP,ASS

INTEGER NODESP,NEQP,NEQM,BANDP,UPPER,I,N,L,J,M

NEQP=NODESP+1

NEQM=NODESP-1

```

2000 DO 2010 N=1,NEQM
      UPPER=MIN(BANDP,NEQP-N)
      DO 2020 L=2,UPPER
        ASS=AP(N,L)/AP(N,1)
        I=N+L-1
        J=0
        DO 2030 M=L,UPPER
          J=J+1
          AP(I,J)=AP(I,J)-ASS*AP(N,M)
2030 CONTINUE
      AP(N,L)=ASS
2020 CONTINUE
2010 CONTINUE
2040 DO 2050 N=1,NEQM
      UPPER=MIN(BANDP,NEQP-N)
      DO 2060 L=2,UPPER
        I=N+L-1
        FP(I)=FP(I)-AP(N,L)*FP(N)
2060 CONTINUE
      FP(N)=FP(N)/AP(N,1)
2050 CONTINUE
      FP(NODESP)=FP(NODESP)/AP(NODESP,1)
      DO 2070 N=NEQM,1,-1
        UPPER=MIN(BANDP,NEQP-N)
        DO 2080 L=2,UPPER
          M=N+L-1
          FP(N)=FP(N)-AP(N,L)*FP(M)
2080 CONTINUE
2070 CONTINUE

```

RETURN

END

APPENDIX III

PROGRAM SORT

```
*****
*****DECLARE DIMENSIONS VARIABLES*****
*****

INTEGER NODESMAX, ESSBCMAX

*****
*****DECLARE PARAMETER*****
*****

PARAMETER (NODESMAX=5000, ESSBCMAX=200)

*****
*****DIMENSION ARRAYS*****
*****

REAL NODX(NODESMAX), NODY(NODESMAX), WS(NODESMAX)
REAL R(NODESMAX), WSN(NODESMAX)
INTEGER SELEC(ESSBCMAX)

*****
*****DECLARE VARIABLES*****
*****

INTEGER NODES, ESSBC, NODESAV, COUNT, NUM, I, J

REAL RF, PI

*****
*****DECLARE PARAMETERS*****
*****

PARAMETER (RF=3.5E0, PI=3.141592654E0)

*****
*****READ NUMBER OF NODES*****
*****

OPEN(11, FILE='NODES.MES', STATUS='OLD')

READ(11, *) NODES

PRINT*, 'NODES=', NODES

CLOSE (11)

*****
*****READ NUMBER OF ESSBC*****
*****

OPEN(11, FILE='ESSBC.MES', STATUS='OLD')
```

```

READ(11,*) ESSBC

PRINT*,'ESSBC=',ESSBC

CLOSE (11)

*****
*****READ MESH AND SIMULATION DATA FOR THIS TIME*****
*****

OPEN(11,FILE='NODX.MES',STATUS='OLD')
OPEN(12,FILE='NODY.MES',STATUS='OLD')
OPEN(13,FILE='WS.DAT',STATUS='OLD')

DO 10 I=1,NODES

    READ(11,*) NODX(I)
    READ(12,*) NODY(I)
    READ(13,*) WS(I)

10    CONTINUE

CLOSE (11)
CLOSE (12)
CLOSE (13)

*****
*****OPEN NEW DATA FILES TO WRITE TO*****
*****

OPEN(11,FILE='R.DAT',STATUS='NEW')
OPEN(12,FILE='WSN.DAT',STATUS='NEW')

*****
*****INPUT WHICH ANGULAR LINE YOU ARE INTERESTED IN*****
*****

35    PRINT*,'THERE ARE ',ESSBC,' ISO-ANGLE LINES TO SELECT'

PRINT*,'HOW MANY ISO-ANGLES DO YOU WISH TO GENERATE'

READ*,NUM

IF (NUM.GT.ESSBC) THEN

    PRINT*,'INVALID ENTRY! PLEASE ENTER AGAIN!'

    GOTO 35

ENDIF

DO 100 I=1,NUM

36    PRINT*,'ENTER ISO-ANGLE LINE FOR SELECTION #',I

READ*,SELEC(I)

```

```

IF ((SELEC(I).GT.ESSBC) .OR. (SELEC(I).LE.0)) THEN

  PRINT*, 'INVALID ENTRY!  PLEASE ENTER AGAIN!'

  GOTO 36

ENDIF

PRINT*, 'THE ISO-ANGLE IS ',180.0/PI*ASIN(NODY(SELEC(I))/RF)

*****
*****WRITE SOME INTRODUCTORY DATA TO THE FILE*****
*****

WRITE(11,*) 'THIS IS ISO-ANGLE #',SELEC(I)
WRITE(12,*) 'THIS IS ISO-ANGLE #',SELEC(I)

*****
*****SAVE ALL X AND WS DATA ON THIS ISO-ANGLE LINE*****
*****

COUNT=1

NODESAV=SELEC(I)

DO 40 WHILE(NODESAV.LE.NODES)

*****
*****COMPUTE VALUE FOR R*****
*****

R(COUNT) = ((NODX(NODESAV)+RF)**2+(NODY(NODESAV))**2)**0.5-RF

WSN(COUNT)=WS(NODESAV)

COUNT = COUNT + 1
NODESAV = NODESAV + ESSBC

40  CONTINUE

COUNT = COUNT - 1

DO 50 J=1,COUNT

  WRITE(11,*) R(J)
  WRITE(12,3000) WSN(J)

50  CONTINUE

3000  FORMAT (E15.5)

WRITE(11,*)
WRITE(12,*)

100  CONTINUE

```

CLOSE (11)
CLOSE (12)

END

VITA

The author was born on February 5, 1971 in Bluefield, West Virginia. Before graduating from Narrows High School in 1989, he attended New River Community College where he completed his senior year of high school and freshman year of college. In the summer of 1989, he enrolled at Virginia Polytechnic Institute and State University in Blacksburg, VA as a sophomore. He co-oped for one year with Union Carbide Chemicals and Plastics Company in South Charleston, WV. In May of 1993, he earned a Bachelor of Science Degree in Chemical Engineering with minors in Chemistry and Mathematics. In August of 1993, he returned to Virginia Tech to pursue a graduate degree. In February of 1996, he earned a Masters of Science Degree in Chemical Engineering. In August of 1996, he returned to Virginia Tech to pursue a doctoral degree. In December of 1999, he earned a Doctor of Philosophy Degree in Chemical Engineering.